Improving statistical and computational techniques for supernova cosmology

The Path to Uncovering Dark Energy

Patrick James Armstrong — March 2025

A thesis submitted for the degree of

Doctor of Philosophy

at The Australian National University.

FINAL

Australian National University

NATURAM PRIMUM COGNOSCERE RERUM

Typeset in Palatino by TEX and LATEX 2_ε.

Except where otherwise indicated, this thesis is my own original work.

— Patrick James Armstrong

March 2025

To Mama, Papa, my brother, and especially my wife Eve — for getting me through a PhD which almost killed me (literally).

Acknowledgments

With thanks to my external supervisors Sam Hinton, Dillon Brout, and Rick Kessler. I also want to thank all my collaborators throughout DES, in particular Dan Scolnic, Alex Kim, Georgie Taylor, Maria Vincenzi, and Anais Möller. Finally, thanks to my supervisors Brad Tucker and Chris Lidman, whose invaluable guidance made this thesis possible.

Abstract

Modern cosmological analysis is focused on investigating the mechanics of the accelerated expansion of our Universe and uncovering the nature of the mysterious dark energy which drives this acceleration. Accelerated expansion was first discovered in the late 1990s using type Ia supernovae (SNe Ia) as standard candles to probe the evolution of our Universe over time. Since this discovery, significant effort has been devoted to improving the statistical and systematic uncertainties present in supernova cosmology to improve the constraining power of these analyses. Statistical uncertainties were improved by observing orders of magnitude more SNe Ia, whilst improvements in systematic uncertainty were driven by developments in every step in the analysis.

These efforts have culminated in the Dark Energy Survey (DES) supernova program. With 1635 SNe Ia, this represents the largest sample of SNe Ia, and thus the greatest constraining power of any supernova sample to date. DES recently released the results of their five-year supernova cosmology program. When combining constraints on a Flat wCDM cosmology from SNe Ia with other cosmological probes, DES find $(\Omega_{\mathrm{M}}, w) = (0.321 \pm 0.007, -0.941 \pm 0.026)$, the first possible evidence of a $> 2\sigma$ divergence from dark energy as a cosmological constant. This has been the prevailing theory of dark energy since its discovery, leading to the ΛCDM concordance model of our Universe. However, with the improved constraints provided by the DES analysis, this model is thrown into question for the first time.

To achieve the constraining power required to get these results, improving the statistical and systematic uncertainties throughout the entire DES cosmological pipeline is required. These improvements are the result of the work of dozens of researchers around the world. In this thesis, I will focus on my contributions improving Pippin, the overarching pipeline which enables the DES analysis, and developing a new method for evaluating the consistency of the DES results.

The results from the DES analysis are far from conclusive, so if we are to determine the legitimacy of the cosmological constant, further improvements to the statistic and systematic uncertainties are required. Upcoming surveys, such as the Legacy Survey of Space and Time (LSST), aim to observe orders of magnitudes more SNe Ia than DES; however, with these improvements to the sample size come a whole host of challenges which must be addressed. As part of this

thesis, I discuss these challenges and my efforts to develop new statistical techniques to address these challenges. In particular, I investigate likelihood-free, forward-modelled techniques which provide significantly greater control over systematic uncertainties with fewer assumptions, at the cost of much greater computational complexity.

Contents

List of Figures

List of Tables

List of Code Blocks

List of Lists

Chapter 1

Precision Cosmology — An Introduction

Cosmology is concerned with understanding the structure, components, history, and fate of our Universe. In order to achieve this, cosmologists must understand almost 14 billion years worth of complex evolution from observations of our Universe. These observations have revealed astonishing truths about the nature of the Universe and our place within it.

Initial investigations by Greek philosophers gave us the geocentric Ptolemaic model, which suggested that our Universe consisted of the Earth at the centre of the Universe, with the planets and the Sun orbiting the Earth, and the stars fixed at 'some modest distance'.

In the 16th century, the work of astronomers such as Nicolaus Copernicus, Johannes Kepler, and Galileo Galilei showed that in fact it was Earth that orbited the Sun. Additional observations by William Herschel showed that the stars were not fixed in a celestial sphere, but were in fact distributed throughout space.

In 1920 the 'Great Debate' was held at the Smithsonian Museum of Natural History between Harlow Shapley and Heber Curtis on the nature of spiral nebulae and the size of the Universe (Shapley and Curtis, 1921). The debate involved whether the Milky Way galaxy constituted the entire Universe or whether it was one of many galaxies. This debate was eventually resolved by observations of Edwin Hubble (Hubble, 1925) who measured Cepheid variable stars at distances much further than could be contained by the Milky Way, implying that the Universe was much larger than previously suspected. These same Cepheid observations would then be used by Hubble to show that the Universe was not static, but was expanding. Thus, our picture of the Universe changed from a small, geocentric system of perfect spheres to a large, perhaps infinite, chaotic, and dynamic system.

Since Hubble's discoveries, our view of the Universe has only grown more complex, with new discoveries including dark matter (reviewed in Bertone and Hooper, 2018), and dark energy and the accelerated expansion of the Universe (Perlmutter et al., 1999; Riess et al., 1998; Schmidt et al., 1998). In addition, the depth and scale of our observations have improved drastically over time, leading to larger surveys and more data. This in turn has necessitated the development of new statistical techniques to handle the flood of cosmological data being produced. In the field of supernova cosmology, we are now entering the next phase of cosmological research, with the completion of the Dark Energy Survey supernova program 5 year analysis (DES-SN5YR; DES Collaboration et al., 2024a) and the upcoming Legacy Survey of Space and Time (LSST; LSST Science Collaboration et al., 2009).

The scale of supernova surveys has been increasing in size and complexity with each successive survey, leading to increased precision in cosmological parameters. With the next phase of supernova cosmology surveys, we may be able to differentiate between time-dependent models of dark energy and finally discover the truth behind the mysterious force that governs our Universe. To achieve this goal, we will need to develop techniques to reduce uncertainties and remove biases as much as possible.

This chapter will describe the formalism of modern cosmological research, including both the physics and statistics that allowed us to understand the Universe thus-far. I will describe the concordance model of our Universe, the ΛCDM model, and the numerous techniques used to rigorously investigate this model. Additionally, I will examine how the techniques of SN cosmology have changed since the discovery of the accelerating universe. Finally, I will discuss the shortcomings of modern cosmological techniques and where improvements can be made.

1.1 ΛCDM Cosmology

Modern cosmological theory is derived from Einstein's General Theory of Relativity (GR; Einstein, 1917). In their book *Gravitation* (Misner et al., 1970), the physicist John Archibald Wheeler described this theory as stating:

> Space tells matter how to move
> Matter tells space how to curve

When given an appropriate metric ($g_{\mu\nu}$) the Einstein field equations describe the behaviour and interaction between space-time and matter:

$$G_{\mu\nu} + \Lambda g_{\mu\nu} = \frac{8\pi G}{c^4} T_{\mu\nu} \tag{1.1}$$

$$G_{\mu\nu} \equiv R_{\mu\nu} - \frac{1}{2} R g_{\mu\nu} \tag{1.2}$$

Where $G_{\mu\nu}$ is the Einstein tensor, with the Ricci tensor $R_{\mu\nu}$ measuring the variation from Euclidean space and the scalar curvature R measuring the curvature throughout space. Λ is the cosmological constant which measures the energy density of a uniform vacuum and represents the curvature of spacetime in the absence of matter (i.e. when $T_{\mu,\nu} = 0$). The right-hand side of Equation (1.1) contains the stress-energy tensor $T_{\mu\nu}$ along with the physical constants $G = 6.67 \times 10^{-11}\ m^3\ kg^{-1}\ s^{-2}$, the gravitational constant, and the speed of light $c = 3 \times 10^8\ m\ s^{-1}$.

By defining a metric and a stress-energy tensor and solving the Einstein field equations, one is able to describe the interplay between space-time and the matter that resides within. The metric used in modern cosmology is the Friedmann-Lemaître-Robertson-Walker (FLRW) metric (Friedmann, 1922; Lemaître, 1927; Robertson, 1929; Walker, 1935). This metric exactly solves Equation (1.1), and makes the assumptions that our Universe is homogeneous and isotropic. The FLRW metric is given as:

$$-c^2 d\tau^2 = -c^2 dt^2 + a(t)^2 d\mathbf{\Sigma}^2 \tag{1.3}$$

Where c is the speed of light, $d\tau$ is an infinitesimal change in 'proper time' (or observer time) between two events, dt is the associated change in the cosmological time coordinate, $a(t)$ is the scale of the Universe at cosmological time t, and $d\mathbf{\Sigma}$ is the change in 3-dimensional spatial coordinates. The scale factor $a(t)$ is defined to be 1 at the present time, and measures the size of the Universe relative to its current size.

As the curvature of the Universe is not known a priori, $d\mathbf{\Sigma}$ is often written in terms of the curvature parameter k:

$$d\mathbf{\Sigma}^2 = dr^2 + S_k(r)^2 d\mathbf{\Omega}^2 \tag{1.4}$$
$$d\mathbf{\Omega}^2 = d\theta^2 + \sin(\theta)^2 d\phi^2 \tag{1.5}$$
$$S_k(r) = \begin{cases} \sqrt{k}^{-1}\sin(r\sqrt{k}) & k > 0 \\ r & k = 0 \\ \sqrt{|k|}^{-1}\sinh r\sqrt{|k|} & k < 0 \end{cases} \tag{1.6}$$

Where r is the radial distance coordinate, θ is the polar angle coordinate, and ϕ is the azimuthal angle coordinate.

This gives rise to three paradigms:

- $k > 0$: The Universe has positive, spherical curvature
- $k = 0$: The Universe has zero, flat curvature
- $k < 0$: The Universe has negative, hyperbolic curvature

In addition to the FLRW metric, we use the stress-energy tensor of a perfect fluid, which is described as:

$$T_{\mu\nu} = (\rho c^2 + P)U_\mu U_\nu + P g_{\mu\nu} \tag{1.7}$$

Where ρ is the mass density, P the isotropic pressure, and U the 4-velocity vector field.

When the FLRW metric is applied to Einstein's field equations, alongside the stress-energy tensor for a perfect fluid, Einstein's field equations can be solved and simplified to form the Friedmann Equation[1]:

$$\frac{\mathrm{H}(t)^2}{\mathrm{H}_0^2} = \Omega_{0,\mathrm{R}} a(t)^{-4} + \Omega_{0,\mathrm{M}} a(t)^{-3} + \Omega_{0,\mathrm{DE}} a(t)^{-3(1+w)} + (1 - \sum_{i\in\{\mathrm{R,M,DE}\}} \Omega_{0,\mathrm{i}} a^{-2}) \tag{1.8}$$

Where $\mathrm{H}(t)$ is the Hubble parameter, which describes the expansion rate of the

[1] The Friedmann Equation can more generally be written as the sum over all Ω components, for which each component has a different equation-of-state parameter. The version presented in Equation (1.8) is a special case for a Universe consisting of radiation, matter, and dark energy.

Universe, usually in units of $km/s/Mpc$, with $\mathrm{H}_0 = \mathrm{H}(t_0)$ the Hubble parameter at the current time. The Ω parameters describe the energy density of the constituent components of the Universe, including radiation (Ω_R), dark and baryonic matter (Ω_M), and dark energy (Ω_DE).

As in H_0, the Ω_0 parameters are the values of the Ω parameters at the current time. All Ω parameters are defined relative to the critical density ρ_c which describes the energy density needed for a flat ($k = 0$) Universe:

$$\Omega \equiv \frac{\rho}{\rho_c} = \frac{8\pi G}{3H^2}\rho \tag{1.9}$$

Finally, w is the dark energy equation of state parameter. It represents the ratio of the pressure and the energy density of dark energy and parameterises different models of dark energy. When $w = -1$, Ω_DE no longer scales with $a(t)$, instead acting as a cosmological constant (Ω_Λ).

Given the Friedmann equations, we can calculate the scale factor of the Universe at any cosmological time t, and thus understand its history and evolution. However, the parameters H_0, $\Omega_{0,\mathrm{R}}$, $\Omega_{0,\mathrm{M}}$, $\Omega_{0,\mathrm{DE}}$, and w are not known a priori. Thus, it is the aim of modern cosmology to use observational techniques to measure these unknown parameters, and through this better understand our Universe.

1.1.1 Ω_R: Radiation

The FLRW metric implies a dynamic Universe, and allows for extrapolating both forwards and backwards in time to probe the state of the Universe throughout its history. Extrapolating this expansion backward through time eventually leads to a scale factor of 0, i.e. a Universe that consisted in its entirety of a single, infinitesimal point (Lemaitre, 1934). This is the Big Bang Theory, which suggests that the extremely early Universe was small, dense, and extremely hot. At this stage, the energy density of the Universe was dominated by radiation (Ω_R). The cooling of this radiation can still be observed as the Cosmic Microwave Background (CMB).

1.1.2 Ω_M: Matter

As the Universe expanded and cooled, particles were able to coalesce and form atoms and eventually matter. Over time, large-scale structures formed as gravitational forces acted on matter, leading to the first stars, galaxies, and clusters.

Observations of the Coma and Virgo Clusters (Smith, 1936; Zwicky, 1933, respectively) revealed large velocity dispersions when applying the virial theorem to these clusters. Rubin and Ford (1970) found discrepancies between the observed rotational curve of the spiral galaxy M31 and the rotational curve predicted from the observed mass distribution. Similar discrepancies were found for elliptical galaxies (Davies et al., 1983; Faber and Jackson, 1976). All of these observations pointed to the same conclusion that there was more matter in the Universe than could be seen; this unseen matter was coined 'Dark Matter'. In order to produce the observed effects, dark matter must have the following properties:

- Interact gravitationally (i.e. has mass)
- No electromagnetic interaction (i.e. dark)
- A non-uniform distribution throughout the Universe

Additionally, different models of dark matter will describe 'hot', 'warm', or 'cold' dark matter, which refers to the average velocity of dark matter particles in the early Universe. Hot dark matter theories suggest that dark matter particles had relativistic velocities, whilst cold dark matter theories suggest that Dark matter particles had non-relativistic velocities. Evidence from N-body simulations (Blumenthal et al., 1984; Springel et al., 2005) seems to favour cold dark matter (CDM).

There have been several proposed candidates for dark matter, including weakly interacting massive particles (WIMPS; Roszkowski et al., 2018), and axions (Adams et al., 2023). One possibility, which was suggested but has since been proven insufficient, is baryonic matter which was simply too dim to be observed. Dubbed massive compact halo objects (MACHOs; Bennett et al., 1995), these included brown dwarfs, white dwarfs, and neutron stars. Though these objects do exist, they do not account for the total mass needed for the observed properties of dark matter (Alcock et al., 2000). As it stands, dark matter is an ongoing field of research, with many questions and few answers.

1.1.3 Ω_{DE} & w: Dark Energy and the Accelerated Expansion of our Universe

The final and most significant contribution to the total energy density of our Universe is dark energy (also known as vacuum energy). In the 1990s it was understood that the universe was expanding, but the rate of this expansion and how it evolved over time were unknown. Most common theories postulated that the expansion rate was either constant or decaying over time, which would eventually lead to a maximal size of the Universe and eventually a contracting, instead of expanding, Universe.

The 'deceleration parameter' $q = -\frac{\ddot{a}a}{\dot{a}^2}$[1] is a dimensionless measure of the acceleration of the expansion of our Universe at a given time. q can be written in terms of the Ω parameters as:

$$q = \Omega_\mathrm{R} + \frac{1}{2}\Omega_\mathrm{M} + \frac{1+3w}{2}\Omega_\mathrm{DE} \tag{1.10}$$

$$= \frac{1}{2}\Omega_\mathrm{M} - \Omega_\Lambda;\ \text{for } w = -1 \text{ and } \Omega_\mathrm{R} \approx 0 \tag{1.11}$$

Thus, the question of whether the expansion of the Universe is accelerating or decelerating can be answered by constraining the Ω parameters, and using Equation (1.10) to determine whether q is positive (decelerating expansion) or negative (accelerating expansion).

To measure q and discover the expansion history of our Universe, two teams of astronomers — the Supernova Cosmology Project (SCP; Perlmutter et al., 1999), and the High-Z Supernova Search Team (HZT; Riess et al., 1998; Schmidt et al., 1998), used type Ia supernovae to produce a high redshift Hubble diagram. Both teams independently found evidence of an accelerated expansion.

This accelerated expansion is driven by an unknown energy density dubbed 'Dark Energy' which accounts for the majority of the total energy density of the modern Universe. This energy density component is often characterised by the dark energy equation of state parameter $w = \frac{p}{\rho}$. There are numerous theories as to the physical nature of dark energy, though the true origin of dark energy is as yet unknown.

Different models of dark energy can be characterised by the predicted evolution of w over time. To this end, w is often parameterised relative to the scale factor a using the Chevallier–Polarski–Linder (CPL; Chevallier and Polarski, 2001; Linder, 2003) parameterisation:

$$w(a) = w_0 + (1-a)w_a$$

Where the equation of state parameter is described by a constant term w_0 and a linear term w_a, which is well-behaved between $a = 0$ and $a = 1$.

[1] q being negative and called the 'deceleration' parameter come from the historical belief that the Universe was decelerating and thus $\ddot{a} < 0$.

Some models of dark energy include, but are not limited to:

- Vacuum energy or cosmological constant (Λ). Dark energy represents the energy density of a uniform vacuum, providing a constant curvature term to the total curvature of space-time which is independent of radiation, dark matter, or baryonic matter. This is among the simplest theories and is currently favoured by observational evidence. Under this model $w = -1$ and does not evolve with time.
- Quintessence Models. Dark energy is a dynamic scalar field that evolves with time. This theory limits w to the bounds $-1 \leq w \leq 1$, although only $w < -1/3$ allows for accelerated expansion.
- Barotropic Models. These are a class of models in which dark energy pressure can be expressed as some fixed function of dark energy density $p = f(\rho)$. Examples of barotropic models include Chaplygin Gas (Bento et al., 2002; Bilić et al., 2002; Kamenshchik et al., 2001), the linear (Babichev, 2005; Holman and Naidu, 2004), affine (Ananda and Bruni, 2006; Bozza and Bruni, 2009), and quadratic (Ananda and Bruni, 2006) equation of state models, and the Van der Walls equation of state model (Capozziello et al., 2005; Kremer, 2003).

The existence of dark energy heavily relies on the completeness of GR, and there have been several attempts to modify Einstein's original theory to remove the need for Dark Energy. A review of these modified gravity theories is presented in Joyce et al. (2016) but so far none have been able to improve on GR.

1.1.4 Redshift

Redshift (z) is a measure of how much a photon's wavelength has shifted between being emitted (λ_{emit}), and observed (λ_{obs}):

$$1 + z = \frac{\lambda_{obs}}{\lambda_{emit}} \tag{1.12}$$

The source of this shift depends on the state of the emitter at the time of emission, the state of the observer at the time of observation, and on the spacetime between the emitter and the observer that the photon must traverse. The overall redshift of a given photon is often described as the combination of three different sources of redshift, those being Doppler redshift (z_D), cosmological redshift (z_C), and gravitational redshift (z_G).

1.1.4.1 Combining redshifts

A common approximation for combining distinct redshift sources into an overall redshift is:

$$z = z_a + z_b \tag{1.13}$$

with the correct equation being

$$1 + z = (1 + z_a)(1 + z_b) \tag{1.14}$$

Davis et al. (2019) show that making such an approximation can lead to a shift in derived cosmological parameters on the order of 1%, which in the age of precision cosmology is an unacceptable error for an approximation which is not computationally beneficial.

1.1.4.2 Doppler Redshift

Analogous to the auditory Doppler effect, Doppler redshift is caused by the relative motion (consisting of the relative velocity v, and relative angle θ) between the emitter and the observer, and can be expressed as:

$$1 + z_D = \frac{1 + v\cos(\theta)/c}{\sqrt{1 - v^2/c^2}} \tag{1.15}$$

Accounting only for motion along the line of sight ($\theta = 0$) this reduces to:

$$1 + z_{D,\theta=0} = \sqrt{\frac{1 + v/c}{1 - v/c}} \tag{1.16}$$

Which is often called the peculiar redshift (z_P) and can be approximated to $z \approx \frac{v}{c}$ when $v << c$.

It is important to note that the above equations are only valid in a flat Minkowski spacetime, or at least on a small enough scale that a flat Minkowski spacetime is a good approximation.

1.1.4.3 Cosmological Redshift

When considering the redshift of a photon traversing across cosmologically significant distances, the assumption of a flat Minkowski spacetime is no longer valid, and instead cosmological redshift should be considered. Cosmological redshift is caused by the expansion of the Universe between the time of emission (t_{emit}), and the time of observation (t_{obs}):

$$1 + z_C = \frac{a(t_{obs})}{a(t_{emit})} \tag{1.17}$$

Where a is the scale factor of the Universe at a given time.

Often the cosmological redshift is described as the expansion of the Universe 'stretching' the wavelength of a travelling photon. However, as described in Bunn and Hogg (2009), this interpretation can be misleading. Instead, Bunn and Hogg (2009) advocate for interpreting the shift in a photon's wavelength as it traverses an expanding spacetime as:

> [...] the accumulation of infinitesimal Doppler shifts along the line of sight.

Consider a photon which is emitted as $t_{emit} = t_0$, then travels some distance $\delta D_{0\to1} << c/\mathrm{H}_0$ before being observed at some later time $t_{obs} = t_1 = t_0 + \delta t_{0\to1}$. Using the Hubble-Lemaître law, the relative velocity between the emitter at t_0 and the observer at t_1 is $\delta v_{0\to1} = \mathrm{H}\delta D_{0\to1}$ where H is the Hubble parameter. Since $\delta v_{0\to1} << c$ we can compute the redshift using the non-relativistic Doppler shift as:

$$\begin{aligned}
1 + z_{0\to1} &= 1 + \frac{\delta v_{0\to1}}{c} && (1.18)\\
&= 1 + \frac{\mathrm{H}(t_0)\delta D_{0\to1}}{c} && (1.19)\\
&= 1 + \mathrm{H}(t_0)\delta t_{0\to1} && (1.20)\\
&= 1 + \frac{1}{a(t_0)}\frac{da}{dt}\delta t_{0\to1} && (1.21)\\
&= 1 + \frac{\delta a_{0\to1}}{a(t_0)} && (1.22)\\
&= 1 + \frac{a(t_1) - a(t_0)}{a(t_0)} && (1.23)\\
&= \frac{a(t_1)}{a(t_0)} && (1.24)
\end{aligned}$$

It follows that the next 'step' the photon takes induces a redshift $1 + z_{1\to2} =$

$\frac{a(t_2)}{a(t_1)}$ with the total redshift $1+z_{0\to2} = (1+z_{0\to1})(1+z_{1\to2}) = \frac{a(t_1)}{a(t_0)}\frac{a(t_2)}{a(t_1)} = \frac{a(t_2)}{a(t_0)}$. In other words, the final redshift depends only on the scale factor of the final observer and the scale factor of the original emitter[1].

1.1.4.4 Gravitational Redshift

This final source of redshift is time dilation experienced within a strong gravitational well. The observed frequency of a photon emitted from within a gravitational well will appear lower (fewer cycles per second) to an observer outside the gravitational well. The exact relationship depends on the gravitational field, but for an uncharged, non-rotating, spherically symmetric object with mass M and radius r, the redshift is:

$$1 + z_G = \frac{1}{\sqrt{1 - \frac{2GM}{rc^2}}} \tag{1.25}$$

Where G is the gravitational constant.

1.2 Cosmological Probes

To measure the H_0, Ω_0 and w parameters which describe the evolution of our Universe, cosmologists employ a number of cosmological probes — astronomical phenomena which allow us to constrain the cosmological parameters of interest. There are many varied cosmological probes that constrain cosmological parameters through a variety of physical processes. Different cosmological probes are able to constrain different cosmological parameters, so it is only by combining multiple probes together that a complete understanding of our Universe can be attained.

1.2.1 Type Ia Supernovae

The main concern of this work, type Ia supernovae (SNe Ia), are among the most luminous optical transients that can be observed, and are particularly useful as their peak brightness has a consistent relationship with the duration of the supernova and its colour at maximum light, allowing their luminosities (and thus their absolute magnitudes) to be standardised. This in turn allows the distance to a supernova to be estimated from its observed luminosity.

[1] Bunn and Hogg (2009) argue that because this is the case, the overall cosmological redshift should be considered as a single (non-infinitesimal) Doppler shift.

Given the redshift of a SN Ia, the distance modulus of that SN Ia can be predicted from cosmological parameters:

$$\mu_{predict} = 5\log_{10}(D_L/10[pc]) \tag{1.26}$$

$$D_L = (1+z)\frac{c}{\mathrm{H}_0}\int_0^z E^{-1}(z')dz' \tag{1.27}$$

$$E(z')^2 = \Omega_\mathrm{R}(1+z')^4 + \Omega_\mathrm{M}(1+z')^3 + \Omega_\mathrm{DE}(1+z')^{3(1+w)} + (1-\sum\Omega_0)(1+z')^2 \tag{1.28}$$

SNe Ia are an example of standard candles, astronomical objects which provide the opportunity to constrain cosmological parameters by virtue of a measurable or theoretically determined absolute magnitude (M). When combined with an observable apparent magnitude (m), the observed distance modulus is:

$$\mu_{observe} = m - M \tag{1.29}$$

Constraints on cosmological parameters are attained by equating $\mu_{observe}$ with $\mu_{predict}$.

Type Ia supernovae provide a relative distance measure, so must be calibrated to an absolute distance to be used to constrain the Hubble constant. This is typically done via a 'distance ladder' in which a nearby absolute distance measure is used to calibrate a relative distance measure. Once a relative distance measure has been calibrated, it can in turn be used to calibrate other relative distance measures, and eventually SNe Ia. The first 'rung' of the distance ladder are distances determined from nearby geometric measurements, which are typically only accurate to about 10kpc (Bailer-Jones et al., 2021). From parallaxes, relative distance measures such as Cepheid Variables (Freedman and Madore, 2023) can be calibrated to an absolute distance, which can then be used to calibrate supernova distances.

The role of Type Ia supernovae in cosmological research is discussed in greater detail in Section 1.4.

1.2.2 Baryon Acoustic Oscillations

Baryon Acoustic Oscillations (BAOs) are a pattern of sound waves that travelled through the early universe, leaving a distinctive imprint on the large-scale distribution of galaxies and cosmic matter. These oscillations are a result of density fluctuations in the early universe, and their measurement provides important information about the geometry, expansion rate, and history of the cosmos. Bassett and Hlozek (2009) provides an extensive review on the use of BAO as cosmological probes, which is briefly summarised here.

BAOs are an example of a 'standard ruler', an object with a measurable or theoretically determined physical size analogous to the absolute magnitude of standard candles. In the case of BAOs the measurable size is the characteristic scale of galaxy clustering throughout the Universe. This characteristic scale can be measured along the line-of-sight ($s_{||}(z)$) or tangential to the line-of-sight ($s_{\perp}(z)$) which provides the following cosmological constraints:

$$H(z) = \frac{c\Delta z}{s_{||}(z)} \tag{1.30}$$

$$D_A(z) = \frac{s_{\perp}(z)}{\Delta\theta(1+z)} \tag{1.31}$$

Where Δz is the difference in redshift between the closest and furthest points on the line-of-sight characteristic scale, $\Delta\theta$ is the angular size of the tangential characteristic size, and $D_A(z) = (1+z)^2 D_L(z)$ is the angular diameter distance, which relates to cosmological parameters via Equation (1.27). One method of measuring the characteristic scale from galaxy clustering is via the two-point correlation function. BAOs are used as part of the Dark Energy Survey, as described in Macaulay et al. (2019).

BAOs provide an alternative to the distance ladder, known as the 'inverse distance ladder', in which high redshift BAOs are used to calibrate type Ia supernovae at lower redshifts. Aubourg et al. (2015) use an inverse distance ladder to calibrate JLA supernovae using BAO data from BOSS and CMB measurements from Planck. Camilleri et al. (2024a); Macaulay et al. (2019) use the same method to measure H_0 with DES SNe Ia.

1.2.3 Cosmic Microwave Background

The Cosmic Microwave Background (CMB) was initially theorised by Gamow (1946) as a photometric remnant of the extremely early universe. Observational evidence of the CMB was first taken by accident by Penzias and Wilson (1965), who observed a powerful microwave signal visible in all directions whilst trying to correct for background noise. Work conducted alongside Dicke et al. (1965) lead to the discovery that the likely source of this signal was the CMB.

Subsequent measurements with the COsmic Background Explorer (COBE; Smoot et al., 1992), Wilkinson Microwave Anisotropy Probe (WMAP; Hinshaw et al., 2003; Komatsu et al., 2009), and most recently Planck (Planck Collaboration et al., 2014, 2016, 2020), have successively improved the resolution of the CMB.

The CMB presents an astonishingly uniform temperature profile, with an average temperature of ~ 2.7K, and temperature fluctuations from the mean on the order of 1 part in 100,000. Only with the extreme precision of surveys like Planck can the temperature anisotropy of the CMB be measured. The power spectrum of the CMB temperature reflects the conditions of the early Universe and the resultant expansion of the Universe. The CMB temperature power spectrum can be directly modelled from cosmological parameters, allowing constraints to be placed on them.

Observations of the CMB are typically analysed after a Fourier transform and a decomposition into spherical harmonics. This transforms the data into an angular power spectrum with a monopole term ($l = 0$) corresponding to the spherically symmetric 2.7K signal. Higher-order multipoles exhibit additional peaks in signal, which correspond to anisotropies at smaller angular scales. The angular size of higher order peaks is related to the spatial curvature of the Universe, whilst the amplitude of higher order peaks is related to the Ω density of baryons and dark matter. Furthermore, CMB anisotropies are directly related to H_0. Thus, by modelling and fitting the angular power spectrum of the CMB, precise constraints can be found for a number of important cosmological parameters.

1.2.4 Weak Lensing & Large-Scale Structure

In addition to constraining cosmological expansion parameters, such as w and the Ω parameters, cosmologists are also interested in constraining the growth of large-scale structure in our Universe. This is typically parameterised with the parameter σ_8, which quantifies density fluctuation over a scale of 8 h^{-1} Mpc, where $h = Ho/(100\text{km / s / Mpc})$.

One method of constraining σ_8 is through weak lensing, or the distortion of the shape of galaxies due to gravitational lensing caused by large-scale structure. The size of this distortion is typically rather small, so rather than individual galaxies, weak lensing is focused on the aggregate distortion of many galaxies. Much like BAOs, a two-point correlation function is a common method for evaluating the scale of weak lensing present in an image containing several galaxies.

Although weak lensing was theoretically predicted in the early 1990s (Kaiser, 1992; Miralda-Escude, 1991), large samples of galaxy observations were required before weak lensing had the statistical power required for cosmological constraints. The first detections of cosmic shear, the distortion of many galaxies due to large-scale structure, occurred in the year 2000 across four independent studies (Bacon et al., 2000; Kaiser et al., 2000; Van Waerbeke et al., 2000; Wittman et al., 2000).

Weak lensing is a particularly useful cosmological probe, as it is able to constrain both the growth of structure (σ_8) and the expansion history (Ω, w) of our Universe. Several prominent surveys used weak lensing for cosmological constraints, including (but not limited to) CTIO (Jarvis et al., 2006), COSMOS (Massey et al., 2007; Schrabback et al., 2010), SDSS (Huff et al., 2014; Lin et al., 2012), CFHTLenS (Heymans et al., 2013; Joudaki et al., 2016; Kilbinger et al., 2013), KiDS (Asgari et al., 2021; Burger et al., 2023; Heymans et al., 2021; Hildebrandt et al., 2016), and DES (Abbott et al., 2018).

Additional methods of constraining the growth of structure include comparing measurements of the number density of galaxy clusters and the large-scale distribution of galaxies to theoretical predictions and N-body simulations.

1.2.5 Gravitational Waves

Gravitational waves (GWs) are transverse waves that propagate through spacetime at the speed of light. Theorised by Einstein and Rosen (1937) as a consequence of General Relativity, these waves were first observed in 2015 thanks to the efforts of the Laser Interferometer Gravitational-Wave Observatory (LIGO; LIGO Collaboration, 2016b). Modelling of this GW event, dubbed GW150914, constrained the source of the wave to a binary black hole (BBH) merger with initial black hole masses of $36^{+5}_{-4} M_\odot$ and $29^{+4}_{-4} M_\odot$, and a final black hole mass of $62^{+4}_{-4} M_\odot$. This corresponds to a GW event with energy $3.0^{+0.5}_{-0.5} M_\odot c^2$ being radiated away from the merger. Following this initial detection, significant electromagnetic follow-up occurred, covering radio, optical, near-infrared, X-ray, and gamma-ray wavelengths (LIGO Collaboration, 2016a). As the source of the GW event was expected to be a BBH merger, there was no expectation of a detectable electromagnetic component; however, this follow-up proved an invaluable proof-of-concept for future GW event detections.

GW observation runs typically last a few months, with intervening months spent maintaining and upgrading GW detectors. So far there have been four such observation runs, dubbed O1, O2, O3, and O4.

O1 and O2 (LIGO Collaboration et al., 2019) consisted of observations from LIGO and the Advanced Virgo Interferometer (Virgo Collaboration, 2014) and detected GW events from ten BBH mergers and one binary neutron star inspiral (GW170817, discussed in more detail below). O3 was split into O3a (LIGO Collaboration and Virgo Collaboration, 2021) and O3b (LIGO Collaboration et al., 2021) due to disruption caused by COVID-19. O3a found 39 GW candidates. In O3b, LIGO and VIRGO were joined by the Japanese KAGRA observatory (KAGRA Collaboration, 2019, 2020), which continued to observe alongside LIGO and VIRGO in the currently ongoing O4 run. Although not yet operational, an interferometer in India is planned for O5 (LIGO-India; Unnikrishnan, 2023).

During the O2 observing run, a binary neutron star (BNS) inspiral was observed for the first time (LIGO Collaboration and Virgo Collaboration, 2017). Dubbed GW170817, this was also the first GW event with associated electromagnetic observations in the form of the gamma-ray burst GRB 170817A. This was the first 'bright siren', or GW event with an associated electromagnetic component, as opposed to 'dark sirens' which have no observed electromagnetic component.

Both bright sirens and dark sirens can be used as a new independent cosmological probe, primarily constraining H_0. The methodology for constraining H_0 with GWs (the so-called 'standard siren' method) was first theorised by Schutz (1986) and further developed by Chen et al. (2018); LIGO Collaboration et al. (2019); Palmese et al. (2020). By comparing the observed waveform of a GW to prediction from general relativity, constraints can be placed on the luminosity distance (D_L) of the GW source, alongside a number of other source properties. To use the GW luminosity distance for cosmological parameter predictions, the redshift of the GW source must also be known. In the case of bright sirens, the redshift of the electromagnetic counterpart can be measured directly (e.g. LIGO Collaboration and Virgo Collaboration, 2017). In the case of dark sirens, a number of possible candidate host galaxies are chosen, and weighted by their likelihood of being the true host, as determined by the localisation of the GW event. The redshifts of these candidate host galaxies are then marginalised over to produce a statistical measure of cosmological parameters (e.g. Palmese et al., 2023, 2020).

1.3 Statistics in Supernova Cosmology

When attempting to constrain cosmological parameters, there are two types of uncertainty which must be accounted for — statistical and systematic. Statistical uncertainties are those inherent to the randomness of nature, such as photon shot noise. Statistical uncertainty can be reduced by collecting additional data and averaging results over this larger dataset. In general, the statistical uncertainty of the average of a parameter is reduced by the square-root of the number of averaging elements.

Systematic uncertainties (often shortened to systematics) are biases, flaws, or choices made within an analysis. These include, but are not limited to: Malmquist bias, zero-point and filter uncertainty, choice of supernova model, and non-Ia contamination. Unlike statistical uncertainties, systematics cannot be improved by collecting more data. Here I briefly describe the most common sources of systematic uncertainty in supernova cosmology, this is not an exhaustive list, nor does every SN survey account for all of these systematics.

1.3.1 Calibration uncertainties

Astronomical images are typically measured in the number of ADUs that pass through a bandpass filter and are collected on the instrument CCD. These images must be calibrated to convert CCD counts into astrophysically useful flux and magnitude units. For an object observed by a system S in a bandpass filter p with transmission curve $p(\lambda)$, the calibrated system magnitude is:

$$m_{S,p} = -2.5\log_{10}(C) + ZP_{S,p} \tag{1.32}$$

Where C is the number of counts (usually ADUs) per second of exposure detected, and $ZP_{S,p}$ is the zero-point for this system and bandpass filter. The choice of zero-point determines to what magnitude system the observations will be calibrated to.

One common system is the AB magnitude system (Fukugita et al., 1996; Oke and Gunn, 1983), defined as:

$$m_{AB}(\nu) = -2.5\log_{10}\left(\frac{f_\nu}{1\text{Jy}}\right) + 8.9\text{mag} \tag{1.33}$$

Where f_ν is the flux per unit frequency (ν) of the observed object. To measure the AB magnitude in a particular bandpass filter with transmission curve $p(\nu)$:

$$m^p_{AB} = 2.5\log_{10}\left(\frac{\int (h\nu)^{-1} p(\nu) f_\nu \, d\nu}{\int (h\nu)^{-1} p(\nu) 3631\text{Jy} \, d\nu}\right) \tag{1.34}$$

Where $h = 6.626 \times 10^{-34}$J Hz^{-1} is the Planck constant. This leads to the typical method for calculating $ZP_{S,p}$. The first step is to identify a number (N) of standard stars $(\vec{ss})$ visible to your system that have measured or modelled spectral energy distributions. Next, observe these standard stars with the same system and bandpass filter as your object. Finally, $ZP_{S,p}$ can be calculated using:

$$ZP_{S,p} = \frac{1}{N}\sum_{i=1}^{N} m^{p}_{AB}(\vec{ss}_i) + 2.5\log_{10}(C_i) \tag{1.35}$$

There are two major sources of systematic uncertainty present in this method of calibration, the uncertainties present in the observing and reduction of images with the system, and the uncertainty in the magnitude of the standard stars. This is an important consideration when combining data from multiple systems, as any uncertainty in the standard star measurements will lead to correlated uncertainties between the systems.

1.3.2 Lightcurve modelling uncertainties

There are numerous methods of modelling and standardising SN Ia, each of which have uncertainties associated with them. The exact nature of these uncertainties are dependent on the modelling method. As an example, the SALT2 methodology (Guy et al., 2007) relies on training its model on a representative sample of SNe Ia. The uncertainties, biases, and wavelength coverage of this sample all contribute to the accuracy of the model.

1.3.3 Intrinsic scatter

Intrinsic scatter refers to variations in SN Ia brightness which remain after standardisation. This scatter has been shown to depend on redshift (Betoule et al., 2014), wavelength range (Mandel et al., 2011), host galaxy properties (Uddin et al., 2017), and spectroscopic features (Fakhouri et al., 2015). As the underlying source of this scatter depends greatly on the specifics of a given analysis, it is a difficult systematic to correct. For instance, Brout and Scolnic (2021) attribute this scatter to variations in the extinction parameter R_v between SN host galaxies, and rely on a host galaxy dust model to account for the effects of intrinsic scatter. Although this treatment reduces intrinsic scatter, the choice of which model to use induces its own systematic uncertainty due to the assumptions and uncertainties present in each model.

1.3.4 Milky Way extinction

In addition to extinction from host galaxy dust, the dust present in the Milky Way also causes an observed reduction in the brightness of SNe Ia. Measuring the scale of this extinction involves large-scale surveys of intragalactic stars, measuring the difference between predicted and observed colour (see for example Schlafly et al., 2010). Uncertainties in these surveys and the techniques for estimating the Milky Way extinction will lead to a systematic uncertainty in the corrected SN brightness.

1.3.5 Host galaxy mismatch

Correctly identifying the host galaxy of a SN Ia is a vital component of a cosmological SN survey. A host galaxy spectrum provides much more accurate redshifts than the associated SN spectrum. Additionally, it has been shown that there is a link between host galaxy properties and SN brightness (Sullivan et al., 2010, ; see Section 1.4.2 for more details), so an accurate measure of the host galaxy stellar mass is necessary to correct for this effect. If a host galaxy is misidentified, then both the redshift and host mass correction for that SN will be incorrect, leading to a systematic offset.

1.3.6 Core-collapse contamination

All the SN cosmology techniques used in modern cosmology require SNe Ia. If a SN is misclassified as a Ia, then any analysis performed on the SN will lead to biases. Uncertainty in the classification can arise from low signal-to-noise spectra or uncertainties in photometric classification methodologies.

1.3.7 Redshift and Peculiar velocity corrections

The redshift of a SN is used to determine the expansion velocity of the Universe at that SN. The redshift is typically measured from a spectrum of the SN host galaxy, and the peculiar velocity of the host galaxy is determined from peculiar velocity maps. Both processes have inherent uncertainties which can affect the final redshift associated with the SN.

1.3.8 Blinded Analyses

A less obvious source of systematic uncertainty is the unconscious bias of researchers involved in the analysis. Croft and Dailey (2015) analyse constraints on cosmological parameters from 1990 — 2010. In this analysis, they find possible evidence of confirmation bias, with only 2 of the 28 measurements of Ω_Λ varying by more than 1σ — a statistical anomaly. They advocate for blinded analyses, in which a random offset is introduced to the final results of an analysis, forcing researchers to build and validate their analysis frameworks independently of the final result. This sentiment is echoed by Maccoun and Perlmutter (2015) who motivate the implementation of blinded analyses throughout science, discuss some common objections, and suggest best practices for the implementation of a blinded analysis.

1.4 SNe Ia Cosmological Surveys

Type Ia supernovae have been considered as possible standard candles since the 1980s, with Sandage and Tammann (1985) presenting evidence of low variability in the peak brightness of low-redshift SNe Ia. Additional evidence came with the discovery of a high-redshift SN Ia at $z = 0.31$ using the 1.5m Danish telescope (Nørgaard-Nielsen et al., 1989), which matched the behaviour of previously discovered low-redshift SNe Ia, however it was only observed post-maximum, so this was not conclusive.

Phillips (1993) and Pskovskii (1977) independently derived from a sample of nine SNe Ia a linear relationship between the absolute magnitude and the decline rate of SNe Ia light curves, known as the 'Phillips relation'. Early low redshift ($z < 0.1$) surveys such as the Calán/Tololo SN survey (Hamuy et al., 1996) and the Center for Astrophysics Data Release 1 (Riess et al., 1999) produced samples of 32 and 22 SNe Ia, respectively. Both surveys confirmed the Phillips relation. However, the sample's redshift range was not deep enough to effectively constrain cosmological parameters.

The first convincing evidence that a SN Ia could constrain cosmological parameters provided by Leibundgut et al. (1996) who presented evidence that the light curve of SN 1995K, a SNe Ia, was dilated by cosmological expansion. At nearly the same time, Goobar and Perlmutter (1995) presented a feasibility study of using type Ia supernovae to constrain cosmological constant (Ω_Λ) and mass density (Ω_M). They found that, if measured with uncertainties of less than 0.15 mag in the distance modulus of individual SNe out to a redshift of $z = 1$, a sample of roughly 50 SNe Ia could provide enough constraining power to distinguish between cosmological models.

Only a few years later, two teams used SNe Ia to discover the accelerated expansion of the Universe. The two teams were the High-Z Supernova Search Team (Riess et al., 1998; Schmidt et al., 1998), and the Supernova Cosmology Project (Perlmutter et al., 1999). Their discovery earned them the 2011 Nobel Prize in Physics. Their work was followed by decades of advancements in SN cosmology, iteratively improving the constraining power of SNe Ia by increasing the sample size, and improving many aspects of the analysis. In this section I will summarise the many SN Ia cosmological surveys, discuss the current state of modern SN cosmology, and explore some of the challenges that will need to be overcome in future surveys. A summary of cosmological constraints from all surveys discussed in this section is presented in Table 1.1. A graphical summary of constraints on Flat wCDM and Flat w_aCDM are presented in Figure 1.1 and Figure 1.2, respectively.

Table 1.1: A summary of cosmological constraints from major supernova cosmology surveys. Unless otherwise specified, uncertainties are statistical only. Where possible, constraints from combining the survey sample with previous SNe Ia samples and alternative cosmological probes is quoted to show the tightest constraints provided by the survey.

Phase I

Survey	Model*	Probes+
Ω_M	Ω_{DE}	$q_0^{\times}$
HZT[1]	ΛCDM	SN
$0.24^{+0.56}_{-0.24}$ (stat)	$0.72^{+0.72}_{-0.48}$ (stat)	$-0.75^{+0.32}_{-0.32}$ (stat)
	Flat ΛCDM	SN
$0.24^{+0.1}_{-0.1}$ (stat)	—	$-0.64^{+0.11}_{-0.11}$ (stat)
SCP[2]	ΛCDM†	SN
$0.73^{+0.125}_{-0.125}$ (stat)	$1.32^{+0.167}_{-0.167}$ (stat)	$-0.96^{+0.178}_{-0.178}$ (stat)
	Flat ΛCDM	SN
$0.28^{+0.09}_{-0.08}$ (stat)	—	$-0.58^{+0.085}_{-0.085}$ (stat)

Phase II

Survey	Model*	Probes+	
Ω_M	$\Omega_{DE}^{\ddagger}$	w_0	w_a
ESSENCE[3]	Flat wCDM	SN, BAO	
$0.267^{+0.028}_{-0.018}$ (stat)	—	$-1.069^{+0.091}_{-0.093}$ (stat) $^{+0.130}_{-0.130}$ (sys)	—
Union[4]	wCDM	SN, BAO, CMB	
$0.285^{+0.02}_{-0.02}$ (stat) $^{+0.01}_{-0.01}$ (sys)	$0.725^{+0.022}_{-0.023}$ (stat) $^{+0.012}_{-0.010}$ (sys)	$-1.001^{+0.069}_{-0.073}$ (stat) $^{+0.080}_{-0.082}$ (sys)	—

SDSS-II[5]	ΛCDM	SN, BAO, CMB	
$0.312^{+0.022}_{-0.022}$ (stat) $^{+0.001}_{-0.001}$ (sys)	$0.705^{+0.018}_{-0.018}$ (stat) $^{+0.004}_{-0.004}$ (sys)	—	—
	wCDM	SN, BAO, CMB	
$0.307^{+0.019}_{-0.019}$ (stat) $^{+0.023}_{-0.023}$ (sys)	—	$-0.76^{+0.07}_{-0.07}$ (stat) $^{+0.11}_{-0.11}$ (sys)	—
Union2[6]	wCDM	SN, BAO, CMB	
$0.282^{+0.018}_{-0.016}$ (stat+sys)	$0.731^{+0.019}_{-0.018}$ (stat+sus)	$-1.038^{+0.093}_{-0.097}$ (stat+sys)	—
SNLS[7]	ΛCDM	SN, BAO, CMB	
$0.274^{+0.017}_{-0.016}$ (stat+sys)	$0.732^{+0.016}_{-0.017}$ (stat+sys)	—	—
	wCDM	SN, BAO, CMB	
$0.272^{+0.017}_{-0.016}$ (stat+sys)	—	$-1.058^{+0.078}_{-0.082}$ (stat+sys)	—
	w_aCDM	SN, BAO, CMB	
$0.271^{+0.015}_{-0.015}$ (stat+sys)	—	$-0.905^{+0.196}_{-0.196}$ (stat+sys)	$-0.984^{+1.094}_{-1.097}$ (stat+sys)
Union2.1[8]	ΛCDM	SN, BAO, CMB	
$0.272^{+0.014}_{-0.014}$ (stat+sys)	$0.726^{+0.015}_{-0.015}$ (stat+sys)	—	—
	wCDM	SN, BAO, CMB	
$0.271^{+0.014}_{-0.014}$ (stat+sys)	—	$-1.013^{+0.068}_{-0.073}$ (stat+sys)	—
	w_aCDM	SN, BAO, CMB	
$0.27^{+0.015}_{-0.014}$ (stat+sys)	—	$-1.046^{+0.179}_{-0.170}$ (stat+sys)	$0.14^{+0.60}_{-0.76}$ (stat+sys)
Pan-STARRS1[9]	ΛCDM	SN, BAO, CMB	
$0.308^{+0.033}_{-0.030}$ (stat+sys)	$0.693^{+0.024}_{-0.025}$ (stat+sys)	—	—
	wCDM	SN, BAO, CMB	
$0.28^{+0.013}_{-0.012}$ (stat+sys)	—	$-1.166^{+0.072}_{-0.069}$ (stat+sys)	—

JLA[10]	ΛCDM	SN, BAO, CMB	
$0.305^{+0.01}_{-0.01}$ (stat+sys)	$0.693^{+0.01}_{-0.01}$ (stat+sys)	—	—
	wCDM	SN, BAO, CMB	
$0.303^{+0.012}_{-0.012}$ (stat+sys)	—	$-1.027^{+0.055}_{-0.055}$ (stat+sys)	—
	Flat w_aCDM	SN, BAO, CMB	
$0.304^{+0.012}_{-0.012}$ (stat+sys)	—	$-0.957^{+0.124}_{-0.124}$ (stat+sys)	$-0.336^{+0.552}_{-0.552}$ (stat+sys)
Pantheon[11]	ΛCDM	SN, BAO, CMB	
$0.303^{+0.007}_{-0.007}$ (stat+sys)	$0.695^{+0.007}_{-0.007}$ (stat+sys)	—	—
	Flat wCDM	SN, BAO, CMB	
$0.299^{+0.007}_{-0.007}$ (stat+sys)	—	$-1.047^{+0.038}_{-0.038}$ (stat+sys)	—
	Flat w_aCDM	SN, BAO, CMB	
$0.3^{+0.008}_{-0.008}$ (stat+sys)	—	$-1.007^{+0.089}_{-0.089}$ (stat+sys)	$-0.222^{+0.407}_{-0.407}$ (stat+sys)
Foundation[12]	wCDM	SN, BAO, CMB	
$0.301^{+0.008}_{-0.008}$ (stat+sys)	—	$-1.014^{+0.04}_{-0.04}$ (stat+sys)	—
	Flat w_aCDM	SN, BAO, CMB	
$0.305^{+0.008}_{-0.008}$ (stat+sys)	—	$-0.895^{+0.095}_{-0.095}$ (stat+sys)	$-0.597^{+0.439}_{-0.439}$ (stat+sys)

Phase III

Survey	Model*	Probes+	
Ω_{M}	Ω_{DE}‡	w_0	w_a
DES-SN3YR[13]	ΛCDM	SN, BAO, CMB	
$0.308^{+0.007}_{-0.007}$ (stat+sys)	$0.69^{+0.008}_{-0.008}$ (stat+sys)	—	—
	Flat wCDM	SN, BAO, CMB	
$0.311^{+0.009}_{-0.009}$ (stat+sys)	—	$-0.977^{+0.047}_{-0.047}$ (stat+sys)	—
	Flat w_aCDM	SN, BAO, CMB	
$0.316^{+0.011}_{-0.011}$ (stat+sys)	—	$-0.885^{+0.114}_{-0.114}$ (stat+sys)	$-0.387^{+0.43}_{-0.43}$ (stat+sys)
Pantheon+[14]	ΛCDM	SN	
$0.306^{+0.057}_{-0.057}$ (stat+sys)	$0.625^{+0.084}_{-0.084}$ (stat+sys)	—	—
	Flat wCDM	SN, BAO, CMB	
$0.316^{+0.005}_{-0.008}$ (stat+sys)	—	$-0.978^{+0.024}_{-0.031}$ (stat+sys)	—
	Flat w_aCDM	SN, BAO, CMB	
$0.316^{+0.009}_{-0.005}$ (stat+sys)	—	$-0.841^{+0.066}_{-0.061}$ (stat+sys)	$-0.65^{+0.28}_{-0.32}$ (stat+sys)
Union3[15]	ΛCDM	SN, BAO, CMB	
$0.31^{+0.006}_{-0.006}$ (stat+sys)	$0.679^{+0.006}_{-0.006}$ (stat+sys)	—	—
	Flat wCDM	SN, BAO, CMB	
$0.314^{+0.007}_{-0.007}$ (stat+sys)	—	$-0.98^{+0.032}_{-0.033}$ (stat+sys)	—
	Flat w_aCDM	SN, BAO, CMB	
$0.321^{+0.008}_{-0.008}$ (stat+sys)	—	$-0.796^{+0.096}_{-0.093}$ (stat+sys)	$-0.71^{+0.35}_{-0.38}$ (stat+sys)

DES-SN5YR[16]	ΛCDM	SN, BAO, CMB, 3×2pt	
$0.318^{+0.011}_{-0.010}$ (stat+sys)	$0.68^{+0.012}_{-0.010}$ (stat+sys)	—	—
	Flat wCDM	SN, BAO, CMB, 3×2pt	
$0.321^{+0.007}_{-0.007}$ (stat+sys)	—	$-0.941^{+0.026}_{-0.026}$ (stat+sys)	—
	Flat w_aCDM	SN, BAO, CMB, 3×2pt	
$0.325^{+0.008}_{-0.008}$ (stat+sys)	—	$-0.773^{+0.075}_{-0.067}$ (stat+sys)	$-0.83^{+0.33}_{-0.42}$ (stat+sys)

[*]Cosmological Models — Flat: $\{\Omega_{\rm M} + \Omega_{\rm DE} = 1\}$, ΛCDM: $\{w_0 = -1, w_a = 0\}$, wCDM: $\{w_a = 0\}$
[+]Cosmological Probes — SN: Supernovae, BAO: Baryon Acoustic Oscillation, CMB: Cosmic Microwave Background, 3×2pt: Weak lensing and Galaxy clustering.
[×]For the Flat ΛCDM models, q_0 was not explicitly provided, and instead was calculated as $q_0 = \frac{\Omega_{\rm M}}{2} - \Omega_{\rm DE}$.
[†] SCP did not directly provide uncertainties for the ΛCDM model, instead these were approximated from the provided relationship $0.8\Omega_{\rm M} - 0.6\Omega_{\rm DE} = 0.2 \pm 0.1$.
[‡] Union, JLA, and DES-SN5YR quote $\Omega_{\rm M}$ and $\Omega_{\rm k} = 1 - (\Omega_{\rm M} + \Omega_{\rm DE})$. This is transformed into $\Omega_{\rm DE}$ to allow for easier comparison to other surveys.
[1](Riess et al., 1998; Schmidt et al., 1998), [2](Perlmutter et al., 1999), [3](Wood-Vasey et al., 2007), [4](Kowalski et al., 2008), [5](Kessler et al., 2009a), [6](Amanullah et al., 2010), [7](Astier et al., 2006; Conley et al., 2011; Guy et al., 2010; Sullivan et al., 2011), [8](Suzuki et al., 2012), [9](Rest et al., 2014; Scolnic et al., 2014), [10](Betoule et al., 2014), [11](Scolnic et al., 2018), [12](Jones et al., 2019), [13](Abbott et al., 2019), [14](Brout et al., 2022a), [15](Rubin et al., 2023), [16](DES Collaboration et al., 2024a; Vincenzi et al., 2024)

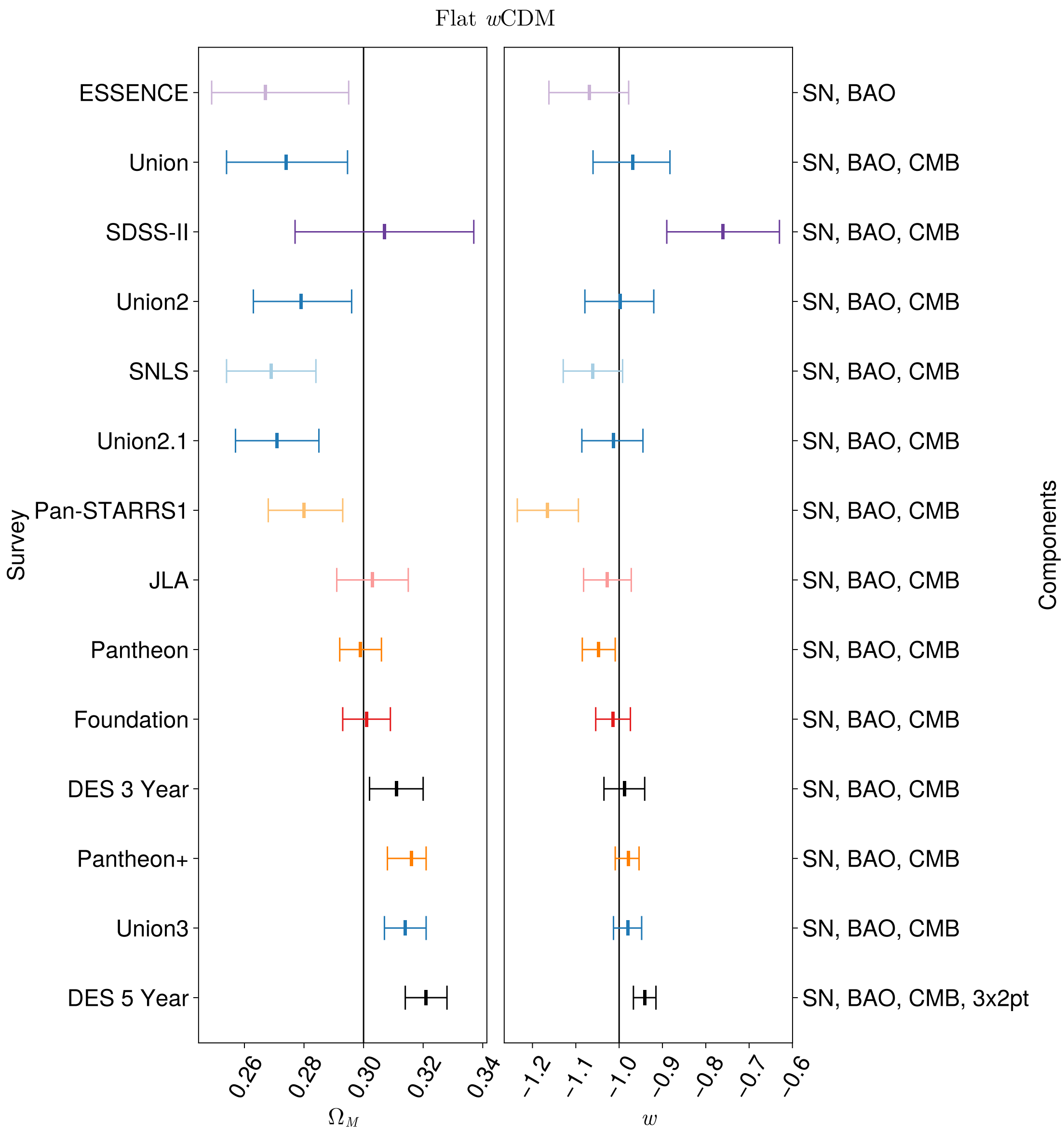

Figure 1.1: Evolution of Flat wCDM constraints over time. The latest constraints, provided by the Dark Energy Survey's 5-year SN analysis, exhibit a 2.3σ tension with the cosmological constant ($w = -1$). See Table 1.1 for more details.

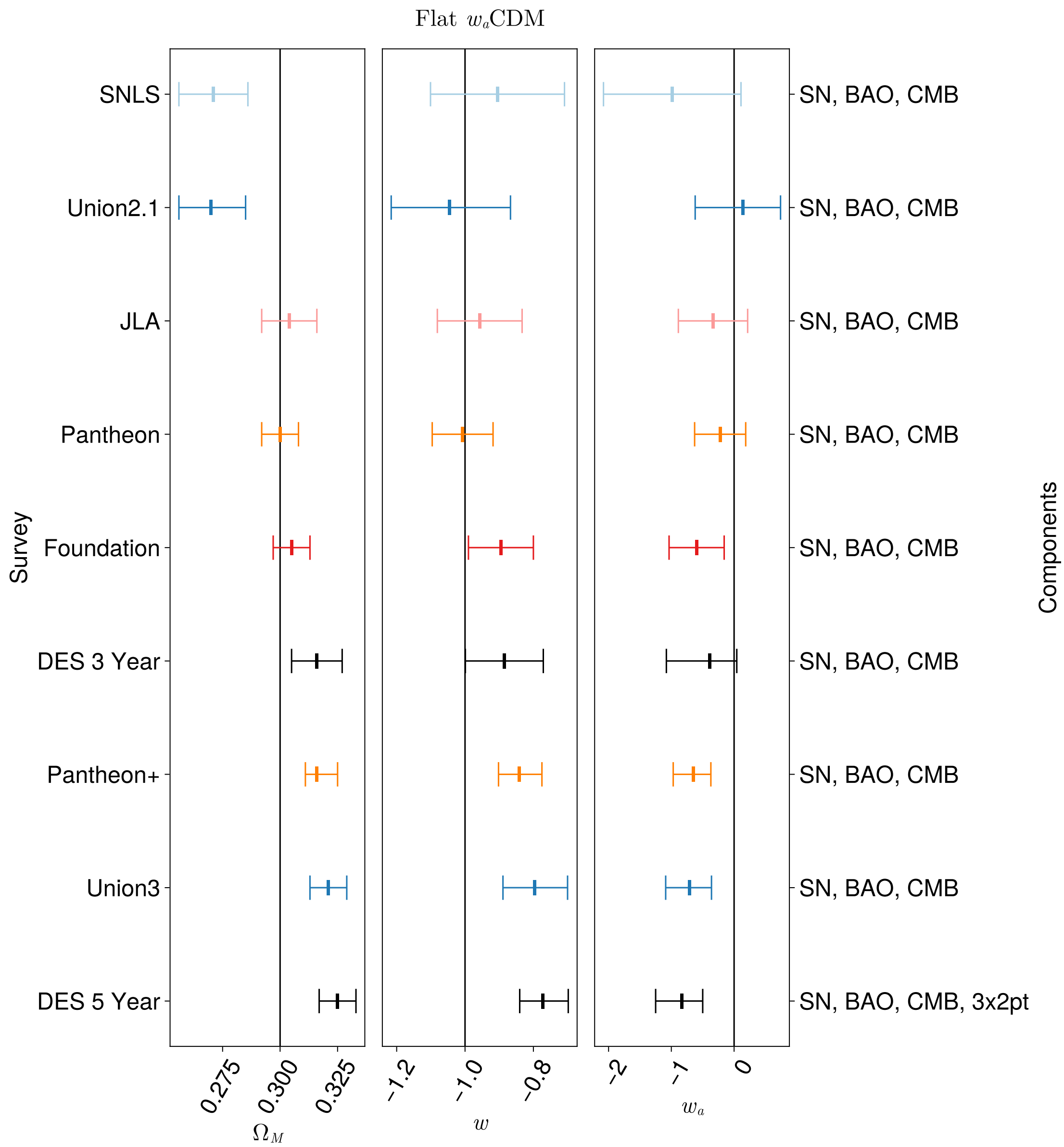

Figure 1.2: Evolution of Flat w_aCDM constraints over time. All 3 of the most recent constraints (DES-SN5YR, Union3, and Pantheon+) exhibit evidence of an evolving dark energy equation of state parameter. See Table 1.1 for more details.

1.4.1 Phase I — HZT & SCP

As mentioned, the discoveries of the High-Z Supernova Search Team (HZT; Riess et al., 1998; Schmidt et al., 1998) (hereafter R98 and S98, respectively), and the Supernova Cosmology Project (SCP; Perlmutter et al., 1999) (hereafter P99) were the progenitor of all modern SN cosmology research.

Formed in 1988, the primary purpose of the SCP was to observe a statistically significant sample of high-redshift SNe Ia, from which cosmological parameters could be constrained; over the next decade, the SCP would discover over 75 SNe Ia. Throughout this period the SCP implemented new search strategies optimised for SN discovery (Perlmutter, 1995; Perlmutter et al., 1996), developed new techniques for analysing SNe which allowed for both Ω_M and Ω_Λ to be measured simultaneously (Goobar and Perlmutter, 1995), and improved upon existing 'K-correction' methodologies (Kim et al., 1996; Nugent et al., 2002).

The SCP collected a cosmological sample of 42 SNe Ia, using the CTIO 4m telescope for candidate discovery, the Keck I and II 10m telescopes, and the ESO 3.6m telescope for spectroscopic follow up, and the CTIO 4m, the WIYN 3.6m, the ESO 3.6m, the Isaac Newton Telescope (INT) 2.5m, and the William Herschel Telescope (WHT) 4.2m for photometric follow up. To ensure SNe were discovered at or before maximum brightness, fields were imaged near the end of a dark run, and then again the beginning of the next dark run. Photometry was performed in the Kron-Cousins R and I band, and the SNe were observed throughout the peak of their explosion, with additional photometry taken two to three months after the explosion.

The HZT searched for candidate SNe with the prime-focus CCD camera on the CTIO Blanco 4m telescope, with a pixel scale of $0.43''$ and a frame which covers 0.06 square degrees. There were two search programs, a 3 night program between October and November 1995, and a 6 night program between February and March 1996. Following the search strategies developed by the SCP team (Perlmutter, 1995; Perlmutter et al., 1996), difference imaging was used to identify transient objects, which were then swiftly followed up spectroscopically with the Keck telescope, Multiple-Mirror Telescope (MMT), or the European Southern Observatory (ESO) 3.6-m. Candidate object classification was performed via visual inspection of their spectra, with 10 candidates being classified as SNe Ia.

Photometry was primarily observed in custom bandpasses, B35, V35, B45, and V45. These bandpasses matched the Johnson B and V bandpasses redshifted to $z = 0.35$ and $z = 0.45$ and are described in S98. These same bandpasses were used to observe both Landolt standard stars and local standards visible in the supernova frame.

Deep images of host galaxies were collected months to a year after the initial observation. These were then subtracted from the SN images to provide high quality light curves. SN redshifts were primarily determined from host galaxy spectra collected with the Keck, MMT, and ESO 3.6m telescopes. In the case that no host-galaxy emission line could be gathered with high enough precision, broad features in the supernova spectra were matched with spectra of low-redshift SNe Ia.

To measure the level of statistical and systematic uncertainty, artificial stars were added to subtracted frames with the same brightness and background as the measured SN. The systematic uncertainty was measured as the difference between the mean magnitude of the artificial star before and after image processing. This systematic error was then applied as a correction to the SN magnitude. The statistical uncertainty was the dispersion of the magnitude of the artificial star after image processing and systematic correction.

Both teams performed 'K-corrections', shifting the light curves of all SNe into their respective rest frames. Both teams use the K-correction detailed in Nugent et al. (2002), in which the cross-filter K-correction is calculated using:

$$\begin{aligned} K_{xy} = -2.5\log_{10}\left(\frac{\int \lambda \mathcal{Z}(\lambda) S_x(\lambda) d\lambda}{\int \lambda \mathcal{Z}(\lambda) S_y(\lambda) d\lambda}\right) + 2.5\log_{10}(1+z) \\ + 2.5\log_{10}\left(\frac{\int \lambda \mathcal{F}(\lambda) S_x(\lambda) d\lambda}{\int \lambda \mathcal{F}(\lambda/(1+z)) S_y(\lambda) d\lambda}\right) \end{aligned} \tag{1.36}$$

Where $\mathcal{F}(\lambda)$ is the spectral energy distribution (SED) of the SN, $S_x(\lambda)$ and $S_y(\lambda)$ are the transmission of the x and y bands, $\mathcal{Z}(\lambda)$ is an idealised SED with $U = B = V = R = I = 0$. The K-corrected y-band magnitude is then:

$$m_y = M_x + K_{xy} + \mu + A_{host} + A_{MW} \tag{1.37}$$

Where M_x is the x-band absolute magnitude, μ is the distance modulus, A_{host} is the host galaxy dust extinction, and A_{MW} is the Milky Way dust extinction.

The next stage of the analysis was to standardise the light curves of the SNe Ia, allowing for the SNe Ia to be used as standard candles. One of the earliest methods of standardisation is the 'Phillips Relation' Phillips (1993) (hereafter P93). A collection of nine historical SNe Ia were chosen for their well-sampled light curves, and accurate relative host galaxy distances based on surface brightness fluctuations or Tully-Fisher relation measures. A linear correlation between the absolute magnitude at peak (M), and $\Delta m_{15}(B)$, the difference between the peak apparent magnitude ($m_{\max}(B)$) and the apparent magnitude 15 days post maximum ($m_{15}(B)$), was discovered, leading to the following standardisation:

$$M = a + b\Delta m_{15}(B) \tag{1.38}$$
$$\mu = m - M = m - a + b(m_{\max}(B) - m_{15}(B)) \tag{1.39}$$

Where a is the $M - \Delta m_{15}(B)$ intercept, and b is the $M - \Delta m_{15}(B)$ slope. The value of these parameters were found using a least-squares fit, the results of which are presented in Table 2 of P93, and repeated in Table 1.2.

Table 1.2: The intercept (a) and slope (b) of the Phillips relation in various bandpasses, found in P93 via a least-squares fit. A correlation between bandpass and the parameters is present, which P93 attribute to a relationship to SN colour which was not accounted for in the Phillips relation standardisation.

Bandpass	a	b
B	-21.725 ± 0.498	2.698 ± 0.359
V	-20.883 ± 0.417	1.949 ± 0.292
I	-19.591 ± 0.415	1.076 ± 0.273

These parameters displayed a correlation with bandpasses, indicating a relationship with SN colour which was not present in the Phillips relation.

To account for this luminosity-colour relationship, HZT use a method known as Multicolor LightCurve Shape (MLCS; Riess et al., 1996), which they had refined and optimised for high-redshift SNe Ia in R98. This method models the apparent magnitude of SNe Ia as:

$$\vec{m_V} = \vec{M_V} + \vec{R_V}\Delta_M + \vec{Q_V}\Delta_M^2 + \mu_V \tag{1.40}$$
$$m_{\vec{B-V}} = M_{\vec{B-V}} + R_{\vec{B-V}}\Delta_M + Q_{\vec{B-V}}\Delta_M^2 + E\,(B-V) \tag{1.41}$$

Where $\rightarrow$ indicates parameters which are a vector of time-dependent values. $\vec{m_V}$ and $m_{\vec{B-V}}$ are the observed light curve and colour-curve, respectively, with $\vec{M_V}$ and $M_{\vec{B-V}}$ being the light and colour curves of template SNe Ia. $\Delta_M = M_v - M_v(\text{standard})$ is the difference between the peak absolute magnitude of a template SN Ia, and the peak absolute magnitude of the SN being standardised. μ_V is the observed distance modulus, and $E\,(B-V)$ the colour excess. $\vec{R_V}$ and $R_{\vec{B-V}}$ are correlation coefficients between Δ_M and the light curve and colour-curve, respectively, with $\vec{Q_V}$ and $Q_{\vec{B-V}}$ being quadratic correlation coefficients.

A number of these parameters ($\vec{M_V}$, $\vec{M_{B-V}}$, $\vec{R_V}$, $\vec{R_{B-V}}$, $\vec{Q_V}$, and $\vec{Q_{B-V}}$) are empirically determined from a training set of SNe Ia, with the other parameters (Δ_M, μ_V, and $E\left(B-V\right)$) being free parameters which must be fit for.

In contrast, the SCP team used a template fitting method described in Perlmutter et al. (1997) which prescribes a stretch factor s that linearly broadens or narrows a rest-frame template light curve. The corrected peak magnitude (m_B^{corr}) can then be calculated from the observed peak magnitude (m_B) using:

$$m_B^{corr} = m_B + \Delta_{corr}(s) \tag{1.42}$$

$$\Delta_{corr}(s) = \alpha(s-1) \tag{1.43}$$

Where Δ_{corr} is a monotonic function of s which corrects the observed m_B for variations from the template SNe. s can be directly fit for each SNe Ia by broadening and narrowing a template light curve until it best matches the SN light curve. α is a nuisance parameter which must be fit alongside the cosmological parameters of interest.

In addition to the stretch factor correction, P99 apply a Galactic extinction correction A_R leading to an effective rest-frame B-band magnitude of:

$$m_B^{effective} = m_R + \Delta_{corr} - K_{BR} - A_R \tag{1.44}$$

Where K_{BR} is the K-correction as described in Equation (1.36).

The Hubble diagram of both the SCP and HZT is provided in Figures 1.3a and 1.3b, respectively.

The final stage of the SCP and HZT analysis is fitting the cosmological parameters. HZT and SCP both rely on a least squares fitting framework, in which a χ^2 function is minimised. HZT use the following χ^2 function:

$$\chi^2_{HZT} = \sum_i \frac{\left(\mu_{cosmo}(z_i) - \mu_i\right)^2}{\sigma^2_{\mu,i} + \sigma^2_v} \tag{1.45}$$

Where μ_{cosmo} is the theoretically predicted distance modulus (as calculated by Equation (1.26)), μ_i is the distance modulus of the ith SN, $\sigma_{\mu,i}$ is the uncertainty in the distance modulus of the ith SN, and σ_v is the dispersion in galaxy redshift due to peculiar velocities.

SCP do not present their χ^2 function in explicit form; however, it is implied to be:

$$\chi^2_{SCP} = \sum_i \frac{\left(m_{B,i}^{effective} - \mathcal{M}_B - \mu_{cosmo}(z_i)\right)^2}{\sigma_i^2 + \sigma_{sys}^2} \tag{1.46}$$

Where $m_{B,i}^{effective}$ is the effective rest-frame peak B-band magnitude of the ith SN, $\mathcal{M}_B = M_B - 5\log_{10}(\mathrm{H}_0) + 25$ is the 'Hubble-constant-free' peak B-band absolute magnitude of an $s = 1$ SN, σ_i is the measurement uncertainty of the ith SN, and σ_{sys} accounts for systematics caused by correlations in photometric calibration uncertainties.

The ΛCDM contours of both SCP and HZT are provided in Figures 1.4a and 1.4b, respectively.

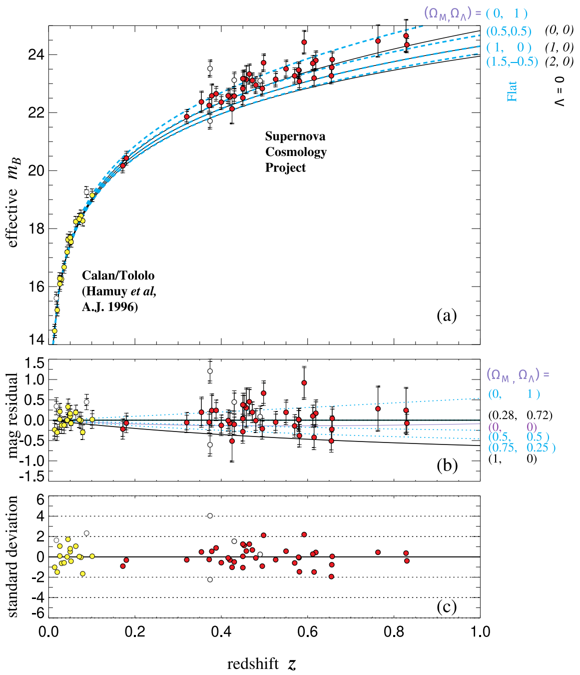

(a) The Supernova Cosmology Project Hubble diagram, Figure 2 of Perlmutter et al. (1999). Contains 42 high redshift supernovae, and 18 low redshift SNe. The residual plot is relative to the best-fitting cosmology with $\Omega_\mathrm{M} = 0.28$ and $\Omega_\Lambda = 0.72$

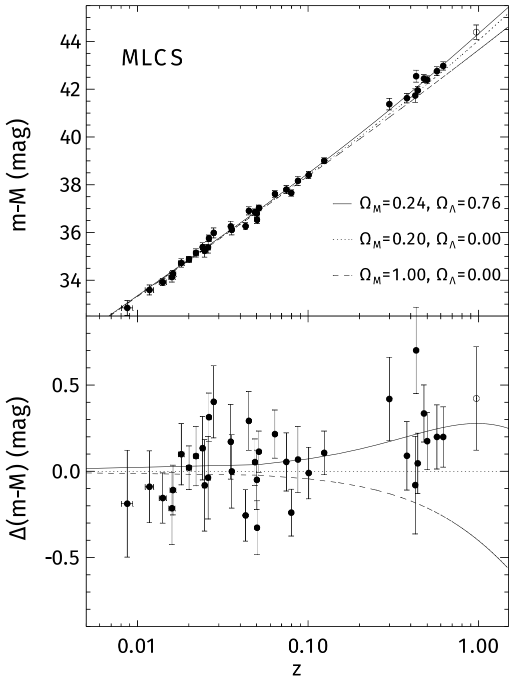

(b) The High-Z Supernova Search Team Hubble diagram, Figure 4 of Riess et al. (1998). Contains 10 high redshift supernovae, and 27 low redshift SNe. The empty circle corresponds to SN 1997ck, a SN at $z = 0.97$ which had an observed light curve shape and peak luminosity consistent with SNe Ia, but which lacked spectroscopic classification. The residual plot is relative to a cosmology with $\Omega_\mathrm{M} = 0.2$ and $\Omega_\Lambda = 0.0$

Figure 1.3: The Hubble diagram of both SCP and HZT.

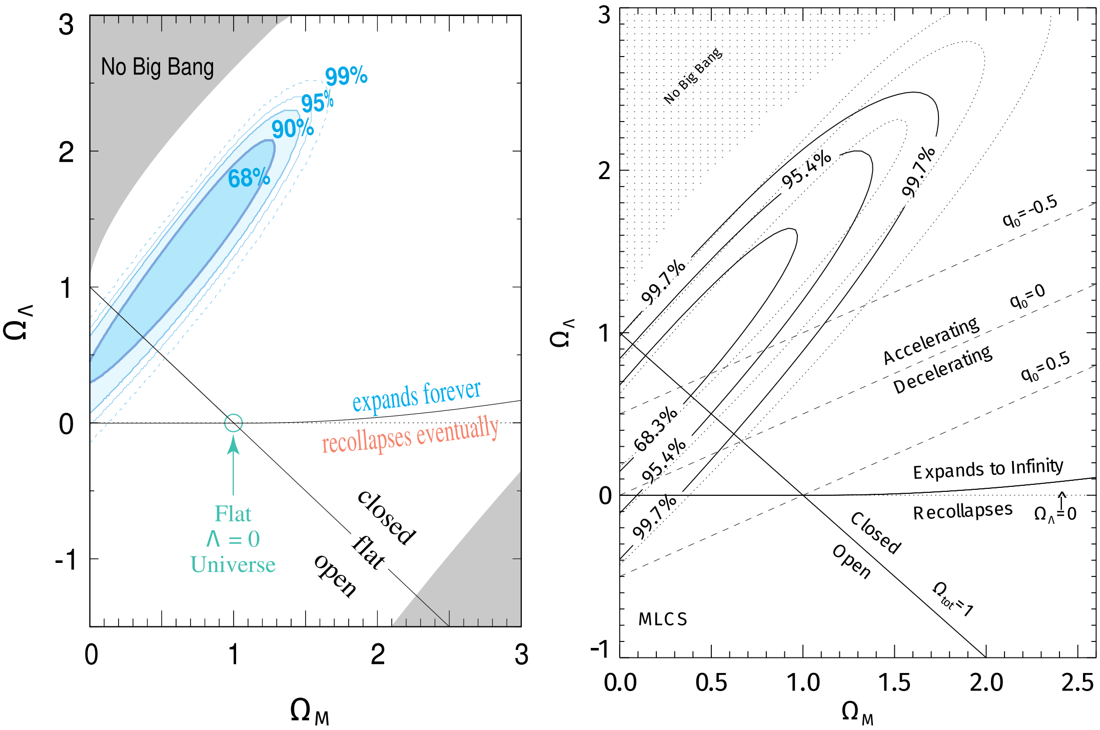

(a) The Supernova Cosmology Project's ΛCDM contour — Figure 7 of Perlmutter et al. (1999).

(b) The High-Z Supernova Search Team's ΛCDM contour — Figure 6 of Riess et al. (1998). The solid contour contains all SNe Ia in the HZT sample, the dotted contour contains a subset excluding the unclassified SN 1998ck.

Figure 1.4: The ΛCDM contours of both SCP and HZT.

Both SCP and HZT found compelling evidence that the Universe was accelerating. Under ΛCDM, acceleration occurs if $\Omega_\Lambda \geq \frac{\Omega_M}{2}$, which can be parameterised in the 'deceleration' parameter $q_0 = -\ddot{a}(t_0)a(t_0)/\dot{a}^2(t_0)$. If $q_0 < 0$ the Universe is accelerating. HZT find $\Omega_M = 0.24^{+0.56}_{-0.24}$, $\Omega_\Lambda = 0.72^{+0.72}_{-0.48}$, and $q_0 = -0.75 \pm 0.32$ for a ΛCDM model, and $\Omega_M = 0.24 \pm 0.1$, and $q_0 = -0.64 \pm 0.11$ for a Flat ΛCDM model. SCP find $\Omega_M = 0.73 \pm 0.125$, $\Omega_\Lambda = 1.32 \pm 0.167$, and $q_0 = -0.96 \pm 0.178$ for a ΛCDM model[1], and $\Omega_M = 0.28^{+0.09}_{-0.08}$, $q_0 = -0.58^{+0.085}_{-0.085}$ for a Flat ΛCDM model.

This was the first evidence for dark energy, which would become a signature focus of SNe Ia cosmology. Both teams investigate the effects of a number of systematic uncertainties on their results, to ensure they can be trusted. This

[1] SCP did not directly provide uncertainties for the ΛCDM model, instead these were approximated from the provided relationship $0.8\Omega_M - 0.6\Omega_{DE} = 0.2 \pm 0.1$.

includes the effect of SNe Ia evolution with time, the uncertainty in galactic extinction, sample selection bias, the effect of a Local Void, the possibility of weak gravitational lensing, the choice of light curve fitting method, and the possibility of non-Ia contamination. These systematic uncertainties are not accounted for in the nominal analysis, instead each systematic is considered separately, with a new analysis performed to investigate the effect of that systematic. This method of handling systematics allows for confidence in the nominal analysis, but assumes all systematics are independent, and doesn't allow for a joint statistical and systematic uncertainty to be found.

1.4.2 Phase II — SNLS, SDSS, Essence, CSP, CFA, Union, & Pantheon

Following the discoveries of the HZT & SCP teams, a focus was placed on improving the statistical power of SNe Ia. This meant observing many more SNe, and reducing systematic uncertainties. To achieve this, a number of SNe Ia surveys were started, including the Supernova Legacy Survey (SNLS; Astier et al., 2006; Conley et al., 2011; Guy et al., 2010; Sullivan et al., 2011), the Sloan Digital Sky Survey Supernova Survey (SDSS; Frieman et al., 2007; Sako et al., 2007), the Equation of State: SupErNovae trace Cosmic Expansion survey (ESSENCE; Miknaitis et al., 2007; Narayan et al., 2016; Wood-Vasey et al., 2007), The Carnegie Supernova Project (CSP; Hamuy et al., 2006), and the continuation of the Center for Astrophysics supernova program (CFA; Hicken et al., 2009, 2012; Jha et al., 2006; Riess et al., 1999). Each of these programs introduced improvements to the observation, processing, and analysis of SNe Ia for cosmology.

1.4.2.1 Supernova Legacy Survey

SNLS was a 5-year program running from 2003 to 2008 as part of the Canada-France-Hawaii Telescope Legacy Survey (CFHTLS; Cfhtls, 2002). To date, a sample of 252 high redshift SNe Ia ($0.15 < z < 1.1$) discovered in the first three years of SNLS have been published (Guy et al., 2010), whilst the full five-year results are still being analysed (private communication). Additionally, constraints obtained by combining the three-year dataset with other SNe Ia samples Conley et al. (2011), and other cosmological probes Sullivan et al. (2011) have been published.

SNLS was the first supernova survey to employ a 'rolling search' survey strategy. This strategy involves a single telescope continuously observing the same areas of the sky at a regular cadence, with SNLS observing every three to four days. This continuous, wide-field imaging is ideal for discovery many

SNe Ia over the lifetime of a SN survey. Additionally, SNe Ia can be discovered well before peak flux, leading to early classification and follow-up. Other advantages include consistent photometric sampling independent of light curve phase, better quality reference images, allowing for high quality subtraction, and reducing the impact of weather.

Rolling search surveys must accurately classify transient events based on only a few early epochs, to allow for efficient spectroscopic follow-up. The selection strategy employed by SNLS is described in Sullivan et al. (2006), and involves fitting SNe Ia template light curves to the candidate transient, with the likelihood of the transient being a Ia calculated from the quality of the template fit. Spectroscopic follow-up comes from the Keck (Ellis et al., 2008), ESO VLT (Balland et al., 2009, 2018), and Gemini (Bronder et al., 2007; Howell et al., 2005) telescopes.

SNLS introduce a new photometric technique, which is compared to the classic subtraction method used to reduce SN light curves. This technique, described in Astier et al. (2006), involves resampling images to the pixel grid of the best quality image, then simultaneously fitting an image of the host galaxy, alongside the position and flux of the SN. This method has the advantage of providing both more accurate SN fluxes, and a covariance matrix between the SN flux and the host galaxy brightness, allowing for more accurate uncertainties than simple subtractions.

Two light curve fitting methods, SALT2 (Guy et al., 2007, 2005) and SiFTO (Conley et al., 2008), were compared, to evaluate the scale of systematic uncertainty which arises from choice of light curve fitter. Both of these fitters are empirical models of SNe Ia spectral sequences, as compared to the template modelling used in previous analyses. This has the advantage of not requiring K-correction to account for redshift difference between template and observed SN.

Both SALT2 and SiFTO model the SNe Ia light curve as a time-varying spectral energy density (SED). SALT2 models this SED as a linear combination of several principal components, multiplied by a wavelength dependant colour law. Typically, two principal components are used, which corresponds to the SED of the 'average' SN Ia, and the 'average variation' between SNe Ia SEDs. This model parameterises a SN light curve from three parameters, the peak rest-frame B-band magnitude (m_B), a stretch parameter (x_1), and a colour parameter ($\mathcal{C}$).

SiFTO models the SED by starting with a base model of some fiducial SN Ia, which is then adjusted by some additional parameters to match the SN Ia of interest. Typically, a parameter for overall flux normalisation and another for overall time offset, alongside a stretch (s) and a number of colour parameters are used. Unlike SALT2, colour is not modelled from a single parameter, instead each filter is prescribed a colour parameter. After fitting, these colour parameters are combined back into a single parameter, which is then used to correct the SN Ia light curve. In general, SiFTO is a simpler model than SALT2. This has the advantage that SiFTO is more robust to changes in the training sample used, but is less able to model individual features. Over time, SALT2 became the light curve fitting model of choice in SN analyses.

The distance modulus of SNe Ia fit to either SALT2 or SiFTO can be calculated using:

$$\mu = m_B - \mathcal{M} + \alpha S - \beta \mathcal{C} \tag{1.47}$$

Where m_B is the observed peak magnitude, $\mathcal{M}$ is the absolute peak magnitude of the SN, S is a shape parameter (x_1 for SALT2 and $(s-1)$ for SiFTO), $\mathcal{C}$ is the colour parameter, and α and β are nuisance parameters representing the slope of the stretch-luminosity, and colour-luminosity relations. Alongside $\mathcal{M}$, the nuisance parameters α and β are marginalised over as part of the cosmology fit.

Cosmological fitting involved minimising the following χ^2 function:

$$\chi^2 = \sum_{SN} \frac{(\mu - \mu_{cosmo})^2}{\sigma^2(\mu) + \sigma^2_{int}} \tag{1.48}$$

Where μ_{cosmo} is the predicted cosmology as calculated in Equation (1.26), $\sigma(\mu)$ is the measurement uncertainty, and σ_{int} is an additional uncertainty term known as the intrinsic scatter. σ_{int} is chosen such that the reduced χ^2 is equal to 1, and represents all uncertainty not included in $\sigma(\mu)$. To account for Malmquist bias, a redshift-dependant correction is applied to distance moduli, based on simulated survey detection and classification efficiency.

Systematic uncertainties are not considered during the nominal analysis, instead they are propagated to the uncertainty in cosmological parameters after fitting is done. The systematic uncertainties considered include:

- Choice of light curve fitter
- Light curve fitter training sample
- Photometric calibration
- Uncertainty in Malmquist bias correction
- Uncertainty in intrinsic scatter

- Potential for redshift dependant β evolution
- SNe Ia brightness & host galaxy mass correlation

Of particular interest is the final systematic source. At the time of the SNLS analysis, evidence of a correlation between the brightness of SNe Ia, and the mass of the host galaxy was being discovered. Sullivan et al. (2010) identify with 4σ significance an increase in brightness in SN with a massive ($> 10^{10} M_{\odot}$) host galaxy after colour and stretch corrections. Additionally, a less significant correlation ($\sim 2.7\sigma$) is found between β and the specific star-formation rate of the host. The source of this host galaxy dependency is still a matter of active investigation, with possibilities including dust attenuation (Brout and Scolnic, 2021; Meldorf et al., 2022; Popovic et al., 2021), metallicity (Campbell et al., 2016; Galbany et al., 2022; Pan et al., 2013), and specific star-formation rate (Childress et al., 2013; Dixon et al., 2022; Galbany et al., 2022; Lampeitl et al., 2010; Rigault et al., 2020). This host galaxy dependency is discussed in further detail in Section 4.1.1.

Guy et al. (2010) fit a Flat ΛCDM to the high redshift SNLS SNe Ia sample *with no additional low-z survey* and find $\Omega_{\mathrm{M}} = 0.211 \pm 0.034(\mathrm{stat}) \pm 0.069(\mathrm{sys})$ with the uncertainty dominated by calibration uncertainties, contributing ± 0.048 of the total uncertainty.

Conley et al. (2011) combine the SNLS supernovae with 93 SDSS SNe Ia (see Section 1.4.2.3), 14 SNe Ia from the Hubble Space Telescope, and 123 low redshift SNe Ia (see Section 1.4.2.5), alongside constraints from BAO and CMB. They find $\Omega_{\mathrm{M}} = 0.274^{+0.017}_{-0.016}(\mathrm{stat{+}sys})$, and $\Omega_{\Lambda} = 0.732^{+0.016}_{-0.017}(\mathrm{stat{+}sys})$ for a ΛCDM model, $\Omega_{\mathrm{M}} = 0.272^{+0.017}_{-0.016}(\mathrm{stat{+}sys})$, and $w = -1.058^{+0.087}_{-0.082}(\mathrm{stat{+}sys})$ for a Flat wCDM model, and $\Omega_{\mathrm{M}} = 0.271^{+0.015}_{-0.015}(\mathrm{stat{+}sys})$, $w = -0.905^{+0.196}_{-0.196}(\mathrm{stat{+}sys})$, and $w_a = -0.984^{+1.094}_{-1.097}$ for a w_aCDM model.

1.4.2.2 ESSENCE

The ESSENCE survey was designed with the goal of measuring the dark energy equation of state parameter (w) to a precision of 10% (Miknaitis et al., 2007; Narayan et al., 2016). To this end, a redshift range of $0.2 < z < 0.8$ was targeted with the Blanco 4m telescope at CTIO over a period of 6 years. As with SNLS, image subtraction and light curve template fitting is used to identify SN Ia candidates within a few hours of observation. Further classification and redshifting is provided by spectroscopy from the KECK I and II, VLT, Gemini North and South, the Magellan Baade and Clay, and MMT telescopes. Much thought was placed on reducing systematic uncertainty from photometric calibration, as this was identified as one of the largest sources of systematic uncertainty. Unlike SNLS, SN fluxes were measured via image subtraction rather than simultaneous modelling of host galaxy and SN fluxes.

Preliminary results from the ESSENCE survey are provided by Wood-Vasey et al. (2007), an analysis of the final dataset was not performed, instead ESSENCE SNe Ia were included in various joint analyses which are discussed in Section 1.4.2.6. At the time of release, 213 (Narayan et al., 2016) SNe Ia between $0.15 < z < 0.7$ had been spectroscopically confirmed by the ESSENCE team. To supplement this, the nearby SNe sample used for training MLCS2k2 was included to anchor the Hubble diagram. Light curve fitting was performed with the MLCS2k2 method (Jha et al., 2007), with a comparison to the SALT (Guy et al., 2005) algorithm used by SNLS (at the time of publishing, the updated SALT2 method had not been developed). MLCS2k2 is an updated version of the Multicolor LightCurve Shape method used by the HZT team. This method involves producing a continuum of template light curves from a training set of SNe Ia. MLCS2k2 (named as such because it was designed in 2002) includes more accurate K-corrections at low redshift, better handling of host-galaxy extinction, a method for separating the intrinsic colour of a SN Ia, and reddening due to host galaxy extinction, and an updated training sample.

As with SNLS, χ^2 minimisation is used to fit a cosmology, with only statistical measurement error included in the χ^2 function. An analogue of the scatter parameter (σ_{int}) included in the SNLS χ^2 function is pre-calculated by fitting a ΛCDM model to the nearby sample only, and calculating a σ_{add} needed for $\chi^2/\text{DoF} = 1$. For the MLCS2k2 method $\sigma_{add} = 0.1$, and for the SALT model they find $\sigma_{add} = 0.13$. This additional uncertainty includes both the intrinsic dispersion of SNe Ia luminosity, and the model uncertainty in the light curve fitting method, and is added in quadrature to the measurement uncertainty.

Many sources of systematic uncertainty were considered as part of this initial analysis, including photometric calibration, K-correction and bandpass filter uncertainty, extinction and the choice of prior assumption on extinction, selection effects such as Malmquist Bias, the possibility of SNe Ia evolving with redshift, the effect of local large-scale structure, and gravitational lensing. These systematic uncertainties are propagated through to an additional uncertainty in the final results.

ESSENCE's preliminary analysis find $w = -1.059^{+0.091}_{-0.093}(\text{stat}) \pm 0.13(\text{sys})$ and $\Omega_\text{M} = 0.267^{+0.028}_{-0.018}(\text{stat})$ for Flat wCDM model, combining with SNLS and low-z SNe Ia as well as BAO constraints.

1.4.2.3 SDSS-II Supernova Survey

The SDSS-II supernova survey ran for three years between 2005 and 2007, and made use of the SDSS telescope — a 2.5m telescope situated at the Apache Point Observatory (York et al., 2000), and observing in five broad optical bands (*ugriz*). Spectroscopic follow-up was performed by a number of telescopes, include the HET, NTT, ARC, Subaru, MDM, WHT, KPNO, Keck, NOT, and SALT telescope. Spectroscopy was used for both SN classification, and redshift, with host-galaxy spectra preferred.

The SDSS-II Supernova Survey was motivated by a lack of SNe Ia in the so-called 'redshift desert' — $0.1 \leq z \leq 0.3$. Additionally, SDSS aimed to collect both high ($z > 0.1$) and low ($z < 0.1$) redshift SNe Ia with the same instrument, thus reducing systematic uncertainties due to photometric calibration. To this end, SDSS targeted SNe Ia in the range $0.05 \leq z \leq 0.35$.

Like SNLS and ESSENCE, SDSS was a rolling survey, repeatedly observing the same patch of sky. As SDSS had been continuously monitoring these same patches of sky prior to the supernova survey, co-added reference images were used to perform difference imaging. Template fitting of different SN types and redshifts identified SNe Ia candidates for spectroscopic follow up. Final photometry was measured via 'scene-modelling' (Holtzman et al., 2008). This method was similar to the SNLS photometric reduction technique, in that it simultaneously fits every frame with a model of SN photometry and background galaxy photometry. However, unlike SNLS, this method did not require any resampling of pixels, allowing for per-pixel error propagation.

Kessler et al. (2009a) presents cosmological constraints from the first year of the SDSS-II Supernova Survey, in conjunction with SNe Ia from ESSENCE (Wood-Vasey et al., 2007), SNLS (Astier et al., 2006), the Hubble Space Telescope (HST; Riess et al., 2007), and a compilation of nearby SNe Ia described in Jha et al. (2007). This analysis made use of both the MLCS2k2 (Jha et al., 2007) and SALT2 (Guy et al., 2007) light curve fitters. Unique to this analysis was a new method of accounting for survey incompleteness and selection effects. Typically, these effects are corrected by detailed simulations of fake SN Ia embedded directly into survey images. However, due to the multi-survey nature of this analysis the computational cost of computing full image-level simulations for every survey was too great. Instead, the software package SuperNovaANAlysis (SNANA; Kessler et al., 2009b) was developed to perform Monte-Carlo simulations of light curves based on actual survey conditions. SNANA is described in detail in Section 2.3.2. SNANA simulates SN light curve using either MLCS2k2 or SALT2, and then converts this simulated model into fake CCD counts by using the measured point spread function, zero-point, CCD gain, and sky background at each survey epoch and sky location. The initial simulation draws a redshift from a power law distribution determined by predicted SN Ia rates (Dilday et al., 2008), and model parameters (Δ and A_v for MLCS2k2, or x_1 and $\mathcal{C}$ for SALT2) from distributions inferred from the data. An empirically determined model of the intrinsic scatter of SNe Ia is added to bring the total level of variation in SN brightness in line with that observed in the data. Finally, estimates of the survey search efficiency are used to determine simulated SNe Ia which would have been missed by the survey under normal observing conditions, informing the bias present in the data samples, which is included as a source of systematic uncertainty.

Cosmological fitting was performed by minimising a χ^2 function; however, unlike previous analyses, the uncertainty term of the χ^2 function is:

$$\sigma_\mu^2 = \sigma_{fit}^2 + \sigma_{int}^2 + \sigma_z^2 \tag{1.49}$$

Where σ_{fit} is the measurement uncertainty reported by the light curve fitter, $\sigma_{int} = 0.16$ is the intrinsic scatter, and σ_z is the uncertainty associated with redshift and is composed of both the uncertainty in determining the redshift from either the SN or its host galaxy, and the peculiar motion of the host galaxy. SNe Ia constraints are combined with constraints from baryon acoustic oscillations and the cosmic microwave background. For a Flat wCDM model, the MLCS2k2 fitter resulted in $w = -0.76 \pm 0.07(\text{stat}) \pm 0.11(\text{sys})$ and $\Omega_\text{M} = 0.307 \pm 0.019(\text{stat}) \pm 0.023(\text{sys})$, whereas the SALT2 fitter resulted in $w = 0.96 \pm 0.06(\text{stat}) \pm 0.12(\text{sys})$, $\Omega_\text{M} = 0.265 \pm 0.016(\text{stat}) \pm 0.025(\text{sys})$

1.4.2.4 Pan-STARRS1

The Panoramic Survey Telescope and Rapid Response System (Pan-STARRS1 (PS1); Chambers et al., 2016) project consists of a number of imaging surveys using the Pan-STARRS Telescope, with two focused on supernova cosmology — the 3π Steradian Survey and the Medium Deep Survey (MDF), both of which ran from 2009 to 2014. The former is a wide-field imaging survey in five filters, $grizy_\text{P1}$, covering the sky north of Dec=-30°. This survey is ideal for observing bright, low-redshift transients. The latter consists of 12 deep fields which were continuously monitored every three days over 6–8 month observing seasons. The first day of the cycle observed in g_P1 and r_P1, the second observed in i_P1, and the third in z_P1. The MDF survey was focused on observing high-redshift transients.

Initial cosmology results from the first year and half of PS1 are presented in

Rest et al. (2014), while Scolnic et al. (2014) explore the systematic uncertainties present in the cosmological analysis. Spectroscopic follow-up and light curve extraction is similar to previous surveys, with difference imaging used for initial transient detection, template fitting used for candidate identification, and the final SN light curves are determined by fitting a SN model to the images.

The SALT2 methodology is used for light curve fitting, with the addition of the SALT2mu method (Marriner et al., 2011), which fits the SALT2 α and β parameters to a nominal cosmology, typically the concordance cosmology. Previous analyses treated α and β as nuisance parameters which were simultaneously fit alongside cosmological parameters. The SALT2mu method allowed these parameters to be determined prior to constraining cosmological parameters, enabling the construction of a Hubble diagram independent of cosmological model. This decoupling of SN distance measures and cosmological models has many advantages, including:

- Analysing and improving SN distance uncertainties prior to cosmological fitting.
- Enabling direct comparison between SN distance moduli independent of cosmology.
- Providing consistent SN distances which can be used interchangeably with different cosmology fitters, improving reproducibility.

Unlike previous analyses, systematic uncertainties are considered at the fitting stage, rather than propagated after a statistics only fit is performed. This method was first published in Conley et al. (2011), which combined the SNLS three year data with low-z, SDSS, and HST SNe Ia. Under this method:

$$\chi^2 = \Delta\vec{\mu}^T \cdot \mathbf{C} \cdot \Delta\vec{\mu} \tag{1.50}$$

Where $\Delta\vec{\mu} = \vec{\mu} - \mu_{cosmo}(\vec{z})$, and $\mathbf{C} = \mathbf{D}_{\rm stat} + \mathbf{C}_{\rm sys}$ is the sum of the diagonal statistical uncertainties, and the covariant systematic uncertainties between SNe Ia. $\mathbf{D}_{\rm stat}$ is determined by propagating measurement uncertainties, and $\mathbf{C}_{\rm sys}$ is determined by varying each source of systematic uncertainty and measuring the resultant change in distance. More specifically:

$$\mathbf{C}_{i,j,sys} = \sum_{k=1}^{K} \left(\frac{\partial \mu_i}{\partial S_k}\right) \left(\frac{\partial \mu_j}{\partial S_k}\right) \left(\sigma_{S_k}\right)^2 \tag{1.51}$$

Where K is the number of systematic uncertainties, S_k is the kth systematic uncertainty, and thus $\left(\frac{\partial \mu_i}{\partial S_k}\right)$ is the change in the ith distance induced by shifting the kth systematic. The kth systematic is shifted by σ_{S_k} and the distances are recalculated and subtracted from the nominal distances. This formalism includes covariance between SNe, but not between systematic sources[1]. Additionally, it is assumed that all systematics are Gaussian in nature.

By including systematic uncertainties at the fitting stage, the resultant likelihood contour is more representative of the true uncertainty in cosmological constraint because it includes both statistic and systematic uncertainties.

Significant effort was placed on understanding and reducing systematic uncertainties in the PS1 analysis.

- Flux calibration errors were reduced by producing an improved photometric system which all samples were translated into.
- Selection effects were incorporated via SNANA simulations.
- Though the effect of host galaxy mass were not included in the main analysis, the change induced by considering host galaxy effects was included as a systematic uncertainty.
- Each SN was corrected for Milky Way extinction, with the uncertainty in the correction factor included as a systematic uncertainty.
- The redshift of each SN was corrected for peculiar velocity, with the uncertainty in the redshift correction included as a systematic uncertainty.

The constraints found by this preliminary PS1 analysis are $\Omega_{\mathrm{M}} = 0.256^{+0.201}_{-0.174}$(stat+sys) and $w = -1.120^{+0.450}_{-0.357}$(stat+sys) when considering SN only, and $\Omega_{\mathrm{M}} = 0.280^{+0.013}_{-0.012}$(stat+sys) and $w = -1.166^{+0.072}_{-0.069}$(stat+sys) when combining SN with BAO and CMB constraints.

1.4.2.5 Nearby Supernova Surveys

Thus-far all the surveys discussed have been mostly high-redshift ($z \gtrsim 0.1$), where the luminosity distance of SNe Ia is more sensitive to changes in w, providing better constraints on the nature of dark energy. However, low-redshift ($z \lesssim 0.1$) surveys are important for 'anchoring' the Hubble diagram — providing a robust fit of the y-intercept of the Hubble diagram. There are a number of prominent surveys which have observed low redshift supernovae including:

- The Calán/Tololo SN Survey (Hamuy et al., 1996), 1990 — 1993, 32 SNe Ia.

[1] Though they can be introduced, see Amanullah et al. (2010, Eq. C11) for a description of how

- The Center for Astrophysics Data Release 1 (CfA1; Riess et al., 1999), 1993 — 1996, 22 SNe Ia.
- The Center for Astrophysics Data Release 2 (CfA2; Jha et al., 2006), 1997 — 2001, 44 SNe Ia.
- The LICK Observatory Supernova Search (LOSS; Ganeshalingam et al., 2010), 1998 — 2008, 165 SNe Ia.
- The Centre for Astrophysics Data Release 3 (CfA3; Hicken et al., 2009), 2001 — 2008, 185 SNe Ia.
- The Carnegie Supernova Project Data Release 1 (CSP1; Contreras et al., 2010), 2004 — 2006, 35 SNe Ia.
- The Carnegie Supernova Project Data Release 2 (CSP2; Stritzinger et al., 2011), 2006 — 2009, 50 SNe Ia.
- The Centre for Astrophysics Data Release 4 (CfA4; Hicken et al., 2012), 2006 — 2011, 94 SNe Ia.
- The Foundation Supernova Survey (Foley et al., 2017; Jones et al., 2019) which uses the PS1 telescope, 2015 — 2019, 180 SNe Ia.
- The Zwicky Transient Facility Data Release 2 (ZTF DR2; Rigault et al., 2025), 2018 — 2020, 3628 SNe Ia. The photometry of DR2 is not yet ready for cosmological analysis though this will be addressed in the upcoming DR2.5.
- The Dark Energy Bedrock All Sky Survey (DEBASS), an ongoing survey using the same instrument as the DES survey, 2021 — present, ~ 350 SNe Ia thus-far. See Section 4.1 for more details.

Early low-z SN surveys (Calán/Tololo, CfA1, CfA2, and LOSS) transformed their observations into the 'Standard' UBVRI Johnson/Cousins photometric system (Cousins, 1976; Johnson and Morgan, 1953). In contrast, later low-z SN surveys (CfA3 and 4, CSP1 and 2, and Foundation) report observations in the natural photometric system of the observing telescope. The former is less desirable as the method used to transform from the observing instrument's natural system to the Standard system is often unreported and can be imprecise, leading to systematic uncertainties.

When combining samples from multiple surveys, care must be taken as to the photometric calibration of each pass-band present in the combined sample. Each pass-band introduces two systematics — the uncertainty in the position of the central wavelength, and the uncertainty in the filter zero-point. Therefore, the decrease in statistical uncertainty from the increased number of SN may be offset by the increased systematic uncertainty from including more band-passes.

The Foundation SN survey aimed to address this issue by observing low-z SN Ia using the same instrument as the high-z Pan-STARRS1 sample, leading to lower systematic uncertainties at the cost of higher statistical uncertainties due to the 'missing' low-z SN from other surveys. This combined Foundation+PS1 sample is presented in Jones et al. (2019), when combining with CMB constraints, they find $w = -0.938 \pm 0.053$ for a ΛCDM model.

1.4.2.6 Joint Analyses — Union, JLA, and Pantheon

Whilst all the surveys discussed have performed cosmological analysis on their data, the real constraining power comes from combining these survey samples together, increasing the total number of SNe Ia, and therefore lowering the statistical noise. Riess et al. (2007, 2004) present the first such compilation, combining HST supernovae with low redshift SNe Ia from the Calán-Tololo SN Survey (Hamuy et al., 1996), CfA1 (Riess et al., 1999), and CfA2 (Jha et al., 2006), and high redshift SNe Ia compiled from Knop et al. (2003); Riess et al. (1998, 2001); Tonry et al. (2003); and Barris et al. (2004). From this compiled list of supernovae, a 'gold' sample of 157 SNe Ia was produced from SNe Ia with both high confidence classification and a well sampled light curve. This sample provided strong evidence for a 'cosmic jerk', when the Universe transitioned from decelerating to accelerating. The gold sample also took the role of a representative sample of SNe Ia in many following cosmological studies.

When combining many surveys together, there are a number of important considerations to reduce the impact of systematic errors on cosmological constraints. Foremost amongst these is the need to place all photometry on the same scale. As discussed in Section 1.3.1, the process of calibrating SN CCD counts to astronomical fluxes and magnitudes depends on stars of known magnitude or known SED, and has evolved considerably since the first SN surveys.

Differences in the precise details of this calibration between different surveys can lead to systematic offsets amongst the combined sample. As such, where possible joint analyses will rescale the measurements using various approaches, ensuring consistency amongst all surveys in the combined sample.

Along a similar vein, any analysis performed on the samples, such as light curve fitting, standardisation, and extinction correction should be consistent amongst all surveys. Since each survey may choose their preferred analysis procedure, this typically means redoing all stages of the analysis on the combined sample.

As a final consideration, different surveys will have their own considerations for what is a 'high quality' or 'good' supernova. Once again, consistency is key when performing a joint analysis, so a well-defined method of SN Ia selection is needed across all surveys.

Union, Union2, & Union2.1: Though there have been many small-scale combinations of SN surveys, there have only been a handful of analyses which compile hundreds of SN across dozens of surveys, owing to the difficulty of effectively performing such an analysis. One of the first large-scale compilations is the 'Union' compilation (Kowalski et al., 2008). This compilation includes low-z supernovae from Hamuy et al. (1996, 17 SNe Ia), Riess et al. (1999, 11 SNe Ia), Jha et al. (2006, 16 SNe Ia), Krisciunas et al. (2001, 2004a,b, 6 SNe Ia), and a new sample of 22 SNe Ia discovered as part of the SCP Nearby 1999 Supernova Campaign (Aldering, 2000), totalling 48 nearby SNe Ia. Alongside this come high-z supernovae from Knop et al. (2003, 11 SNe Ia), Perlmutter et al. (1999, 42 SNe Ia), Riess et al. (1998); Schmidt et al. (1998, 16 SNe Ia), Barris et al. (2004, 22 SNe Ia), Tonry et al. (2003, 8 SNe Ia), Astier et al. (2006, 73 SNe Ia), Riess et al. (2007, 2004, 37 SNe Ia), and Miknaitis et al. (2007); Wood-Vasey et al. (2007, 84 SNe Ia). In total, 404 SNe Ia were included in the sample.

To ensure only cosmologically useful SNe Ia were included in the sample, a series of selection cuts were applied to the sample:

- A redshift > 0.015 ($414 \to 382$ SNe Ia)
- A successful light curve fit with the SALT framework (Guy et al., 2005) ($382 \to 366$ SNe Ia)
- Data from at least two bands between 3470Å and 6600Å (U and R band, respectively) ($366 \to 351$ SNe Ia)
- At least five observations ($351 \to 320$ SNe Ia)
- At least one observation between 15 days pre-max and 6 days post-max ($320 \to 315$ SNe Ia)
- Outlier rejection cut ($315 \to 307$ SNe Ia)

The outlier rejection was performed by performing a mock cosmology fit, and identifying SNe which deviate from the predicted Hubble diagram by a statistically significant margin. These SNe are likely to be contaminate non-Ia SNe.

The Union compilation employed a blind analysis, in which the fitted Ω_M was stored but hidden, and the data rescaled from the best fit cosmology to an arbitrary cosmology ($\Omega_M = 0.25, \Omega_\Lambda = 0.75$).

After unblinding, the Union compilation found for a wCDM model, $\Omega_M = 0.285^{+0.02}_{-0.02}(\text{stat})^{+0.01}_{-0.01}(\text{sys})$, $\Omega_\Lambda = 0.725^{+0.022}_{-0.023}(\text{stat})^{+0.012}_{-0.01}(\text{sys})$, and $w = -1.001^{+0.069}_{-0.073}(\text{stat})^{+0.08}_{-0.082}(\text{sys})$ when combined with BAO and CMB constraints.

Union was followed a number of years later by the Union2 compilation (Amanullah et al., 2010) which includes 6 new HST SNe Ia, and additional SNe Ia from Amanullah et al. (2008, 5 SNe Ia), Hicken et al. (CfA3, 2009, 185 SNe Ia), and Holtzman et al. (SDSS, 2008, 146 SNe Ia), bringing the new total to 557 SNe Ia. In addition to the increased sample size, the analysis was improved in a number of ways, including using the updated SALT2 light curve fitter (Guy et al., 2007) allowing more SNe Ia to pass selection cuts as SALT2 has a broader wavelength range. Following these improvements, the updated Union2 wCDM constraints are $\Omega_M = 0.281^{+0.018}_{-0.016}$(stat+sys), $\Omega_\Lambda = 0.725^{+0.02}_{-0.017}$(stat+sys), and $w = -1.035^{+0.093}_{-0.097}$(stat+sys) when combined with BAO and CMB constraints.

Shortly after Union2, Suzuki et al. (2012) produced the Union2.1 compilation, which includes an additional 20 SNe Ia from the HST Cluster Supernova Survey, and implements a host mass correction. This updated sample found for a wCDM model, $\Omega_M = 0.272^{+0.015}_{-0.014}$(stat+sys), $\Omega_\Lambda = 0.726^{+0.017}_{-0.016}$(stat+sys), and $w = -1.03^{+0.091}_{-0.095}$(stat+sys) when combined with BAO and CMB constraints. They also provide fits to a w_aCDM model, finding $\Omega_M = 0.274^{+0.016}_{-0.015}$(stat+sys), $\Omega_\Lambda = 0.699^{+0.02}_{-0.19}$(stat+sys), $w_0 = -1.198^{+0.1}_{-0.112}$(stat+sys), and $w_a = 1.19^{+0.13}_{-0.13}$(stat+sys).

Joint Lightcurve Analysis: Following the completion of the SNLS (Astier et al., 2006; Sullivan et al., 2011) and the SDSS-II (Kessler et al., 2009b) surveys, The Joint Light-curve Analysis (JLA; Betoule et al., 2014) combined these two surveys with the C11 (Conley et al., 2011) low-z compilation, producing a sample consisting of a vast majority of all SNe Ia observed at the time. In addition to the increased statistical power of this compilation, JLA improve systematic uncertainties through a detailed recalibration of SNLS and SDSS-II (Betoule et al., 2013). As an additional systematic improvement, JLA add SDSS-II SNe Ia to the Guy et al. (2010) SALT2 training sample, leading to improvements of the SALT2 SED model at UV wavelengths.

To account for observational biases in each sample, JLA follow Mosher et al. (2014) who leverage highly detailed SNANA (Kessler et al., 2009b) simulations to directly measure the level of bias present in a number of redshift bins. The bias is found by comparing the simulated distance modulus of each SNe Ia in a redshift bin to the distance modulus of these simulated SNe Ia as predicted by the JLA analysis.

Following these analysis improvements, JLA found $\Omega_M = 0.303 \pm 0.012$, $w =$

-1.027 ± 0.055 for a Flat wCDM model, combined with BAO and CMB constraints, and $\Omega_M = 0.304 \pm 0.012$, $w_0 = -0.957 \pm 0.124$, $wa = -0.336 \pm 0.552$ for a Flat w_aCDM model, combined with BAO and CMB constraints. At the time of release, the JLA analysis provided the best constraints on Dark Energy.

Pantheon: Upon the completion of the Pan-STARRS1 SN survey (PS1; Rest et al., 2014; Scolnic et al., 2014), JLA was superseded by the Pantheon compilation (Scolnic et al., 2018), which combined the JLA SNe Ia with 279 PS1 SNe Ia leading to a total sample size of 1048 SNe Ia. As part of the Pantheon analysis, a new cross-calibration method known as SuperCal (Scolnic et al., 2015) was developed. Rather than calibrating SN to a small sample of bright HST standard stars, SuperCal instead aims to calibrate surveys to the PS1 system. PS1 covered 3π steradians of the sky, overlapping the observing fields of most other SN surveys. This allowed direct comparison of secondary standard stars observed by PS1 and each survey in the Pantheon sample, and thus tying the photometry of every survey to the PS1 system. It is worth noting that 74 of the 85 systematic uncertainties considered in the Pantheon analysis are associated with photometric calibrations, so a reduction in calibration uncertainties has the greatest effect on the total systematic uncertainty.

Pantheon also iterated on the Bias Correction methodology of JLA through the BEAMS with Bias Correction (BBC; Kessler and Scolnic, 2017) method. As with JLA, BBC correct for observation bias by leveraging detailed SNANA simulation. However, instead of only measuring bias in the distance modulus, extremely large ($> 10^6$ SNe Ia) simulations allow for measuring the effect of observational bias on the SALT2 SN light curve parameters $(x_1, \mathcal{C})$. Another advantage of the BBC method is the introduction of SALT2mu (Marriner et al., 2011) (discussed previously in Section 1.4.2.4), which enabled the determination of SALT2 nuisance parameters (α, β) in a cosmologically independent manner. Section 2.3.5 discusses the BBC methodology in more detail.

When combined with CMB and BAO constraints, the Pantheon analysis finds $\Omega_M = 0.299 \pm 0.007$, $w = -1.047 \pm 0.038$ for a Flat wCDM model, and $\Omega_M = 0.3 \pm 0.008$, $wo = -1.007 \pm 0.089$, $wa = -0.222 \pm 0.407$ for a Flat w_aCDM model.

1.4.3 Phase III — DES, ZTF, Pantheon+, & Union3

This phase of cosmological surveys includes ongoing or recently completed analyses. These surveys represent the forefront of cosmological research, and contain the tightest constraints of cosmological parameters thus-far achieved. Of particular importance are the results of the Union3 (Rubin et al., 2023) and DES-SN5YR analyses. Though these surveys used largely independent datasets, employed different analysis techniques, and had little overlap in contributing researchers, both analyses found a $> 2\sigma$ tension with $w = -1$, indicating that dark energy may not be a cosmological constant as predicted by the current concordance cosmology (Flat ΛCDM). Additionally, both teams discovered evidence that the dark energy equation of state parameter may evolve with time. Though these results aren't conclusive, they do represent a burgeoning frontier of cosmological research in which the accepted model of our Universe is coming in to question.

1.4.3.1 Dark Energy Survey — 3 Year Supernova Analysis

DES is a multinational collaboration between more than 25 institutes, consisting of over 400 scientists. DES was initially proposed almost two decades prior to this work, with the primary goal of constraining w with four different cosmological probes, all to within 5% statistical uncertainty (The Dark Energy Survey Collaboration, 2005). The four probes were type Ia Supernovae (DES Collaboration et al., 2024a; Vincenzi et al., 2024), Baryon Acoustic Oscillations (DES Collaboration et al., 2024b; Mena-Fernández et al., 2024), Weak Lensing and Galaxy Clustering (Abbott et al., 2022, 2023). To this end, a new wide-field imager (DECam) was designed for use on the Blanco 4m telescope at the Cerro-Tololo International Observatory (CTIO; Flaugher, 2006). The DECam began observing in 2013, and continued for six years, with the final observations occurring in 2019.

The final DES-SN5YR sample consists of over 1500 *photometrically* classified SNe Ia. Whilst this sample was being collected and processed, a preliminary analysis of 251 spectroscopically confirmed SNe Ia from the first three years of DES observations was performed, known as the DES-SN3YR analysis. This preliminary analysis served both to present the high quality of DECam SN light curves, and the improvements to SN cosmological analysis developed by DES scientists. As part of this analysis, DES-SN3YR released eight supporting papers alongside the final analysis. These supporting papers covered:

- Search and discovery of SNe Ia (Kessler et al., 2015)
- Spectroscopic follow-up (Smith et al., 2020a)
- Photometric calibration (Lasker et al., 2019)
- Scene Modelled Photometry pipeline (Brout et al., 2019a)
- Correcting observational bias using detailed simulations (Kessler et al., 2019a)
- The effect of host galaxy properties on SNe Ia (Smith et al., 2020b)

- Constraints on H_0 via a reverse distance ladder (Macaulay et al., 2019)
- Analysis, Systematic Uncertainty, and Validation methodologies (Brout et al., 2019b)
- Bayesian Hierarchical alternative to constraining cosmological parameters (Hinton et al., 2019)

Though the preliminary DES-SN3YR sample was a third the size of the Pantheon sample, the constraint on w from this sample was only 1.4 times larger the Pantheon constraints; finding $\Omega_M = 0.311 \pm 0.009$, $w = -0.977 \pm 0.047$ for a Flat wCDM model with CMB (Planck Collaboration et al., 2016) and BAO (Alam et al., 2017; Beutler et al., 2011; Ross et al., 2015) constraints, and $\Omega_M = 0.316 \pm 0.011$, $wo = -0.885 \pm 0.114$, $wa = -0.387 \pm 0.43$ for a Flat w_aCDM model with CMB and BAO constraints.

1.4.3.2 Zwicky Transient Facility

High redshift SN surveys, like the Dark Energy Survey, require a sample of low redshift SNe Ia to anchor the Hubble Diagram. Typically, these low-z SNe Ia are drawn from a compilation of historical low redshift surveys. These compilations require careful calibration to reduce systematic uncertainty, and are increasingly limited in both the quality and number of SNe Ia, relative to the improvements in high redshift samples.

The Zwicky Transient Facility supernova survey (ZTF; Dhawan et al., 2021) aims to supersede these historical compilations by leveraging the Zwicky Transient Facility (Bellm et al., 2018), capable of observing the entire visible northern sky at a rate of ~3760 deg^2 per hour. Over the course of ZTF's first observing phase, from March 2018 to November 2020, one in every three nights was dedicated to an untargeted rolling survey of the complete northern sky, in g and r filters, and with a fiducial exposure time of 30s. To date, over 5000 objects have been discovered and spectroscopically classified by ZTF (ZTF Bright Transient Survey, 2024). Dhawan et al. (2021) present an investigation of 761 SNe Ia discovered in the first year of the ZTF supernova survey, of which 305 had a measured host galaxy redshift. This restricted sample is already comparable in size to the entire historical catalogue of low-z SNe Ia, whilst boasting a median first detection 10 days earlier than the historical catalogue, and a median redshift almost double that of the literature, at $\bar{z} = 0.057$. Following extensive spectroscopic follow-up (Fremling et al., 2020; Perley et al., 2020) ZTF's second data release (DR2; Rigault et al., 2025) was published, containing 3628 spectroscopically classified SNe Ia. Though the DR2 photometry is not yet ready for cosmological analysis (with the upcoming DR2.5 release planned to address this), Rigault et al. (2025) show that the existing sample already attains a typical Hubble residual scatter of ~ 0.15 mag.

Though the impressive size of the ZTF SN survey will improve statistical uncertainties, it remains to be seen what the impact of the relatively small wavelength coverage afforded by using only two filters (g and r) has on the systematic uncertainties of the ZTF SN survey.

1.4.3.3 Pantheon+

Like its predecessor, the Pantheon analysis, Pantheon+ is a carefully cross-calibrated sample of major SNe Ia surveys. Pantheon+ includes 1550 spectroscopically confirmed SNe Ia from 18 surveys (Detailed in Scolnic et al., 2022). In addition to a larger sample, Pantheon+ also developed many impactful improvements to the cosmological analysis of SNe Ia. Of particular note are the development of an improved model of intrinsic SNe Ia scatter based of physical dust models (Popovic et al., 2021), and the SuperCal-Fragilistic photometric recalibration (Brout et al., 2022b) which not only improved the precision of the Pantheon+ cross-calibration, but determined a calibration specific systematic covariance matrix. This covariance matrix allows for correlations between calibration systematics to be accounted for in the final cosmological constraints.

As part of the Pantheon+ analysis, Brout et al. (2021) discovered that the impact of systematic uncertainties could be reduced by a factor of 1.5 if the final cosmological fit is performed on an unbinned dataset, rather than summarising the dataset into a number of redshift bins. The cause of this improvement was attributed to the increased number of individual data points in the unbinned analysis allowing for 'self-calibration' of certain systematics. For systematics which are independent of redshift, large datasets have enough constraining power as to separate the impact of the systematic from a shift in cosmological parameters. Although the statistical uncertainty of binned data is smaller, Brout et al. (2021) show that a binned dataset could no longer differentiate a cosmological shift from a systematic shift. It is important to note that the impact of systematics that are dependent on redshift is indistinguishable from a cosmological shift, so the size of these systematic uncertainties is unaffected by binning.

Owing to the larger sample, and improved analysis techniques, Pantheon+ attained cosmological constraints with half the total uncertainty of the Pantheon analysis. For a Flat wCDM model with CMB and BAO constraints, Pantheon+ found $\Omega_{\mathrm{M}} = 0.315^{+0.005}_{-0.008}$, and $w = -0.978^{+0.024}_{-0.031}$. For a Flat w_aCDM model with CMB and BAO constraints, Pantheon+ found $\Omega_{\mathrm{M}} = 0.316^{+0.009}_{-0.005}$, $-0.81^{+0.066}_{-0.061}$, and $w_a = -0.65^{+0.28}_{-0.32}$.

1.4.3.4 Union3

The Union3 analysis (Rubin et al., 2023), much like the Pantheon+ analysis, is a compilation of many SNe Ia samples. The Union3 compilation includes 2087 SNe Ia across 24 datasets, the largest compilation thus-far. Pantheon+ recalibrated all samples to the PS1 system before cross-calibrating each survey to ensure consistency in observations of common tertiary standard stars.

In contrast, the Union3 analysis recalibrates all samples to the HST CALSPEC system (Bohlin et al., 2014), and do not perform cross-calibration corrections, instead validating that any inconsistencies present between surveys in the Union3 compilation has a negligible effect on the analysis constraints.

Perhaps the greatest departure from previous cosmological analyses by the Union3 analysis is the use of the UNITY Bayesian Hierarchical Model for cosmological parameter estimation. The standard method used by previous analyses is to first construct a Hubble Diagram by standardising SN Ia light curves, then constrain cosmological models by comparing predicted distance moduli with the observed distance moduli of the sample. In contrast, UNITY builds a model to predict the SALT m_B, x_1, and $\mathcal{C}$ parameters of SNe Ia. If this model were perfect, it would account for everything which could affect a SN Ia light curve, including the effect of cosmological expansion under different cosmological models. At present the UNITY model includes thousands of free parameters which account for intrinsic and extrinsic SN properties, intrinsic and extrinsic host galaxy properties, contamination of core-collapse supernovae, observational bias from incomplete data, uncertainties in the calibration of each sample in the Union3 compilations, and others. The SALT3 light curve fitter is used to determine m_B, x_1, and $\mathcal{C}$ of every SNe Ia in the Union3 compilation, and the thousands of free parameters are fit simultaneously with cosmological parameters to fit the true values of these fitted SALT3 parameters.

This methodology allows UNITY to unify the efforts of the entire SN cosmology community into a single model which produces robust Bayesian contours that can be analysed and validated with statistical rigour. Additionally, the high-z SNe Ia in the Union3 compilation are mostly independent of the DES-SN5YR analysis, with the only overlap being the 251 spectroscopically confirmed SNe Ia presented in the DES-SN3YR analysis. Having a (nearly) independent dataset analysed with a completely different technique allows for invaluable comparisons between the Union3 and DES-SN5YR cosmological constraints.

For a Flat wCDM model with BAO and CMB constraints, Union3 find $\Omega_{\rm M} = 0.314 \pm 0.007$, $w = -0.98^{+0.032}_{-0.033}$, and for a Flat w_aCDM model with BAO and CMB constraint, $\Omega_{\rm M} = 0.321 \pm 0.008$, $w_0 = -0.796^{+0.96}_{-0.93}$, $w_a = -0.71^{+0.35}_{-0.38}$. In both cases Union3 find weak tension with ΛCDM on the order of $1-2\sigma$.

1.4.3.5 The Dark Energy Survey — 5 Year Supernova Analysis

The final DES-SN5YR sample of 1635 SNe Ia is, to date, the largest and most constraining single instrument SNe Ia sample in existence. The improved analysis methodologies of the DES-SN5YR analysis are described in detail in Chapter 2 with a brief overview of the most impactful presented here.

The DES-SN3YR analysis made use of the SALT2 model for fitting and standardising SNe Ia light curves. Between the 3 and 5 year analyses an updated SALT3 model was produced, with a wider wavelength range, improved uncertainty estimation, and simpler, open source training software (Kenworthy et al., 2021). The difference between cosmological analyses using the SALT2 or SALT3 models is investigated by Taylor et al. (2023) and found to be negligible. The modelling of SNe Ia is improved by both by the shift to SALT3 and new models of SNe Ia intrinsic scatter which account for the effect of host galaxy properties such as host mass and colour (Kelsey et al., 2023; Popovic et al., 2021).

Both the internal calibration of DES-SN5YR photometry (Sevilla-Noarbe et al., 2021) and the cross-calibration between DES-SN5YR and the low-z SNe Ia compilation (Brout et al., 2022a) were updated, and all photometry included correction for atmospheric effects (Lee et al., 2023) and chromatic corrections (Lasker et al., 2019).

Following on from the findings of Brout et al. (2021) as to the importance of unbinned data, a new method in which data is re-binned into redshift, colour, and stretch cells was developed which provided the same benefit of an unbinned analysis whilst drastically reducing the size of the cosmological uncertainty covariance matrix, reducing the computational cost of cosmology fits on large-scale datasets.

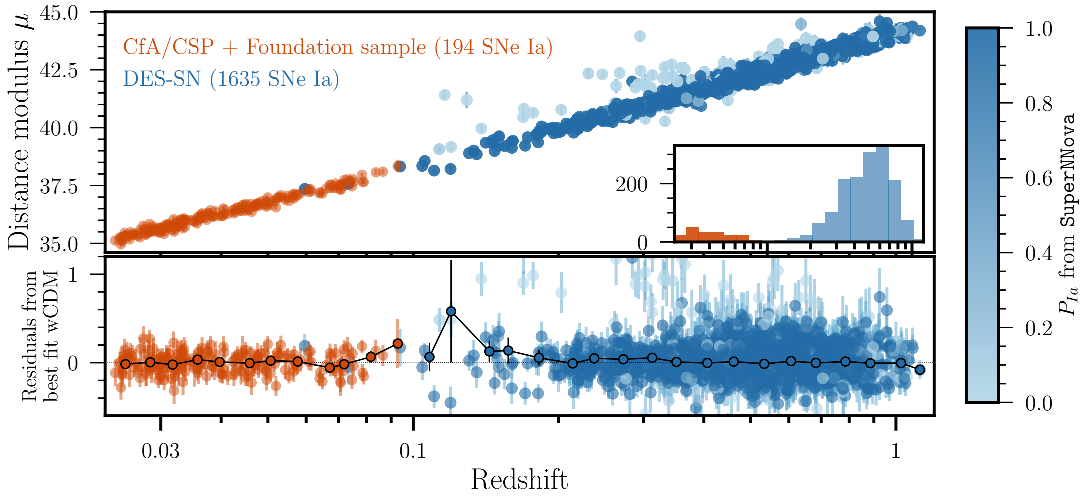

Figure 1.5: Hubble diagram of the DES-SN5YR analysis. DES-SN5YR SN are photometrically classified with the probability of being a Ia represented by the colour of the data. The constraining power of each SN Ia is scaled by this probability. The inset in the upper panel shows the redshift distribution of the low-z compilation of SNe Ia and the DES-SN5YR sample.

The Hubble Diagram of the DES-SN5YR analysis is presented in Figure 1.5, with the constraints on a Flat wCDM (Figure 1.6a) and a Flat w_aCDM (Figure 1.6b) model presented in Figure 1.6. For a Flat wCDM model, DES-SN5YR find $\Omega_M = 0.321 \pm 0.007$, $w = -0.941 \pm 0.026$. The constraint on w is $\sim 2.3\sigma$[1] from $w = -1$, which corresponds to the concordance cosmology model of dark energy as a cosmological constant. For a Flat w_aCDM model, DES-SN5YR found $\Omega_M = 0.325 \pm 0.008$, $w_0 = -0.773^{+0.075}_{-0.067}$, $w_a = -0.83^{+0.33}_{-0.42}$, ($\sim 2.7\sigma$[1] tension with ΛCDM). Both of these results are consistent with the constraints of the Union3 analysis.

When combining the DES-SN5YR SNe Ia constraints with BAO constraints from the Dark Energy Spectroscopic Instrument (DESI; DESI Collaboration et al., 2024a), DESI Collaboration et al. (2024b) find $w_0 = -0.727 \pm 0.067$, $w_a = -1.05^{+0.31}_{-0.27}$, which corresponds to a 3.9σ tension with ΛCDM, the strongest evidence for time evolving dark energy thus-far.

The unique contributions to cosmological constraints offered by SNe Ia can be seen clearly in Figure 1.6a where the 'cross-cutting' between the DES-SN5YR and CMB posteriors provide significant constraining power. As shown in Table 1.3, which details the individual constraining power of each probe used

[1] Approximately, as this assumes a Gaussian distribution and independent parameters

in the DES-SN5YR analysis, SNe are particularly sensitive to w. They provide some of the tightest constraints available on w and serve as a fundamental tool for understanding the nature of dark energy.

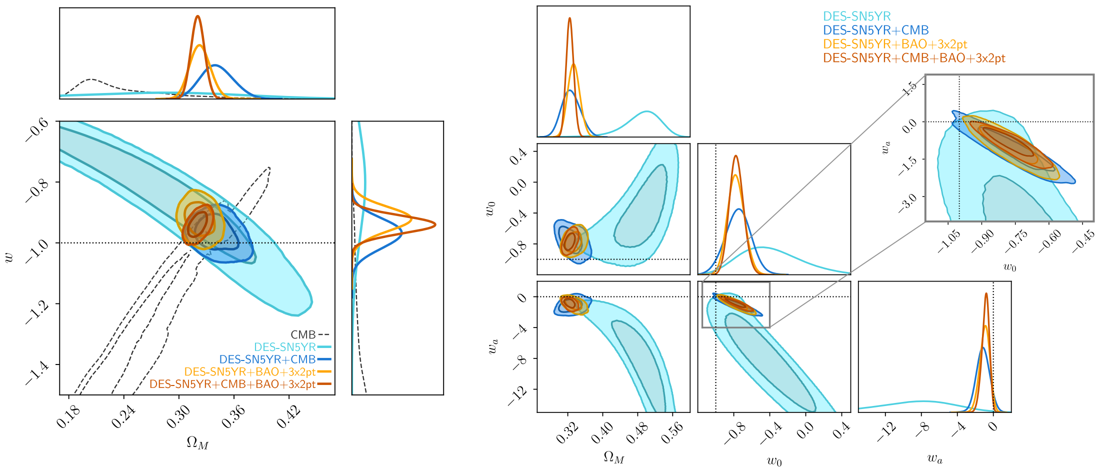

(a) Constraints on a Flat wCDM model. The horizontal dashed line corresponds to $w = -1$, consistent with ΛCDM. The best fitting $w = -0.941 \pm 0.026$ is in tension with $w = -1$ with $\sim 2.3\sigma$ significance.

(b) Constraints on a Flat w_aCDM model. The inset shows the $w - w_a$ contour about the constraints from multiple probes. The vertical and horizontal dashed lines correspond to $w_0 = -1.0$ and $w_a = 0.0$, respectively, consistent with ΛCDM. The best fitting $w_0 = -0.773^{+0.075}_{-0.067}$ and $w_a = -0.83^{+0.33}_{-0.42}$ are in tension with ΛCDM with $\sim 2.7\sigma$ significance.

Figure 1.6: DES-SN5YR constraints on cosmological models when combined with other cosmological probes. The tightest constraint on w come from combining DES-SN5YR SNe Ia with CMB, BAO, and 3×2pt galaxy cluster and weak lensing constraint.

Table 1.3: A comparison of Flat wCDM cosmological constraints provided by each probe used in the DES-SN5YR analysis. These constraints highlight the importance of combining multiple probes, and in particular the impact SNe Ia constraints have on Ω_M and w.

Survey	Probes[+]	
	Ω_M	w
DES-SN5YR[1]	SN, BAO, CMB, 3×2pt	
	$0.321^{+0.007}_{-0.007}$ (stat+sys)	$-0.941^{+0.026}_{-0.026}$ (stat+sys)
	SN Only	
	$0.264^{+0.074}_{-0.096}$ (stat+sys)	$-0.80^{+0.14}_{-0.16}$ (stat+sys)
eBoss[2]	BAO Only	
	$0.272^{+0.038}_{-0.017}$ (stat+sys)	-0.69 ± 0.15 (stat+sys)
Planck 2018[3]	CMB Only	
	$0.198^{+0.014}_{-0.055}$ (stat+sys)	$-1.58^{+0.16}_{-0.35}$ (stat+sys)
DES3×2pt[4]	3×2pt Only	
	$0.352^{+0.035}_{-0.041}$ (stat+sys)	$-0.98^{+0.32}_{-0.20}$ (stat+sys)

[+]Cosmological Probes — SN: Supernovae, BAO: Baryon Acoustic Oscillation, CMB: Cosmic Microwave Background, 3×2pt: Weak lensing and Galaxy clustering.
[1](DES Collaboration et al., 2024a; Vincenzi et al., 2024), [2](Alam et al., 2021; Dawson et al., 2016), [3](Planck Collaboration et al., 2020), [4](Abbott et al., 2022, 2023)

1.5 Thesis Statement

This thesis details many of the computational and statistical techniques which form a structural underpinning to the DES-SN5YR analysis, and my contributions to this analysis. Chapter 2 provides a detailed overview of the Pippin SN cosmology pipeline which was used as the primary analysis pipeline of the DES-SN5YR analysis. This pipeline is an end-to-end SN cosmology pipeline which takes SN light curves from the DES-SN5YR survey, performs SN Ia standardisation, corrects the sample for observation biases, calculates accurate statistical and systematic uncertainties, and constrains cosmological parameters. Throughout the DES-SN5YR analysis I developed and maintained the Pippin pipeline, integrating updates and improvements to the pipeline which enhanced its flexibility, modularity, and ease-of-use. This chapter describes each stage in the Pippin analysis pipeline, including both the specific configuration used by the DES-SN5YR analysis, and the improvements made by myself to that stage.

Chapter 3 contains the work of Armstrong et al. (2023), in which myself and my collaborators develop a novel method for measuring the consistency of cosmological constraints in a statistically rigorous manner. This method, dubbed the 'Neyman Approximation' utilises repeated simulations to compute a Frequentist confidence region which can be compared to the Bayesian posterior contour as a consistency check. This results of this work became one of the unblinding criteria of the DES-SN5YR analysis, providing confidence in the consistency and correctness of the DES-SN5YR results.

Finally, Chapter 4 discusses a number of ongoing projects aimed at preparing for future large-scale SN cosmology surveys, including LSST and Roman. These projects include investigations into new statistical techniques, the ongoing DEBASS survey, and a planned rewrite of the Pippin SN cosmology analysis pipeline.

Chapter 2

Pippin: An end-to-end cosmology pipeline

The Dark Energy Survey (DES) aimed to observe ~ 1900 SNe Ia in the redshift range $0.3 < z < 0.75$, using the Dark Energy Camera (DECam; Flaugher et al., 2015), mounted on the Blanco 4m telescope at CTIO. After three years of observations, a preliminary analysis of 207 spectroscopically confirmed SNe Ia provided the first cosmological constraints from DES (DES-SN3YR Abbott et al., 2019; Brout et al., 2019b). This analysis functioned as a proof of concept of the DES cosmology framework, and served to highlight where this framework excelled, and what improvements could be made for the eventual analysis of the complete DES sample.

One vital area of improvement was to the DES cosmology pipeline. The DES analysis relies on a number of programs including SuperNova ANAlysis (SNANA; Kessler et al., 2009b), SALT3 (Kenworthy et al., 2021; Taylor et al., 2023), SuperNNova (Möller and de Boissière, 2020), Scone (Qu et al., 2021), BEAMS with Bias Correction (BBC; Kessler and Scolnic, 2017), CosmoMC (Lewis and Bridle, 2002), and CosmoSIS (Zuntz et al., 2015). During the DES-SN3YR analysis, bespoke scripts were written on a per-project basis, leading to inconsistent workflows, difficulties in reproducing results, and a high entry barrier for new researchers. To address these issues, an end-to-end pipeline was built for the DES-SN3YR analysis (Pippin; Hinton and Brout, 2020). Pippin allowed for every step of the DES cosmological pipeline to be set up, configured, and run, from a single configuration file. This dramatically improved the consistency of the DES analysis workflow, and the reproducibility of the results.

Though Pippin had improved the DES-SN3YR analysis workflow, its utility outside the DES-SN3YR analysis was limited, as it suffered from a steep learning curve, and an inflexible design which made it difficult to integrate new software and methodologies as the best practices of SN cosmology evolved.

In early 2021, as part of my thesis, I took over the development of Pippin. My work was focused on addressing the aforementioned limitations in the DES-SN3YR implementation, expanding Pippin into a powerful, general purpose cosmological analysis tool for use within the full 5-year DES analysis (DES-SN5YR; DES Collaboration et al., 2024a; Vincenzi et al., 2024) and beyond.

This Chapter details the improvements made to Pippin, and the impact these changes have had, both on the DES-SN5YR analysis, and the greater SN cosmology community. Section 2.1 describes the general design and implementation of Pippin, with Sections 2.3.1 to 2.3.7 expanding on each stage of the Pippin analysis pipeline, detailing:

1. The purpose each stage serves within the Pippin analysis.
2. Technical details of the software underlying each stage, including how the software functions and how the software is integrated into Pippin.
3. How each stage was utilised in the DES-SN5YR analysis.
4. Improvements I made to each stage.

Finally, Section 2.4 summarises how my development of Pippin has improved its utilisation within the broader SN cosmology community.

2.1 The Design of Pippin

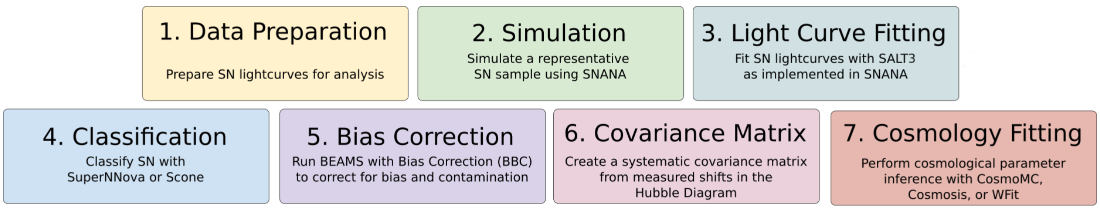

Figure 2.1: Overview of the `Stages` of a Pippin analysis. As part of the end-to-end analysis, Pippin makes use of SuperNova ANAlisys (SNANA; Kessler et al., 2009b), SALT3 (Kenworthy et al., 2021; Taylor et al., 2023), SuperNNova (Möller and de Boissière, 2020), Scone (Qu et al., 2021), BEAMS with Bias Correction (BBC; Kessler and Scolnic, 2017), CosmoMC (Lewis and Bridle, 2002), and CosmoSIS (Zuntz et al., 2015).

Pippin models the DES analysis as a series of `Stages`, each of which is responsible for a distinct component of the overall analysis (see Figure 2.1 for an overview of these `Stages`). For each `Stage`, the user provides configuration options via an input file, which Pippin uses to create a number of `Tasks` which setup, configure, and execute the underlying software handled by that `Stage`. Note that throughout the Pippin source code and documentation, the terms 'stage' and 'task' are used interchangeably. Here we strictly conform to the convention that a `Stage` represents a distinct step in the analysis pipeline, typically associated with a single, underlying astronomical program, whilst a `Task` represents a particular configuration and execution of a `Stage`. The general syntax used to configure a `Stage` is presented in Code Block 2.1 with the purpose of each component described in List 2.1.

Code Block 2.1: An example of the typical syntax for configuring a Pippin `Stage`. See List 2.1 for a description of each component.

```
STAGE_NAME:
    TASK_NAME_1:
        MASK: PREV_TASK
        SETUP_OPT_1: VALUE
        SETUP_OPT_2: VALUE
        OPTS:
            TASK_OPT_1:
                - VALUE
                - VALUE
            TASK_OVERRIDE_1: VALUE
    TASK_NAME_2:
        MASK: OTHER_PREV_TASK
        SETUP_OPT_1: VALUE_2
        SETUP_OPT_2: VALUE_2
        OPTS:
            TASK_OPT_1:
                - VALUE_2
                - VALUE_2
            TASK_OVERRIDE_1: VALUE_2
        GLOBAL:
            OPTS:
                TASK_OPT: VALUE_3
```

List 2.1: Overview of the keys and values typically used to configure a Pippin `Stage`

- `STAGE_NAME`: The unique name of the `Stage` in Pippin. There are currently 9 `Stages` in Pippin:
  - `DATAPREP`: Prepare survey light curves for analysis.
  - `SIM`: Simulate realistic SN light curves and data-driven survey samples.
  - `CLASSIFY`: Photometrically classify SNe.
  - `AGGREGATE` & `MERGE`: Convenience `Stages` which aggregate and merge the results of `DATAPREP`, `SIM`, and `CLASSIFY` in preparation for upcoming `Stages`. The `AGGREGATE` and `MERGE` `Stages` are not discussed.
  - `BIASCOR`: Correct SN data samples for observational biases and core-collapse contamination.
  - `CREATECOV`: Calculate a systematic uncertainty covariance matrix for SN data samples.
  - `COSMOFIT`: Constrain cosmological parameters.
  - `ANALYSE`: Convenience `Stage` which provides generic plotting and analysis `Tasks`. This `Stage` is not discussed.
- `TASK_NAME`: Human readable names for distinct `Tasks`. Each `Task` represents a particular configuration and execution of the underlying software.
- `GLOBAL`: An optional set of configurations shared amongst all `Tasks`, allowing for consistency between `Tasks` and reduced duplication of code. Any components which are defined underneath a `TASK_NAME` may also be defined under `GLOBAL`
- `MASK`: Most `Stages` depend on the results of previous `Stages`; however, any given `Task` is likely to only require a subset of these results. Pippin determines which previous `Tasks` to associate with this `Task` based on whether `MASK` partially matches the previous `Task`'s `TASK_NAME`. Thus, an empty `MASK` will match every previous `Task`. Depending on the specifics of the `Stage`, multiple matching `Tasks` are either combined or a new `Task` is spawned for each match (often with `TASK_NAME=CURRENT_TASK_NAME_MATCHING_TASK_NAME`)
- `SETUP_OPT`: In general, options defined at this depth (directly underneath `TASK_NAME`) are either necessary for execution of the underlying software, or control large-scale configuration of the underlying software which dramatically change its behaviour.
- `OPTS`, `TASK_OPT`, & `TASK_OVERRIDE`: Options defined within the `OPTS` scope are typically responsible for more fine-grained control over software execution, overwriting defaults in the large-scale configuration, or modifying the behaviour of Pippin without affecting the underlying software (such as determining the computational resources available to Pippin for this `Task`).

Code Block 2.2: Command line arguments which modify the behaviour of Pippin. `--syntax`, `--compress`, and `--uncompress` are recent additions and described in more detail in Section 2.1.1

```
usage: pippin.sh [-h] [--config CONFIG] [-v] [-s START] [-f FINISH] [-r] [-c]
                 [-p] [-i IGNORE] [-S [SYNTAX]] [-C | -U]
                 [yaml [yaml ...]]

positional arguments:
    yaml                    the name of the yml config file to run. For
        ↪  example:
                            configs/default.yml

optional arguments:
    -h, --help              show this help message and exit
    --config CONFIG         Location of global config (i.e. cfg.yml)
    -v, --verbose           increase output verbosity
    -s START, --start START
                            Stage to start and force refresh. Accepts either
                                ↪  the
                            stage number or name (i.e. 1 or SIM)
    -f FINISH, --finish FINISH
                            Stage to finish at (it runs this stage too).
                                ↪  Accepts
                            either the stage number or name (i.e. 1 or SIM)
    -r, --refresh           Refresh all Tasks, do not use hash
    -c, --check             Check if config is valid
    -p, --permission        Fix permissions and groups on all output, don't
        ↪  rerun
    -i IGNORE, --ignore IGNORE
                            Don't rerun Tasks with this stage or less. Accepts
                            either the stage number of name (i.e. 1 or SIM)
    -S [SYNTAX], --syntax [SYNTAX]
                            Get the syntax of the given stage. Accepts either
                                ↪  the
                            stage number or name (i.e. 1 or SIM). If run
                                ↪  without
                            argument, will tell you all stage numbers / names.
    -C, --compress          Compress pippin output during job. Combine with -c
        ↪  /
                            --check in order to compress completed pippin job.
    -U, --uncompress        Do not compress pippin output during job. Combine
        ↪  with
                            -c / --check in order to uncompress completed
                                ↪  pippin
                            job. Mutually exclusive with -C / --compress
```

Once a Pippin input file is prepared, the user can invoke Pippin via `pippin.sh /path/to/input.yml`. Pippin has a number of command line arguments which modify its behaviour, presented in Code Block 2.2. Of particular importance are the `-i, --ignore STAGE`, `-r, --refresh`, `-s, --start STAGE`, and `-f, --finish STAGE` arguments, which determine what subset of the configured `Stages` are actually executed. Be default, before executing each `Stage`, Pippin will first check whether that `Stage` had previously been executed, and whether the configuration used for the previous execution differs from the current configuration. A `Stage` will only be run if the configuration options for that `Stage` have changed, ensuring time and computing resources are efficiently spent.

Passing the `--ignore STAGE` argument to Pippin will ensure all `Stages` up to and including `STAGE` will not be re-run, even if their configuration has changed since the last execution. Conversely, the `--refresh` argument forces all `Stages` to be re-run, skipping any checking of the previous execution's configurations. The `--start STAGE` forces `STAGE` and all following `Stages` to be re-run. Note that previous `Stages` with modified configurations will still re-run as normal, though combining `--start STAGE` with `--ignore PREV_STAGE` (where `PREV_STAGE` is the `Stage` immediately preceding `STAGE`) can overcome this. Finally, the `--end STAGE` argument will force Pippin to quit once `STAGE` completes, even if more `Stages` exist in the input file.

From the provided command-line arguments and input file, Pippin creates a `Manager` object, which is responsible for setting up the analysis environment, generating all `Tasks` required for the analysis, monitoring and executing of `Tasks` in response to available system resources, and handling failed `Tasks`. The `Manager` calls helper functions implemented in each `Stage` which act as a compatibility layer between the `Manager` and the software underlying each `Task`. When initialising a `Stage`, the `Manager` will call the `get_tasks()` function of that `Stage`, which generates all `Tasks` for that `Stage` based on the `TASK_NAME` input file configuration, and the results of previous `Stages`. When a `Task` is created, the `Task`'s configuration is analysed for any obvious issues, such as missing arguments, arguments with incorrect values (wrong type, non-physical value, etc...), or missing dependencies from previous `Stages`. If no issues can be found, then a `Task` object is created, which contains all the data, configuration, and functionality needed to execute that `Task`. Once all `Tasks` are successfully created, the `Manager` begins Pippin's main loop, presented as pythonic pseudocode in Code Block 2.3. This pseudocode demonstrates a number of `Task`-specific helper functions including:

- `task.check_completion()` : Check if the `Task` has completed. If it has, determine whether the `Task` completed successfully, and return the corresponding status. Often, the underlying software will report on its completion status by writing `SUCCESS` or `FAILURE` to a file, which can then be read by Pippin.
- `task.run()` : Begin execution of the `Task`, returning `True` or `False` based on the success of the execution. Additionally, if the `Task` was previously run, determine whether the configuration of the `Task` has changed, skipping execution if no changes are detected. This latter step involves storing the current configuration in a hash and, if it exists, comparing the current configuration hash with the configuration hash of the previous execution.

Once all `Tasks` have either successfully run, or been blocked from running due to the failure of a dependency, this main loop exits and Pippin reports on the final status of all `Tasks` (`SUCCESS` , `FAILURE` , or `BLOCKED`) and provides details on any errors which occurred during the run. Where possible, when a failure is detected, Pippin will attempt to identify the cause of the failure (by reading logs produced by the underlying software), or at a minimum point the user at log files which are likely to contain details about the cause of the error.

For each run, Pippin creates a directory `PIPPIN_RUN_NAME/` which contains:

- `PIPPIN_RUN_NAME/`
  - `pipin_run_name.yml` : A copy of the Pippin input file used to produce these results
  - `PIPPIN_RUN_NAME.log` : A log file containing detailed information regarding the execution of the latest Pippin run
  - `pippin_status.txt` : A file containing the final status of all `Tasks`
  - `STAGE_NAME/` : A directory containing the output and results of all `STAGE_NAME` `Tasks`
    - `TASK_NAME/` : A directory containing the output and results of `TASK_NAME` . The contents, and structure of this directory is `Stage` and `Task` dependent, but will often include:
      - `hash.txt` : The configuration hash of the latest run of this `Task` . Used to determine whether the `Task` 's configuration has changed on subsequent runs and thus whether the `Task` should be rerun
      - `software_config` : The configuration files used for the execution of the underlying software
      - `software_log` : The log files generated by the underlying software

- `software_input`: Input files required by the underlying software
- `software_output`: Files and folders produced by the underlying software over the course of its execution

Code Block 2.3: Pseudocode of the main-loop of Pippin which monitors the status of running `Tasks`, and executes new `Tasks` as resources become available.

```python
# Continue looping as long as there are Tasks running or Tasks waiting to be run
while (len(running_tasks) > 0) or (len(unqueued_tasks) > 0):
    for running_task in running_tasks: # Monitor the status of all running Tasks
        completion_status = running_task.check_completion() # Check if `running_task` is still running, or has stopped
        # If completed, will return a "success" or "failure" status
        # Otherwise `running_task` is still running
        if completion_station in ["success", "failure"]
            if completion_status == "success": # `running_task` completed successfully
                completed_tasks.append(running_task)
                running_tasks.remove(running_task)
            else: # `running_task` was not successful
                running_tasks.remove(running_task)
                failed_task.append(running_task)
                block_dependent_tasks(running_task) # Block any Task which depends on `running_task` from initialising
            resources_used -= running_task.required_resources # Free up computing resources allocated to `running_task`
            resources_available += running_task.required_resources
    while resources_used < resources_available: # If there are computing resources available, initialise new Tasks
    for unqueued_task in unqueued_tasks: # Determine what Task to execute
        is_executable = True
        # `unqueued_task` can only execute when all Tasks it depends on have successfully completed
        for dependency in unqueued_task.dependencies:
            if dependency not in completed_tasks:
                is_executable = False
        # `unqueued_task` can only execute when enough resources become available
        if resources_used + unqueued_task.required_resources > resources_available:
            is_executable = False
        if is_executable: # If `unqueued_task` is executable, run `unqueued_task`
            unqueued_tasks.remove(unqueued_task)
            has_started = unqueued_task.run() # Task.run() returns True when a Task successfully starts, and False otherwise
            if has_started:
                resources_used += unqueued_task.required_resources
                running_tasks.append(unqueued_task)
                break # Since we executed a new Task, stop search for Tasks to execute
            else:
                failed_task.append(unqueued_task)
                block_dependent_tasks(unqueued_task) # Block any Task which depends on `unqueued_task`
```

2.1.1 Overarching Improvements to Pippin's Design

In addition to the `Task` and `Stage` specific improvements highlighted in the upcoming sections, much of my development was focused on improving the fundamental structure and design of Pippin. A summary of major changes are provided here, with a complete list of every commit made by myself to the Pippin source code available online.

2.1.1.1 Flexibility

Changes listed here enabled Pippin's use beyond the DES-SN5YR analysis by reducing DES-specific assumptions throughout the code base (so-called *hard-coded* values), and allowing the user greater control over the fine details of a Pippin analysis.

Modular Batch Processing Pippin was designed to be run in a high-performance computing (HPC) environment, and has always had native support for batch-based processing, with each `Task` requesting resources from the HPC server based on the scale and demands of the underlying software. As Pippin was initially developed on the Midway2 Cluster[1] at the University of Chicago's Research Computing Center[2], this batch processing was implemented for the SLURM (Yoo et al., 2003) resource management tool used on Midway2, restricting Pippin from being installed on systems without this tool. Additionally, the resources each `Task` would request were hard-coded to sensible values within the source code, and could not be modified by the user.

To address this, I generalised the batch processing functionality, allowing for any resource management tool to be used, and allowing users to determine the resource requirements per-`Task`. This latter functionality was particularly important, both for the photometric classifiers SuperNNova (Möller and de Boissière, 2020) and SCONE (Qu et al., 2021) which required flexible memory allocation, and for analyses of systematics in the DES-SN5YR analysis (e.g. Vincenzi et al., 2024) which rely on larger simulated samples than the average Pippin analysis. Modular Batch Processing was used in the DES-SN5YR analysis[3].

[1] https://rcc.uchicago.edu/support-and-services/midway2
[2] https://rcc.uchicago.edu/
[3] See `CLASSIFY`

2.1.1.2 Ease of Use

Changes listed here focused on reducing the complexity of performing a Pippin analysis, by simplifying the user experience and improving the information provided to a user, either through documentation, or logs generated throughout the course of a Pippin analysis.

Dedicated Documentation Page Rather than providing information regarding the installation and use of Pippin through the GitHub README file, I created a dedicated documentation site which documents the usage of every task, as well as best practices and usage tips for running a Pippin analysis, and detailed instructions for the development of Pippin.

`--syntax` **Command Line Argument** A new command line argument was introduced to allow users to quickly reference the Pippin documentation from within the command line. `--syntax` accepts either the name or number of a `Task`, and prints the corresponding documentation, directly from the documentation's source code ensuring it is always up-to-date.

Automatic Testing and Documentation To improve the consistency of Pippin analyses during its active development cycle, I utilised GitHub Actions to automate the building of Pippin's documentation, and the running of standardised tests.

Automatic Compression and Decompression of analysis results With both an increase in the number of researchers using Pippin, and the complexity of the analysis being performed, the space requirements of a Pippin analysis began to become prohibitively large. To address this, I implemented the ability for Pippin analyses to be automatically compressed or decompressed, drastically reducing the impact of Pippin on a user's overall storage budget. This behaviour can be controlled by the user through the `--compress` and `--decompress` command line arguments.

Improved configuration defaults and constraints Pippin was designed with the ability to prevent configuration errors by using the context of previous `Stages` to constrain how following `Stages` can be configured. I improved upon this functionality by enabling the entirety of the Pippin analysis to be considered when determining a given `Stages` constraints, thus allowing earlier `Stages` to account for how the user expects to *use* their results when determining configuration details.

2.1.1.3 Functionality

Changes listed here introduced new functionality to Pippin, enabling Pippin's use as a general purpose SN cosmology analysis tool beyond the DES-SN5YR analysis.

Implementation of new state-of-the-art tools As new tools for improved cosmological analysis were developed, I worked directly with their developers to implement these tools into Pippin. Prominent examples include the SCONE photometric classifier (Qu et al., 2021), the improved SALT3 (Kenworthy et al., 2021; Taylor et al., 2023) light curve fitter, and the WFit cosmology fitter implemented in SNANA (Kessler et al., 2009b). The implementation of new cosmological fitters necessitated a restructuring of the COSMOFIT `Stage`, which previously only provided functionality for the CosmoMC (Moshafi and Bahraminasr, 2018) cosmological fitter. Scone[1], SALT3[2] and WFit[3] were all vital components of the DES-SN5YR analysis.

Improved ability to reuse analysis components A core functionality of Pippin is the ability to reuse the results of a previous analysis rather than erroneously rerunning `Tasks` or `Stages`. The initial implementation of this functionality required an exact match between the new `Task` and the original `Task` being reused, restricting how this functionality could be used. To address this, I implemented an `EXTERNAL_MAP` key which allowed users to explicitly define how Pippin should apply the results of previous analyses to their current analysis. This functionality was used by the Amalgame analysis (Popovic et al., 2024), the first purely photometric analysis of a combined supernova sample.

Combine multiple Pippin config files Often, a user will need to define variables which have the same value for different `Tasks` and `Stages` throughout the Pippin analysis, for example ensuring the cosmological parameters used within `SIM` match the cosmological parameters used within `BIASCOR`. As Pippin config files use the `yaml` specification[4] these variables can be defined once as a `yaml anchor`[5], and reused throughout a single Pippin config file. However, sharing these variables between multiple Pippin config files was not possible until I implemented a custom `yaml` pre-processor which allowed multiple Pippin config files to be combined. With this a single config file could be created

[1] See `CLASSIFY`
[2] See `LCFIT`
[3] See `COSMOFIT`
[4] https://yaml.org/spec/1.2.2/
[5] https://yaml.org/spec/1.2.2/#3222-anchors-and-aliases

containing all `yaml anchor` definitions, which would then be shared across config files as needed. This behaviour was utilised extensively throughout the DES-SN5YR analysis, and was essential for investigations into the complex systematic uncertainties present within the DES-SN5YR analysis.

2.2 SNANA

The Pippin analysis pipeline heavily relies on the SuperNovaANAlysis (SNANA; Kessler, 2024; Kessler et al., 2009b) software as the underlying program driving most `Stages` in Pippin.

Originally developed for the SDSS-II Supernova Survey (Frieman et al., 2007; Kessler et al., 2009a), SNANA provides a suite of tools for SN cosmology analyses. The SNANA software is partitioned into a number of binary executables which take as input an SNANA input file and a number of optional command-line overrides. When it was originally designed, SNANA included executables for SN light curve simulations (`snlc_sim.exe`, see `SIM`), SN light curve fitting (`snlc_fit.exe`, see `LCFIT`), and included a simple, fast cosmological fitter (`wfit.exe`, see `COSMOFIT`). Since its initial inception, the scope of SNANA's capabilities have grown to include:

- Photometric Classification (`psnid.exe`, see `CLASSIFY`)
- Core-collapse contamination, nuisance variable fitting, and observational bias correction (`SALT2mu.exe`, see `BIASCOR`)

Additionally, SNANA provides a number of utilities for the preparation and analysis of SNANA processes. These tools include:

- `snana.exe`: General entry-point for many intermediary steps of the SNANA program. Used in `DATAPREP` to approximate the `PKMJD` of a SN sample (see Code Block 2.5)
- `kcor.exe` & `kcordump.exe`: Create and analyse 'K-Correction' files, prerequisite files for `snlc_sim.exe` and `snlc_fit.exe` that contain instrument specific information.
- `combined_fitres.exe`: The results of SNANA processes are typically stored in a tabular file format known as a `.FITRES` file. The `MERGE` and `AGGREGATE` Pippin `Stages` utilise the `combined_fitres.exe` executable to merge the results of preceding `Stages` together in preparation for `BIASCOR`
- `simlib_coadd.exe`: Utility to co-add `.SIMLIB` exposures into a single effective co-added exposure per filter per night. Discussed in greater detail in `SIM`

To facilitate the growing scope and complexity of SNANA, in 2020 a convenience wrapper known as `submit_batch_jobs.sh` was created for the SNANA system which simplified both the execution of SNANA jobs, and the process of submitting these jobs to a batch queue. When `submit_batch_jobs.sh` was first created and integrated into Pippin, it provided methods for `SIM`, `LCFIT`, and `BIASCOR`. I have since integrated `submit_batch_jobs.sh` into `CREATECOV`, and `COSMOFIT`.

2.2.1 Dr. Evil-ABORT-Face

A particularly useful feature of SNANA is its extensive error checking, which attempts to abort the program early if any issues are identified. This error checking covers pre-processing checks of the user's input file, post-processing checks of each intermediary stage of an SNANA job, and sanity checks to ensure all data being processed and produced fall within physically realistic limits. If an issue is identified, SNANA will abort with a message from '**Dr. Evil-ABORT-Face**', an example of which is provided in Code Block 2.4. A significant portion of my development of Pippin was dedicated to catching and correcting bugs which occurred throughout the active development cycles of both Pippin and SNANA[1].

Code Block 2.4: **Dr. Evil-ABORT-Face** - The harbinger of error messages produced by SNANA. Where possible, the abort message will include the `FUNCTION_NAME` of the SNANA function which caused the error, and a message guiding the user toward the possible source of the error, and any files which might be related.

```
‘|‘‘‘‘‘‘‘|‘
<| o\ /o |>
 | ’ ; ’ |
 |  ___  |       ABORT program on Fatal Error.
 | |’ ’| |
 | ‘---’ |
 \_______/

 FATAL ERROR ABORT called by FUNCTION_NAME
    error message
    related_file.fitres
```

[1] Over time, **Dr. Evil-ABORT-Face** and I seem to have come to an understanding, and now consider each other friendly co-workers rather than bitter rivals

2.3 `Stages` of Pippin

2.3.1 `DATAPREP` — Data preparation

The starting point of the Pippin analysis pipeline is `DATAPREP`, which prepares photometrically calibrated SN data samples for use in upcoming `Stages`. Broadly this involves gathering and recording details about the SN data sample, formatted to match the output of a simulated data sample (See `SIM`), ensuring consistent handling of all data, whether real or simulated.

Additionally, `DATAPREP` provides:

- An estimate of the time of peak brightness (`PKMJD`) for each SN in the data sample. This is a pre-requisite for several `Stages` in the Pippin analysis pipeline, including `LCFIT`, and `CLASSIFY`.
- A flag for whether the data should be *blinded*. This causes all subsequent `Stages` to modify results associated with this data, such that any inference of real-world constraints are impossible, with the aim of reducing researcher confirmation bias (Section 1.3.8).

Finally, though the specific subtype of a given SN is often known, most `Stages` only require a delineation between SNe Ia, and non-Ia SNe. As such `DATAPREP` provides a definition for which SN subtypes found within the data sample belong to Ia and non-Ia SNe.

The data samples passed as input to `DATAPREP` must be formatted according to the SNANA LightCurve Output Format (Section 4.36.1; Kessler, 2024).

Under this convention, SN data samples are stored as two standard `.FITS` files, an `XXX.HEAD.FITS` file (known as the `HEAD` file), and an `XXX.PHOT.FITS` files (known as the `PHOT` file).

The `HEAD` file contains summary information for each SN in the data sample. This information includes, but is not limited to, the redshift, sky coordinates, MJD of first and last detection, and host galaxy properties of the associated SN.

The `PHOT` file contains photometry information for each observation of each SN, including the MJD, bandpass, calibrated flux, and its uncertainty, among other details. Observations are written sequentially to the `PHOT` file, such that the light curve of a given SN is stored contiguously between the rows containing its earliest and latest observations. Pointers to these rows are included in the `HEAD` file under the `PTROBS_MIN` and `PTROBS_MAX` keys. To assist in identifying mismatches between observations in the `PHOT` file, and SN in the `HEAD` file, a fake observation with an MJD of -777 is written to the `PHOT` file after each SN light curve, to clearly identify the end of a light curve. See the DES-SN5YR

Data Release (Appendix 1; Sánchez et al., 2024) and its associated web pages[1] for more details.

Code Block 2.5: An example SNANA `SNLCINP` (supernova light curve input) configuration file. The `PRIVATE_DATA_PATH` and `VERSION_PHOTOMETRY` options define the path to the raw data (`/{PRIVATE_DATA_PATH}/{VERSION_PHOTOMETRY}`). `SNTABLE_LIST`, `TEXTFILE_PREFIX`, and `OPT_YAML` configure the output of SNANA to include a `.YAML` file, formatted for use in the SuperNNova photometric classifier (see `CLASSIFY`). Finally, `PHOTFLAG_MSKREJ` determines which SN observations should be cut from the analysis, and `OPT_SETPKMJD` controls how SNANA should estimate the time of peak brightness of each SN in the data sample. Both `PHOTFLAG_MSKREJ` and `OPT_SETPKMJD` are discussed further in the text

```
#
# Obtaining Clump fit
# to run:
# snana.exe SNFIT_clump.nml
# outputs csv file with space delimiters

&SNLCINP

    ! For SNN-integration:
    OPT_SETPKMJD = 16
    SNTABLE_LIST = 'SNANA(text:key)'
    TEXTFILE_PREFIX = 'DES5YR_SMP'
    OPT_YAML = 1

    ! data
    PRIVATE_DATA_PATH = '/project2/rkessler/SURVEYS/DES/ROOT/lcmerge'
    VERSION_PHOTOMETRY = 'DES5YR_SMP'

    PHOTFLAG_MSKREJ   = 1016 !PHOTFLAG eliminate epoch that has errors, not
        ↪ LC

&END
```

Both the `PKMJD` estimate and the gathering and reformatting of data sample details are handled through SNANA. Based on user-provided options, `DATAPREP` produces an SNANA '`SNLCINP`' (supernova light curve input, see

[1] DES-SN5YR Data Release, 0 — DATA: Transient lightcurves from DES

Code Block 2.5 for an example) configuration file which provides SNANA with:

- The path to the raw data files.
- Options for excluding some SN observations from the overall analysis.
- Options for calculating additional parameters from the data, such as `PKMJD`.

SNANA then analyses every SN observation present in the provided data files, identifying any observations which were flagged for exclusion, and calculating any required parameters. The results of this are recorded in an output file containing summary information for every analysed SN observation (included those that were flagged for exclusion). An example of this output file is presented in Code Block 2.6. Though the configuration options available for an `SNLCINP` file are extensive, the most impactful options for the Pippin analysis are `PHOTFLAG_MSKREJ` and `OPT_SETPKMJD`.

SN observations may optionally be flagged with a `PHOTFLAG`, with the value of the `PHOTFLAG` corresponding to some unique property of that observation. For example, a `PHOTFLAG` could indicate the observation is a detection, a trigger, the observation with the maximum signal-to-noise ratio for its light curve, or the observation closest to the time-of-peak brightness for its light curve. A SN observation flagged with `PHOTFLAG=PHOTFLAG_MSKREJ` indicates some error was identified in the observation, and it should be excluded from the analysis. Within the DES-SN5YR analysis, the default `PHOTFLAG_MSKREJ` is 1016. Of the 19706 SN observations included in the DES-SN5YR data release, only 7 were flagged with `PHOTFLAG_MSKREJ=1016`.

Code Block 2.6: A truncated `DATAPREP` output file, containing summary details of different SNe within a data sample. Comments describing each `VARNAME`, and each event, have been added for clarity.

```
# VERSION_PHOTOMETRY: DES5YR_SMP
# SNANA_VERSION:      v11_05c-56-g0ba6ba8
# TABLE_NAME:         SNANA

VARNAMES: CID         IDSURVEY   TYPE        FIELD        CUTFLAG_SNANA
       ↪  zHEL        zHELERR    zCMB        zCMBERR      zHD        zHDERR
       ↪  VPEC        VPECERR    MWEBV       HOST_LOGMASS HOST_LOGMASS_ERR
       ↪  PKMJDINI    SNRMAX1    SNRMAX2     SNRMAX3

# Unknown SN type
SN:       1294480     10         0           X1           1
       ↪  0.34536     0.00100    0.34424     0.00100      0.34424    0.00168
       ↪  0           300        1.84947e-02 10.91700     9.20000e-02
       ↪  57018.0898  14.08429   13.46478    2.56102

# Spectroscopically confirmed Ia
SN:       1536028     10         1           E1+E2        1
       ↪  0.45221     0.00100    0.45115     0.00100      0.45115    0.00176
       ↪  0           300        5.87587e-03 10.77200     4.90000e-02
       ↪  57708.0547  16.03785   11.93347    9.97205

# Spectroscopically confirmed non-Ia
SN:       1487030     10         82          E2           1
       ↪  0.00037     0.00100    -0.00034    0.00100      -0.00034   0.00141
       ↪  0           300        6.24386e-03 5.28100      2.00000e-03
       ↪  57708.0664  64.46701   24.14188    3.31987

# Poor data: No host galaxy mass or redshift
SN:       1552096     10         0           S2           1
       ↪  -999.00000  -9.00000   -999.00000  -9.00000     -999.0000  9.05524
       ↪  0           300        2.70025e-02 -999         -999
       ↪  57702.0938  20.15766   8.66610     5.70157

# Poor data: Low SNR
SN:       1248565     10         0           C3           1
       ↪  0.67939     0.00100    0.67873     0.00100      0.67873    0.00195
       ↪  0           300        6.82067e-03 10.08400     1.00000e-02
       ↪  0.0100      -9         -9          -9

# Bad data, explicitly rejected: No host galaxy mass or redshift, and low SNR
SN:       1375044     10         0           S2           0
       ↪  -999.00000  -9.00000   -999.00000  -9.00000     -999.0000  9.05524
       ↪  0           300        2.73510e-02 -999         -999
       ↪  57626.2812  -9         -9          -9
```

`OPT_SETPKMJD` controls how SNANA should estimate the `PKMJD` of each SN in the data sample. Section 5.5.1 of Kessler (2024) provides extensive details on the various `OPT_SETPKMJD` options; however, for the DES-SN5YR analysis, the default is `OPT_SETPKMJD=16` which corresponds to the `Fmax-clump` method, which tries to reduce the impact of outlier detections in the days before and after the SN explosion by determining the `PKMJD` from the densest 'clump' of SN observations. This method first performs a signal-to-noise ratio cut, filtering out any SN observations with an SNR less than the `SNRCUT_SETPKMJD` parameter (default of 5), then iteratively splits the remaining observations into subsets (`clumps`).

This iterative process involves first defining a window of time between the first detection ($t_0 = t_{\text{min}}$) and the number of days set by the `MJDWIN_SETPKMJD` parameter (t_{win}, default of 60 days). The number of SN observations within this window forms the first `clump` (`clump` $_0$). This window is then shifted by 10 days ($t_0 \to t_{10}$, $t_{\text{win}} \to t_{\text{win}+10}$) and the number of SN observations within this new window forms the next `clump` (`clump` $_1$). This process is repeated until the right-hand edge of the window reaches the last detection ($t_{\text{win}+n} = t_{\text{max}}$). The `clump` with the greatest number of SN observations is selected as the most likely to not contain outliers, and the `PKMJD` is set to the MJD of the maximum flux detection within this `clump` .

A particularly important summary parameter is the `TYPE` of each SN in the data sample. Each SNe type is assigned a unique `SNTYPE` ID, allowing SNe of the same type to be consistently identified and processed throughout the entire Pippin analysis pipeline. Though the precise correlation between `SNTYPE` IDs and SNe types is survey-dependant, the following conventions are followed by default:

List 2.2: `SNTYPE` conventions

- A SN with an unknown type has `SNTYPE` 0.
- A spectroscopically confirmed SN Ia has `SNTYPE` 1.
- The `SNTYPE` of a photometrically confirmed SN, is 100 + the associated spectroscopically confirmed `SNTYPE` .
  - A photometrically identified SN Ia has `SNTYPE` 101.

As part of `DATAPREP` , users are able to define which `SNTYPES` found within a data sample correspond to Ia or non-Ia SN subtypes. This allows any prior classification efforts to be accounted for throughout the analysis pipeline.

2.3.1.1 The DES-SN5YR Data Sample

The raw DES-SN5YR data sample (before quality cuts) is composed of 19706 high redshift SN candidates ($z \gtrapprox 0.1$) observed throughout the 5-year DES program (Sánchez et al., 2024)[1], 342 low redshift SN candidates ($z \lessapprox 0.1$) compiled from the CfA3 (Hicken et al., 2009), CfA4 (Hicken et al., 2012), and CSP (Krisciunas et al., 2017) surveys, and 185 SN candidates from the Foundation (Foley et al., 2017) survey. The `DATAPREP` configuration for the DES-SN5YR analysis is presented in Code Block 2.7.

All surveys in the DES-SN5YR combined data sample are cross-calibrated using the SuperCal-Fragilistic method (Brout et al., 2022b). This method calculates a global solution of bandpass offsets which minimises the difference in observed magnitude between each survey in the DES-SN5YR data sample. SuperCal-Fragilistic improves on its predecessor SuperCal (Scolnic et al., 2015), by calculating the optimal bandpass offset for all surveys simultaneously. This enables the creation of a covariant calibration uncertainty matrix, which provides more accurate calibration uncertainties than previous methodologies.

[1] The DES data sample contains **all** observed SN candidates, including spectroscopically confirmed non-Ia SNe, and other candidates unsuitable for cosmological analysis.

Code Block 2.7: The `DATAPREP` Pippin configuration used in the DES-SN5YR analysis.

```yaml
DATAPREP:
  DATADES5YRSMP:
    OPTS:
      BLIND: True # Defaults to true anyway! Set to false to unblind
      RAW_DIR: "$SNDATA_ROOT/lcmerge/DES-SN5YR/DES-SN5YR_DES"
      TYPES:
        IA: [1, 101]
        NONIA:
          - 0
          - 4
          - 5
          - 23
          - 29
          - 32
          - 33
          - 39
          - 41
          - 66
          - 80
          - 81
          - 82
          - 122
          - 129
          - 139
          - 141
          - 180
  DATAFOUND:
    OPTS:
      BLIND: True
      RAW_DIR: "$SNDATA_ROOT/lcmerge/DES-SN5YR/DES-SN5YR_Foundation"
      TYPES:
        IA: [1, 101]
        NONIA: [20, 30, 120, 130]
  DATALOWZ:
    OPTS:
      BLIND: True # Defaults to true anyway! Set to false to unblind
      RAW_DIR: "$SNDATA_ROOT/lcmerge/DES-SN5YR/DES-SN5YR_LOWZ"
      TYPES:
        IA: [1, 101]
        NONIA: [20, 30, 120, 130]
```

As described in Smith et al. (2020a), the DES program utilised the Dark Energy

Camera (DECam; Flaugher et al., 2015) at the Cerro Tololo International Observatory to repeatedly image 27 deg^2 across 8 shallow fields, and 2 deep fields, with a ~ 1 week cadence. An efficient difference-imaging pipeline (`DiffImg`; Kessler et al., 2015) was used to detect transient events, and measure preliminary light curves of these events. A Random Forest machine learning algorithm was trained to automatically identify likely SN candidates from the `DiffImg` light curves (Goldstein et al., 2015). Host-galaxy spectroscopic follow-up of likely SN candidates was performed by the OzDES survey (Childress et al., 2017; Lidman et al., 2020; Yuan et al., 2015), using the AAOmega spectrograph on the Anglo-Australian telescope.

For each identified SN candidate, high quality photometry was obtained using a Scene Modelling Photometry pipeline (SMP; Brout et al., 2019b). This technique measures the photometry of a transient event by constructing a model of the DECam images of the transient, and fitting this model against the observed data. The SMP model includes:

- The photometry of the transient event.
- The photometry of the transient event's host galaxy.
- The position of the transient event within the host galaxy.
- The impact of atmospheric and instrumental effects on the observed image.

SMP models and fits all observations of a transient simultaneously. This ensures consistency in both the position of the transient within its host galaxy, and the position of tertiary stars within each image. Additionally, as the photometry of the host galaxy is presumed to be constant with time, a single host galaxy model is shared between each observation, constrained using high quality reference images of the host galaxy.

The DES SMP pipeline was applied to all SN candidates, and was able to obtain a convergent model for 19,706 of these, from which the DES data sample used in the DES-SN5YR analysis was formed.

2.3.1.2 `DATAPREP` specific Pippin development

Most of my Pippin development associated with `DATAPREP` involved generalising previously hard-coded components, and implementing SNANA features related to `DATAPREP` as they were developed. Of particular note was adding the ability for users to define `PHOTFLAG_MSKREJ` rather than assuming the default value of 1016, allowing greater control over the DES-SN5YR subsample used within their analyses.

2.3.2 `SIM` — Simulation

Accurate simulations of SN light curves are vital components of many Pippin `Stages`, including the training and testing of light curve fitters and photometric classifiers in `LCFIT` and `CLASSIFY`, respectively, as well as the *BEAMS with Bias Correction* process in `BIASCOR` which produces a Hubble Diagram corrected for observational bias and core-collapse contamination. Additionally, the consistency and correctness of each `Stage` of the Pippin pipeline can be tested through repeated analyses of simulated data (See Chapter 3).

As discussed in Kessler et al. (2009b), simulations of SN light curves must account for survey-specific observational effects (atmospheric seeing, instrument noise, etc...) to accurately emulate real data. The most effective method for capturing these effects involving embedding a PSF with amplitude scaled to match synthetic SN photometry directly into survey images and processing them with the same photometric pipeline as the real data. However, this process is computationally expensive, and is poorly suited for cosmological analyses which require hundreds to thousands of simulated samples, each containing thousands to tens of thousands of SNe. To address this, Pippin utilises SNANA's `snlc_sim.exe` SN light curve simulation which provides extremely fast light curve simulations ($\sim 10^2 - 10^3$ light curves per second) without unduly sacrificing the accuracy of the simulations or the ability to realistically emulate survey-specific observing conditions. `snlc_sim.exe` accomplishes this without expensive pixel- or image-level computation by splitting the simulation into several distinct steps.

First, 'rest-frame' *UBVRI* light curves are generated from a SN model. SNANA supports a number of SN models, including MLCS2k2 (Jha et al., 2007), SALT2 (Guy et al., 2007) and SALT3 (Kenworthy et al., 2021; Taylor et al., 2023), SNooPy (Burns et al., 2010), stretch (Goldhaber et al., 2001) and two-stretch (Hayden et al., 2010), and core-collapse Supernova models (Kessler et al., 2010). Each of these models parameterise SN light curves with a number of 'shape parameters' (e.g. SALT2/3's stretch (x_1) and colour ($\mathcal{C}$) parameters) allowing rest-frame SN light curves to be generated by randomly drawing these shape parameters from user-defined distributions. Next 'observer-frame' light curves are produced through successive transformations of the rest-frame light curves to account for the effects of host-galaxy extinction, k-correction, and Galactic (Milky Way) extinction. Finally, survey specific zero-points transform the simulated *UBVRI* magnitudes into 'survey-frame' CCD counts, which utilise previous observations from the site to account for both atmospheric transmission and telescope efficiency. Some models, including the SALT3 model used by the

DES-SN5YR analysis, directly model observer-frame light curves, effectively combining the rest-frame and observer-frame steps.

2.3.2.1 The DES-SN5YR Simulations

The DES-SN5YR analysis produced eight sets of simulated samples, a 'data' sample and a 'bias-correction' sample of DES-SN5YR Foundation, Low-z, and core-collapse SNe. The data samples were of an equivalent size to the real data samples included in the DES-SN5YR analysis, whilst the bias-correction simulations produced on the order of 10 times the number of SNe compared to the real data samples, and were primarily used in `BIASCOR`. The following sections detail the `snlc_sim.exe` rest-frame, observer-frame, and survey-frame configurations for the DES-SN5YR analysis. For brevity, only the DES-SN5YR data (Code Block 2.8) and bias-correction (Code Block 2.9) samples, alongside the core-collapse data sample (Code Block 2.10), are described in detail. Code Blocks 2.8 and 2.9 present the `SIM` config for the DES-SN5YR data and bias-correction simulations, respectively. These configurations contain aliases for a number of parameters (as these parameters are often shared between multiple simulations). The alias definitions are presented in Code Blocks 2.11 to 2.14. The structure of a `SIM` configuration allows for varying SN types to be simulated within the same `SIM` `Task`. Following the user-defined `Task` name (e.g. `DATADESSIM` in Code Block 2.8), any number of sub-configurations can be defined. Those beginning with `IA_` [1] (e.g. `IA_P21` in Code Block 2.8) are assumed to be SNe Ia simulations, otherwise they are treated as simulations of non-Ia contaminants (e.g. `PECIAX` and `Ibc_TEMPLATES` in Code Block 2.10).

Note that every `SIM` `Task` must provide a `BASE` file containing a number of generic options which are added too or overwritten by the rest of the configuration; SNANA provides many pre-generated `BASE` files for simulating different surveys, including the DES-SN5YR survey.

[1] The user may follow the `IA_` prefix with any label they like. Alternatively, `IA` with no underscore is also a valid label.

Code Block 2.8: The configuration file for the DES-SN5YR data simulation. This simulation will produce a sample of DES-SN5YR SNe Ia of an equivalent size to the real DES-SN5YR data sample. It relies on aliases defined in Code Blocks 2.11, 2.13 and 2.14.

```
SIM:
  DATADESSIM:
    GLOBAL:
      !!merge <<: [*batchinfo, *cosmology, *datasim_size, *mwopt]
    IA_P21:
      !!merge <<: [*des_genpdfp21, *deskcor, *host_des, *p21_inputs,
    ↪  *s3model, *simalpha]
      DNDZ: "POWERLAW 2.27E-5 1.7" ##Frohmaier 2018
      FLUXERRMODEL_FILE:
    ↪  "$SNDATA_ROOT/simlib/DES/DES-SN5YR_DES_FLUXERRMODEL_SIM.DAT"
      GENMAG_SMEAR_ADDPHASECOR: "0.0 10.0"
      HOSTLIB_WGTMAP_FILE:
    ↪  "$SNDATA_ROOT/simlib/DES/DES-SN5YR_WGTmaps/DES-SN5YR_DES.WGT"
```

Code Block 2.9: The configuration file for the DES-SN5YR bias-correction simulations. This simulation will produce a sample of DES-SN5YR SNe Ia on the order of 10 times the size of the real DES-SN5YR data sample. Except for the size of the simulated sample, this simulation is identical to the DES-SN5YR data simulation presented in Code Block 2.8. It relies on aliases defined in Code Blocks 2.11 to 2.14.

```
BIASCORSIM_DES:
  GLOBAL:
    !!merge <<: [*batchinfo, *biascorsim_size, *cosmology, *mwopt]
  IA_P21:
    !!merge <<: [*des_genpdfp21, *deskcor, *host_des, *p21_inputs, *s3model,
    ↪  *simalpha]
    DNDZ: "POWERLAW 2.27E-5 1.7" ##Frohmaier 2018
    FLUXERRMODEL_FILE:
    ↪  "$SNDATA_ROOT/simlib/DES/DES-SN5YR_DES_FLUXERRMODEL_SIM.DAT"
    GENMAG_SMEAR_ADDPHASECOR: "0.0 10.0"
    HOSTLIB_WGTMAP_FILE:
    ↪  "$SNDATA_ROOT/simlib/DES/DES-SN5YR_WGTmaps/DES-SN5YR_DES.WGT"
```

Code Block 2.10: The configuration file for the core-collapse data simulation. This simulation will produce a sample of various non-Ia SNe, including peculiar Iax and 91bg-like, type II, and type Ibc SNe. It relies on aliases defined in Code Blocks 2.13 and 2.14.

```
SIM:
  DATADESCCSIM:
    GLOBAL:
      !!merge <<: [*batchinfo, *cosmology, *datasim_size, *deskcor, *host_des, *mwopt]
      FLUXERRMODEL_FILE: "$SNDATA_ROOT/simlib/DES/DES-SN5YR_DES_FLUXERRMODEL_SIM.DAT"
      GENMAG_SMEAR_ADDPHASECOR: "0.0 10.0"
    II_TEMPLATES:
      BASE: "$SNDATA_ROOT/sample_input_files/DES-SN5YR/base_files/sim/sn_ii_v19_li11revised_nodust.input"
      HOSTLIB_WGTMAP_FILE: "$SNDATA_ROOT/simlib/DES/DES-SN5YR_WGTmaps/DES-SN5YR_DES_TypeII.WGT"
    Ibc_TEMPLATES:
      BASE: "$SNDATA_ROOT/sample_input_files/DES-SN5YR/base_files/sim/sn_ibc_v19_li11revised_nodust.input"
      HOSTLIB_WGTMAP_FILE: "$SNDATA_ROOT/simlib/DES/DES-SN5YR_WGTmaps/DES-SN5YR_DES_TypeIbc.WGT"
    PECIA91BG:
      BASE: "$SNDATA_ROOT/sample_input_files/DES-SN5YR/base_files/sim/sn_ia91bg.input"
      HOSTLIB_WGTMAP_FILE: "$SNDATA_ROOT/simlib/DES/DES-SN5YR_WGTmaps/DES-SN5YR_DES_TypeIa91bg.WGT"
    PECIAX:
      BASE: "$SNDATA_ROOT/sample_input_files/DES-SN5YR/base_files/sim/sn_iax_dust.input"
      HOSTLIB_WGTMAP_FILE: "$SNDATA_ROOT/simlib/DES/DES-SN5YR_WGTmaps/DES-SN5YR_DES_TypeIax.WGT"
```

Code Block 2.11: `SIM` aliases specific to DES-SN5YR data and bias-correction simulations. It uses the `GENPDF_FILE` presented in Code Block 2.16

```
DES_ALIAS:
  DESKCOR: &deskcor
    KCOR_FILE: "$SNDATA_ROOT/kcor/DES/DES-SN5YR/calib_DES-SN5YR_DES.fits.gz"
  DES_GENPDFP21: &des_genpdfp21
    BASE: "$SNDATA_ROOT/sample_input_files/DES-SN5YR/base_files/sim/sn_ia_salt_des5yr.input"
    GENPDF_FILE: "$SNDATA_ROOT/models/population_pdf/DES-SN5YR/DES-SN5YR_DES_S3_P21.DAT"
  HOST_DES: &host_des
    HOSTLIB_FILE: "$SNDATA_ROOT/simlib/DES/DES-SN5YR_DES.HOSTLIB"
    HOSTLIB_MSKOPT: 258
    HOSTLIB_SCALE_PROPERTY_ERR: "0.0(LOGMASS),0.0(LOGSFR),0.0(LOGsSFR),0.0(COLOR)"
    SEARCHEFF_zHOST_FILE: "$SNDATA_ROOT/models/searcheff/SEARCHEFF_zHOST_DES-SN5YR.DAT"
```

Code Block 2.12: `SIM` aliases specific to DES-SN5YR bias-correction simulations.

```
BIAS_ALIAS:
  BIASCORSIM_SIZE: &biascorsim_size
    BATCH_MEM: 8000
    NGEN_UNIT: 10
    RANSEED_CHANGE: "10 6789"
```

Code Block 2.13: `SIM` aliases common to all SN Ia simulations within the DES-SN5YR analysis.

```
SHARED_ALIAS:
  P21_INPUTS: &p21_inputs
    GENMAG_OFF_GLOBAL: -0.12
    GENMAG_SMEAR_MODELNAME: "C11"
    GENMAG_SMEAR_SCALE: 0.0001
    GENMAG_SMEAR_SCALE(c): "0,0"
    GENPDF_OPTMASK: 1
  S3MODEL: &s3model
    GENMODEL: "$SNDATA_ROOT/models/SALT3/SALT3.DES5YR"
  SIMALPHA: &simalpha
    GENPEAK_SALT2ALPHA: 0.15
```

Code Block 2.14: `SIM` aliases common to all simulations within the DES-SN5YR analysis, regardless of SN type.

```
GLOBAL_ALIAS:
  BATCHINFO: &batchinfo
    BATCH_INFO: "sbatch $SBATCH_TEMPLATES/SBATCH_Midway2b.TEMPLATE 5"
  COSMOLOGY: &cosmology
    H0: 70.0
    OMEGA_LAMBDA: 0.685
    OMEGA_MATTER: 0.315
    w0_LAMBDA: -1.0
    wa_LAMBDA: 0
  DATASIM_SIZE: &datasim_size
    BATCH_MEM: 8000
    NGEN_UNIT: 1
    RANSEED_CHANGE: "5 2345"
  MWOPT: &mwopt
    OPT_MWCOLORLAW: 99
    OPT_MWEBV: 3
    RV_MWCOLORLAW: 3.1
```

`snlc_sim.exe` **Step 1: Rest-frame light curves** Simulating the initial rest-frame light curves involves repeatedly sampling the PDFs of a given SN model's shape parameters. The SN model is specified via the `GENMODEL` key[1] which requires a path to a pre-trained SN model —

[1] Aliased to `*s3model`, see Code Block 2.13

`/path/to/MODEL_CLASS.MODEL_INSTANCE`, for example `SNDATA_ROOT/models/SALT3/SALT3.DES5YR` in Code Block 2.13 which provides the `DES5YR` trained version of the `SALT3` model.

The PDFs of the SN model parameters are configured in a `GENPDF_FILE`, and can be described analytically as an asymmetric Gaussian or an exponential, or can be provided explicitly described through a table mapping parameter values to probabilities. The latter is useful as it enabled arbitrary PDFs to be defined, and optionally allows multidimensional mappings between SN model parameters, host-galaxy parameters and probabilities. Code Block 2.16 presents the `GENPDF_FILE` for the DES-SN5YR data simulations. Here the SALT3 $\mathcal{C}$ and x_1 parameters are described via a table, with the x_1 PDF including a dependency on host-galaxy mass. The SALT3 α PDF is described by a delta-function at $\alpha = 0.15$[1], whilst the SALT3 β PDF is described as a uniform Gaussian with $\mu = 2.076$ and $\sigma = 0.217$.

In addition to the `GENMODEL` and `GENPDF_FILE` parameters, there are a number of other important parameters which `snlc_sim.exe` requires, including:

- `GENFILTERS`, `GENRANGE_PEAKMJD`, and `GENRANGE_REDSHIFT`: These parameters, among many others, provide details and constraints on various aspects of the simulated SNe, including which filters, epochs, and redshifts can be simulated.
- `DNDZ`: This parameter describes the dependency between simulated SNe rate and redshift. Setting `DNDZ` to `HUBBLE` results in a constant volumetric rate at all redshifts, whilst `POWERLAW X Y` simulates a redshift-dependent rate of $X \times (1+z)^Y$ SNe per year per cubic Mpc.
- `GENTYPE`: The SN type to simulate, follows the same specifications as the `DATAPREP` `SNTYPE` parameter (List 2.2) where a `GENTYPE` of 1[2] indicates SNe Ia, and other `GENTYPES` map to various SNe non-Ia and peculiar SNe Ia. These are defined in Code Block 2.15.
- `NGENTOT_LC`, `NGEN_LC` or `NGEN_UNIT`: The various `NGEN` keys determine the number of SNe simulated in each sample. `NGENTOT_LC` specifies how many SNe should be simulated *before* survey efficiency and selection cuts are taken into account, whereas `NGEN_LC` specifies how many SNe should be in the final simulated sample *after* survey efficiency and selection cuts. For example, given a survey efficiency of $\sim 10\%$, an `NGENTOT_LC` of 1000 will simulate 1000 SNe, from which ~ 100 will be included in the final simulated sample. An `NGEN_LC` of 1000 will simulate ~ 10000 SNe so that the final simulated sample includes 1000 SNe. The `NGEN_UNIT` determines

[1] α lacks both a `GENSIGMA` and a `GENRANGE` specification, leading to a delta-function.
[2] 101 for photometric SNe Ia

the number of SNe to simulate from physical rates, as determined by the `GENRANGE_PEAKMJD`, `GENRANGE_REDSHIFT`, and `SOLID_ANGLE` parameters. These parameters are used to calculate a 'realistic' `NGENTOT_LC`, which is then multiplied by `NGEN_UNIT` to determine the final number of SNe to simulate. Thus, an `NGEN_UNIT` of 1 produces approximately the same number of SNe as the survey being simulated, whilst an `NGEN_UNIT` of 10 simulates an order of magnitude more SNe[1].

- `GENMAG_SMEAR_*`: These parameters model intrinsic brightness variations which contribute to the 'intrinsic scatter' of a Hubble diagram — scatter not attributed to any known uncertainty. As can be seen in Code Block 2.13, the DES-SN5YR analysis uses the following options to model this variation:
  - `GENMAG_SMEAR_MODELNAME: "C11"`: Describe the smearing as a function of wavelength and/or phase. The value of this parameter selects a pre-compiled function from `sntools_genSmear.c`, and can be either `C11` (based on Chotard et al., 2011) or `G10` (based on Guy et al., 2010).
  - `GENMAG_SMEAR_SCALE: 0.0001`: Scale all magnitude smear values produced by the previous function by this amount, bringing it inline with physical expectations.
  - `GENMAG_SMEAR_SCALE(c): "0,0"`: An additional, colour dependent scaling of magnitude smear values by $x + y * c$, in this case $0 + 0 * c$, i.e. no colour dependent scaling.
  - `GENMAG_SMEAR_ADDPHASECOR: "0.0 10.0"`[2]: A phase dependent brightness variation. The first parameter defines the Gaussian sigma used to generate additional brightness variations (in this case 0.0, meaning no additional brightness variation is applied). The second parameter is a coherence parameter (τ) which controls the correlation between brightness variations over time. If two observations are separated by ΔT days, then the reduced correlation is $\rho = \exp\left(-\Delta t/\tau\right)$. Overall `GENMAG_SMEAR_ADDPHASECOR` ensures that the brightness variation of observations separated by less than 10 days are more correlated, whilst those separated by more than 10 days are less correlated.
- `SEARCHEFF_PIPELINE_*`: These parameters describe the efficiency of a survey's software-pipeline, detailing how likely any given SN is to be observed by the survey.
- `LENSING_PROBMAP_FILE`: Describes the effects of weak lensing on the simulated SN sample, shifting the distance-modulus of a small portion of

[1] As if the survey had run for 10 times longer, surveyed 10 times the area, etc...
[2] Found in Code Blocks 2.8 to 2.10

simulated SNe by $-2.5\log\left(\text{magnification}\right)$ where the magnification level is drawn from a redshift-dependent set of lensing probabilities.

- `CUTWIN_*`: These parameters describe the selection cuts used by the survey, which allows the simulation to quickly discard SNe which don't pass these cuts early, leading to a sizeable performance improvement. Within the DES-SN5YR data simulations, the selection cuts include:
  - `CUTWIN_NEPOCH: 5 -5.` At least 5 epochs with at least one occurring 5 days before max.
  - `CUTWIN_SNRMAX: 3 griz 2 -20. 60.` A signal-to-noise ratio > 3 for at least 2 of the four *griz* filters, occurring between 20 days before max, and 60 days after max.
  - `CUTWIN_MWEBV` A Milky Way $E\left(B-V\right)$ between 0 and 0.3.

Code Block 2.15: The `BASE` file for the DES-SN5YR data simulation.

```
INPUT_FILE_INCLUDE:
    ↪  $DES5YR/base/des/sims_instrument/sim_des_5yr_phot_include.input
GENTYPE: 1
GENMODEL_EXTRAP_LATETIME: $PLASTICC_MODELS/SNIa_Extrap_LateTime_2expon.TEXT
```

Code Block 2.16: The `GENPDF_FILE` for the DES-SN5YR data simulation. Describes the PDFs of the SALT3 $\mathcal{C}$, x_1, α, and β parameters.

```
# Parameters are:
# c_mu:                                  -0.0736862,
# c_std:                                 0.05236237,
# RV_mu_HOST_LOGMASS_low:                3.24740456,
# RV_std_HOST_LOGMASS_low:               0.92648388,
# RV_mu_HOST_LOGMASS_high:               1.66218622,
# RV_std_HOST_LOGMASS_high:              0.94796795,
# EBV_Tau_SIM_ZCMB_low_HOST_LOGMASS_low:    0.11078764,
# EBV_Tau_SIM_ZCMB_low_HOST_LOGMASS_high:   0.13982172,
# EBV_Tau_SIM_ZCMB_high_HOST_LOGMASS_low:   0.1224219,
# EBV_Tau_SIM_ZCMB_high_HOST_LOGMASS_high: 0.15028344,
# beta_mu:                               2.07646589,
# beta_std:                              0.21728215

VARNAMES: SALT2c PROB
PDF: -0.500 0.000
PDF: -0.499 0.000
# ...
PDF: -0.181 0.122
PDF: -0.180 0.127
PDF: -0.179 0.132
# ...
PDF: 4.800 11.80 0.000
PDF: 4.900 11.80 0.000

MAG_OFFSET:  -0.12
GENPEAK_SALT2ALPHA:  0.15
GENPEAK_SALT2BETA: 2.07646589
GENSIGMA_SALT2BETA: 0.21728215 0.21728215
GENRANGE_SALT2BETA: .4 3

VARNAMES: SALT2x1 LOGMASS PROB
PDF: -5.000 8.20 0.000
PDF: -4.900 8.20 0.000
# ...
PDF: 4.800 9.00 0.000
PDF: 4.900 9.00 0.000
PDF: -5.000 9.20 0.000
PDF: -4.900 9.20 0.000
# ...
PDF: 4.800 11.80 0.000
PDF: 4.900 11.80 0.000
```

Code Block 2.17: The `DEFAULTS` file for the DES-SN5YR data simulation.

```
SIMLIB_FILE: $DES_ROOT/simlibs/DES_DIFFIMG.SIMLIB
UVLAM_EXTRAPFLUX: 500
HOSTLIB_GENRANGE_NSIGZ: -3. +3.
SOLID_ANGLE: 0.0082
GENFILTERS: griz
GENRANGE_PEAKMJD: 56535 58178
OPT_SETPKMJD: 16
GENRANGE_TREST: -40 100
GENRANGE_REDSHIFT: 0.05 1.3
GENSIGMA_REDSHIFT: 0.00001
GENSIGMA_VPEC: 300
VPEC_ERR: 300
SMEARFLAG_FLUX: 1
SMEARFLAG_ZEROPT: 3
APPLY_SEARCHEFF_OPT: 5
SEARCHEFF_PIPELINE_EFF_FILE:
    ↪ $SNDATA_ROOT/models/searcheff/SEARCHEFF_PIPELINE_DES.DAT
SEARCHEFF_PIPELINE_LOGIC_FILE:
    ↪ $SNDATA_ROOT/models/searcheff/SEARCHEFF_PIPELINE_LOGIC.DAT
NEWMJD_DIF: 0.4
SEARCHEFF_SPEC_FILE: ZERO
LENSING_PROBMAP_FILE:
    ↪ $SNDATA_ROOT/models/lensing/LENSING_PROBMAP_LogNormal+MICECATv1.DAT
APPLY_CUTWIN_OPT: 1
CUTWIN_NEPOCH: 5 -5.
CUTWIN_SNRMAX: 3 griz 2 -20. 60.
CUTWIN_MWEBV: 0 0.30
SIMGEN_DUMP: 37
 CID GENTYPE SNTYPE NON1A_INDEX GENZ GALZTRUE
 LIBID RA DEC MWEBV MU PEAKMJD
 PEAKMAG_g PEAKMAG_r PEAKMAG_i PEAKMAG_z
 SNRMAX_g SNRMAX_r SNRMAX_i SNRMAX_z
 SNRMAX SNRMAX2 SNRMAX3
 NOBS TRESTMIN TRESTMAX TGAPMAX
 CUTMASK SIM_EFFMASK
 HOSTMAG_g HOSTMAG_r HOSTMAG_i HOSTMAG_z
 SBFLUX_g SBFLUX_r SBFLUX_i SBFLUX_z
```

`snlc_sim.exe` **Step 2: Observer-frame light curves** For rest-frame SN models, this step involves transforming the light curves from Step 1 to mimic the effects of host-galaxy extinction, k-correction, and Galactic extinction; observer-frame models like SALT3 directly model these effects instead. Regardless, both types of SN model require the same information to produce observer-frame light curves, so the Pippin configuration is the same for either model type.

To effectively model host-galaxy extinction effects, each SN is assigned a random 'host-galaxy' from a set of simulated host galaxies, provided in a `HOSTLIB` file (Code Block 2.18). The likelihood of a particular SN being assigned a given host-galaxy can be weighted by SN or host-galaxy properties via a `HOSTLIB_WGTMAP_FILE` (Code Block 2.19). Combining the `HOSTLIB_WGTMAP_FILE` with host-galaxy dependent SN model parameters (see Code Block 2.16) allows `snlc_sim.exe` to accurately simulate correlations between SNe and their host. Additional complexity can be introduced to the host-galaxy simulation through the following keys:

- `HOSTLIB_SCALE_PROPERTY_ERR`: Scales the error of each property. This is used in Code Block 2.11 to remove the simulated error on host-galaxy mass, star formation rate, specific star formation rate, and colour.
- `HOSTLIB_MSKOPT`: This parameter controls a number of binary flags which enable or disable different components of the `snlc_sim.exe` host-galaxy simulation. Code Block 2.11 shows that the DES-SN5YR data simulations use a `HOSTLIB_MSKOPT` of 258, or $2 + 256$. These switches correspond to:
  - $+2$: Include host-galaxy contributions to SN Poisson noise.
  - $+4$: Shift the magnitudes of simulated SNe by the `SNMAGSHIFT` value associated with their allocated host-galaxy, potentially dimming SNe allocated to more massive galaxies.
  - $+8$: Shift the coordinates of simulated SNe to coordinates randomly generated from their host galaxy's surface brightness profile.
  - $+256$ Increase verbosity of output, has no effect on `snlc_sim.exe` outcomes.
- `SEARCHEFF_zHOST_FILE`: Describes the redshift-dependent probability of determining the spectroscopic redshift of a galaxy. SNe for which a spectroscopic host galaxy redshift can not be determined are rejected. An example is provided in Code Block 2.20.
- `HOSTLIB_GENRANGE_*`: Numerous keys exist to constrain the range and distribution of various host-galaxy properties. In Code Block 2.17 `HOSTLIB_GENRANGE_NSIGZ` is used to constrain the maximum host-galaxy photometric redshift in units of sigma ($NSIGZ = (z_{phot} - z_{true})/z_{err}$).

Code Block 2.18: A truncated view of the `HOSTLIB` file for the DES-SN5YR data simulation. The real data file contains several thousand additional host galaxies.

```
VARNAMES: GALID RA_GAL DEC_GAL ZTRUE ZERR g_obs r_obs i_obs z_obs a0_Sersic b0_Sersic n0_Sersic a_rot LOGMASS LOGSFR a_DLR b_DLR DLR_area Sersic_area g_obs_auto r_obs_auto i_obs_auto z_obs_auto u_restmag r_restmag obs_gr_auto COLOR  NBR_LIST
GAL: 2200000040 35.14463 -6.40364 0.6456649999999999 0.5151945811357359 24.508278 23.346 23.219117 22.535616 0.7767333 901978909 0.6075429929448157 1.557354 -61.872505 9.961 0.1 0.561372 0.440812 0.247459514064 0.471898928601 25.688708885 23.80913282 23.263537186 22.43774305 -19.077 -20.173 1.879576065000002 1.0959999999999965  40
GAL: 2200000045 35.135322 -6.403468 0.56084 0.3321944481940645 24.906136 23.393696 22.955189 22.486968 1.2095298231524678 0.6422554979746679 0.300471 41.730526 9.788 0.192 0.649003 0.484002 0.314118750006 0.7768271788840002 25.13130631 23.441470325 23.110234143000003 22.405567923 -18.687 -19.801 1.6898359849999984 1.1139999999999972 67
GAL: 2200000050 35.108543 -6.403292 0.831 0.2125724008339033 24.596458 23.780611 22.825249 22.700251 0.5288474338747976 0.3969555281035924 0.594681 26.677921 9.55 0.32 0.56094 0.52708 0.2956602552 0.2099289123999999 24.87771962 23.811275597 22.861220770000003 22.84120966 -20.081 -20.431 1.066444022999999 0.3500000000000014  72
GAL: 2200000053 35.019431 -6.40321 0.2159599999999999 0.8861144350152125 24.314421 24.106782 24.067909 23.9342 0.2742704468928032 0.1056681750743903 4.020739 -25.379091 7.599 -0.745 0.400506 0.289114 0.1157918916839999 0.0289816576 24.30794587 24.245727067 24.009015615 24.12837944 -16.103 -16.036 0.06221880300000038 -0.06700000000000017 55
GAL: 2200000054 35.092012 -6.403195 0.30073 1.0920503949722806 24.76887 24.154686 23.982727 24.364043 0.2516657664777634 0.2420694991361998 3.735157 86.811134 7.884 -0.91 0.402872 0.318054 0.128135051088 0.060920606041 24.915493736 24.19986439 24.11285264 24.716665824 -16.547 -16.592 0.715629346 0.04499999999999815  38,66
```

Code Block 2.19: The `HOSTLIB_WGTMAP_FILE` for the DES-SN5YR data simulation. Weights the probability (`WGT`) of an SN being assigned a host-galaxy by the mass (`LOGMASS`) of the host-galaxy, and applies a host-galaxy mass dependent offset (`SNMAGSHIFT`) to the simulated SN magnitudes.

```
VARNAMES_WGTMAP: LOGMASS   WGT         SNMAGSHIFT
WGT:             5.000     1.413e+03   0.000
WGT:             5.070     1.564e+03   0.000
# ...
WGT:             7.940     1.005e+05   0.000
WGT:             8.010     1.112e+05   0.000
# ...
WGT:             13.890    5.632e+08   0.000
WGT:             13.960    6.234e+08   0.000
```

Code Block 2.20: The `SEARCHEFF_zHOST_FILE` for the DES-SN5YR data simulation. Describes the likelihood (`HOSTEFF`) of determining a host-galaxy's spectroscopic redshift, relative to the host galaxy's peak r-band magnitude (`r_obs_auto`) and its g-r colour (`obs_gr_auto`)

```
OPT_EXTRAP: 1

PEAKMJD_RANGE: 56300 57500
FIELDLIST: C1+C2
VARNAMES: r_obs_auto obs_gr_auto HOSTEFF
HOSTEFF:  15.400     0.720       1.000    ##1.000
HOSTEFF:  15.400     1.570       1.000    ##1.000
HOSTEFF:  16.200     0.720       1.000    ##1.000
HOSTEFF:  16.200     1.570       1.000    ##1.000
HOSTEFF:  17.000     0.720       1.000    ##1.000
```

K-corrections are pre-computed[1] on a redshift, epoch, host-galaxy extinction (A_v) grid. For each $(z, epoch, A_v)$ cell in this grid, the Cardelli et al. (1989) colour law is applied to a spectral template, warping the colour of each passband in the spectral template. The k-correction of that $(z, epoch, A_v)$ cell can then be determined from the 'A_v-warped' spectral template, and linear interpolating between $(z, epoch, A_v)$ cells allows the k-correction for any simulated

[1] Uses the `kcor.exe` binary

light curve to be determined. Pre-computing this k-correction table is an expensive, one-time operation, which allows applying appropriate k-corrections to simulated SN light curves to be trivially reduced to a simple table lookup. This k-correction file is provided with the `KCOR_FILE` key (Code Block 2.11).

Finally, applying the effects of Galactic extinction requires specifying the Milky Way R_v (`RV_MWCOLORLAW`), colour law (`OPT_MWCOLORLAW`), and $E(B-V)$ (`OPT_MWEBV`). Both `OPT_MWCOLORLAW` and `OPT_MWEBV` allow users to assign a pre-defined colour law, with DES-SN5YR using the Fitzpatrick (1999) (`OPT_MWCOLORLAW=99`) colour law model, and the Popovic et al. (2021) (`OPT_MWEBV=3`) $E(B-V)$ model.

`snlc_sim.exe` **Step 3: Survey-frame light curves** The final step of `snlc_sim.exe` simulations accounts for survey-specific atmospheric and observing conditions. This step relies on detailed measurements of observing conditions, provided via a `SIMLIB` file (Code Block 2.21). This file contains both general details of a survey, and actual survey data, allowing `snlc_sim.exe` to accurately model the specifics of each survey's observing conditions, including variations in cadence, seeing, atmospheric transparency and readout noise. Each survey is defined in a global `SURVEY.DEF` file (Code Block 2.22) which provides a unique identifier to each survey and their associated filters. The wavelength-dependent transmission curve of each filter is defined in the `KCOR_FILE`. Alongside these general details, the `SIMLIB` file contains lists of real observation sequences taken at the site. Each sequence is assigned a unique `LIBID`, and each observation within the sequence is listed in a table which describes the epoch (`MJD`), filter (`FLT`), the `CCD Gain` in photo-electrons per ADU, the `CCD Noise` in photo-electrons per pixel, the standard deviation of the sky (`SKYSIG`) in ADU per pixel, and the PSF, defined as a double-Gaussian with widths $\sigma_1 =$ `PSF1`, and $\sigma_2 =$ `PSF2`. `PSF_RATIO` describes the ratio between the amplitude of each Gaussian at the origin. Finally, `ZPTAVG` and `ZPTSIG` describe the zero-point and its uncertainty, for each observation in the sequence, such that:

$$\frac{F}{\mathrm{ADU}} = 10^{-0.4(m-\,\texttt{ZPTAVG}\,)} \tag{2.1}$$

These recorded observing conditions enable `snlc_sim.exe` to transform the observer-frame light curves into realistic survey-frame light curves. The uncertainty of the simulated flux is calculated as:

$$\sigma_F^2 = \left[F + (A \times b) + (F \times \hat{\sigma}_{\mathrm{ZPT}})^2 + \left(\hat{\sigma}_0 \times 10^{0.4 \times \mathrm{ZPT}_{\mathrm{pe}}}\right) + \sigma_{\mathrm{host}}^2\right] \hat{S}_{\mathrm{SNR}}^2 \quad (2.2)$$

where,

- F is the simulated flux, converted to photoelectrons.
- $A = \left[2\pi \int \int \mathrm{PSF}^2(r) r dr\right]^{-1}$ is the noise-equivalent area defined by the PSF.
- b is the background per unit area.
- $\hat{\sigma}_{\mathrm{ZPT}}$ is the zero-point uncertainty, calculated from the `ZPTSIG` parameters in the `SIMLIB` file.
- $\hat{\sigma}_{\mathrm{host}}$ is the uncertainty in SN flux caused by host-galaxy contributions to the overall Poisson noise.

The $\hat{S}_{\mathrm{SNR}}$ and $\hat{\sigma}_0$ describe global flux scaling and offset parameters, which account for many astrophysical and instrument-level noise sources including the gain and read-out-noise. These parameters are determined from a survey-specific multidimensional function which can depend on the `MJD`, `PSF`, `SKYSIG`, `ZP`, signal-to-noise ratio (`LOGSNR`), host-galaxy surface brightness (`SBMAG`), total host-galaxy magnitude (`GALMAG`), and SN-host separation (`SNSEP`). These functions are defined in a `FLUXERRMODEL_FILE`.

2.3.2.2 `SIM` specific Pippin development

Most of the development for `SIM` was concerned with improving how Pippin handles the numerous auxiliary files associated with `snlc_sim.exe`, including automatically searching for the `GENTYPE` and `GENMODEL` parameters within auxiliary files included in the `BASE` file.

Additionally, in collaboration with Rick Kessler (SNANA's developer) I developed improvements to the handling of systematic uncertainties within `snlc_sim.exe`. Initially, systematic uncertainties could be defined via a number of `RANSYSTPAR` parameters, which would randomly determine systematic offsets for each SN in the sample. For example `RANSYSTPAR_RANGESHIFT_W0: -0.5 0.5` would randomly select a Δw between -0.5 and 0.5 for each simulated SNe, shifting the w parameter used for each SN in the simulation by Δw. Whilst this was useful for small-scale systematic analyses, it did not allow for finer control over the systematic offsets — in particular correlations between systematics could not be simulated. To address this, I introduced the `INPUT_INCLUDE_FILE` key which allowed the user to define a file containing a list of paths to `snlc_sim.exe` input files so that each successive simulation

Code Block 2.21: The `SIMLIB` file for the DES-SN5YR data simulation. This file contains examples of real observations from DECAM, spanning the length of the DES SN survey. Each entry is assigned an ID (`LIBID`) and details the time (`MJD`), bandpass filter (`FLT`), CCD gain and noise, sky noise and dark current (`SKYSIG`), and PSF of the observation.

```
SURVEY: DES
FILTERS: griz
PIXSIZE: 0.27
PSF_UNIT: ARCSEC_FWHM
NLIBID: 10000

#---------------------------------------------------------------------------
BEGIN LIBGEN

# --------------------------------------------
LIBID: 1
RA: 41.159644    DEC: -1.404657   NOBS: 526
MWEBV: 0.000   PIXSIZE: 0.270
FIELD: S2
CCDNUM: 47
TEMPLATE_ZPT: 30.818 30.852 31.066 31.509
TEMPLATE_SKYSIG:    3.80    5.41    7.86   14.98
#                            CCD  CCD            PSF1 PSF2 PSF2/1
#     MJD      IDEXPT  FLT GAIN NOISE  SKYSIG  (pixels)  RATIO ZPTAVG ZPTSIG MAG
S: 56534.283     228764 g  3.86  0.00    8.15  1.64 0.00 0.000  30.82  0.016 99.000
S: 56534.288     228766 i  4.04  0.00   20.94  1.32 0.00 0.000  31.07  0.005 99.000
S: 56534.286     228765 r  3.80  0.00   12.22  1.52 0.00 0.000  30.85  0.012 99.000
S: 56534.290     228767 z  4.02  0.00   41.71  1.24 0.00 0.000  31.51  0.006 99.000
# ...

# --------------------------------------------
LIBID: 2
RA: 41.372733    DEC: -0.542711   NOBS: 526
MWEBV: 0.000   PIXSIZE: 0.270
FIELD: S2
CCDNUM: 16
TEMPLATE_ZPT: 30.794 30.842 31.072 31.511
TEMPLATE_SKYSIG:    3.92    5.28    7.91   15.15
#                            CCD  CCD            PSF1 PSF2 PSF2/1
#     MJD      IDEXPT  FLT GAIN NOISE  SKYSIG  (pixels)  RATIO ZPTAVG ZPTSIG MAG
S: 56534.283     228764 g  3.58  0.00    8.42  1.63 0.00 0.000  30.79  0.009 99.000
S: 56534.288     228766 i  3.92  0.00   21.30  1.31 0.00 0.000  31.07  0.004 99.000
S: 56534.286     228765 r  3.71  0.00   12.35  1.54 0.00 0.000  30.84  0.008 99.000
S: 56534.290     228767 z  3.90  0.00   42.43  1.28 0.00 0.000  31.51  0.005 99.000
# ...
```

Code Block 2.22: A truncated view of the SNANA `SURVEY.DEF` file, highlighting the DES-SN5YR survey details.

```
                 SNANA
         name      ID
-------------------------------
SURVEY:  DES       10  geo:-30.24,-70.75,2200 # Dark Energy Survey

# DES Fields
FIELD: E1   1   DES shallow (Elias)
FIELD: E2   2   DES shallow
FIELD: S1   3   DES shallow (SDSS stripe 82)
FIELD: S2   4   DES shallow
FIELD: C1   5   DES shallow (CDF_S)
FIELD: C2   6   DES shallow
FIELD: C3   7   DES deep
FIELD: X1   8   DES shallow (XMM_LSS)
FIELD: X2   9   DES shallow
FIELD: X3  10   DES deep
```

in a `SIM` `Task` could use a different input file. As I describe in Section 4.2.1, this enabled simulations with correlated systematic uncertainties by drawing covariant systematic offsets from some covariance matrix, and created a new `snlc_sim.exe` input file for each simulated SN.

2.3.3 `LCFIT` — Light curve Fitting

Following the preparation of real data in `DATAPREP`, and the generation of simulated data in `SIM`, all SN events are treated identically, with no distinction made between simulated or real SNe. The next several `Stages`, including `LCFIT`, `CLASSIFY`, and `BIASCOR`, are focused on producing a cosmologically useful Hubble diagram, by standardising the apparent magnitude of each SNe. The resulting distance moduli are defined by:

$$\mu_{obs} = m + \alpha x_1 - \beta \mathcal{C} + \gamma G_{\text{host}} - \mathcal{M} - \Delta\mu_{\text{bias}} \tag{2.3}$$

Here, m, x_1, and $\mathcal{C}$ are per-SN light curve parameters determined by the SALT3 SN model (Kenworthy et al., 2021; Taylor et al., 2023), α, and β are global scale factors[1] which determine the amplitude of the *stretch-luminosity*, and

[1] These are often referred to as 'nuisance parameters'; however, as their values are fitted with BBC before cosmological parameters are fit, rather than marginalised over, this is not technically correct.

colour-luminosity corrections, respectively, and $\mathcal{M}$ is the absolute magnitude of a SN Ia with $x_1 = 0$ and $\mathcal{C} = 0$ (i.e. a 'standard' SN Ia)

γ, and G_{host} encapsulate dependencies between the luminosity of a SN, and the properties of its host galaxy. Lampeitl et al. (2010); Smith et al. (2020b); Sullivan et al. (2010) found that SNe in high mass ($M_{\mathrm{host}} > 10^{10}M_\odot$) are on average brighter than those in low mass galaxies, after stretch and colour corrections. Recent work by Brout and Scolnic (2021); Kelsey et al. (2023) also showed that the host galaxy luminosity step was also correlated with SN colour — redder SNe exhibited a greater effect than bluer SNe. Ongoing analyses have since shown additional correlations with other host galaxy properties, including metallicity (Campbell et al., 2016; Galbany et al., 2022; Pan et al., 2013) and specific star formation rate (Childress et al., 2013; Dixon et al., 2022; Galbany et al., 2022; Lampeitl et al., 2010; Rigault et al., 2020).

Within the DES-SN5YR analysis, the *host-luminosity* correction was modelled as a step function:

$$\gamma G_{\mathrm{host}} = \begin{cases} +\gamma/2, & \text{if } P > P_{\mathrm{step}}, \\ -\gamma/2, & \text{otherwise}, \end{cases} \tag{2.4}$$

For some host galaxy property P with step threshold P_{step}. As the underlying cause of the *host-luminosity* correction is still unknown, both a host galaxy mass ($P = M_{\mathrm{host}}, P_{\mathrm{step}} = 10^{10}M_\odot$) and colour ($P = (u-r)_{\mathrm{host}}, P_{\mathrm{step}} = 1$) were implemented, with the difference in the *host-luminosity* corrections treated as a systematic (See Section 2.3.6).

Finally, $\Delta\mu_{\mathrm{bias}}$ (discussed in Section 2.3.5) corrects for biases arising from selection effects, non-Ia contamination, and analysis choices.

Though the role of `LCFIT` is primarily to fit a SN model to light curves from `DATAPREP` and `SIM`, this `Stage` also applies preliminary quality cuts to the data, and determines the sources of systematic uncertainty accounted for in `CREATECOV`.

2.3.3.1 The DES-SN5YR Light curve Fits

The DES-SN5YR `LCFIT` configuration (presented in Code Block 2.23 for the data and data-like simulations, and Code Block 2.24 for the bias simulations) configures the SNANA `snlc_fit.exe` binary, and is structured similarly to `snlc_sim.exe`, requiring a `BASE` file from which default options are added to or overwritten by the rest of the `LCFIT` configuration.

The `SNLCINP` key defines both SNe selection criteria, and Milky Way and Galactic Reddening details, using similar keys to `SIM`. SN selection can be based on numerous properties of SNe and their host galaxies, including:

- The minimum number of epochs at different stages of the light curve. `cutwin_Trestmin`, `CUTWIN_TREST`, and `cutwin_Trestmax` ensure at least one epoch exists in the provided range of days prior to, during, and following peak, respectively. `CUTWIN_NEPOCH` sets a minimum number of total epochs.
- `CUTWIN_SNRMAX` provides the minimum signal-to-noise ratio required in at least one epoch, for the number of filters specified by `CUTWIN_NFILT_SNRMAX`.
- A redshift within the `CUTWIN_REDSHIFT` range and with a maximum uncertainty defined by `CUTWIN_REDSHIFT_ERR`.
- The scale of various photometric effects, including Milky Way $E(B-V)$ (`CUTWIN_MWEBV`), the FWHM of the PSF (`CUTWIN_PSF`), and the zero-point (`CUTWIN_ZPNPE`) in units of number of photo-electrons.

One interesting addition to the DES-SN5YR `SNLCINP` configuration is the `MAGCOR_FILE` file which includes per-epoch magnitude corrections for the data SN light curves. In addition to the chromatic corrections used in the DES-SN3YR analysis (Lasker et al., 2019), Lee et al. (2023) determined the correction for differential chromatic refraction (DCR) caused by the wavelength-dependent index of refraction of our atmosphere, and wavelength-dependent seeing effects.

`FITINP` describes post-fit selection criteria on the $\mathcal{C}$ (`FITWIN_COLOR`), x_1 (`FITWIN_SHAPE`), minimum and maximum epoch (`FITWIN_TREST`), and goodness-of-fit (`FITWIN_PROB`). Additionally, a uniform prior on x_1 can be defined via `PRIOR_SHAPE_RANGE`. This x_1 prior is typically a broad constraint which ensures fits remain physically bounded — avoiding fit parameters which can lead to code crashes.

SN light curve parameter estimation is performed in three steps. First, initial estimates for the `PKMJD` and amplitude are determined as described in Section 2.3.1, if they were not already found in `DATAPREP` if they were not already found in `DATAPREP`. Next, CERNLIB's `MINUIT` program (James, 1994) is used to perform a preliminary maximum-likelihood fit of the parameters, providing a covariance matrix of best-fit parameters and their uncertainties. This covariance matrix is used by SNANA as the initial conditions to a marginalisation algorithm which performs a multidimensional integration over the posterior described by the `MINUIT` covariance matrix.

To account for systematic uncertainties related to light curve fitting, a number of variations to the light curve fit can be provided in a `FITOPTS` file (See Code Block 2.29 for the DES-SN5YR `FITOPTS` file). For each key in this file, `LCFIT` will be repeated with the given variation applied. The DES-SN5YR analysis includes 13 `FITOPTS` which account for:

- `CALSPEC`: Uncertainties in the HST CALSPEC zero-points used to calibrate DES-SN5YR fluxes (Brout et al., 2022b).
- `COLORLAW` & `MWEBV`: Choice of Milky Way extinction model, and uncertainties in that model.
- `zshift`: A systematic shift in the redshift to account for the possibility of a local void.
- `cal-{1-9}`: To account for variations in the SALT3 training caused by uncertainties in the DES-SN5YR zero-points and filter transmission curves, a set of 10 SALT3 models were produced, each with a different covariant offset in the zero-point and filter curves of the training data. As the training of new SALT3 models is a computationally expensive task (~3 hours per model) producing additional SALT3 models to better capture the effect of these systematics is impractical. In Section 4.2.1.1, I describe a preliminary method I developed for approximating the training of SALT models significantly faster (~30 seconds per model), enabling greater control over this systematic uncertainty.

Code Block 2.23: The configuration file for the DES-SN5YR lightcurve fits. The file relies on aliases defined in Code Blocks 2.25 to 2.27, and the `BASE` file presented in Code Block 2.28.

```
LCFIT:
  Dsys:
    BASE: "$SNDATA_ROOT/sample_input_files/DES-SN5YR/base_files/lcfit/desSMP_5yr.nml"
    FITINP:
      !!merge <<: [*opt_fitinp, *s3fit]
    FITOPTS: ["$SNDATA_ROOT/sample_input_files/DES-SN5YR/base_files/lcfit/fitopts.yml"]
    MASK: "DATADES"
    OPTS:
      !!merge <<: *batchinfo
      OPT_SNCID_LIST: 1
    SNLCINP:
      !!merge <<: [*dcr_corrections, *deskcor, *minos_on, *opt_snlcinp]
      FLUXERRMODEL_FILE: "$DES_ROOT/starterKits/make_fluxerr_model/OUT_SMP/FLUXERRMODEL_FAKE.DAT"
```

Code Block 2.24: The configuration file for the DES-SN5YR simulated lightcurve fits. The file relies on aliases defined in Code Blocks 2.25 to 2.27, and the `BASE` file presented in Code Block 2.28.

```
LCFIT:
  D3:
    BASE: "$SNDATA_ROOT/sample_input_files/DES-SN5YR/base_files/lcfit/desSMP_5yr.nml"
    FITINP:
      !!merge <<: [*opt_fitinp, *s3fit]
    MASK: "DES"
    OPTS:
      !!merge <<: [*appendfitres_des, *batchinfo]
      BATCH_MEM: "16GB"
    SNLCINP:
      !!merge <<: [*deskcor, *minos_on, *opt_snlcinp]
```

Code Block 2.25: `LCFIT` aliases common to all light curve fits within the DES-SN5YR analysis, regardless of SN type.

```
GLOBAL_ALIAS:
  APPENDFITRES: &appendfitres
    APPEND_TABLE_VARLIST: "TGAPMAX TrestMIN TrestMAX"
  BATCHINFO: &batchinfo
    BATCH_INFO: "sbatch $SBATCH_TEMPLATES/SBATCH_Midway2b.TEMPLATE 5"
```

Code Block 2.26: `LCFIT` aliases specific to light curve fits of the DES-SN5YR data.

```
DES_ALIAS:
  DESKCOR: &deskcor
    KCOR_FILE: "$SNDATA_ROOT/kcor/DES/DES-SN5YR/calib_DES-SN5YR_DES.fits.gz"
```

Code Block 2.27: `LCFIT` aliases common to all SN Ia light curve fits within the DES-SN5YR analysis.

```
ALIAS_SHARED:
  DCR_CORRECTIONS: &dcr_corrections
    MAGCOR_FILE: "$SNDATA_ROOT/simlib/DES/DES-SN5YR_DES_DCR+CHROM.DAT"
  MINOS_ON: &minos_on
    USE_MINOS: "T"
  OPT_FITINP: &opt_fitinp
    FITWIN_COLOR: "-0.5, +0.5"
    FITWIN_PROB: "0.0,  1.01"
    FITWIN_SHAPE: "-5.0, +5.0"
    FITWIN_TREST: "-15.0, 45.0"
    PRIOR_SHAPE_RANGE: "-6.0, 6.0"
  OPT_SNLCINP: &opt_snlcinp
    MWEBV_SCALE: 1.0
    MWEBV_SHIFT: 0.0
    OPT_MWCOLORLAW: 99
    OPT_MWEBV: 3
    OPT_SETPKMJD: 20
    ROOTFILE_OUT: "ROOTFILE.ROOT"
    RV_MWCOLORLAW: 3.1
    SNTABLE_LIST: "FITRES(text:host)"
    cutwin_Trestmax: "5.   99999."
    cutwin_Trestmin: "-9999.0   5.0"
  S3FIT: &s3fit
    FITMODEL_NAME: "$SNDATA_ROOT/models/SALT3/SALT3.DES5YR"
    RESTLAMBDA_FITRANGE: "3500.0 8000.0"
```

Code Block 2.28: `snlc_fit.exe` `BASE` file used by the DES-SN5YR light curve fits. The file provides default selection criteria, priors, and fit parameters.

```
CONFIG:
  APPEND_TABLE_VARLIST: RA DEC HOST_ANGSEP TGAPMAX TrestMIN TrestMAX FLUXCALMAX_g SNRMAX_g FLUXCALMAX_r SNRMAX_r FLUXCALMAX_i SNRMAX_i FLUXCALMAX_z SNRMAX_z m0obs_r m0obs_i m0obs_g
#END_YAML
&SNLCINP
    PRIVATE_DATA_PATH  = '$SNDATA_ROOT/lcmerge/DES-SN5YR'
    VERSION_PHOTOMETRY = 'DES-SN5YR_DES'
    NFIT_ITERATION = 3
    INTERP_OPT     = 1

    ABORT_ON_NOEPOCHS = F
    ABORT_ON_TRESTCUT = F
    ABORT_ON_DUPLCID  = F

    CUTWIN_NEPOCH    =  5
    CUTWIN_REDSHIFT  =  0.05, 1.2
    CUTWIN_REDSHIFT_ERR =  0.0, 0.01
    CUTWIN_TREST     = -20.0,   60.0
    cutwin_Trestmin  = -9999.0   5.0
    cutwin_Trestmax  = 5.   99999.
    CUTWIN_MWEBV     = 0.0 0.25
    CUTWIN_SNRMAX       =  5.0, 1.0E8   ! SNRMAX > 5 ...
    CUTWIN_NFILT_SNRMAX =  2.0, 99.     ! in at least 2 bands
    CUTWIN_PSF = 0.5, 2.75
    CUTWIN_ZPNPE = 30.5, 100.  ! cut on ZP in Npe
&END
&FITINP
    FILTLIST_FIT        = 'griz'
    ! loose priors to avoid crazy fit
    PRIOR_MJDSIG       = 10        ! Gauss prior on initial PEAKMJD estimater
    DELCHI2_REJECT    = 10         ! reject obs with chi2_obs>10 on 1st fit iteration
    FUDGEALL_ITER1_MAXFRAC = 0.05 ! add .05*Fpeak error on 1st iteration (for stability)
&END
```

Code Block 2.29: `FITOPTS` files used by the DES-SN5YR light curve fits. The file defines variations to the nominal `LCFIT` which account for various systematic uncertainties. The number preceding each `FITOPT` definition is a scaling factor equal to $\mathcal{W}_S$, the systematic scaling factor described in `CREATECOV`.

```
GLOBAL:
  CALSPEC: "1.0 MAGOBS_SHIFT_ZP_PARAMS 0 0.00714 0"
  COLORLAW: "0.3 OPT_MWCOLORLAW 89 RV_MWCOLORLAW 3.0"
  MWEBV: "1.0 MWEBV_SCALE 0.95 MWEBV_SHIFT 0.00"
  cal_1: "0.3 FITMODEL_NAME
    ↪ '$SNDATA_ROOT/models/SALT3/SALT3.DES5YR-SYS/SALT3.MODEL001'"
  cal_2: "0.3 FITMODEL_NAME
    ↪ '$SNDATA_ROOT/models/SALT3/SALT3.DES5YR-SYS/SALT3.MODEL002'"
  cal_3: "0.3 FITMODEL_NAME
    ↪ '$SNDATA_ROOT/models/SALT3/SALT3.DES5YR-SYS/SALT3.MODEL003'"
  cal_4: "0.3 FITMODEL_NAME
    ↪ '$SNDATA_ROOT/models/SALT3/SALT3.DES5YR-SYS/SALT3.MODEL004'"
  cal_5: "0.3 FITMODEL_NAME
    ↪ '$SNDATA_ROOT/models/SALT3/SALT3.DES5YR-SYS/SALT3.MODEL005'"
  cal_6: "0.3 FITMODEL_NAME
    ↪ '$SNDATA_ROOT/models/SALT3/SALT3.DES5YR-SYS/SALT3.MODEL006'"
  cal_7: "0.3 FITMODEL_NAME
    ↪ '$SNDATA_ROOT/models/SALT3/SALT3.DES5YR-SYS/SALT3.MODEL007'"
  cal_8: "0.3 FITMODEL_NAME
    ↪ '$SNDATA_ROOT/models/SALT3/SALT3.DES5YR-SYS/SALT3.MODEL008'"
  cal_9: "0.3 FITMODEL_NAME
    ↪ '$SNDATA_ROOT/models/SALT3/SALT3.DES5YR-SYS/SALT3.MODEL009'"
  zshift: "0.4 REDSHIFT_FINAL_SHIFT 0.0001"
```

2.3.3.2 `LCFIT` specific Pippin development

`LCFIT` requires as input SN light curves defined in a preceding `DATAPREP` or `SIM` `Stage`. Since the same `LCFIT` `Task` can be applied to multiple SN light curve samples, Pippin concatenates the name of the `DATAPREP` / `SIM` `Task` and the `LCFIT` `Task` to produce a unique `Task` name used in later `Stages`. This presents an issue however when attempting to utilise external `LCFIT` results to avoid unnecessary recalculations. If the concatenated name of the external `LCFIT` `Task` does not exactly match the concatenated name of the user's `LCFIT` `Task`, Pippin would be unable to determine which `LCFIT` `Task` should be associated with the external `LCFIT` `Task`. To address this, I developed a new `EXTERNAL_MAP` key, allowing the user to directly specify which external `LCFIT` `Task` to associate with each `LCFIT` `Task`.

2.3.4 `CLASSIFY` — Photometric Classification

For the preliminary DES[3] analysis, spectroscopic classification (Childress et al., 2017; Lidman et al., 2020; Yuan et al., 2015) was used to identify SNe Ia and non-Ia contaminants. By contrast, the DES[5] analysis utilises photometric classification techniques, both in response to the growing size of the DES sample, and as a proof of concept for future SN surveys such as LSST (Ivezić et al., 2019), which will deliver orders of magnitude larger SN samples for which spectroscopic follow-up is no longer viable.

The DES[5] analysis compares three photometric classification algorithms, SuperNNova (SNN; Möller and de Boissière, 2020), Supernova Classification with a Convolutional Neural Network (SCONE; Qu et al., 2021), and Supernova Identification with Random Forest (SNIRF; Kovacs, 2024). The principle analysis used SNN, with the choice of using either SCONE or SNIRF treated as systematic uncertainties. Each classifier provides a mechanism for determining the probability that a given SN is a type Ia (P_{Ia}), which is utilised in `BIASCOR` and in the cosmological fit.

2.3.4.1 SuperNNova

Underlying the SuperNNova photometric classifier is a Recurrent Neural Network (RNN), a class of neural network, which is well suited to sequential data, including SN light curves. In a traditional neural network, data is provided as the input to a network of nodes, structured as a series of layers. Each layer transforms the result of the previous layer non-linearly, ultimately resulting in a final output layer whose value represents the result of the network. In the case of photometric classifiers, this output is the likelihood that the input light curve is of a type Ia SN.

Unlike a traditional neural network (NN), which processes all data in a single pass, an RNN processes each observation in a light curve sequentially, storing the results of the previous observation to inform the processing of the next observation. Not only does this allow processing of light curves with varying epochs, the recursive feedback-loop inherent to RNNs allows the networks to retain or discard information from preceding epochs when determining the type Ia classification likelihood. This in turn allows for correlations between epochs over time to inform the classification process. SNN employs an additional improvement to RNNs which allows a statistically rigorous interpretation of uncertainty in the NN's classification probability. The training of traditional NNs involves optimising the values of the *weights* (node $\rightarrow$ node interaction) and *biases* (layer $\rightarrow$ layer interaction) which determine the functionality of a NN. Rather than treating each of these weights and biases as

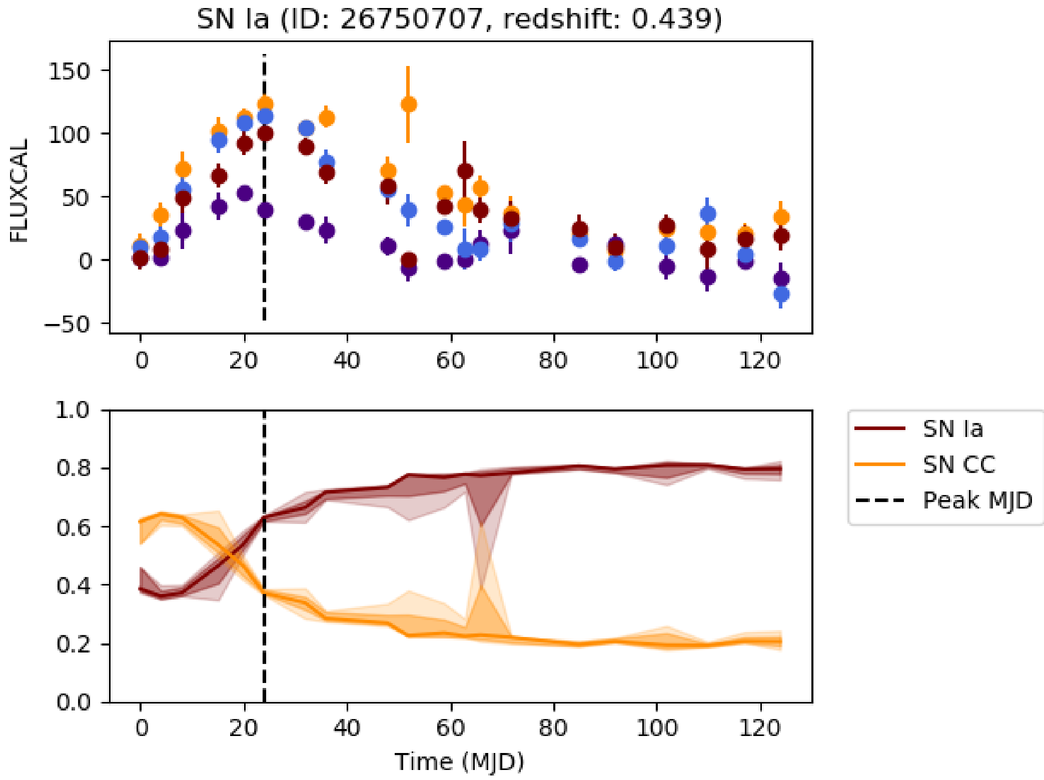

Figure 2.2: Example classification output using the SNN Bayesian RNN methodology. The probability that the given SN is a type Ia or CC supernova is shown in the lower panel, highlighting both the measurable classification uncertainty, and the improvements to the type Ia classification likelihood as more epochs are sequential processed by the RNN. Taken from the SNN Visualisation Walk-through.

a single value, SNN follows Fortunato et al. (2017) and instead optimises a posterior distribution for each weight and bias, allowing the contribution of each node to the overall classification uncertainty to be accurately measured (See Figure 2.2 for an example classification using this Bayesian RNN).

The Pippin configuration for SNN used in the DES[5] analysis is presented in Code Block 2.30. As Pippin integrates with many SN classifiers, `CLASSIFY` allows the user to choose between classifiers through the `CLASSIFIER` key. Each classifier provides both a 'train' and 'predict' `MODE`, which allows the user to train a model, and use a trained model for classification, respectively. Alongside the `CLASSIFIER` and `MODE` keys, each classifier has their own set of keys which modify various aspects of the training and classification process. In the case of SNN, these additional keys include:

- `GPU`: Whether the training or classification process should use GPU-acceleration. Only useful on extremely large datasets, like the `SIM` bias-correction samples.
- `NORM`: Control how light curves are normalised, choosing between a global (`cosmo`) or per-filter (`perfilter`) normalisation scheme. Normalising the input to a NN can lead to improvements in the overall accuracy[1] of the NN.
- `REDSHIFT`: Controls whether redshift information is provided to SNN when classifying SNe. Though SNN is capable of classifying SNe without any redshift information, its accuracy is greatly improved when this information is provided ($96.92 \pm 0.09\%$ accuracy without redshift $\rightarrow 99.55 \pm 0.06\%$ accuracy with redshift).
- `VARIANT`: Whether to use the traditional RNN (`VARIANT: "vanilla"`) or the Bayesian RNN (`VARIANT: "bayesian"`) discussed previously.

Finally, three SNN models were produced after training on three different core-collapse templates, Vincenzi et al. (2019), Jones et al. (2017), and core-collapse templates from DES data (Hounsell et al. in prep.). The variation in classification probability from each of these models is treated as a source of systematic uncertainty.

[1] Defined as the number of correct predictions relative to the number of total predictions.

Code Block 2.30: Pippin configuration for the SuperNNova classifier.

```
CLASSIFICATION:
  GLOBAL:
    CLASSIFIER: "SuperNNovaClassifier"
    GPU: False
    MASK: "DATADES"
    MODE: "predict"
    OPTS:
      BATCH_REPLACE:
        REPLACE_MEM: "4GB"
        REPLACE_WALLTIME: "01:00:00"
      NORM: "cosmo" # How to normalise LCs. Other options are "perfilter" or "cosmo".
      REDSHIFT: True # Use redshift info when classifying. Defaults to True.
      VARIANT: "vanilla" # or "variational" or "bayesian". Defaults to "vanilla"
  SNNTESTDESCC_z_data:
    OPTS:
      MODEL: "$SNDATA_ROOT/models/classifiers/DES-SN5YR/SNNTRAINDESCC_z_TRAINDES_DESCC/model.pt"
  SNNTESTJ17_z_data:
    OPTS:
      MODEL: "$SNDATA_ROOT/models/classifiers/DES-SN5YR/SNNTRAINJ17_z_TRAINDES_J17/model.pt"
  SNNTESTV19_z_data:
    OPTS:
      MODEL: "$SNDATA_ROOT/models/classifiers/DES-SN5YR/SNNTRAINV19_z_TRAINDES_V19/model.pt"
```

2.3.4.2 SCONE

SCONE performs photometric classification utilising a Convolutional Neural Network, a machine learning algorithm typically used in image recognition applications. To accomplish this, each SN light curve is transformed via a Gaussian process model to produce an MJD-wavelength-flux heat-map. These heat-maps are then processed with the CNN to classify the SN. In contrast to traditional NN, the weights and biases of a CNN are convolution matrices which transform the heat-maps and extract features which ultimately lead to a classification likelihood. SCONE is trained purely on photometric data, achieving a classification accuracy of $99.73 \pm 0.26\%$ without redshift information. Whilst the accuracy of SCONE is impressive, the pre-processing step of transforming all light curves to heat-maps, in combination with the increased complexity inherent in training a CNN, makes SCONE a particularly expensive model to train and test.

Code Block 2.31: Pippin configuration for the SCONE classifier.

```
CLASSIFICATION:
  GLOBAL:
    CLASSIFIER: "SconeClassifier"
    GPU: False # --> set this to True if your testing sample is LARGE (e.g.
     ↪ if your testing sample is a BiasCor simulation)
    MASK: "DATADES"
    MODE: "predict"
    OPTS:
      BATCH_REPLACE:
        REPLACE_MEM: "20GB"
        REPLACE_WALLTIME: "01:00:00"
  SCONETESTV19_z_data:
    MODEL: "$SNDATA_ROOT/models/classifiers/DES-SN5YR/SCONEV19"
    TRAINED_MODEL: "$SNDATA_ROOT/models/classifiers/DES-SN5YR/SCONEV19"
```

2.3.4.3 SNIRF

Unlike SNN and SCONE, SNIRF utilises a non-NN based machine learning technique known as Random Forest (RF). This technique recursively subdivides the data into a set of 'Decision Trees'. User-determined features of the data are used to subdivide data into increasingly specific classes, building a tree structure from these subdivisions. For example a SN may have x_1 greater or lesser than 1, $\mathcal{C}$ greater or lesser than 0, and redshift greater or lesser than 0.1. Each of these features forms a branch in the decision tree, with the final branch being whether the SN is a type Ia, or CC SNe. The training involves determining the probability associated with each possible traversal of the decision tree. To avoid over-fitting and improve accuracy, RF models involve building and training many decision trees, and determining the classification likelihood by averaging over the result of each tree.

RF models have the advantage of being extremely fast to train, whilst also avoiding typical pitfalls of traditional NNs, in particular over-fitting. The main disadvantage of the RF technique is that it requires supervised learning, requiring the user to determine the best features of the data to use for classification.

Code Block 2.32: Pippin configuration for the SNIRF classifier.

```
CLASSIFICATION:
  GLOBAL:
    CLASSIFIER: "SnirfClassifier"
    MASK: "DATADES"
    MODE: "predict"
  SNIRFTESTV19_data:
    OPTS:
      MODEL: "$SNDATA_ROOT/models/classifiers/DES-SN5YR/
      ↪ SNIRFTRAIN_V19_T_TRAINDES_V19/model.pkl"
```

2.3.4.4 `CLASSIFY` specific Pippin development

Owing to the flexibility of the `CLASSIFY` `Stage`, much of my development involved working directly with the developers of SNN, SCONE, SNIRF, and other classifiers, to integrate any changes to these classifiers into Pippin. In particular, between the DES[3] and DES[5] analyses, the SCONE classifier was built and integrated into Pippin for the first time. Additionally, both SCONE and SNN underwent significant refactorisations which required major changes to Pippin. To ensure backwards-compatibility, I developed automatic detection of pre- and post-refactor configurations.

2.3.5 `BIASCOR` — Observational Bias and Core-collapse Contamination

The `BIASCOR` `Stage` is responsible for producing a Hubble Diagram (HD) which is corrected for observational bias, non-Ia contamination, with accurate measurements of the statistical uncertainty, and a cosmologically-independent fit to the global scale factors (α and β). The end result is an HD which can used for cosmological constraints, independently of the remaining Pippin pipeline.

`BIASCOR` implements BEAMS with Bias Correction (BBC; Kessler and Scolnic, 2017), an extension to the Bayesian Estimation Applied to Multiple Species (BEAMS; Kunz et al., 2012) framework which incorporates both the SALT2mu method presented in Marriner et al. (2011) for independently constraining the global scale factors, and the modelling and correction of selection effects which lead to observational biases.

The foundation of the BEAMS framework is the construction of a likelihood function which models both the probability of a given SN being a type Ia, and the probability of observing that SN given some assumption about the underlying population of type Ia, and core-collapse SNe.

$$\mathcal{P}^i_{\mathrm{BEAMS}} = \frac{\mathcal{L}^i_{\mathrm{Ia}}}{\mathcal{L}^i_{\mathrm{Ia}} + \mathcal{L}^i_{\mathrm{CC}}} \tag{2.5}$$

$$\mathcal{L}^i_{\mathrm{Ia}} = P^i_{\mathrm{Ia}} \times D^i_{\mathrm{Ia}}(z_i, \mu_i, \mu_{\mathrm{ref}}) \tag{2.6}$$

$$\mathcal{L}^i_{\mathrm{CC}} = \left(1 - P^i_{\mathrm{Ia}}\right) \times D^i_{\mathrm{CC}}(z_i, \mu_i, \mu_{\mathrm{ref}}) \tag{2.7}$$

Here, P_{Ia} is the type Ia classification likelihood determined in `CLASSIFY`, and D_{Ia} and D_{CC} are the likelihood of observing a type Ia / CC SN with the given redshift and distance modulus, assuming some reference cosmology μ_{ref}. The choice of μ_{ref} is arbitrary, and is typically set to ΛCDM with $\Omega_{\mathrm{M}} = 0.3$. D_{CC} is determined from detailed simulations of four classes of contaminant SNe — SN Iax, 91bg-like, stripped-envelope, and hydrogen-rich CC SNe (Vincenzi et al., 2019). Once a reference cosmology is defined, D_{Ia} is calculated as:

$$D^i_{\mathrm{Ia}} = \exp\left(-\frac{\left(\mu_i + M_\zeta - \mu_{\mathrm{ref}}(z_i)\right)^2}{\sigma^2_{\mu,i}}\right) \tag{2.8}$$

Here, M_ζ is the average difference between μ_i (defined in Equation (2.3)) and μ_{ref} in ζ redshift bins. For the DES[5] analysis, 20 redshift bins were used, evenly distributed in log-space. The M_ζ offsets serve to encapsulate the *cosmological error* in the arbitrary reference cosmology, effectively correcting for the fact that the reference cosmology is very likely not the true cosmology. This in turn allows for a cosmologically independent fit to the α and β global scale factors. Given the expression for μ_i defined in Equation (2.3), α and β can be constrained by maximising $\mathcal{P}_{\mathrm{BEAMS}}$, and thus minimising the difference between μ_i and $\mu_{\mathrm{ref}}(z_i) - M_\zeta$ for all SNe[1].

An important component of Equation (2.3) which is calculated in `BIASCOR` is the $\Delta\mu_{\mathrm{bias}}$ term, which corrects for systematic shifts in the Hubble Diagram caused by biases in the observed sample owing to survey limitations, which induce a preference for observing nearer, brighter SNe (See Figure 2.3 for an explanatory diagram).

[1] This is the SALT2mu technique described in Marriner et al. (2011)

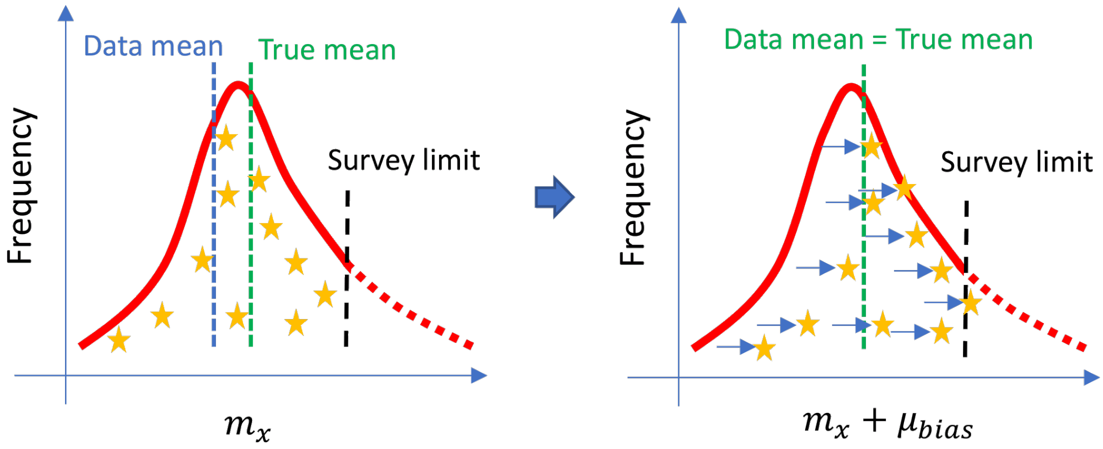

Figure 2.3: BIASCOR is responsible for calculating the $\Delta\mu_{\rm bias}$ term which corrects for a systematic shift in the Hubble Diagram, caused by survey limitations which cause a biased preference for observing brighter SNe. This diagram highlights the effect of this observational bias, and the role of $\Delta\mu_{\rm bias}$. This diagram was taken from Figure 2 of Vincenzi et al. (in prep.), a response to criticisms of the DES[5] analysis presented in Efstathiou (2024).

Calculating $\Delta\mu_{\rm bias}$ requires simulating and fitting large (~10× the data sample size) simulated survey samples with known $\alpha^{\rm true}$, $\beta^{\rm true}$, $\gamma^{\rm true}$, $\mathcal{M}^{\rm true}$, and $\mu^{\rm true}$ values. Comparing these known values with those produced in LCFIT enables the calculation of $\Delta\mu_{\rm bias}$:

$$\Delta\mu_{\rm bias} = m + \alpha^{\rm true}x_1 - \beta^{\rm true}\mathcal{C} + \gamma^{\rm true}G_{\rm host} - \mathcal{M}^{\rm true} + \mu^{\rm true} \tag{2.9}$$

Following the calculation of μ_i for each SN in the sample, the statistical uncertainty in the distance modulus can also be calculated as:

$$\sigma^2_{\mu,i} = f(z_i, \mathcal{C}_i, \mathcal{M}_i)\sigma^2_{\rm S3fit,i} + \sigma^2_{\rm floor}(z_i, \mathcal{C}_i, \mathcal{M}_i) + \sigma^2_{z,i} + \sigma^2_{{\rm vpec},i} + \sigma^2_{{\rm lens},i} \tag{2.10}$$

where,

- $f(z_i, \mathcal{C}_i, \mathcal{M}_i)$ and $\sigma^2_{\rm floor}(z_i, \mathcal{C}_i, \mathcal{M}_i)$ are factors that ensure the reduced χ^2 between μ_i and $\mu_{\rm ref}(z_i) - M_\zeta$ is close to one. These terms are determined from the same bias-correction simulations used to calculate $\Delta\mu_{\rm bias}$. $f \leq 1$ accounts for an overestimation of the SALT3 light curve fit uncertainty due to the observational biases previously discussed. $\sigma^2_{\rm floor} = \sigma^2_{\rm scatter}(z_i, \mathcal{C}_i, \mathcal{M}_i) + \sigma^2_{\rm gray}$ accounts for additional scatter which is not already included in the other uncertainty terms. The gray term is a global uncertainty term which is computed such that the reduced χ^2 of the BBC fit is one. If $f < 1$, then $\sigma_{\text{floor}} = 0$ to ensure all covariances are positive, otherwise $f = 1$ and σ_{floor} is included (See Vincenzi et al., 2024, for more details).

- $\sigma_{\text{S3fit},i} = (\sigma_m)^2 + (\alpha\sigma_{x_1})^2 + (\beta\sigma_{\mathcal{C}})^2 + 2\alpha\sigma_m^{x_1} - 2\beta\sigma_m^{\mathcal{C}} - \alpha\beta\sigma_{x_1}^{\mathcal{C}} + 2$: where σ_x^y is the covariant uncertainty between x and y.
- $\sigma^2_{z,i}$ is the uncertainty in redshifts determined from host-galaxy spectroscopic follow-up.
- $\sigma^2_{\text{vpec},i}$ is the uncertainty in the peculiar velocity measurements.
- $\sigma^2_{\text{lens},i}$ is the uncertainty induced by weak lensing.

During the DES[3] analysis, the redshift-binned HD produced by BBC was used directly for fitting cosmological constraints; however, as shown by Brout et al. (2021), this binned approach introduced a systematic bias in w. Kessler et al. (2023) extended this work to show that an unbinned, bias-free HD can be produced by scaling $\sigma_{\mu,i}$ by $\mathcal{S}_\zeta/\sqrt{\mathcal{P}_{\text{BEAMS}}}$ where $\mathcal{S}_\zeta$ is a per-redshift bin (ζ) scale factor which is calculated to ensure the weighted average uncertainty in each bin is equal to the uncertainty in the BBC offset M_ζ:

$$\frac{1}{\sigma^2_{M_\zeta}} = \sum_{i\in\zeta} \frac{\mathcal{P}_{\text{BEAMS},i}}{(\mathcal{S}_\zeta\sigma_{\mu,i})^2} \tag{2.11}$$

Kessler et al. (2023) also provide a method of *re-binning* the HD into redshift, x_1, $\mathcal{C}$ bins which allow for the improved computational efficiency of a binned HD without introducing additional biases.

2.3.5.1 DES[5] `BIASCOR` configuration

In addition to producing the bias-corrected HD, `BIASCOR` is also responsible for implementing a number of systematic variations to the nominal analysis, enabling the measurement of the scale of systematic uncertainty in `CREATECOV`. These variations are implemented as `MUOPTS` and are analogous to the `FITOPTS` from `LCFIT`. For each `MUOPT`, a new HD is produced with the associated systematic variation implemented. The difference between the new HD and the initial (nominal) HD provides a measure of the expected scale of the associated systematic. Within the DES[5] analysis (the configuration for which is presented in Code Blocks 2.9 and 2.33) the systematics being accounted for include[1]:

- `ALPHAEVOL`: Allow α to have a dependence on redshift.

[1] Which keys are associated with which variations is a poorly documented feature of SNANA, though is available in comments at the top of the SALT2mu.c SNANA file

- `BETAEVOL` : Allow β to have a dependence on redshift.
- `GAMMAEVOL` : Allow γ to have a dependence on redshift.
- `CC_PRIOR_H11` : Change the prior on $D_{\rm CC}$ from Vincenzi et al. (2019) to a polynomial function as in Hlozek et al. (2012).
- `CC_SCONE` : Use $P_{\rm Ia}$ as determined by SCONE instead of SNN.
- `CC_SNIRF` : Use $P_{\rm Ia}$ as determined by SNIRF instead of SNN.
- `CC_SNNDESCC` : Use $P_{\rm Ia}$ as determined by SNN trained on Hounsell et al. (in prep.) instead of Vincenzi et al. (2019).
- `CC_SNNJ17` : Use $P_{\rm Ia}$ as determined by SNN trained on Jones et al. (2017) instead of Vincenzi et al. (2019).
- `MASSSEPLOC` : Shift the location of the host-galaxy mass step from $P_{\rm step} = 10^{10} M_\odot$ to $P_{\rm step} = 10^{10.2} M_\odot$

The rest of the options in `BIASCOR` determine the nominal analysis, including what data to include (`DATA`), what classification probability to use (`CLASSIFIER`), what simulations to use for bias-correction (`SIMFILE_BIASCOR` , and `SIMFILE_CCPRIOR`), and various details specific to the BBC / SALT2mu fits.

Code Block 2.33: The Pippin configuration of `BIASCOR` for the DES[5] analysis

```
NOMINAL:
  BASE: "$DES5YR/base/SALT2mu_5yr.input"
  CLASSIFIER: "PROB_SNNV19"
  CONSISTENT_SAMPLE: True
  DATA: ["Dsys_DATADES5YRSMP", "Fsys_DATAFOUND", "Lsys_DATALOWZ"]
  MUOPTS:
    ALPHAEVOL:
      OPTS:
        u3: 1
        !!merge <<: *no_chi2max
    BETAEVOL:
      OPTS:
        u4: 1
        !!merge <<: *no_chi2max
    CC_PRIOR_H11:
      CLASSIFIER: "PROB_SNNV19"
      OPTS:
        simfile_ccprior: "H11"
        u17: 1
        u20: 1
        !!merge <<: *no_chi2max
    CC_SCONE:
      CLASSIFIER: "PROB_SCONE"
      OPTS:
        !!merge <<: *no_chi2max
    CC_SNIRF:
      CLASSIFIER: "PROB_SNIRFV19"
      OPTS:
        !!merge <<: *no_chi2max
    CC_SNNDESCC:
      CLASSIFIER: "PROB_SNNDESCC"
      OPTS:
        !!merge <<: *no_chi2max
    CC_SNNJ17:
      CLASSIFIER: "PROB_SNNJ17"
      OPTS:
        !!merge <<: *no_chi2max
    GAMMAEVOL:
      OPTS:
        u6: 1
        !!merge <<: *no_chi2max
    MASSSTEPLOC:
      OPTS:
        p7: 10.2
        !!merge <<: *no_chi2max
  OPTS:
    BATCH_MEM: 32000
    !!merge <<: [*apply_chi2max, *batchinfo20, *bbc4d_sigint_color,
  ↪   *bbc_general]
  SIMFILE_BIASCOR: ["D3_BIASCORSIM_DES", "F3_BIASCORSIM_FOUND",
  ↪   "L3_BIASCORSIM_LOWZ"]
  SIMFILE_CCPRIOR: "D3_BIASCORSIM_DESCC"
```

Code Block 2.34: Aliases used by the DES[5] `BIASCOR` configuration.

```
ALIAS:
  APPLY_CHI2MAX: &apply_chi2max
    chi2max: 16
  BATCHINFO20: &batchinfo20
    BATCH_INFO: "sbatch $SBATCH_TEMPLATES/SBATCH_Midway2b.TEMPLATE 20"
  BBC4D_SIGINT_COLOR: &bbc4d_sigint_color
    nbin_logmass: 2
    opt_biascor: 4336
    sig1: 0.01
    u2: 3
  BBC_GENERAL: &bbc_general
    CUTWIN_FITPROB: "0.001 1.1"
    CUTWIN_cERR: "0 1.5"
    cid_reject_file: "/project2/rkessler/SURVEYS/DES/ROOT/analysis_photoIa_5yr/base/exclude_SN_zSN.txt"
    fieldGroup_biascor: "X3,C3,X1+X2,S1+S2,E1+E2+C1+C2"
    fitflag_sigmb: 2
    iflag_duplicate: 0
    interp_biascor_logmass: 0
    logmass_max: 35
    logmass_min: -15
    ndump_nobiascor: 500
    p1: 0.150 # same value as sims
    p10: 0.0
    p11: -1.0
    p12: 0.0
    p2: 2.87
    p5: 0.00001
    p8: 0.001
    p9: 0.685
    surveygroup_biascor: "CFA1+CFA2+CFA3S+CFA3K+CFA4p1+CFA4p2+CSP(zbin=0.02),FOUNDATION(zbin=0.02),DES(zbin=0.075)"
    u5: 1
    zmin: 0.025
  NO_CHI2MAX: &no_chi2max
    chi2max: 10000000
BIASCOR:
```

2.3.5.2 `BIASCOR` specific Pippin developments

Owing to the numerous dependencies between `BIASCOR` and previous `Stages`, much of the `BIASCOR` development occurred in previous `Stages`, preparing data for use in the BBC method. One useful feature which I implemented was the ability to specify `SIMFILE_BIASCOR_FITOPTS` and `SIMFILE_CCPRIOR_FITOPTS`, allowing control over which `FITOPTS` are associated with which simulations. This was used by Chen et al. (2024) to investigate the impact of cosmological biases when using photometric — rather than spectroscopic — redshifts.

2.3.6 `CREATECOV` — Determining the Systematic Covariance Matrix

The penultimate `Stage` of the DES[5] analysis, `CREATECOV` provides a robust measure of the uncertainty inherent to the analysis, in the form of an $N_{\text{SNe}} \times N_{\text{SNe}}$ covariance matrix $\mathbf{C} = \mathbf{C}_{\text{stat}} + \mathbf{C}_{\text{sys}}$, where $\mathbf{C}_{\text{stat}}$ is a diagonal matrix representing the statistical uncertainty σ_μ^2 for each SNe, as calculated in `BIASCOR`, and $\mathbf{C}_{\text{sys}}$ is the covariant systematic uncertainty *between* each SN in the analysis. Each term of $\mathbf{C}_{\text{sys}}$ is calculated as:

$$\mathbf{C}_{\text{sys}}^{i,j} = \sum_{\mathcal{S}=1}^{N_{\mathcal{S}}} \left(\Delta\mu_i^{\mathcal{S}}\right)\left(\Delta\mu_j^{\mathcal{S}}\right)\mathcal{W}_{\mathcal{S}}^2 \tag{2.12}$$

Here, $\mathcal{S}$ is a particular systematic, of which there are $N_{\mathcal{S}} = N_{\texttt{FITOPTS}} + N_{\texttt{MUOPTS}}$[1]. $\Delta\mu_i^{\mathcal{S}}$ is then the difference in the ith SN's distance modulus between the nominal HD, and the HD which includes the systematic $\mathcal{S}$. Each $\mathcal{S}$ also has an associated scaling factor $\mathcal{W}_{\mathcal{S}}$, used to de-weight systematics which are typically subcomponents of an overall systematic source. Examples of systematics with $\mathcal{W}_{\mathcal{S}} \neq 1$ are:

- $\mathcal{S} =$ `cal_{1-9}`: The 10 SALT3 realisations used as `FITOPTS` to account for systematic uncertainties in the SALT3 training. Each realisation is treated as its own systematic, and de-weighted with $\mathcal{W}^2_{\mathcal{S}=\texttt{cal\_\{1-9\}}} = 1/10$ so that when added in quadrature, their total contribution is effectively 1.
- $\mathcal{S} =$ `COLORLAW`: The nominal analysis uses the Fitzpatrick (1999) Milky Way reddening law with $R_v = 3.1$. An alternative considered as a systematic is the Cardelli et al. (1989) reddening law with $R_v = 3.0$. Schlafly et al. (2010) showed that this alternative was the second-most preferred model by the data with a $\chi^2 \approx 5/3$ that of the Fitzpatrick (1999) model. Setting $\mathcal{W}^2_{\mathcal{S}=\texttt{COLORLAW}} = (3/5)^2 \approx 1/3$ accounts for this data preference.
- $\mathcal{S} =$ `ZSHIFT`: Following Calcino and Davis (2017), a global redshift shift

[1] $N_{\mathcal{S}} = \left(N_{\texttt{FITOPTS}} \equiv 13\right) + \left(N_{\texttt{MUOPTS}} \equiv 9\right) = 22$ for the DES[5] analysis

of 4×10^{-5} is considered as a systematic to account for the possibility of local voids or other systematic redshift errors. This systematic is weighted by $\mathcal{W}_{\mathcal{S}=\texttt{ZSHIFT}} = {}^{1}\!/_{6} \approx 0.4^2$, as this allowed the SNANA program to shift the redshifts by 10^{-4}, and scale the effect of that shift by 0.4 — an equivalent process to shifting the redshifts by 4×10^{-5} which is more computationally efficient.

Code Block 2.35: Configuration of `CREATECOV` used in the DES[5] analysis.

```
CREATE_COV:
  COV_SYST:
    MASK: "NOMINAL"
    OPTS:
      BATCH_INFO: "sbatch $SBATCH_TEMPLATES/SBATCH_Midway2b.TEMPLATE 5"
      BINNED: False
      COVOPTS:
        - "[ALPHAEVOL] [=DEFAULT,=ALPHAEVOL]"
        - "[BETAEVOL] [=DEFAULT,=BETAEVOL]"
        - "[CALSPEC] [=CALSPEC,=DEFAULT]"
        - "[CAL_SALT2] [+cal,=DEFAULT]"
        - "[CCPRIOR_H11] [=DEFAULT,=CC_PRIOR_H11]"
        - "[COLORLAW] [=COLORLAW,=DEFAULT]"
        - "[GAMMAEVOL] [=DEFAULT,=GAMMAEVOL]"
        - "[MASSLOC] [=DEFAULT,+MASS]"
        - "[MWEBV] [=MWEBV,=DEFAULT]"
        - "[NOSYS] [=DEFAULT,=DEFAULT]"
        - "[SCONE] [=DEFAULT,=CC_SCONE]"
        - "[SNIRF] [=DEFAULT,=CC_SNIRF]"
        - "[SNN] [=DEFAULT,+CC_SNN]"
        - "[ZSHIFT] [=zshift,=DEFAULT]"
      SUBTRACT_VPEC: False
```

An important observation of Equation (2.12) is that there is no covariant interaction *between* systematic sources, i.e. there is an underlying assumption that all systematics are *independent* of each other. In Section 4.2.1 I investigate possible solutions to removing this assumption.

Specifying each systematic $\mathcal{S}$ (called a `COVOPT` in the configuration file) uses the syntax: `[COVOPT_NAME] [FITOPT_NAME,MUOPT_NAME]`. This specified that the `COVOPT_NAME` systematic uses the `FITOPT_NAME` `FITOPT`, and the `MUOPT_NAME` `MUOPTS`. To use the nominal parameters instead, both `FITOPT_NAME` and `MUOPT_NAME` can be set to `DEFAULT`. Each name must also be prepended with either `=` (exact match), `+` (partial match), or `-` (partial inverse match). Some example `COVOPTS` are as follows (see Code Block 2.35 for all `COVOPTS` used in the DES[5] analysis):

- `[NOSYS] [=DEFAULT,=DEFAULT]`: Use nominal analysis with no systematic uncertainty
- `[CAL_SALT2] [+cal,=DEFAULT]`: Use all `FITOPTS` whose name contains `cal`. This matches the $\mathcal{S} =$ `cal_{1-9}` SALT surfaces.
- `[SNN] [=DEFAULT,+CC_SNN]`: Use all alternative SuperNNova `MUOPTS`, i.e. those trained on Jones et al. (2017), and Hounsell et al. (in prep.).

2.3.6.1 `CREATECOV` Specific Pippin Development

Between the DES[3] and DES[5] analyses, I developed many improvements to `CREATECOV`, including integration into SNANA's `submit_batch` program, implementations of the re-binning method described in Kessler et al. (2023), and the introduction of a new `SYSTEMATIC_HD` option which produces a full HD for each systematic, rather than simply calculating the difference between the systematic HD and the nominal HD. I use this feature in Section 4.2.1 to investigate various alternative statistical techniques, and their effectiveness in accurately measuring systematic uncertainties in cosmological analyses.

2.3.7 `COSMOFIT` — Cosmology

The final `Stage` of Pippin takes the HD and systematic covariance matrix calculated in the previous `BIASCOR` and `CREATECOV` `Stages`. During the DES[3] analysis, cosmological constraints were computed using the CosmoMC program (Moshafi and Bahraminasr, 2018). Since then, a number of new cosmological fitters have been developed, including the SNANA `wfit.exe` program, a '*quick-and-dirty*' cosmological fitter, useful for systematic analyses and tests, and CosmoSIS (Zuntz et al., 2015), a modular cosmological fitter which provides in depth tools for constraining cosmological parameters using multiple cosmological probes.

To allow Pippin to utilise these new technologies, I completely refactored `COSMOFIT` to behave similarly to `CLASSIFY`, in that the same `Stage` can be used to run multiple underlying programs. In the case of `COSMOFIT`, this modularity allows the user to choose between `wfit.exe`, and CosmoMC, with CosmoSIS integration planned for the future. As can be seen in Code Block 2.36, choosing a cosmological fitter simply requires specifying the name of the fitter before any of the other options[1].

[1] In Section 4.3 I discuss the importance this modularity will have in future analyses, and my plans to improve the modularity of the Pippin pipeline for future cosmological surveys.

Code Block 2.36: The `COSMOFIT` configuration for the DES[5] analysis

```
COSMOFIT:
  WFIT:
    SN_CMB_OMW: # CMB prior as in Planck et al 2020
      MASK: "COV"
      OPTS:
        BATCH_INFO: "sbatch $SBATCH_TEMPLATES/SBATCH_Midway2b.TEMPLATE 20"
        WFITOPTS: ["/cmb18_pri/ -cmb_sim -sigma_Rcmb 0.0057 -speed_flag_chi2
      ↪ 2 -wsteps 801 -ommin 0.2 -ommax 0.4 -omsteps 501"]
    SN_NOPRIOR_OMW:
      MASK: "COV"
      OPTS:
        BATCH_INFO: "sbatch $SBATCH_TEMPLATES/SBATCH_Midway2b.TEMPLATE 20"
        WFITOPTS: ["/omw_nopri/ -wsteps 501 -ommin 0.0 -ommax 1.0 -omsteps
      ↪ 501 -speed_flag_chi2 2 -ompri 0.315 -dompri 10"]
```

2.4 Pippin's Usage Beyond the DES-SN5YR Analysis

Though most of Pippin's development has been directed at improving its use within the DES-SN5YR analysis, the improvements I've made to the modularity, flexibility, and ease-of-use of Pippin have seen its use outside the DES-SN5YR analysis grow rapidly.

2.4.1 Surveys

One area in which Pippin's improved usability is most obvious is the numerous non-DES surveys which also chose to use Pippin as their primary analysis pipeline.

2.4.1.1 Pantheon+

The Pantheon+ analysis (Brout et al., 2022a; Scolnic et al., 2022) was released between the DES-SN3YR and DES-SN5YR analyses, and served as an important validation test for many of the techniques introduced to the DES analysis following DES-SN3YR — in particular the improvements to dust modelling (Popovic et al., 2021), cross-calibration (Brout et al., 2022b), and binned HD biases (Brout et al., 2021).

The Pantheon+ survey is a compilation of 18 surveys totalling 1550 spectroscopically classified SNe Ia. Combining both the statistical weight of a sample of this size, with the improvements made to the handling of systematic uncertainties, Pantheon+ provided impressive constraining power, finding Flat wCDMconstraints of $\Omega_M = 0.316^{+0.005}_{-0.008}$, and $w = -0.978^{+0.024}_{-0.031}$ when combined with Planck and BAO data.

Pippin was used throughout the Pantheon+ analysis with my efforts to integrate the updated analysis techniques into Pippin directly contributing to the survey's results.

Brout et al. (2019b) highlighted some limitations to Pippin in the Pantheon+ analysis; to quote:

> *The Pippin framework (Hinton and Brout, 2020), used extensively in this work, was intentionally developed to automate and asynchronise this multistep type of analysis; however, it has yet to incorporate aspects such as the SALT2 retraining (Taylor et al., 2021) or population fitting (Popovic et al., 2021).* **Likely, this framework will need to expand for future analyses.**[1]

I discuss these limitations and my plans for improving them in Section 4.3.

2.4.1.2 DEHVILS

The Dark Energy, H_0, and peculiar Velocities using Infrared Light from Supernovae (DEHVILS[2]; Peterson et al., 2023) survey presents a cosmological analysis of 83 SNe with high-quality, near infrared light curves. This region of wavelength space is poorly sampled relative to the optical[3], but has distinct advantages over optical SN light curves. Chief among these is the minimal impact of dust on SN luminosity, making these SNe nearer to true standard candles than their optical counterparts. As many of the tools used throughout a cosmological analysis had been constructed for use with optical data, the flexibility provided by Pippin was invaluable. For example, when fitting the SN light curves with SALT3, an extended model was used which was trained on an additional 166 light curves with data in the near-infrared (SALT3-NIR; Pierel et al., 2022) — integrating this model into the overall analysis simply required changing a single key in the `LCFIT` configuration.

2.4.1.3 Amalgame

The Amalgame survey (Popovic et al., 2024) combines photometrically classified SNe from the SDSS and Pan-STARRS surveys. This combined sample was

[1] Emphasis mine
[2] Gotta love astronomy acronyms...
[3] ~2000 optical supernovae compared to ~200 near-infrared SNe (Peterson et al., 2023).

analysed *without* a low-redshift anchor to investigate the viability of purely photometric cosmological analyses, including photometric estimates of both host galaxy redshifts and masses. To effectively evaluate the viability of photometric analyses, this paper makes use of many of the improvements to the handling of systematics and observational biases implemented in Pippin for the DES-SN5YR analysis.

2.4.2 Research

In addition to surveys using Pippin as an end-to-end cosmological analysis pipeline, improvements to Pippin has enabled using a subset of `Stages` to perform cosmological research. Some examples of the research conducted using Pippin include:

- Investigations into the cause of the mass step (Brout and Scolnic, 2021; Meldorf et al., 2022; Popovic et al., 2023; Rose et al., 2022).
- Systematic analyses, such as:
  - SuperCal-Fragilistic Cross Calibration (Brout et al., 2022b)
  - Redshift and Peculiar Velocities (Carr et al., 2022; Peterson et al., 2022)
  - Biases from Photometric Classification (Vincenzi et al., 2023)
  - Binning is Sinning (Brout et al., 2021)
  - Selection Efficiency and core-collapse contamination (Vincenzi et al., 2021)
  - redMaGiC Galaxies (Chen et al., 2022)
  - Host Galaxy Photometric Redshifts (Mitra et al., 2022)
  - Gray Photometric Zero-point Uncertainties (Brownsberger et al., 2023)
  - Host Galaxy Mismatch (Qu et al., 2024)
  - Beyond ΛCDM (Camilleri et al., 2024b)
- Understanding SN physics:
  - Rates and Delay Times (Wiseman et al., 2021)
  - SALT2/3 (Dai et al., 2023; Kenworthy et al., 2021; Taylor et al., 2023, 2021)
  - SN Ia subpopulation models (Taylor et al., 2024)

Chapter 3

Probing the Consistency of Cosmological Contours for Supernova Cosmology

Throughout the Dark Energy Survey's 5-year SN analysis (DES-SN5YR; DES Collaboration et al., 2024a; Vincenzi et al., 2024), great care was taken to ensure all cosmological parameter constraints from real data were blinded such that no cosmological constraints could be inferred before the blind was lifted. As discussed in Section 1.3.8, blinding an analysis serves to reduce the impact of the unconscious bias of researchers performing the analysis. Prior to unblinding, a number of criteria were chosen which the data and analysis pipeline must pass (Vincenzi et al., 2024). These include:

- Accurate simulations: Requires that the reduced χ^2 between the data and simulations across a number of observables, including redshift, SALT3 parameters, SALT3 goodness of fit, maximum signal-to-noise ratio at peak, and host stellar mass, is between 0.7 and 3.0.
- Pipeline validation: Requires that the Pippin pipeline (discussed in detail in Chapter 2) recovers input cosmologies without introducing bias. This is determined by simulating 25 data sized samples assuming a Flat ΛCDM model with Ω_M equal to the best-fit Planck value. Each of these simulated samples are analysed using the Pippin pipeline as if they were real data, and fit with a Flat wCDM model using a Planck prior. The bias of each sample is then the difference between the best fit w and the input $w_{\text{true}} = -1$. The mean bias across all 25 samples was found to be $w - w_{\text{true}} = 0.001 \pm 0.02$ which was deemed minimal enough to pass.
- Independent of reference cosmology: Requires that cosmological constraints are independent of the assumed cosmology used in bias correction (see Sections 2.3.2 and 2.3.5 for more details). This criterion was

tested and passed in Camilleri et al. (2024b).

- Validation of contours: Requires that the uncertainties in cosmological parameters produced by our pipeline are an accurate reflection of the true likelihood of each cosmological model.

As part of my thesis, I evaluated the final criterion — validation of contours. Alongside my collaborators, I developed a new statistical technique known as the 'Approximate Neyman construction' which optimised a Frequentist methodology known as the Neyman construction (Neyman, 1937) to perform a statistically rigorous check of the consistency of the Pippin pipeline. This new statistical technique was published alongside the DES-SN5YR criterion test in Armstrong et al. (2023), and is presented here.

This chapter is published in Publications of the Astronomical Society of Australia, Volume 40, article ID. e038 as Armstrong et al. (2023).

3.1 Abstract

As the scale of cosmological surveys increases, so does the complexity in the analyses. This complexity can often make it difficult to derive the underlying principles, necessitating statistically rigorous testing to ensure the results of an analysis are consistent and reasonable. This is particularly important in multi-probe cosmological analyses like those used in the Dark Energy Survey and the upcoming Legacy Survey of Space and Time, where accurate uncertainties are vital. In this paper, we present a statistically rigorous method to test the consistency of contours produced in these analyses, and apply this method to the Pippin cosmological pipeline used for type Ia supernova cosmology with the Dark Energy Survey. We make use of the Neyman construction, a Frequentist methodology that leverages extensive simulations to calculate confidence intervals, to perform this consistency check. A true Neyman construction is too computationally expensive for supernova cosmology, so we develop a method for approximating a Neyman construction with far fewer simulations. We find that for a simulated data-set, the 68% contour reported by the Pippin pipeline and the 68% confidence region produced by our approximate Neyman construction differ by less than a percent near the input cosmology; however, show more significant differences far from the input cosmology, with a maximal difference of 0.05 in Ω_{M} and 0.07 in w. This divergence is most impactful for analyses of cosmological tensions, but its impact is mitigated when combining supernovae with other cross-cutting cosmological probes, such as the Cosmic Microwave Background.

3.2 Introduction

For much of the history of supernova cosmology, parameter estimation was performed via Bayesian methods which maximise the likelihood by minimising a χ^2 function between the observed distance modulus of type Ia supernovae (SNe Ia) and the distance modulus predicted by cosmological theory.

This method of parameter estimation is shown in Equation 4 of Riess et al. (1998) and Equation 4 of Perlmutter et al. (1999), which detail the discovery of the accelerated expansion of the Universe using type Ia supernovae.

Since these early efforts, parameter estimation has expanded in complexity to account for additional systematic uncertainties (Conley et al., 2011), and to leverage large simulated data-sets to correct for contamination of core-collapse supernovae (Kunz et al., 2012), and observational biases (Kessler and Scolnic, 2017). This increased complexity is facilitated by cosmological pipelines to perform accurate parameter estimation. Due to the complex structure of modern cosmological pipelines, it is no longer possible to analytically define a likelihood function which describes the analysis being performed by these pipelines. As such, it is difficult to rigorously test the final cosmological contours produced by these cosmological pipelines, and to validate that the reported uncertainties are accurate.

There have been a number of attempts at developing alternative Bayesian frameworks which do not suffer from a non-analytic likelihood function. One such example is Approximate Bayesian Computation (ABC; Jennings and Madigan, 2017; Jennings et al., 2016), which uses realistic simulations to perform likelihood free parameter inference, at the cost of dramatically increased computation time due to the large number of simulations required. Another alternative Bayesian framework is Bayesian hierarchical models (BHM), which was implemented for supernova cosmology in (Steve; Hinton et al., 2019), (UNITY; Rubin et al., 2015), and (BayeSN; Mandel et al., 2021). BHMs utilise multiple layers of connected parameters, allowing for a more complex analytical likelihood function to be defined.

Though these alternative frameworks have significant advantages over the χ^2 minimisation methods, there has not been wide-spread adoption of these techniques, and many modern cosmological analyses, such as the Dark Energy Survey (DES; Dark Energy Survey Collaboration et al., 2016), PANTHEON+ (Brout et al., 2022a), and simulations of the upcoming Legacy Survey of Space and Time (LSST; LSST Science Collaboration et al., 2009; Mitra et al., 2022; Sánchez et al., 2022) still use the simpler χ^2 method.

As modern analyses still use cosmological pipelines which rely on the

χ^2 methodology, it is important to rigorously test these cosmological pipelines. While each individual component of the SN Ia analysis pipeline is well-tested (Kelsey et al., 2023; Kessler et al., 2019b; Lasker et al., 2019; Popovic et al., 2021; Taylor et al., 2023; Toy et al., 2023; Vincenzi et al., 2023), a complete end-to-end consistency check is still necessary to understand the effects and assumptions that propagate between each individual step of the pipeline, and account for any systematic issues that may arise.

In this paper, we present a new methodology to validate the reported cosmological contours of current pipelines. For this effort, we utilise Pippin (Hinton and Brout, 2020), which automates a number of key components of the SuperNova ANAlysis framework (SNANA; Kessler et al., 2009b) used in DES, LSST's Dark Energy Survey Collaboration, and PANTHEON+. Pippin and SNANA provide substantial functionality, including simulations, light curve fitting, photometric classification training and evaluation, SNe Ia standardisation and bias corrections, and cosmological fitting.

Previous efforts to construct a confidence region include those published in Brout et al. (2019b), who used 200 simulated samples to demonstrate that the distribution of best fitting cosmologies produced by their pipeline is consistent with the average of many cosmological contours, which they took as an estimate of the confidence region (CR). This estimate of the CR, while informative, is not statistically rigorous.

To rigorously estimate the confidence region, we make use of the Neyman construction (Neyman, 1937), a Frequentist methodology that leverages simulations to produce a confidence region. The Neyman construction does not assume the CR is Gaussian or elliptical, and is robust to small sample sizes. We compare the Frequentist confidence region produced from the Neyman construction with the Bayesian contour produced by our cosmological pipeline in order to test for consistency. Producing a CR and comparing it to cosmological contours is a powerful, rigorous, and independent method of evaluating the output of a cosmological pipeline.

In Section 3.3 we describe the formalism employed by the Pippin cosmological pipeline. Section 3.4 describes our Neyman construction methodology. Finally, the results of applying our methodology to the Pippin cosmological pipeline are presented in Section 3.5.

3.3 Simulation & Analysis with Pippin

Here we briefly describe the simulation of realistic data-sets of spectroscopically confirmed SN Ia, and the analysis procedure used to produce a cosmological contour. Throughout this analysis we make use of SNANA for simulation and analysis, integrated into the Pippin pipeline.

3.3.1 Simulating a Supernova Data-set

We use the SALT2 (Guy et al., 2007) framework within SNANA for simulating SNe Ia. This framework models type Ia supernovae with five parameters: redshift, day of peak rest-frame B-band brightness, stretch, colour, and apparent peak brightness in rest-frame B-band. SNANA produces simulated observed fluxes by randomly selecting these model parameters from associated probability distributions. SNANA also applies host-galaxy extinction, k-correction, and galactic extinction.

For this analysis we use the SALT2 model produced by Taylor et al. (2021), which was trained on a sample of 420 SNe Ia spanning a redshift range of $\sim$0.1 to $\sim$0.9 with improved zero-point calibration offsets and Milky Way extinction compared to previous SALT2 models.

3.3.1.1 Bias Correction Simulations

In addition to data-like simulations, we also simulate much larger data-sets to correct observational biases. As part of this analysis, we investigate the impact of the cosmology on these bias corrections. Our principal analysis uses only a single bias correction simulation with the input cosmology set to our nominal input cosmology ($\Omega_{\mathrm{M}} = 0.3$, $w = -1.0$), but we repeat our analysis using many bias correction simulations, with input cosmologies equal to the input cosmology of the data-set they are correcting, to see if this affects the Neyman construction.

3.3.2 Analysis

The supernovae in each simulated data-set are fit to determine the SALT2 parameters: amplitude (x_0), stretch (x_1), and colour ($\mathcal{C}$). From here, the distance modulus of each SN Ia can be computed via the Tripp equation (Tripp, 1998).

$$\mu = m_B + \alpha x_1 - \beta \mathcal{C} - \mathcal{M} - \Delta\mu_{\mathrm{bias}} \tag{3.1}$$

Here α and β are global stretch and colour nuisance parameters, $\mathcal{M}$ is a global offset, and $\Delta\mu_{\text{bias}} = \mu - \mu_{true}$ is a distance bias correction, where μ_{true} is the true distance modulus.

Pippin makes use of the BEAMS with Bias Correction (BBC; Kessler and Scolnic, 2017) framework to produce a Hubble Diagram (HD) that has been corrected for both selection effects and contamination. BBC uses the detailed simulations described in Section 3.3.1.1 alongside the BEAMS (Kunz et al., 2012) method to correct for both distance biases, contamination, and selection effects (Kessler et al., 2019a). It then uses a cosmology-independent method (Marriner et al., 2011, SALT2mu;) to fit for global nuisance parameters and standardise the SNe Ia magnitudes.

In order to fit α, β, and $\mathcal{M}$, BBC adopts the likelihood $\mathcal{L} = \prod_{i=1}^{N} \mathcal{L}_i$ where

$$\mathcal{L}_i = P_{Ia,i} D_{Ia,i} + (1 - P_{Ia,i}) D_{CC,i} \tag{3.2}$$

Here $P_{Ia,i}$ is the photometric classification probability for the ith supernova to be a SN Ia. This is usually calculated via a photometric classifier such as SuperNNova (Möller and de Boissière, 2020), or Scone (Qu et al., 2021); however, for our analysis we do not simulate contamination, so $P_{Ia,i} = 1$. $D_{Ia,i}$ encodes the influence of SNe Ia on the likelihood, including corrections for observational biases in the data-set. Details of $D_{Ia,i}$ are presented in Kessler and Scolnic (2017). The $D_{CC,i}$ component encodes the effects of contaminants; however, since our simulations are contaminant free, it is unimportant for this analysis.

The end result of the BBC framework is a redshift-binned HD. BBC can also provide an unbinned HD which Brout et al. (2021) shows can result in smaller systematic uncertainties, but is more computationally expensive. Since our analysis only includes statistical uncertainties, we gain no benefit from using an unbinned HD, therefore we only use the default, binned HD.

This binned HD is passed to a cosmological fitter to produce the final cosmological contours. In this analysis we make use of WFit, which measures a χ^2 likelihood over a grid within the parameter space. WFit has the advantage of being much faster than other methods, although is only suitable for simple test cases such as the one used in this paper, and not necessarily suitable for final survey cosmological analysis. We allow the parameter space of Ω_{M} to vary below 0, something which is not usual for cosmological analyses, as our analysis requires WFit to explore large sections of the Ω_{M}, w parameter space, and we do not wish to artificially truncate the likelihood surface we produce.

3.3.3 Producing an experiment data-set

Our methodology can be used to validate the contour produced by any cosmological pipeline, and is not dependent on the details of the data-set investigated by the cosmological pipeline. As such, we test our methodology on a simple, simulated dataset which mimics the 3-year DES data-set (Brout et al., 2019a), including the cadence, spectroscopic selection, and observational noise (Smith et al., 2020a) of this data-set. We assume a flat, cold dark matter ($wCDM$) cosmology with $Ho = 70$km/s/Mpc, $\Omega_{\mathrm{M}} = 0.3$, and $w = -1.0$. The DES 3 year data-set includes a previously released low-z sample from several sources. We simplify the low-z simulation by generating a DES-like sample for $0.0 \leq z \leq 0.08$ with the same statistics as the low-z sample. Additionally, we only simulate SNe Ia and do not consider contamination from core-collapse supernovae, so that we can keep our analysis as simple as possible. The true DES data-set includes data from a variety of telescopes, as well as misclassified core-collapse SNe, so if our methodology were to be used to test the DES analysis, these details will need to be included in all simulations. The redshift distribution of our DES and low-z simulated sample is presented in Figure 3.1. An example of a simulated light curve is presented in Figure 3.2.

We analyse this simulated data-set with Pippin in order to produce the cosmological contour we check (shown in Figure 3.3), and to calculate the best fitting cosmology:

$$\begin{aligned} \Omega_{\mathrm{M}}^{best} &= 0.32^{+0.054}_{-0.075} \\ w^{best} &= -1.00 \pm 0.16 \end{aligned} \tag{3.3}$$

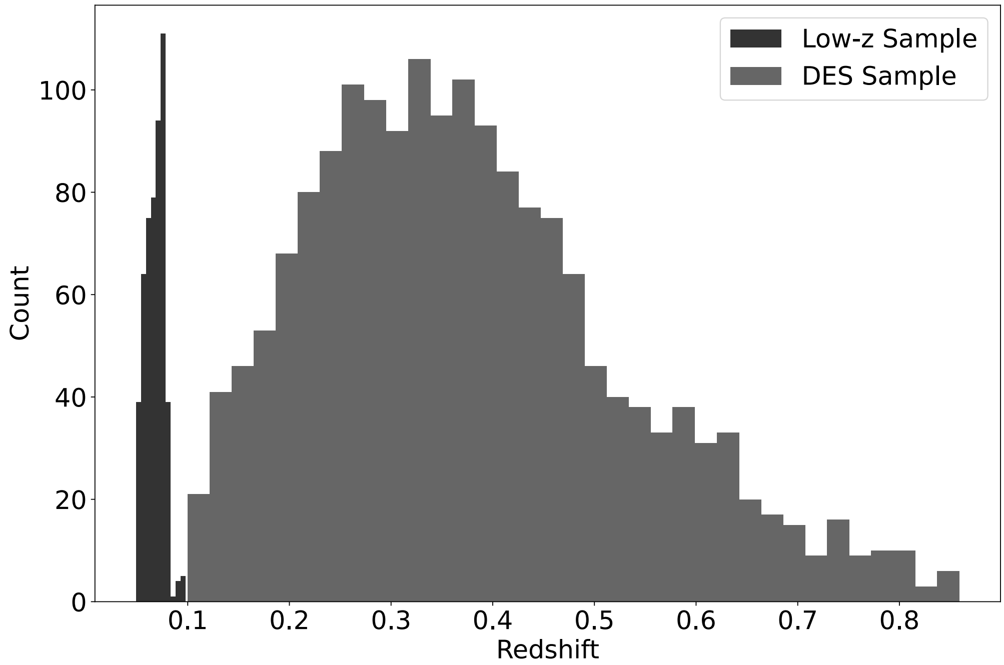

Figure 3.1: The redshift distribution of the simulated DES sample and simulated low-z sample.

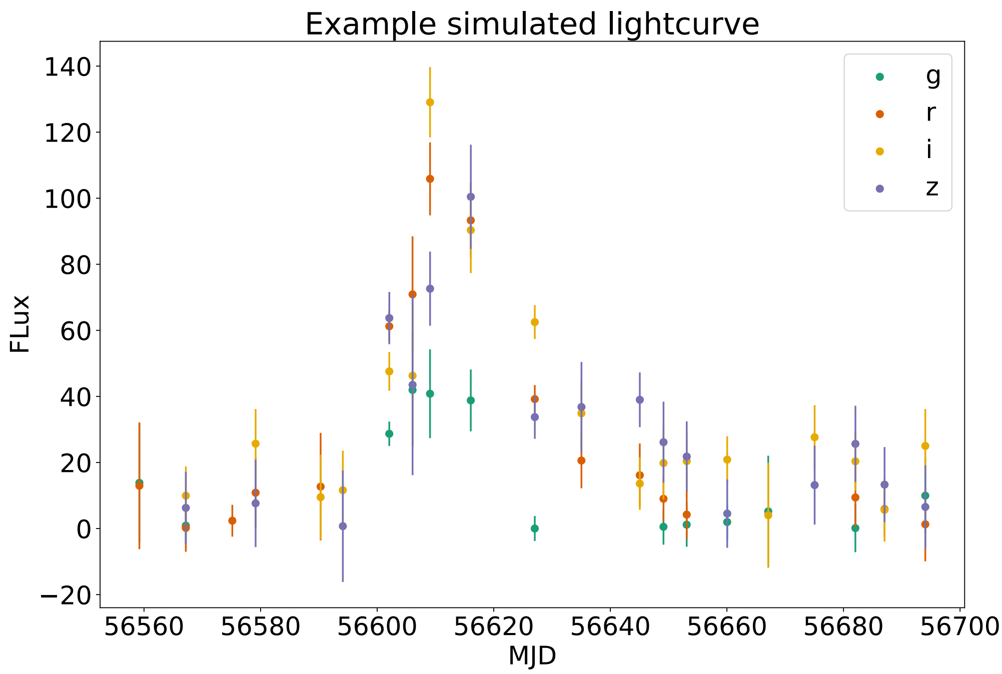

Figure 3.2: An example of a simulated lightcurve in our simulated sample which lies at $z = 0.4$.

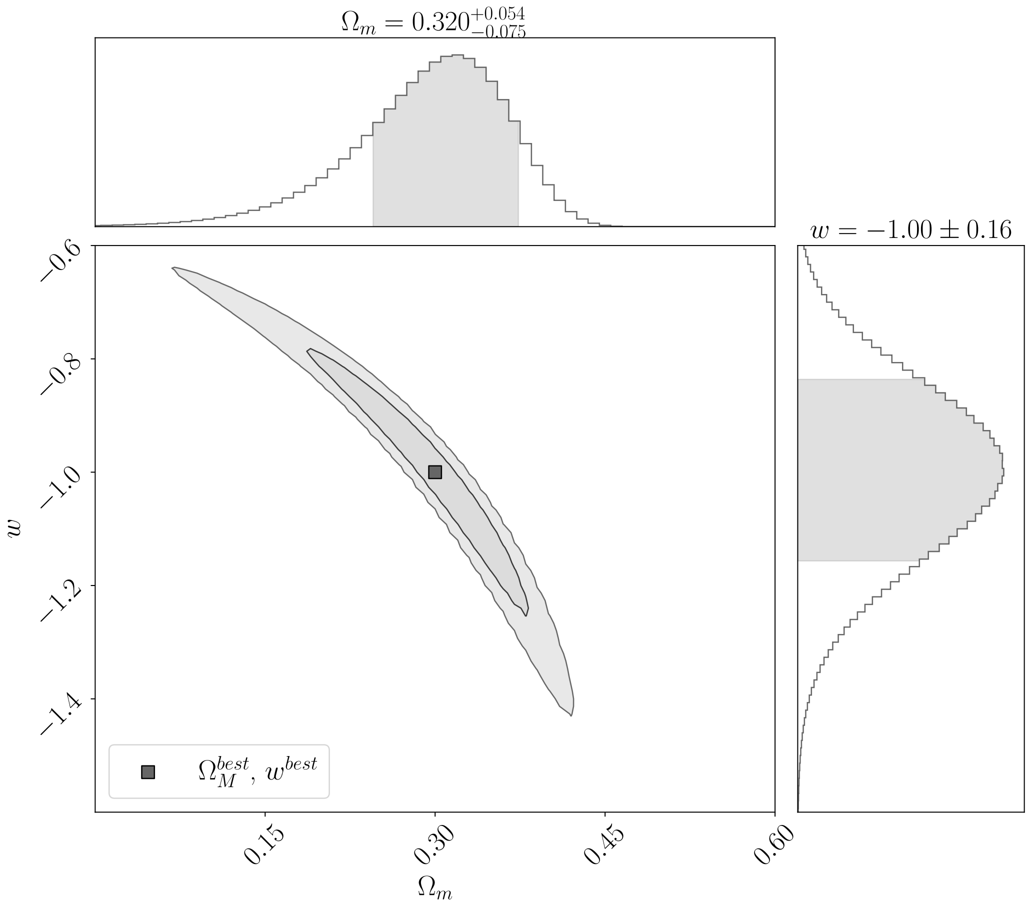

Figure 3.3: The cosmological contour produced by Pippin for our simulated data-set. The aim of our methodology is to test the consistency of this contour. The central panel shows the 2-D 68% and 95% contours, whilst the top and right panel show the marginalised, 1-D contour for Ω_{M} and w, respectively. Here $\Omega_{\mathrm{M}}^{best} = 0.320^{+0.054}_{-0.075}$ and $w^{best} = -1.00 \pm 0.16$.

3.4 Methods

Here we describe our methodology for estimating the confidence region of a cosmological data-set using Neyman construction. To aid the reader, a glossary of terms used throughout is provided in Table 3.1.

Parameter	Description
$\Omega_{\mathrm{M}}^{best}$, w^{best}	The best-fitting output cosmology for our experiment data-set. Described in Section 3.3.3.
Ω'_{M}, w'	A strategically selected input cosmology from which 150 realisations will be drawn. Described in Section 3.4.1.
$\vec{\Omega}_{\mathrm{M}}$, $\vec{w}$	A distribution of 150 best-fitting cosmologies, produced by processing the 150 realisations of Ω'_{M}, w' with Pippin. Described in Section 3.4.1.
$w^{*}(\Omega_{\mathrm{M}})$	A one dimensional function that approximates $\vec{\Omega}_{\mathrm{M}}$, $\vec{w}$. Found by fitting a Gaussian process through $\vec{\Omega}_{\mathrm{M}}$, $\vec{w}$. Described in Section 3.4.1.1.

Table 3.1: A glossary of terms used in our methodology, which are defined throughout the text.

For a given input cosmology, the Neyman construction provides a prescription for using simulations to calculate the percentile contour, or the boundary of a confidence region, that input cosmology lies on. By calculating these percentile contours for a grid of input cosmologies, the confidence region can be estimated as the set of input cosmologies which lie on percentile contours less than or equal to the desired confidence level. The extensive compute time of supernova simulations makes it difficult to densely sample the parameter space, so we instead create an approximate Neyman construction by strategically choosing a few input cosmologies at representative locations on the 68% contour.

In Section 3.4.1 we describe how to calculate the percentile contour for a single cosmological input. In Section 3.4.2 we describe how we find cosmological inputs which lie on the 68% percentile contour, and how we estimate the confidence region.

3.4.1 Calculating the percentile contour

To calculate the percentile contour at any given cosmology (Ω'_{M}, w', which as noted above is chosen to lie at representative locations of the 68% contour), we simulate 150 SNe Ia data-sets with Ω'_{M}, w' as the true cosmological input, using the procedure described in Section 3.3.3. Each data-set is produced with a different random seed, allowing for statistical fluctuations between realisations. We analyse each of these data-sets with Pippin to produce a distribution of best fitting cosmologies ($\vec{\Omega}_{\mathrm{M}}$, $\vec{w}$) in the space of measured Ω_{M} and w. The Neyman construction predicts that the percentile contour for Ω'_{M}, w' is the percentage of these best fitting cosmologies encompassed by a coverage ellipse of this distribution. The coverage ellipse is defined to be centred on Ω'_{M}, w' and to intersect $\Omega_{\mathrm{M}}^{best}$, w^{best}, which were calculated in Section 3.3.3, Equation (3.3). This ellipse represents the probability of a data-set with true cosmology Ω'_{M}, w' having a best fitting cosmology equal to $\Omega_{\mathrm{M}}^{best}$, w^{best}. Figure 3.4 shows an example of this calculation for $\Omega'_{\mathrm{M}} = 0.188$, $w' = -0.783$, which lies at one extreme end of the 68% contour we are testing. Figure 3.5 presents an example Hubble Diagram for both $\Omega_{\mathrm{M}}^{best}$, w^{best} and Ω'_{M}, w'.

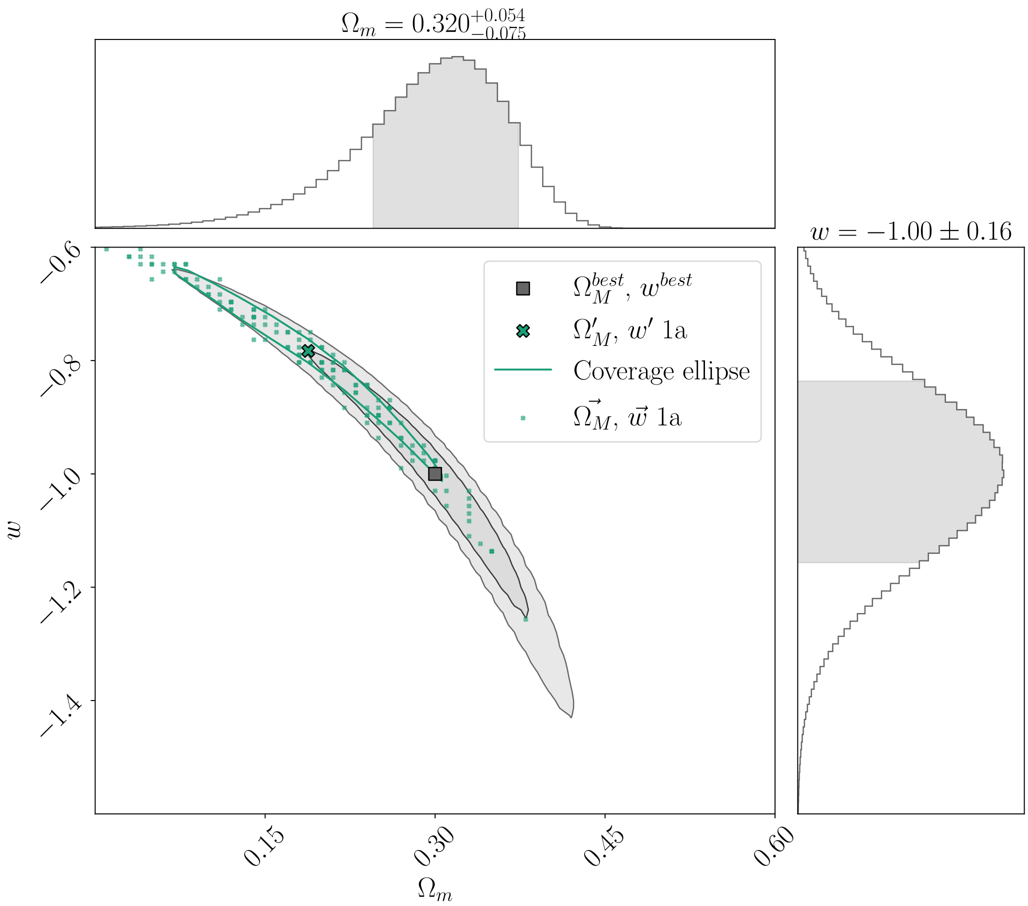

Figure 3.4: An example of using simulations to calculate the percentile contour for Ω'_{M}, w', where $\Omega_{\mathrm{M}}^{best}$, w^{best} represent the best fitting cosmology for our test data-set. We simulate 150 data-sets using Ω'_{M}, w' as the input, and process each data-set with Pippin to find the best fitting cosmology. The coverage ellipse is defined to intersect $\Omega_{\mathrm{M}}^{best}$, w^{best}. The percentile contour for Ω'_{M}, w' is the percentage of best fitting cosmologies contained within this coverage ellipse.

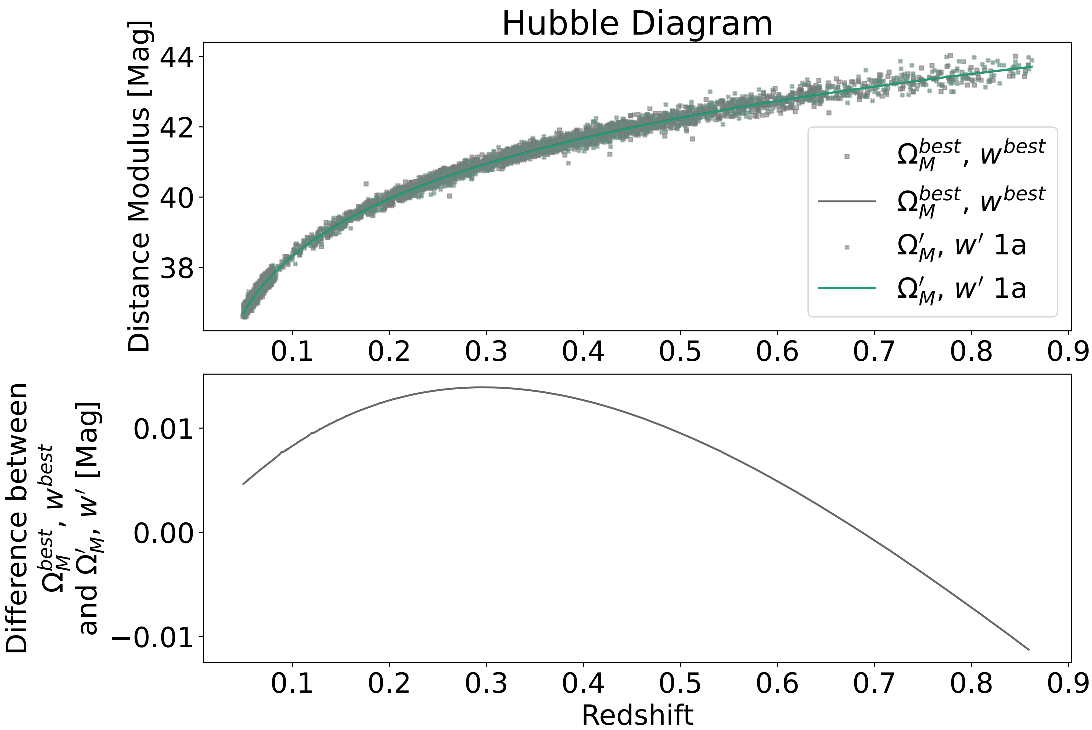

Figure 3.5: Top Panel: Hubble Diagram for $\Omega_{\mathrm{M}}^{best} = 0.3$, $w^{best} = -1.0$ and $\Omega'_{\mathrm{M}} = 0.188$, $w' = -0.783$. This includes both simulated distance moduli and the analytic distance moduli based on the input cosmology. Bottom Panel: Difference between the analytic distance moduli of $\Omega_{\mathrm{M}}^{best}$, w^{best} and Ω'_{M}, w'.

3.4.1.1 Fitting the coverage ellipse

The distribution of best fitting cosmologies about Ω'_{M}, w' usually follows the 'banana' distribution that is typical of supernova cosmology, and is due to the inherent degeneracy between Ω_{M} and w. This contour shape makes it difficult to determine an accurate coverage ellipse around this distribution. To determine a coverage ellipse, we first fit a Gaussian Process (GP) through $\vec{\Omega_{\mathrm{M}}}$, $\vec{w}$ to produce the one-dimensional function $w^*(\Omega_{\mathrm{M}})$, which approximates w as a function of Ω_{M} in the plane of $\vec{\Omega_{\mathrm{M}}}$, $\vec{w}$. Next we subtract $w^*(\vec{\Omega_{\mathrm{M}}})$ from $\vec{w}$ to transform the distribution of best fitting cosmologies into a more elliptical distribution. We fit a coverage ellipse to this transformed distribution which is centred on Ω'_{M}, w' and intersects $\Omega_{\mathrm{M}}^{best}$, w^{best}.

The percentile contour for Ω'_{M}, w' is then the percentage of the best fitting cosmologies covered by this coverage ellipse. Figure 3.6 shows an example of this transformation and ellipse fitting technique for $\Omega'_{\mathrm{M}} = 0.188$, $w' = -0.783$, the same cosmology as shown in Figure 3.4.

The uncertainty in the computed percentage is estimated by performing 1000 bootstrap resamples of the distribution of best fitting cosmologies, and typically results in an uncertainty in the percentile contour of $\pm 4\%$.

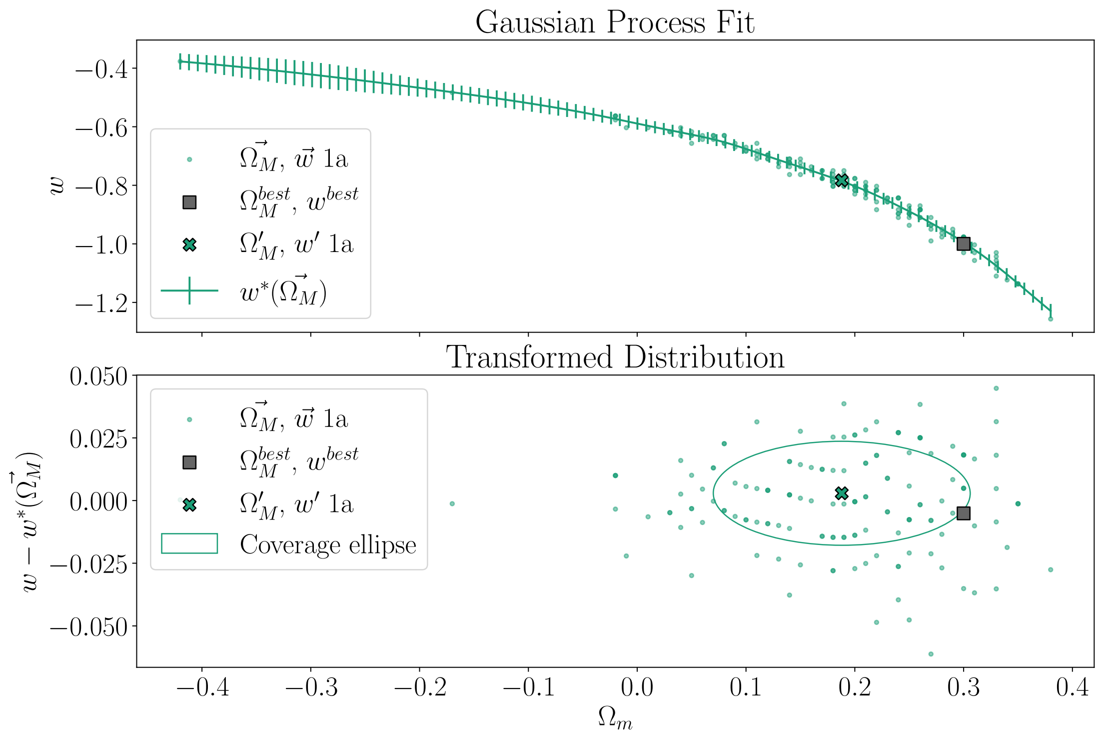

Figure 3.6: **Top panel:** A GP fit ($w^*(\vec{\Omega_{\mathrm{M}}})$) to the best fitting output cosmologies of the 150 realisations with input cosmology: $\Omega'_{\mathrm{M}} = 0.188$, $w' = -0.783$. **Bottom panel:** The same distribution of maximum likelihood output cosmologies, transformed by subtracting $w^*(\vec{\Omega_{\mathrm{M}}})$ from $\vec{w}$. This transformed distribution is more elliptical than the original distribution, and is more appropriate for fitting coverage ellipses. We show one such coverage ellipse in the bottom panel, scaled to intersect with the experiment cosmology input. In this example 46% of the simulations are covered by the ellipse, so this Ω'_{M}, w' lies on the 46% percentile contour.

3.4.2 Estimating the confidence region

We now have a statistically rigorous method of calculating the percentile contour over the cosmological parameter space. Using this method, we could compute a Neyman construction by computing the percentile contour across a grid that covers the cosmological parameter space, and from this determine a

Cosmology Input	Input Ω_{M}	Input w	Percentile Contour
Experiment	0.3	-1.0	—
1a	0.188	-0.783	$46\% \pm 4\%$
1b	0.38	-1.25	$74\% \pm 4\%$
1c	0.307	-0.977	$47\% \pm 4\%$
1d	0.292	-1.02	$62\% \pm 4\%$
2a	0.145	-0.725	$65\% \pm 4\%$
2b	0.37	-1.204	$66\% \pm 4\%$
2c	0.3075	-0.9765	$67\% \pm 4\%$
2d	0.2917	-1.0205	$70\% \pm 4\%$

Table 3.2: The input Ω_{M} and w values for the experiment and approximate Neyman construction input cosmologies, as well as the percentile contour each cosmological input lies on.

confidence region. However, each evaluation of the percentile contour requires 150 simulated data-sets, which is computationally expensive.

To more efficiently determine a confidence region, we develop an approximate Neyman construction method which requires far fewer simulations. Instead of evaluating the percentile contour over the entire cosmological parameter space, we use the bisection method to iteratively find the input cosmologies that lie on the 68% percentile contour. These cosmologies define the edge of the 68% confidence region.

We first calculate the percentile contour for cosmologies at several representative locations on the 68% contour. We select two input cosmologies which are at the furthest extent of the 68% contour, and two input cosmologies which are at the closest region of the 68% contour to $\Omega_{\mathrm{M}}^{best}$, w^{best}. This enables us to probe the consistency of the 68% contour across its entire span. The cosmological inputs used in defining the approximate Neyman construction, and the percentile contour for each input are shown in Figure 3.7, and detailed in Table 3.2. Inputs 1a, 1b, 1c, and 1d were chosen to lie on the 68% contour of the original experiment cosmology posterior. A second set of inputs (2a, 2b, 2c, and 2d) were chosen to compensate for how far the previous set of coverage ellipses differed from 68% coverage, as described below.

If the input cosmologies lie at a percentile contour of $< 68\%$ confidence, we select a new cosmology further from $\Omega_{\mathrm{M}}^{best}$, w^{best}, and conversely select a cosmology closer to $\Omega_{\mathrm{M}}^{best}$, w^{best} if the initial percentile contour is $> 68\%$ confidence. This allows us to find an input cosmology which lies on a percentile contour within one standard deviation of 68%, as measured by bootstrap resampling.

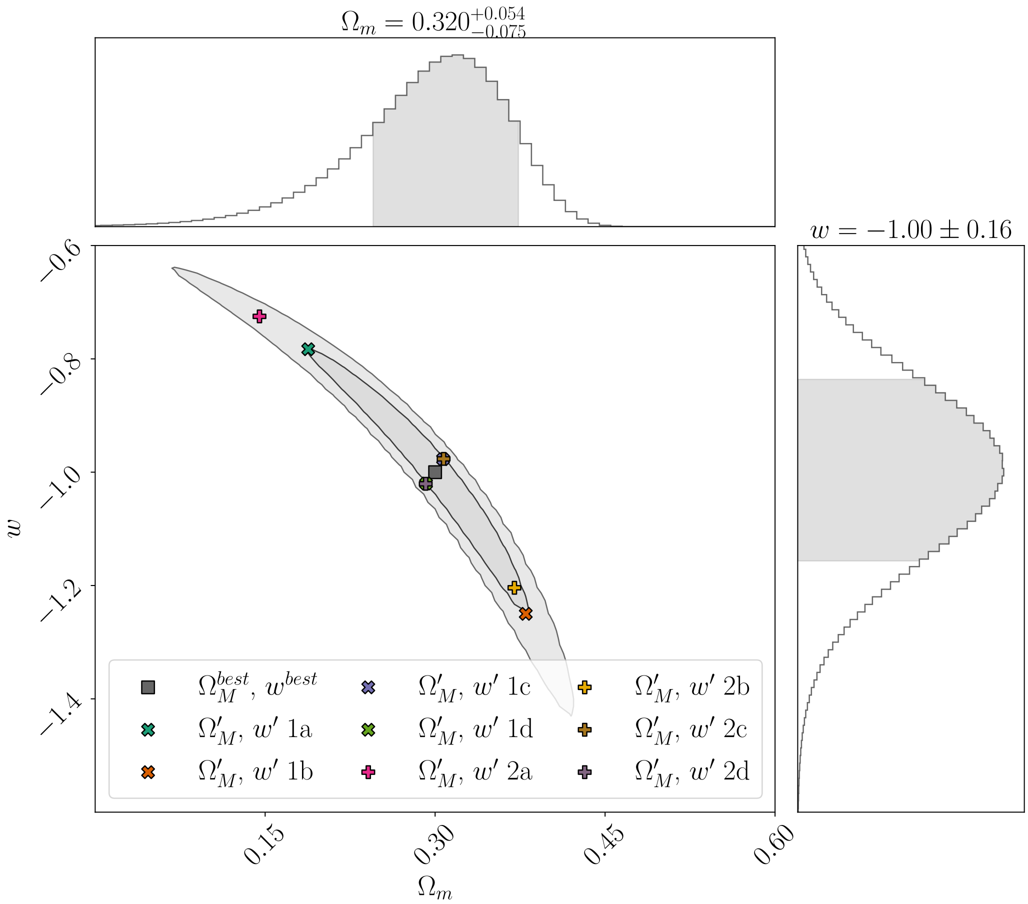

Figure 3.7: The input Ω_M and w values for the experiment (Ω_M^{best}, w^{best}) and the approximate Neyman construction (Ω'_M, w').

Though the iterative method typically converges to a percentile contour within one standard deviation of 68% within 2 or 3 iterations, converging to exactly 68% would take significantly more iterations. As such, once we are within one standard deviation of 68%, we linearly interpolate or extrapolate to find an input cosmology which lies exactly on the 68% percentile contour.

See Figure 3.8 for an example of this approximate Neyman Construction technique for $\Omega'_M = 0.188$, $w' = -0.783$, the same cosmology shown in Figures 3.4 and 3.6. This cosmology was found to lie on the $46\% \pm 4\%$ percentile contour, and after iteration the cosmology $\Omega'_M = 0.145$, $w' = -0.725$ was found to lie on the $65\% \pm 4\%$ percentile contour, which is within one standard deviation of 68%. We linearly extrapolated from these two input cosmologies to find that $\Omega'_M = 0.138$, $w' = -0.716$ lay on the 68% percentile contour. Figure 3.9 shows the coverage ellipses fit to each cosmological input.

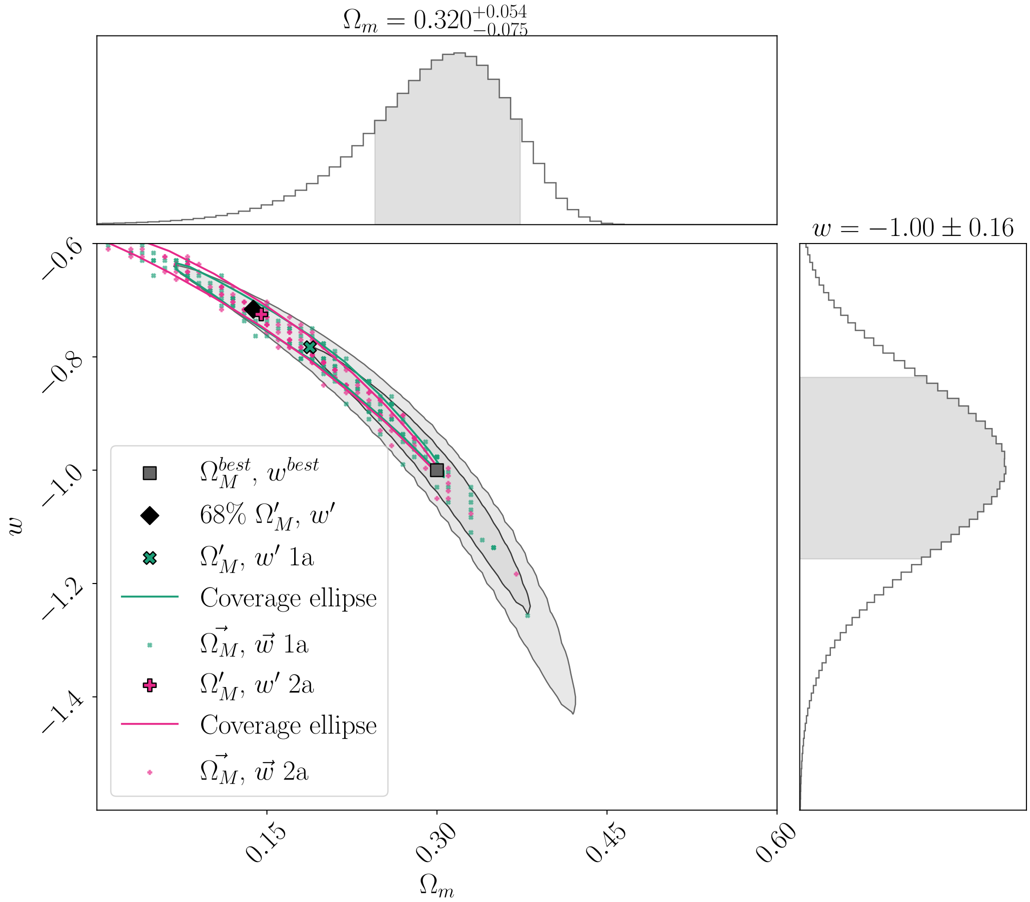

Figure 3.8: Example of finding the edge of the 68% confidence region. Ω'_{M}, w' 1a was defined with an input cosmology on the extreme end of the Pippin 68% contour, and was found to lie on the 46% $\pm$ 4% percentile contour. Ω'_{M}, w' 2*a* was found iteratively, and lies on the 65% $\pm$ 4% percentile contour. Linearly extrapolating from these two cosmological inputs gives us 68% Ω'_{M}, w'.

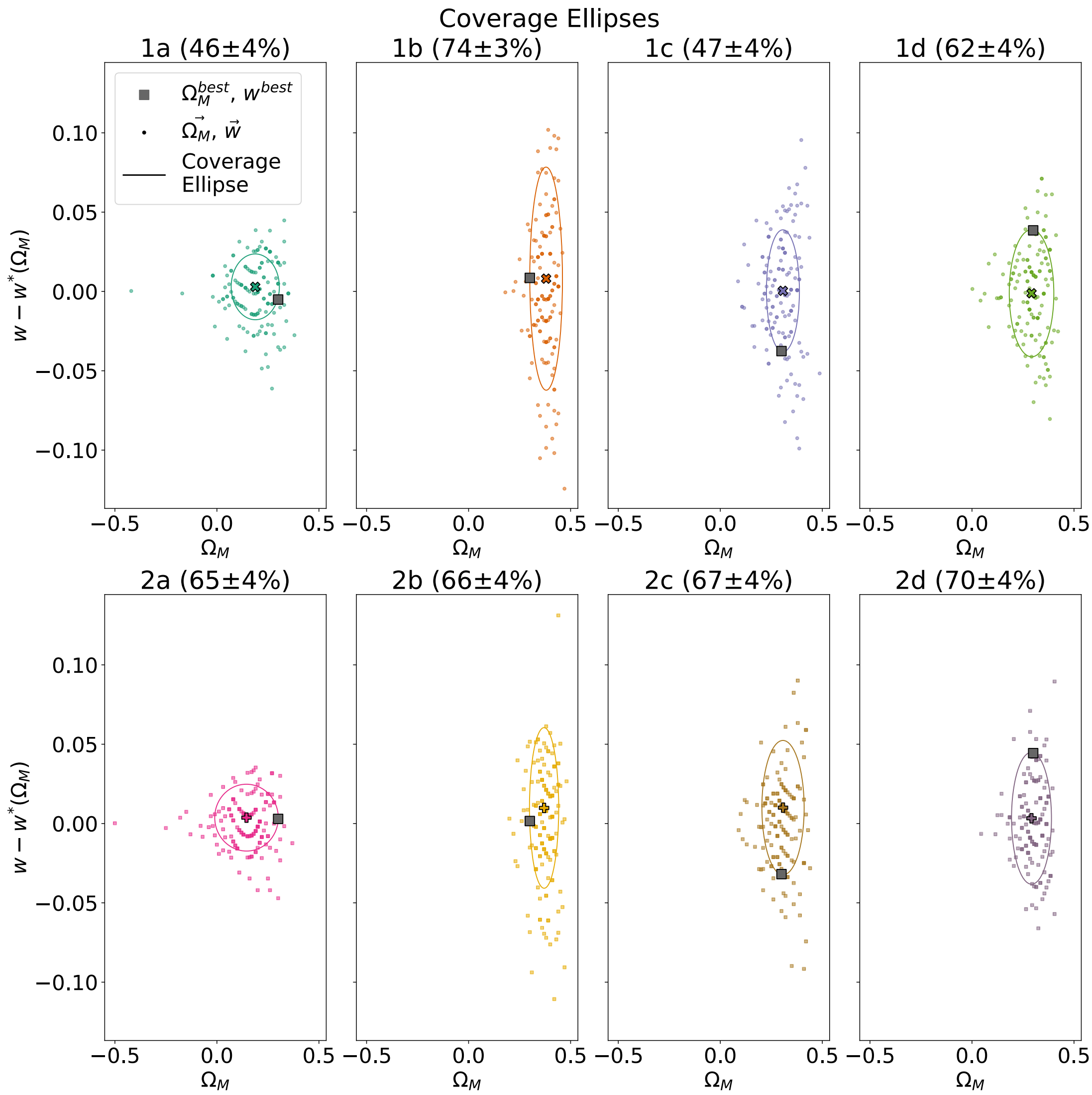

Figure 3.9: Coverage ellipses fit to the maximum likelihood distribution of each Neyman input cosmology, transformed to $\{\Omega_\mathrm{M}, w - w^*(\Omega_\mathrm{M})\}$. The coverage ellipse is defined to be centred on the Neyman input, scaled such that it contains the experiment cosmology input. The title of each plot shows the percentage of maximum likelihood output cosmologies covered by the ellipse, this is our numerical estimate of likelihood. The uncertainty in this estimate is calculated via 1000 bootstrap resamples and is 4%.

3.5 Results

In the previous section we describe how we computed the location of the 68% confidence region at four strategically selected cosmological inputs in the $\Omega_M - w$ plane using an approximate Neyman construction. The results are presented in Table 3.3 and shown in Figure 3.10.

We see the largest difference between the experiment cosmology 68% contour and the 68% confidence region in the first input cosmology, which lies in the top left quadrant of the cosmological contour. We find a shift of $\sim$0.05 in Ω_M and a shift of $\sim$0.07 in w. The second input cosmology, which lies in the bottom right quadrant has a shift of $\sim$0.007 in Ω_M and $\sim$0.03 in w. These input cosmologies lie at the furthest extent of the 68% cosmological contour from Ω_M^{best} and w^{best}. In contrast, the third and fourth input cosmologies, which lie much closer to the experiment input cosmology, have a shift of $\lesssim$0.001 in both Ω_M and w. The increase in discrepancy as we probe parameter space that is further from the experiment input cosmology is expected, as the bias correction used by BBC is most accurate near the input cosmology, and performs a lower quality correction further from the input. By contrast, our Neyman construction method applies this bias correction in a cosmologically dependent manner across the entire parameter space, removing this offset.

This offset is important to consider, especially when combining supernova contours with other cosmological probes such as the cosmic microwave background. Fortunately, it is the region of posterior space close to the input cosmology which overlaps with the contours of other cross-cutting probes. As such this offset is unlikely to significantly affect multi-probe cosmological analyses.

Where this offset could be significant is in the investigation of cosmological tensions, where accurate uncertainties of the tails are vital to successfully assess the significance of the tension. In these cases, it may be useful to use a method like our approximate Neyman construction to produce more accurate and statistically rigorous measure of the uncertainty in a cosmological fit.

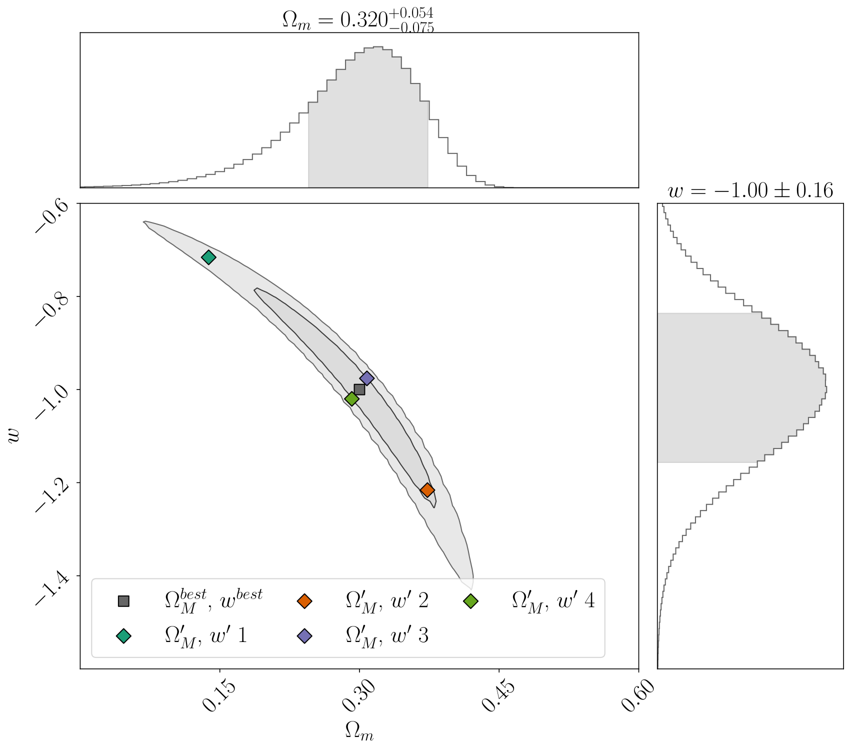

Figure 3.10: Comparison between the 68% confidence region determined from our approximate Neyman construction, and the 68% contour of the experiment cosmology. The confidence region is consistent with the contour close to the input cosmology, but displays an offset at the extreme ends of the contour. This offset is likely due to the bias correction method used by BBC, which is most accurate close to the input cosmology.

Cosmology Input	Ω'_M	w'	Ω_M Absolute Difference	wAbsolute Difference
1	0.138	-0.716	0.05	0.07
2	0.373	-1.216	0.007	0.03
3	0.308	-0.976	0.001	0.001
4	0.2918	-1.02	0.0002	0.0

Table 3.3: Comparison between the 68% confidence region determined from our approximate Neyman construction, and the 68% contour of the experiment cosmology. The absolute difference is the difference between the cosmologies at the edge of the 68% contour produced by Pippin, and the cosmologies at the edge of the 68% confidence region produced by our approximate Neyman construction.

3.5.1 Effect of Bias Correction Input Cosmology

We repeat our analysis with bias correction simulations that use a cosmology that is nearer to the data-set they are attempting to correct, rather than a single bias correction shared amongst all realisations; Figure 3.11 and Table 3.4 show the results of this repeat analysis. Our results are very similar to the case when we shared the bias correction simulation amongst all realisations, with the first and second cosmological input deviating the most. Overall, these results reinforce our suggestion that the offset present between the cosmological contour and confidence region is caused by the BBC bias correction; however, the choice of bias correction does not significantly affect our consistency test. If computational cost is a concern, using only one bias correction simulation shared amongst all realisations will significantly reduce the computational cost of our approximate Neyman construction method, without significantly reducing the quality of the consistency test.

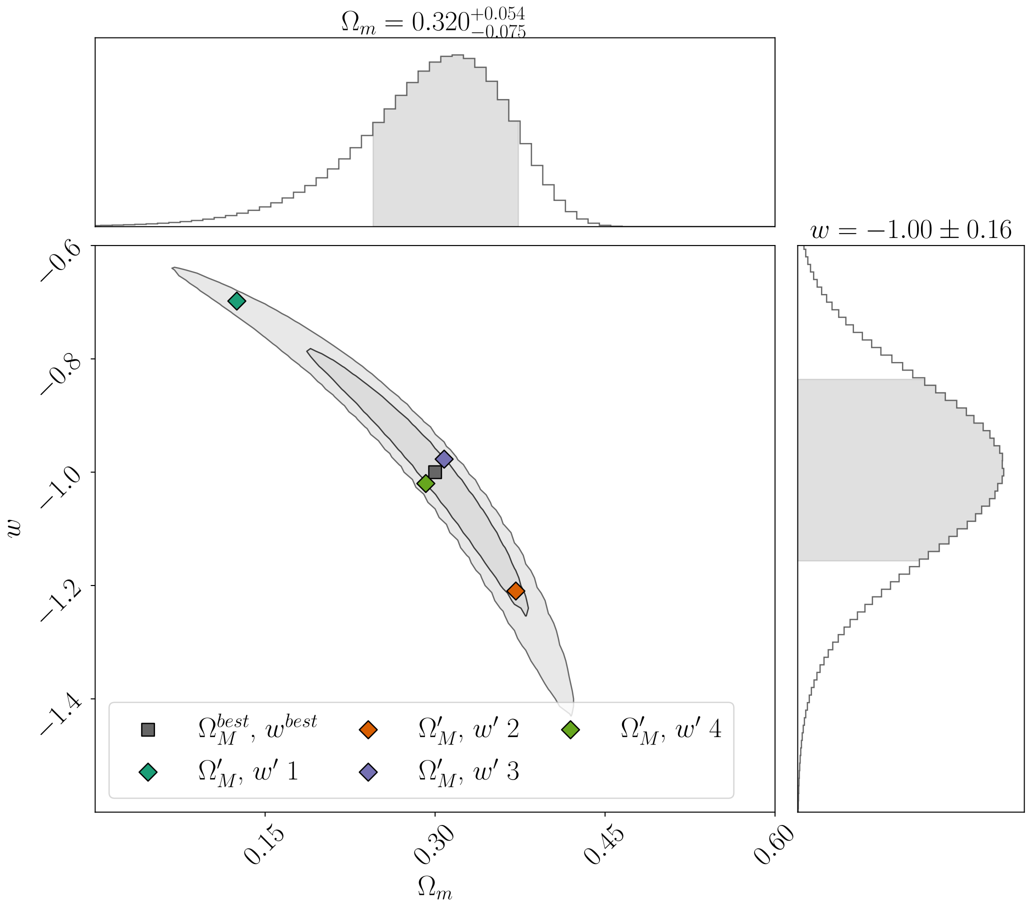

Figure 3.11: As per Figure 3.10, but varying the bias correction simulation to match the input cosmology. Very similar results are found, indicating that the cosmology used for the bias correction is not significantly impacting the results.

Cosmology Input	Ω'_M	w'	Ω_M Absolute Difference	w Absolute Difference
1	0.125	-0.698	0.063	0.085
2	0.371	-1.21	0.009	0.004
3	0.308	-0.977	0.001	0.0
4	0.292	-1.02	0.0	0.0

Table 3.4: As for Table 3.3, but varying the bias correction simulation to match the input cosmology.

3.6 Conclusions

In this paper we present a statistically rigorous method for checking the consistency of contours produced in a cosmological analysis. To achieve this, we implement an approximate Neyman construction which requires far less computation than a true Neyman construction. This approximate Neyman construction is then used to define the 68% confidence region for a single cosmological realisation. We use this confidence region to test the consistency of the 68% contour produced by the BBC framework, as integrated in Pippin, although this method can be used to test the consistency of any cosmological parameter estimation method. This represents the first time the BBC framework has been tested with a statistically rigorous methodology.

Our analysis showed that, for a DES[3] like dataset, Pippin is producing reasonable, consistent parameter estimates. There was some discrepancy between the CR and the cosmological contour when considering the farthest extent of the 68% contour. This discrepancy was, at maximum, a shift of $\sim$0.05 in Ω_M, and $\sim$0.07 in w, and was likely due to the accuracy of BBC's bias correction being best when close to the input cosmology, and degrading in regions of parameter space which are far from the input cosmology. It is also important to recognise that this does not correspond to an equivalent error in the reported maximum posterior cosmological parameters. When considering cosmological inputs close to the experiment cosmology input, the confidence region and cosmological contour had near perfect agreement. As such any overall discrepancy is unlikely to significantly affect the results of a cosmological analysis, especially when multiple cross-cutting probes are combined. However, this shift is important when considering analyses concerned with assessing cosmological tensions — where the precise shape and size of the contour are vitally important to the analysis.

We see very similar results when each realisation had its own bias correction simulation, rather than sharing one bias correction simulation amongst all realisations, indicating that a sensible choice of bias correction is not likely to significantly affect our consistency checks.

Overall, we believe our method for consistency checking cosmological contours with an approximate Neyman construction represents an important improvement in the statistical rigour applied to cosmological analyses, and should be considered carefully when a survey analysis is performed. Our methodology can also be used to rigorously test cosmological contours for other cosmological probes, which have similarly complex pipelines. We believe this method will be particularly useful for future analyses, such as the DES 5-year supernova analysis, and the upcoming LSST survey. We plan to repeat this analysis using simulations that match the DES 5-year supernova analysis to test the consistency of those results.

Chapter 4

The Future of Cosmology and the ongoing role of type Ia Supernovae

The DES-SN5YR analysis contains the largest cosmological sample of type Ia SNe from a single survey. This statistical power in combination with cross-cutting constraints from other cosmological probes, has provided the strongest evidence for time evolving dark energy thus-far (3.9σ tension with ΛCDM when combined with the DESI Collaboration et al. (2024b) constraints). Though this constraining power is impressive, it is not yet at the statistical significance needed to reject ΛCDM as the prevailing cosmological theory — typically ~5σ is required, though for highly impactful discoveries $> 10\sigma$ is not an unreasonable expectation[1]. Additionally, the DES-SN5YR analysis revealed a number of important sources of uncertainty which affect SN Ia cosmological analysis, the most impactful of which are modelling and calibration uncertainties, and the effects of dust (Vincenzi et al., 2024). As can be seen in Figure 12 of Vincenzi et al. (2024), the impact of systematics alone on the total uncertainty budget is approximately half that of statistical uncertainties. With future SN cosmological analyses using SN Ia samples that are one to two orders of magnitude larger than DES-SN5YR, systematics are likely to be the limiting factor on the constraining power of these future surveys.

Tackling these systematic uncertainties will require building a better understanding of the physics underlying the observed brightness of SNe, including the impact of dust, improving the methodologies underpinning our analyses, and creating toolkits capable of handling the growing scale and complexity of SN cosmology as a field. This chapter serves to highlight a number of projects started during my PhD. In Section 4.1 I discuss the Dark Energy All

[1] The discovery of the accelerated expansion of the Universe had a significance of ~12σ (Perlmutter et al., 1999; Riess et al., 1998; Schmidt et al., 1998).

Sky Bedrock Survey (DEBASS), a continuing effort to produce a modern low-redshift SN Ia sample using DECam, which was used for the DES-SN5YR sample. Section 4.2 details my investigations into alternative statistical and computational techniques for SN cosmology. Finally, Section 4.3 describes my plans for the future of the Pippin cosmological pipeline.

4.1 The Dark Energy All Sky Bedrock Survey

The DEBASS survey began observing low-redshift SNe in March 2021 with an aim to observe over 500 SNe Ia over the course of the survey. SN light curves are observed with the Dark Energy Camera (DECam; Flaugher et al., 2015) on the CTIO 4m telescope in Chile. Spectroscopic follow-up is performed by the Wide-Field Spectrograph (WiFeS; Dopita et al., 2007) on the ANU 2.3m telescope at Siding Spring Observatory in Coonabarabran, NSW. It is this spectroscopic follow-up that myself and other researchers at the Australian branch of DEBASS are focused on. At the time of writing, 592 SNe have been observed and spectroscopically followed-up, of which 311 are spectroscopically confirmed type Ia SNe. My role within this survey has been as Infrastructure Lead, primarily tasked with building and maintaining the DEBASS spectroscopic database, available through the DEBASS website[1] which I also created and maintain.

When comparing the prospects of the DEBASS sample to the combined CfA, CSP, and Foundation sample used by the DES-SN5YR analysis for its low redshift anchor, we expect the DEBASS sample to provide improved statistical and systematic uncertainties, both due to the larger sample size (~500 vs the 247 in the DES low-z sample[2]), and a reduction in the number of surveys that need to be cross-calibrated.

When combining SN samples together, not only does each filter of each sample need to be correctly calibrated, but each sample must be cross-calibrated to ensure all SN light curves are on the same flux scale. This cross-calibration introduces additional systematic uncertainties which affect both the photometric calibration and the training of light curve models. This calibration uncertainty is the second-largest systematic uncertainty in the DES-SN5YR analysis, accounting for 34% of the total uncertainty budget (Table 7. Vincenzi et al., 2024). As the DEBASS sample does not contain SNe from multiple surveys, the impact of cross-calibration systematic uncertainties when combining the DEBASS sample with other surveys is expected to be significantly reduced. In addition,

[1] https://www.mso.anu.edu.au/debass/
[2] Before quality cuts

the DEBASS sample will be used to retrain the SALT3 model (Dai et al., 2023; Kenworthy et al., 2021; Pierel et al., 2022; Taylor et al., 2023), eliminating any systematic uncertainties arising from training SALT3 on SNe observed with multiple photometric systems.

4.1.1 Investigating the Host Galaxy Relation

In addition to the primary goal of the DEBASS survey (producing a high-quality single survey low-z SN sample), we have also started research utilising the preliminary DEBASS sample to improve our understanding of the SN host galaxy luminosity step (discussed in detail in Section 2.3.3). This relationship between host galaxy properties and SN luminosities remains a significant source of systematic uncertainty in modern SN cosmology analysis.

When considering the relationship between host galaxy properties and the luminosity step, it's important to differentiate between properties which are *tracers* of the luminosity step, and those that are *drivers* of the luminosity step. As described in Briday et al. (2021), a driver is a host galaxy property which splits the SNe population into two subgroups (a and b) *with different mean luminosities*; possible drivers include host galaxy age or SN progenitor age. Tracers are an observable environmental property of the host galaxy which is correlated with an underlying driver, such as host galaxy mass, colour, specific star formation rate, and so on. The strength of this correlation determines the accuracy of the tracer as a measure of SN luminosity variation. As the underlying driver of the SN luminosity step is not known, determining which tracers are most effective for probing the luminosity step, is necessary for understanding and correcting this systematic error in SN cosmology analyses.

To date, the DEBASS group has investigated the effectiveness of the equivalent width (EW) of the [O II] $\lambda\lambda$ 3727, 3729 doublet as a tracer of the underlying driver of the SN host galaxy luminosity step. As presented in Martin et al. (2024), the EW of [O II] was found to be a better tracer of this driver than host galaxy mass when applied to the Foundation (Foley et al., 2017) survey. Work is currently ongoing to determine whether the EW of [O II] remains a better tracer for the DEBASS sample.

4.2 Alternative Cosmological Techniques

Between the DES-SN3YR and DES-SN5YR analyses, many of the techniques and best practices of SN cosmology changed, leading to improvements in photometric classification, observational biases, systematic uncertainties, and ultimately tighter cosmological constraints. The interim between the DES-SN5YR analysis and the next generation of SN cosmology surveys presents a similar opportunity to investigate improvements to various components of the analysis pipeline.

4.2.1 Forward Modelled Cosmology

As described in Section 2.3.6, the current system for determining systematic uncertainties requires an assumption of independence between all systematic sources. To address this assumption, I investigated the viability of a forward modelled approach, where covariant systematic uncertainties are integrated directly into simulated SN samples during the `SIM Stage` rather than being handled in the later `CREATECOV Stage`. This allows fine-grained control over the behaviour of systematic uncertainties, allowing complex interactions to be modelled.

For my initial investigations, I focused on implementing covariant calibration systematics. Each filter in a SN sample has two systematic calibration uncertainties, the uncertainty in the mean (central) wavelength of the filter transmission curve (σ_λ), and the uncertainty in the zero-point of the filter σ_{ZP}. Though the uncertainties in the central wavelength of different filters are independent, the zero-point offsets of different filters may be based on the same set of standard stars, and thus share a dependency on the uncertainty in those standard stars.

Following the methodology of Betoule et al. (2014), the calibration uncertainty can be represented as a $2N \times 2N$ covariance matrix ($\mathbf{C}_{\mathrm{calib}}$), where N is the number of filters being calibrated. The first $N \times N$ elements describe a diagonal matrix containing the central wavelength uncertainties, calculated using:

$$\mathbf{C}_{\mathrm{calib},\lambda}^{i<N,j<N} = \begin{cases} \sigma_{\lambda,i}^2 + \left[\left(1 + \sigma_{\mathrm{SuperCal}}\right) \Delta_{\mathrm{SuperCal},i}\right]^2 & i = j \\ 0 & \text{otherwise} \end{cases} \tag{4.1}$$

Here, $\sigma_{\lambda,i}$ is the uncertainty in the central wavelength of the ith filter (sourced from the original survey), $\Delta_{\mathrm{SuperCal},i}$ is a cross-calibration correction for the ith filter determined by the SuperCal-Fragilistic calibration method (Brout et al., 2022b), and $\sigma_{\mathrm{SuperCal}} = \frac{1}{3}$ accounts for systematic uncertainties in the SuperCal-Fragilistic process.

The next $N \to 2N \times N \to 2N$ elements describe the covariant zero-point uncertainties, calculated using:

$$\mathbf{C}_{\text{calib,ZP}}^{N\leq i<2N,N\leq j<2N} = \begin{cases} \sigma_{\text{ZP}}^2 + \sigma_{\text{CALSPEC}}^2 \left[\lambda_i - \bar{\lambda}\right]^2 & i = j \\ \sigma_{\text{CALSPEC}}^2 \left[\lambda_i - \bar{\lambda}\right]\left[\lambda_j - \bar{\lambda}\right] & i \neq j \end{cases} \tag{4.2}$$

Here, $\sigma_{\text{ZP},i}$ is the uncertainty in the zero-point of the ith filter (sourced from the original survey), σ_{CALSPEC} is the systematic uncertainty associated with CALSPEC spectra, λ_i is the central wavelength of the ith filter (sourced from the original survey), and finally $\bar{\lambda}$ is the effective mean wavelength of the SALT2 model integrated in the filter.

Building this covariance matrix requires detailed knowledge of how each individual survey is calibrated for a given cosmological analysis[1]. As historical low-z samples are replaced with modern alternatives, this process should be simplified. In particular, combining the DEBASS sample (presented in Section 4.1) with the DES-SN5YR sample will provide a SN sample in which both low and high redshift SNe are on the same photometric system (i.e. $\mathbf{C}_{\text{calib}}$ will be an 8×8 matrix).

By treating this matrix as the covariance matrix of a multivariate normal distribution, we can draw vectors from this distribution to produce offsets to the zero-point and central wavelengths of each filter in the analysis. These systematic calibration offsets can then be applied to the filters and SALT models used in a simulation, effectively applying a covariant systematic shift to this simulation. Repeating this process of drawing systematic calibration offsets, and using them to produce a covariantly shifted simulation is the basis of the forward modelling technique.

As discussed in `SIM`, I worked with the developer of SNANA to integrate a method for individually assigning specific central wavelength and zero-point offsets to a simulation. The challenging step of this process is integrating these shifts into the SALT surface used for the simulation and fitting of SN light curves. Though applying an offset to the zero-points and central wavelengths of the filters used by the SALT training process is possible, offsetting these filters necessitates retraining the SALT model, a computationally expensive process. As the forward modelling technique requires hundreds of iterations to attain a statistically significant measure of the impact of these covariant systematic uncertainties, the SALT retraining process becomes prohibitively expensive. As such, I developed a method for approximating the SALT retraining process which produces highly accurate surfaces in a fraction of the time.

[1] Sometimes this information may not even be readily available

4.2.1.1 Approximate SALT surface

A SALT model of the spectral energy distribution of SNe Ia can be represented as a 'surface' in wavelength (with N_λ elements), phase (with N_ϕ elements), and flux space, alongside a colour law written as a fourth-order polynomial (with N_{CL} elements). The goal of my approximate SALT surface method is to efficiently approximate the change in a SALT surface and colour law induced by a change in one of the filters used to train that surface and colour law.

The method I developed for this involves training $2N$ SALT surfaces corresponding to the N zero-point and central wavelength offsets in the previously discussed covariance matrix. For each filter, a surface is produced with the zero-point offset by 0.01 mag, and another surface produced with the central wavelength offset by 1.0 nm.

From these $2N$ surfaces, an $N_\lambda \times N_\phi + N_{\mathrm{CL}} \times 2N$ Jacobian matrix $\mathcal{J}$ is calculated from the difference in each surface $\mathcal{S}(\Delta_i)$ and a base, unperturbed SALT surface $\mathcal{S}_{\mathrm{Base}}$:

$$\mathcal{J}_i = \{(\mathcal{S}_{\mathrm{Base,Surface}} - \mathcal{S}_{\mathrm{Surface}}(\Delta_i)), (\mathcal{S}_{\mathrm{Base,CL}} - \mathcal{S}_{\mathrm{CL}}(\Delta_i))\} \tag{4.3}$$

From this Jacobian, the approximate surface for an arbitrary set of central wavelength and zero-point offsets $\Delta_{\mathcal{S}}$ can be calculated as:

$$\mathcal{S}(\Delta_{\mathcal{S}}) = \mathcal{S}_{\mathrm{Base}} - \mathcal{J} \times \Delta_{\mathcal{S}} \tag{4.4}$$

Though this technique is still being developed, initial tests show that this can produce an approximate surface in ~30 seconds, which matches the associated SALT surface to within half a percent. This work is ongoing, with the final steps of this project involving updating the method for the SALT3 analysis, and testing whether the approximate surfaces produce any bias in constrained cosmological parameters.

4.2.2 Approximate Bayesian Computation

The method of constraining cosmological parameters used in the DES-SN5YR analysis (discussed in `COSMOFIT`) requires defining a likelihood function $\mathcal{L}$ which encapsulates both the residual between the data and a cosmological model, and the statistical and systematic uncertainties in the data.

Owing to the complexity of the DES-SN5YR analysis, in particular the calculation of the bias correction in `BIASCOR`, this likelihood function *cannot* be written as an analytical function of the SN light curves used for cosmological constraints. This makes it difficult to evaluate the 'correctness' of the resulting probability distribution functions, requiring advanced statistical techniques (see Chapter 3). Additionally, measuring the systematic uncertainty of various choices made throughout the analysis (which photometric classifier to use, which dust model to assume, etc...) is non-trivial, and implementing new systematic uncertainties, such as the covariant uncertainty between calibration systematic discussed above, is not possible under the current framework.

To address this, I have begun investigations into a likelihood-free method of producing cosmological constraints known as Approximate Bayesian Computation (ABC; Pritchard et al., 1999). Under a typical Bayesian framework, the posterior distribution $P(M(\theta)|D)$ of a given model M with parameters θ for some data D is:

$$P(M(\theta)|D) = \frac{P(D|M(\theta))P(M(\theta))}{P(D)} \tag{4.5}$$

Here, $P(D|M(\theta))$ is the likelihood that D is observed assuming $M(\theta)$ were true, and is equivalent to the likelihood function $\mathcal{L}$ used in the DES-SN5YR analysis. $P(M(\theta))$ is the prior distribution on $M(\theta)$, and provides the likelihood the $M(\theta)$ is true in general; The prior often encodes physical constraints such as $0 \leq \Omega_\mathrm{M} \leq 1$. The final term $P(D)$ is a normalisation factor which ensures the integral of $P(M(\theta)|D)$ over all θ is 1.

Rather than defining an analytical likelihood function which compares data to a model, ABC utilises detailed simulations and replaces the likelihood function with a distance function $\delta(D, S(\theta))$ between the data and a simulation $S(\theta)$. The basic ABC algorithm involves randomly drawing simulation parameters (θ) from the prior distribution, measuring the distance between the data and this random simulation, to determine which parameters produce simulations most similar to the data. In the limiting case that the distance function is zero, this iterative process is equivalent to the likelihood function used in the original Bayesian analysis.

The advantage of this technique over traditional Bayesian analyses is that simulations may include far greater complexity in their handling of systematic and statistical uncertainties when compared to an analytical likelihood function. For example, the systematic covariance matrix used by the DES-SN5YR analysis (discussed in Section 2.3.6) assumes each source of systematic uncertainty is independent of any other systematic source. The ABC technique can drop this assumption by implementing dependencies between systematic sources directly into the simulations.

In practice, simulations are often computationally expensive, and the distance function typically never measures exactly zero, owing to the uncertainties in the data and simulation. As such real-world applications of ABC often use a more complex algorithm, such as the Sequential Monte Carlo (SMC; Beaumont et al., 2009) ABC method for which pythonic pseudocode is provided in Code Block 4.1.

Previous efforts to develop SMC-ABC algorithms for supernova cosmology (See Jennings and Madigan, 2017; Jennings et al., 2016) have shown that this technique has merit, but has two significant issues which must be resolved. The first is the computational expense inherent to supernova simulations. Jennings and Madigan (2017) implement MPI parallel sampling as a method of speeding up the ABC algorithm, though still report a wall-time of 4–5 days when running fully parallel. A majority of this time is spent during the forward model simulation, and depends on the systematic uncertainties being accounted for. Once my approximate SALT surface methods have been validated, they represent a significant improvement in the computational cost of forward modelled SN simulations, which will improve the overall wall-time of ABC considerably.

The second issue is determining an appropriate definition of the distance function used in the ABC algorithm. Jennings et al. (2016) consider two distance functions. The first is the Tripp metric, defined as:

$$\delta_{\rm Tripp} = |\Delta_{\rm data} - \Delta_{\rm sim}| \tag{4.6}$$

$$\Delta_{\rm data} = \frac{1}{N_{\rm data}} \sum_i^{N_{\rm data}} \frac{\left[\mu_{\rm model}(z_i^{\rm data}, \theta) - \left(m_i^{\rm data} + \alpha {x_1}_i^{\rm data} - \beta C_i^{\rm data} - \mathcal{M}\right)\right]^2}{\sigma_{m,i}^2 + \left(\alpha\sigma_{x_1,i}\right)^2 + \left(\beta\sigma_{C,i}\right)^2 + \sigma_{int}^2} \tag{4.7}$$

$$\Delta_{\rm sim} = \frac{1}{N_{\rm sim}} \sum_j^{N_{\rm sim}} \frac{\left[\mu_{\rm model}(z_j^{\rm sim}, \theta) - \left(m_j^{\rm sim} + \alpha {x_1}_j^{\rm sim} - \beta C_j^{\rm sim} - \mathcal{M}\right)\right]^2}{\sigma_{m,j}^2 + \left(\alpha\sigma_{x_1,j}\right)^2 + \left(\beta\sigma_{C,j}\right)^2 + \sigma_{int}^2} \tag{4.8}$$

Though the Tripp metric is perhaps the most intuitive metric to use for SN cosmology, it does suffer from the need to fit the light curves of every simulated sample, drastically increasing the computational cost of the ABC algorithm. A cheaper alternative proposed by Jennings et al. (2016) is the light curve metric which forgoes fitting a light curve model and instead directly compares SN fluxes.

Code Block 4.1: Pseudocode of the SMC-ABC algorithm

```
def iterate(data, epsilon, num_particles, prev_particles=[], prev_weights=[], step=0):
    particles = []
    weights = []
    for _ in num_particles:
        # Repeatedly simulate sample until num_particles samples are found with a distance function less than epsilon
        while len(particles) < num_particles:
            if step == 0:
                theta = prior() # Draw   from the prior
            else:
                theta = draw(prev_particles, prev_weights) # Draw   from the previous iteration
            simulation = simulate(theta)
            dist = distance(data, simulation)
            if dist <= epsilon:
                particles.append(theta)
                if step == 0:
                    w = 1 / num_particles
                else:
                    w = weight(theta, prev_particles, prev_weights)
                weights.append(w)
    return particles, weights

def abcsmc(max_iterations, data, init_epsilon, init_num_particles, min_epsilon, max_num_particles):
    particles = []
    weights = []
    epsilon = init_epsilon
    num_particles = init_num_particles
    total_particles = 0
    for i in range(1, max_iterations):
        # Quit early if we've reach the minimum epsilon, or maximum number of simulations
        if epsilon < min_epsilon or total_particles > max_num_particles:
            break
        # Iterate the next step of the SMC-ABC algorithm.
        particles, weights = iterate(data, epsilon, num_particles, particles, weights, i)
        # Update parameters
        total_particles += num_particles
        epsilon = update_epsilon(epsilon, particles, weights)
        num_particles = update_num_particles(num_particles, particles, weight)
    return particles, weights
```

The light curve metric requires first generating two simulated samples from the same reference cosmology, a mock 'data' sample d and a mock 'simulation' sample s, each with the same number of SNe. Each SN in the mock data sample is randomly paired with a SN in the mock simulation sample, and the random variable $\chi_i = \frac{d_i - s(d_i)}{\sigma_i}$ is calculated for each epoch in the mock data sample (d_i). Here $s(d_i)$ is the flux of the mock simulated SN at the ith epoch, and σ_i is the uncertainty in the mock data SN at the ith epoch.

Calculating χ_i for every epoch of every SN in the mock data sample produces a distribution of $\chi = \chi_i \forall_i$. When calculating the light curve metric, this calculation is repeated between the real data and simulated sample, and the difference between the mock χ distribution and the real χ distribution is the distance function.

Though the light curve metric has the advantage of being faster than the Tripp metric, its complexity makes it difficult to assess whether it is well suited to SN cosmology. As such, one will need to investigate both of these metrics, as well as any other suitable candidates, to determine which metric is best for SN cosmology.

4.3 The Future of Pippin

The role of the Pippin SN cosmology pipeline within the DES-SN5YR analysis, and the importance of my developments to this pipeline, are detailed in Chapter 2. Though the Pippin pipeline was a vital component of the DES-SN5YR analysis, the rapid developments of the many software packages underlying the DES-SN5YR analysis revealed an issue in the design of Pippin. It was built to perform a DES-SN3YR-like analysis, and required significant effort to integrate any changes to the analysis. As the SN cosmology field continues to evolve, keeping Pippin up to date will incur a greater technical debt over time.

As such, I am planning a complete rewrite of the Pippin pipeline into a modern, flexible, and highly extendable program called Peregrin[1]. The core concept behind this rewrite is to structure the Peregrin analysis pipeline as a network of `Nodes`. Each `Node` takes a particular type of input, and transforms it into a particular type of output. For example, a SALT3 light curve fitting `Node` might take as input a SN light curve, a trained SALT3 surface, etc... and produce as output the SALT3 light curve parameters for that SN.

This `Node` based design allows Peregrin to serve as a general purpose pipeline manager, allowing many SN cosmology analysis frameworks, such as

[1] Pippin but a little fancier.

DES-SN5YR, ABC, Union, and others, to be created, compared, and shared throughout the SN cosmology community. Additionally, this design allows users to write and inject their own custom `Nodes` directly into the pipeline without needing to interact with the Peregrin source code. This modularity allows individual research to build, test, and deploy `Nodes` independent of the core Peregrin development.

If constructed appropriately, Peregrin will be a future-proof tool with the flexibility needed to keep up to date with the continuously expanding complexity of SN cosmology. As the SN cosmology community works to understand the implications of the DES-SN5YR analysis and prepares for future surveys, this brief moment of calm affords an opportunity to deeply scrutinise the tools and techniques used for our research. With the ever-growing impact of systematic uncertainties on our results, the need for these tools to be testable, extendable, and easy to use and understand, is greater than ever.

Following the DES-SN5YR analysis, the concordance model, ΛCDM, is being seriously challenged for the first time, with questions about the nature of Dark Energy, and how it evolves with time being raised. Answering these questions will require great effort in order to overcome the statistical and systematic limitations we face today. The nature of the *host-luminosity* relation will need to be uncovered, and statistical techniques will need to be developed to properly handle all sources of bias and systematic uncertainty. Throughout the DES-SN5YR analysis, I have enjoyed developing tools to improve SN cosmology analyses, and look forward to building many more to meet the demands of the next stage of SN cosmology.

Bibliography

Abbott, T. M. C.; Abdalla, F. B.; Alarcon, A.; Aleksić, J.; Allam, S.; Allen, S.; Amara, A.; Annis, J.; Asorey, J.; Avila, S.; et al., 2018. Dark Energy Survey year 1 results: Cosmological constraints from galaxy clustering and weak lensing. *Phys. Rev. D*, 98, 4 (Aug. 2018), 043526. doi:10.1103/PhysRevD.98.043526. (cited on page 15)

Abbott, T. M. C.; Aguena, M.; Alarcon, A.; Allam, S.; Alves, O.; Amon, A.; Andrade-Oliveira, F.; Annis, J.; Avila, S.; Bacon, D.; et al., 2022. Dark Energy Survey Year 3 results: Cosmological constraints from galaxy clustering and weak lensing. *Phys. Rev. D*, 105, 2 (Jan. 2022). doi:10.1103/physrevd.105.023520. http://dx.doi.org/10.1103/PhysRevD.105.023520. (cited on pages 49 and 56)

Abbott, T. M. C.; Aguena, M.; Alarcon, A.; Alves, O.; Amon, A.; Andrade-Oliveira, F.; Annis, J.; Avila, S.; Bacon, D.; Baxter, E.; et al., 2023. Dark Energy Survey Year 3 results: Constraints on extensions to ΛCDM with weak lensing and galaxy clustering. *Phys. Rev. D*, 107, 8 (Apr. 2023). doi:10.1103/physrevd.107.083504. http://dx.doi.org/10.1103/PhysRevD.107.083504. (cited on pages 49 and 56)

Abbott, T. M. C.; Allam, S.; Andersen, P.; Angus, C.; Asorey, J.; Avelino, A.; Avila, S.; Bassett, B. A.; Bechtol, K.; Bernstein, G. M.; et al., 2019. First Cosmology Results using Type Ia Supernovae from the Dark Energy Survey: Constraints on Cosmological Parameters. *Astrophys. J.*, 872, 2 (Feb. 2019), L30. doi:10.3847/2041-8213/ab04fa. (cited on pages 25 and 58)

Adams, C. B.; Aggarwal, N.; Agrawal, A.; Balafendiev, R.; Bartram, C.; Baryakhtar, M.; Bekker, H.; Belov, P.; Berggren, K. K.; Berlin, A.; et al., 2023. Axion Dark Matter. (cited on page 6)

Alam, S.; Ata, M.; Bailey, S.; Beutler, F.; Bizyaev, D.; Blazek, J. A.; Bolton, A. S.; Brownstein, J. R.; Burden, A.; Chuang, C.-H.; Comparat, J.; Cuesta, A. J.; Dawson, K. S.; Eisenstein, D. J.; Escoffier, S.; Gil-Marín, H.; Grieb, J. N.; Hand, N.; Ho, S.; Kinemuchi, K.; Kirkby, D.; Kitaura, F.; Malanushenko, E.; Malanushenko, V.; Maraston, C.; McBride, C. K.; Nichol, R. C.; Olmstead, M. D.; Oravetz, D.; Padmanabhan, N.; Palanque-Delabrouille, N.; Pan, K.; Pellejero-Ibanez, M.; Percival, W. J.; Petitjean, P.; Prada, F.; Price-Whelan,

A. M.; Reid, B. A.; Rodríguez-Torres, S. A.; Roe, N. A.; Ross, A. J.; Ross, N. P.; Rossi, G.; Rubiño-Martín, J. A.; Saito, S.; Salazar-Albornoz, S.; Samushia, L.; Sánchez, A. G.; Satpathy, S.; Schlegel, D. J.; Schneider, D. P.; Scóccola, C. G.; Seo, H.-J.; Sheldon, E. S.; Simmons, A.; Slosar, A.; Strauss, M. A.; Swanson, M. E. C.; Thomas, D.; Tinker, J. L.; Tojeiro, R.; Magaña, M. V.; Vazquez, J. A.; Verde, L.; Wake, D. A.; Wang, Y.; Weinberg, D. H.; White, M.; Wood-Vasey, W. M.; Yèche, C.; Zehavi, I.; Zhai, Z.; and Zhao, G.-B., 2017. The clustering of galaxies in the completed SDSS-III Baryon Oscillation Spectroscopic Survey: cosmological analysis of the DR12 galaxy sample. *Mon. Notices Royal Astron. Soc.*, 470, 3 (Mar. 2017), 2617–2652. doi:10.1093/mnras/stx721. http://dx.doi.org/10.1093/mnras/stx721. (cited on page 50)

Alam, S.; Aubert, M.; Avila, S.; Balland, C.; Bautista, J. E.; Bershady, M. A.; Bizyaev, D.; Blanton, M. R.; Bolton, A. S.; Bovy, J.; Brinkmann, J.; Brownstein, J. R.; Burtin, E.; Chabanier, S.; Chapman, M. J.; Choi, P. D.; Chuang, C.-H.; Comparat, J.; Cousinou, M.-C.; Cuceu, A.; Dawson, K. S.; de la Torre, S.; de Mattia, A.; Agathe, V. d. S.; des Bourboux, H. d. M.; Escoffier, S.; Etourneau, T.; Farr, J.; Font-Ribera, A.; Frinchaboy, P. M.; Fromenteau, S.; Gil-Marín, H.; Le Goff, J.-M.; Gonzalez-Morales, A. X.; Gonzalez-Perez, V.; Grabowski, K.; Guy, J.; Hawken, A. J.; Hou, J.; Kong, H.; Parker, J.; Klaene, M.; Kneib, J.-P.; Lin, S.; Long, D.; Lyke, B. W.; de la Macorra, A.; Martini, P.; Masters, K.; Mohammad, F. G.; Moon, J.; Mueller, E.-M.; Muñoz-Gutiérrez, A.; Myers, A. D.; Nadathur, S.; Neveux, R.; Newman, J. A.; Noterdaeme, P.; Oravetz, A.; Oravetz, D.; Palanque-Delabrouille, N.; Pan, K.; Paviot, R.; Percival, W. J.; Pérez-Ràfols, I.; Petitjean, P.; Pieri, M. M.; Prakash, A.; Raichoor, A.; Ravoux, C.; Rezaie, M.; Rich, J.; Ross, A. J.; Rossi, G.; Ruggeri, R.; Ruhlmann-Kleider, V.; Sánchez, A. G.; Sánchez, F. J.; Sánchez-Gallego, J. R.; Sayres, C.; Schneider, D. P.; Seo, H.-J.; Shafieloo, A.; Slosar, A.; Smith, A.; Stermer, J.; Tamone, A.; Tinker, J. L.; Tojeiro, R.; Vargas-Magaña, M.; Variu, A.; Wang, Y.; Weaver, B. A.; Weijmans, A.-M.; Yèche, C.; Zarrouk, P.; Zhao, C.; Zhao, G.-B.; and Zheng, Z., 2021. Completed SDSS-IV extended Baryon Oscillation Spectroscopic Survey: Cosmological implications from two decades of spectroscopic surveys at the Apache Point Observatory. *Phys. Rev. D*, 103, 8 (Apr. 2021). doi:10.1103/physrevd.103.083533. http://dx.doi.org/10.1103/PhysRevD.103.083533. (cited on page 56)

Alcock, C.; Allsman, R. A.; Alves, D. R.; Axelrod, T. S.; Becker, A. C.; Bennett, D. P.; Cook, K. H.; Dalal, N.; Drake, A. J.; Freeman, K. C.; et al., 2000. The MACHO Project: Microlensing Results from 5.7 Years of Large Magellanic Cloud Observations. *The Astrophys. J.*, 542, 1 (Oct. 2000), 281–307. doi:10.1086/309512. http://dx.doi.org/10.1086/309512. (cited on page 6)

Aldering, G., 2000. Type Ia supernovae & cosmic acceleration. In *AIP Conference Proceedings*. Aip. doi:10.1063/1.1291697. http://dx.doi.org/10.1063/1.1291697. (cited on page 46)

Amanullah, R.; Lidman, C.; Rubin, D.; Aldering, G.; Astier, P.; Barbary, K.; Burns, M. S.; Conley, A.; Dawson, K. S.; Deustua, S. E.; et al., 2010. Spectra and Hubble Space Telescope light curves of six Type Ia supernovae at $0.511 < z < 1.12$ and the Union2 compilation. *The Astrophys. J.*, 716, 1 (May 2010), 712–738. doi:10.1088/0004-637x/716/1/712. http://dx.doi.org/10.1088/0004-637X/716/1/712. (cited on pages 25, 43, and 47)

Amanullah, R.; Stanishev, V.; Goobar, A.; Schahmaneche, K.; Astier, P.; Balland, C.; Ellis, R. S.; Fabbro, S.; Hardin, D.; Hook, I. M.; et al., 2008. Light curves of five Type Ia supernovae at intermediate redshift. *Astron. & Astrophys.*, 486, 2 (May 2008), 375–382. doi:10.1051/0004-6361:20079070. http://dx.doi.org/10.1051/0004-6361:20079070. (cited on page 47)

Ananda, K. N. and Bruni, M., 2006. Cosmological dynamics and dark energy with a nonlinear equation of state: A quadratic model. *Phys. Rev. D*, 74, 2 (Jul. 2006). doi:10.1103/physrevd.74.023523. http://dx.doi.org/10.1103/PhysRevD.74.023523. (cited on page 8)

Armstrong, P.; Qu, H.; Brout, D.; Davis, T. M.; Kessler, R.; Kim, A. G.; Lidman, C.; Sako, M.; and Tucker, B. E., 2023. Probing the consistency of cosmological contours for supernova cosmology. *Publ. Astron. Soc. Aust.*, 40 (2023). doi:10.1017/pasa.2023.40. https://doi.org/10.1017/pasa.2023.40. (cited on pages 57 and 124)

Asgari, M.; Lin, C.; Joachimi, B.; Giblin, B.; Heymans, C.; Hildebrandt, H.; Kannawadi, A.; Stölzner, B.; Tröster, T.; van, D. B. J. L.; et al., 2021. KiDS-1000 cosmology: Cosmic shear constraints and comparison between two point statistics. *Astron. & Astrophys.*, 645 (Jan. 2021), A104. doi:10.1051/0004-6361/202039070. http://dx.doi.org/10.1051/0004-6361/202039070. (cited on page 15)

Astier, P.; Guy, J.; Regnault, N.; Pain, R.; Aubourg, E.; Balam, D.; Basa, S.; Carlberg, R. G.; Fabbro, S.; Fouchez, D.; et al., 2006. The Supernova Legacy Survey: Measurement of Ω_M, Ω_Λ, and w from the first year data set. *Astron. & Astrophys.*, 447, 1 (Feb. 2006), 31–48. doi:10.1051/0004-6361:20054185. (cited on pages 25, 35, 36, 40, 46, and 47)

Aubourg, E.; Bailey, S.; Bautista, J. E.; Beutler, F.; Bhardwaj, V.; Bizyaev, D.; Blanton, M.; Blomqvist, M.; Bolton, A. S.; Bovy, J.; et al., 2015. Cosmological implications of baryon acoustic oscillation measurements. *Phys. Rev. D*, 92

(Dec. 2015), 123516. doi:10.1103/PhysRevD.92.123516. https://link.aps.org/doi/10.1103/PhysRevD.92.123516. (cited on page 13)

Babichev, E. O., 2005. The Accretion of Dark Energy onto a Black Hole. *J. Exp. Theor. Phys.*, 100, 3 (2005), 528. doi:10.1134/1.1901765. http://dx.doi.org/10.1134/1.1901765. (cited on page 8)

Bacon, D. J.; Refregier, A. R.; and Ellis, R. S., 2000. Detection of weak gravitational lensing by large-scale structure. *Mon. Notices Royal Astron. Soc.*, 318, 2 (Oct. 2000), 625–640. doi:10.1046/j.1365-8711.2000.03851.x. https://doi.org/10.1046/j.1365-8711.2000.03851.x. (cited on page 15)

Bailer-Jones, C. A. L.; Rybizki, J.; Fouesneau, M.; Demleitner, M.; and Andrae, R., 2021. Estimating Distances from Parallaxes. V. Geometric and Photogeometric Distances to 1.47 Billion Stars in Gaia Early Data Release 3. *Astron. J.*, 161, 3 (Mar. 2021), 147. doi:10.3847/1538-3881/abd806. (cited on page 12)

Balland, C.; Baumont, S.; Basa, S.; Mouchet, M.; Howell, D. A.; Astier, P.; Carlberg, R. G.; Conley, A.; Fouchez, D.; Guy, J.; et al., 2009. The ESO/VLT 3rd year Type Ia supernova data set from the supernova legacy survey. *Astron. & Astrophys.*, 507, 1 (Aug. 2009), 85–103. doi:10.1051/0004-6361/200912246. http://dx.doi.org/10.1051/0004-6361/200912246. (cited on page 36)

Balland, C.; Cellier-Holzem, F.; Lidman, C.; Astier, P.; Betoule, M.; Carlberg, R. G.; Conley, A.; Ellis, R. S.; Guy, J.; Hardin, D.; et al., 2018. The ESO's VLT Type Ia supernova spectral set of the final two years of SNLS. *Astron. & Astrophys.*, 614 (Jun. 2018), A134. doi:10.1051/0004-6361/201731924. http://dx.doi.org/10.1051/0004-6361/201731924. (cited on page 36)

Barris, B. J.; Tonry, J. L.; Blondin, S.; Challis, P.; Chornock, R.; Clocchiatti, A.; Filippenko, A. V.; Garnavich, P.; Holland, S. T.; Jha, S.; et al., 2004. Twenty-Three High-Redshift Supernovae from the Institute for Astronomy Deep Survey: Doubling the Supernova Sample at $z > 0.7$. *The Astrophys. J.*, 602, 2 (Feb. 2004), 571–594. doi:10.1086/381122. http://dx.doi.org/10.1086/381122. (cited on pages 45 and 46)

Bassett, B. A. and Hlozek, R., 2009. Baryon Acoustic Oscillations. (cited on page 13)

Beaumont, M. A.; Cornuet, J. M.; Marin, J. M.; and Robert, C. P., 2009. Adaptive approximate Bayesian computation. *Biometrika*, 96, 4 (Oct. 2009), 983–990. doi:10.1093/biomet/asp052. http://dx.doi.org/10.1093/biomet/asp052. (cited on page 153)

Bellm, E. C.; Kulkarni, S. R.; Graham, M. J.; Dekany, R.; Smith, R. M.; Riddle, R.; Masci, F. J.; Helou, G.; Prince, T. A.; Adams, S. M.; et al., 2018. The Zwicky Transient Facility: System Overview, Performance, and First Results. *Publ. Astron. Soc. Pac.*, 131, 995 (Dec. 2018), 018002. doi:10.1088/1538-3873/aaecbe. http://dx.doi.org/10.1088/1538-3873/aaecbe. (cited on page 50)

Bennett, D. P.; Alcock, C.; Allsman, R. A.; Axelrod, T. S.; Cook, K. H.; Freeman, K. C.; Griest, K.; Marshall, S. L.; Peterson, B. A.; Pratt, M. R.; et al., 1995. The MACHO Project Dark Matter Search. (cited on page 6)

Bento, M. C.; Bertolami, O.; and Sen, A. A., 2002. Generalized Chaplygin gas, accelerated expansion, and dark-energy-matter unification. *Phys. Rev. D*, 66, 4 (Aug. 2002). doi:10.1103/physrevd.66.043507. http://dx.doi.org/10.1103/PhysRevD.66.043507. (cited on page 8)

Bertone, G. and Hooper, D., 2018. History of dark matter. *Rev. Mod. Phys.*, 90, 4 (Oct. 2018), 045002. doi:10.1103/RevModPhys.90.045002. (cited on page 2)

Betoule, M.; Kessler, R.; Guy, J.; Mosher, J.; Hardin, D.; Biswas, R.; Astier, P.; El-Hage, P.; Konig, M.; Kuhlmann, S.; et al., 2014. Improved cosmological constraints from a joint analysis of the SDSS-II and SNLS supernova samples. *Astron. & Astrophys.*, 568 (Aug. 2014), A22. doi:10.1051/0004-6361/201423413. (cited on pages 18, 25, 47, and 149)

Betoule, M.; Marriner, J.; Regnault, N.; Cuillandre, J. C.; Astier, P.; Guy, J.; Balland, C.; El, H. P.; Hardin, D.; Kessler, R.; et al., 2013. Improved photometric calibration of the SNLS and the SDSS supernova surveys. *Astron. & Astrophys.*, 552 (Apr. 2013), A124. doi:10.1051/0004-6361/201220610. http://dx.doi.org/10.1051/0004-6361/201220610. (cited on page 47)

Beutler, F.; Blake, C.; Colless, M.; Jones, D. H.; Staveley-Smith, L.; Campbell, L.; Parker, Q.; Saunders, W.; and Watson, F., 2011. The 6dF Galaxy Survey: baryon acoustic oscillations and the local Hubble constant: 6dFGS: BAOs and the local Hubble constant. *Mon. Notices Royal Astron. Soc.*, 416, 4 (2011), 3017–3032. doi:10.1111/j.1365-2966.2011.19250.x. http://dx.doi.org/10.1111/j.1365-2966.2011.19250.x. (cited on page 50)

Bilić, N.; Tupper, G. B.; and Viollier, R. D., 2002. Unification of dark matter and dark energy: the inhomogeneous Chaplygin gas. *Phys. Lett. B*, 535, 1–4 (May 2002), 17–21. doi:10.1016/s0370-2693(02)01716-1. http://dx.doi.org/10.1016/S0370-2693(02)01716-1. (cited on page 8)

Blumenthal, G. R.; Faber, S. M.; Primack, J. R.; and Rees, M. J., 1984. Formation of galaxies and large-scale structure with cold dark matter. *Nature*, 311, 5986 (Oct. 1984), 517–525. doi:10.1038/311517a0. https://doi.org/10.1038/311517a0. (cited on page 6)

Bohlin, R. C.; Gordon, K. D.; and Tremblay, P. E., 2014. Techniques and Review of Absolute Flux Calibration from the Ultraviolet to the Mid-Infrared. *Publ. Astron. Soc. Pac.*, (Jul. 2014), 000–000. doi:10.1086/677655. http://dx.doi.org/10.1086/677655. (cited on page 52)

Bozza, V. and Bruni, M., 2009. A solution to the anisotropy problem in bouncing cosmologies. *J. Cosmol. Astropart. Phys.*, 2009, 10 (Oct. 2009), 014–014. doi:10.1088/1475-7516/2009/10/014. http://dx.doi.org/10.1088/1475-7516/2009/10/014. (cited on page 8)

Briday, M.; Rigault, M.; Graziani, R.; Copin, Y.; Aldering, G.; Amenouche, M.; Brinnel, V.; Kim, A. G.; Kim, Y. L.; Lezmy, J.; et al., 2021. Accuracy of environmental tracers and consequences for determining the Type Ia supernova magnitude step. *Astron. & Astrophys.*, 657 (Dec. 2021), A22. doi:10.1051/0004-6361/202141160. http://dx.doi.org/10.1051/0004-6361/202141160. (cited on page 148)

Bronder, T. J.; Hook, I. M.; Astier, P.; Balam, D.; Balland, C.; Basa, S.; Carlberg, R. G.; Conley, A.; Fouchez, D.; Guy, J.; et al., 2007. SNLS spectroscopy: testing for evolution in Type Ia supernovae. *Astron. & Astrophys.*, 477, 3 (Aug. 2007), 717–734. doi:10.1051/0004-6361:20077655. http://dx.doi.org/10.1051/0004-6361:20077655. (cited on page 36)

Brout, D.; Hinton, S. R.; and Scolnic, D., 2021. Binning is Sinning (Supernova Version): The Impact of Self-calibration in Cosmological Analyses with Type Ia Supernovae. *Astrophys. J.*, 912, 2 (May 2021), L26. doi:10.3847/2041-8213/abf4db. (cited on pages 51, 53, 113, 120, 122, and 128)

Brout, D.; Sako, M.; Scolnic, D.; Kessler, R.; D'Andrea, C. B.; Davis, T. M.; Hinton, S. R.; Kim, A. G.; Lasker, J.; Macaulay, E.; et al., 2019a. First Cosmology Results Using Type Ia Supernovae from the Dark Energy Survey: Photometric Pipeline and Light-curve Data Release. *Astrophys. J.*, 874, 1 (Mar. 2019), 106. doi:10.3847/1538-4357/ab06c1. (cited on pages 49 and 129)

Brout, D. and Scolnic, D., 2021. It's Dust: Solving the Mysteries of the Intrinsic Scatter and Host-galaxy Dependence of Standardized Type Ia Supernova Brightnesses. *The Astrophys. J.*, 909, 1 (Mar. 2021), 26. doi:10.3847/1538-4357/abd69b. http://dx.doi.org/10.3847/1538-4357/abd69b. (cited on pages 18, 38, 98, and 122)

Brout, D.; Scolnic, D.; Kessler, R.; D'Andrea, C. B.; Davis, T. M.; Gupta, R. R.; Hinton, S. R.; Kim, A. G.; Lasker, J.; Lidman, C.; et al., 2019b. First

Cosmology Results Using SNe Ia from the Dark Energy Survey: Analysis, Systematic Uncertainties, and Validation. *Astrophys. J.*, 874, 2 (Apr. 2019), 150. doi:10.3847/1538-4357/ab08a0. (cited on pages 50, 58, 79, 121, and 126)

Brout, D.; Scolnic, D.; Popovic, B.; Riess, A. G.; Carr, A.; Zuntz, J.; Kessler, R.; Davis, T. M.; Hinton, S.; Jones, D.; et al., 2022a. The Pantheon+ Analysis: Cosmological Constraints. *The Astrophys. J.*, 938, 2 (Oct. 2022), 110. doi:10.3847/1538-4357/ac8e04. https://dx.doi.org/10.3847/1538-4357/ac8e04. (cited on pages 25, 53, 120, and 125)

Brout, D.; Taylor, G.; Scolnic, D.; Wood, C. M.; Rose, B. M.; Vincenzi, M.; Dwomoh, A.; Lidman, C.; Riess, A.; Ali, N.; et al., 2022b. The Pantheon+ Analysis: SuperCal-fragilistic Cross Calibration, Retrained SALT2 Light-curve Model, and Calibration Systematic Uncertainty. *The Astrophys. J.*, 938, 2 (Oct. 2022), 111. doi:10.3847/1538-4357/ac8bcc. http://dx.doi.org/10.3847/1538-4357/ac8bcc. (cited on pages 51, 77, 100, 120, 122, and 149)

Brownsberger, S. R.; Brout, D.; Scolnic, D.; Stubbs, C. W.; and Riess, A. G., 2023. Dependence of Cosmological Constraints on Gray Photometric Zero-point Uncertainties of Supernova Surveys. *The Astrophys. J.*, 944, 2 (Feb. 2023), 188. doi:10.3847/1538-4357/acad80. http://dx.doi.org/10.3847/1538-4357/acad80. (cited on page 122)

Bunn, E. F. and Hogg, D. W., 2009. The kinematic origin of the cosmological redshift. *Am. J. Phys.*, 77, 8 (Aug. 2009), 688–694. doi:10.1119/1.3129103. http://dx.doi.org/10.1119/1.3129103. (cited on pages 10 and 11)

Burger, P. A.; Friedrich, O.; Harnois-Déraps, J.; Schneider, P.; Asgari, M.; Bilicki, M.; Hildebrandt, H.; Wright, A. H.; Castro, T.; Dolag, K.; et al., 2023. KiDS-1000 cosmology: Constraints from density split statistics. *Astron. & Astrophys.*, 669 (Jan. 2023), A69. doi:10.1051/0004-6361/202244673. http://dx.doi.org/10.1051/0004-6361/202244673. (cited on page 15)

Burns, C. R.; Stritzinger, M.; Phillips, M. M.; Kattner, S.; Persson, S. E.; Madore, B. F.; Freedman, W. L.; Boldt, L.; Campillay, A.; Contreras, C.; et al., 2010. The Carnegie Supernova Project: Light-Curve Fitting with SNooPy. *The Astron. J.*, 141, 1 (Dec. 2010), 19. doi:10.1088/0004-6256/141/1/19. http://dx.doi.org/10.1088/0004-6256/141/1/19. (cited on page 80)

Calcino, J. and Davis, T., 2017. The need for accurate redshifts in supernova cosmology. *J. Cosmol. Astropart. Phys.*, 2017, 01 (Jan. 2017), 038–038. doi:10.1088/1475-7516/2017/01/038. http://dx.doi.org/10.1088/1475-7516/2017/01/038. (cited on page 117)

Camilleri, R.; Davis, T. M.; Hinton, S. R.; Armstrong, P.; Brout, D.; Galbany, L.; Glazebrook, K.; Lee, J.; Lidman, C.; Nichol, R. C.; et al., 2024a. The Dark Energy Survey Supernova Program: An updated measurement of the Hubble constant using the Inverse Distance Ladder. *arXiv e-prints*, (Jun. 2024), arXiv:2406.05049. doi:10.48550/arXiv.2406.05049. (cited on page 13)

Camilleri, R.; Davis, T. M.; Vincenzi, M.; Shah, P.; Frieman, J.; Kessler, R.; Armstrong, P.; Brout, D.; Carr, A.; Chen, R.; et al., 2024b. The Dark Energy Survey Supernova Program: Investigating Beyond ΛCDM. *arXiv e-prints*, (Jun. 2024), arXiv:2406.05048. doi:10.48550/arXiv.2406.05048. (cited on pages 122 and 124)

Campbell, H.; Fraser, M.; and Gilmore, G., 2016. How SN Ia host-galaxy properties affect cosmological parameters. *Mon. Notices Royal Astron. Soc.*, 457, 4 (Feb. 2016), 3470–3491. doi:10.1093/mnras/stw115. http://dx.doi.org/10.1093/mnras/stw115. (cited on pages 38 and 98)

Capozziello, S.; Cardone, V. F.; Carloni, S.; Martino, S. D.; Falanga, M.; Troisi, A.; and Bruni, M., 2005. Constraining Van der Waals quintessence with observations. *J. Cosmol. Astropart. Phys.*, 2005, 04 (Apr. 2005), 005–005. doi:10.1088/1475-7516/2005/04/005. http://dx.doi.org/10.1088/1475-7516/2005/04/005. (cited on page 8)

Cardelli, J. A.; Clayton, G. C.; and Mathis, J. S., 1989. The relationship between infrared, optical, and ultraviolet extinction. *The Astrophys. J.*, 345 (Oct. 1989), 245. doi:10.1086/167900. http://dx.doi.org/10.1086/167900. (cited on pages 93 and 117)

Carr, A.; Davis, T. M.; Scolnic, D.; Said, K.; Brout, D.; Peterson, E. R.; and Kessler, R., 2022. The Pantheon+ analysis: Improving the redshifts and peculiar velocities of Type Ia supernovae used in cosmological analyses. *Publ. Astron. Soc. Aust.*, 39 (2022). doi:10.1017/pasa.2022.41. http://dx.doi.org/10.1017/pasa.2022.41. (cited on page 122)

Cfhtls, 2002. CFHTLS: Canada-France-Hawaii Telescope Legacy Survey Home Page — cfht.hawaii.edu. Accessed 01-02-2024. (cited on page 35)

Chambers, K. C.; Magnier, E. A.; Metcalfe, N.; Flewelling, H. A.; Huber, M. E.; Waters, C. Z.; Denneau, L.; Draper, P. W.; Farrow, D.; Finkbeiner, D. P.; et al., 2016. The Pan-STARRS1 Surveys. *arXiv e-prints*, (Dec. 2016), arXiv:1612.05560. (cited on page 41)

Chen, H.; Fishbach, M.; and Holz, D. E., 2018. A two per cent Hubble constant measurement from standard sirens within five years. *Nature*, 562, 7728 (Oct.

2018), 545–547. doi:10.1038/s41586-018-0606-0. https://doi.org/10.1038/s41586-018-0606-0. (cited on page 16)

Chen, R.; Scolnic, D.; Rozo, E.; Rykoff, E. S.; Popovic, B.; Kessler, R.; Vincenzi, M.; Davis, T. M.; Armstrong, P.; Brout, D.; et al., 2022. Measuring Cosmological Parameters with Type Ia Supernovae in redMaGiC Galaxies. *The Astrophys. J.*, 938, 1 (Oct. 2022), 62. doi:10.3847/1538-4357/ac8b82. http://dx.doi.org/10.3847/1538-4357/ac8b82. (cited on page 122)

Chen, R.; Scolnic, D.; Vincenzi, M.; Rykoff, E. S.; Myles, J.; Kessler, R.; Popovic, B.; Sako, M.; Smith, M.; Armstrong, P.; et al., 2024. Evaluating Cosmological Biases using Photometric Redshifts for Type Ia Supernova Cosmology with the Dark Energy Survey Supernova Program. *arXiv e-prints*, (2024). doi:10.48550/arxiv.2407.16744. https://arxiv.org/abs/2407.16744. (cited on page 117)

Chevallier, M. and Polarski, D., 2001. Accelerating Universes With Scaling Dark Matter. *Int. J. Mod. Phys. D*, 10, 02 (Apr. 2001), 213–223. doi:10.1142/s0218271801000822. http://dx.doi.org/10.1142/S0218271801000822. (cited on page 7)

Childress, M.; Aldering, G.; Antilogus, P.; Aragon, C.; Bailey, S.; Baltay, C.; Bongard, S.; Buton, C.; Canto, A.; Cellier-Holzem, F.; et al., 2013. Host Galaxies of Type Ia Supernovae from the Nearby Supernova Factory. *Astrophys. J.*, 770, 2 (Jun. 2013), 107. doi:10.1088/0004-637x/770/2/107. (cited on pages 38 and 98)

Childress, M. J.; Lidman, C.; Davis, T. M.; Tucker, B. E.; Asorey, J.; Yuan, F.; Abbott, T. M. C.; Abdalla, F. B.; Allam, S.; Annis, J.; et al., 2017. OzDES multifibre spectroscopy for the Dark Energy Survey: 3-yr results and first data release. *Mon. Notices Royal Astron. Soc.*, 472, 1 (Jul. 2017), 273–288. doi:10.1093/mnras/stx1872. http://dx.doi.org/10.1093/mnras/stx1872. (cited on pages 79 and 105)

Chotard, N.; Gangler, E.; Aldering, G.; Antilogus, P.; Aragon, C.; Bailey, S.; Baltay, C.; Bongard, S.; Buton, C.; Canto, A.; Childress, M.; Copin, Y.; Fakhouri, H. K.; Hsiao, E. Y.; Kerschhaggl, M.; Kowalski, M.; Loken, S.; Nugent, P.; Paech, K.; Pain, R.; Pecontal, E.; Pereira, R.; Perlmutter, S.; Rabinowitz, D.; Runge, K.; Scalzo, R.; Smadja, G.; Tao, C.; Thomas, R. C.; Weaver, B. A.; and Wu, C., 2011. The reddening law of type Ia supernovae: separating intrinsic variability from dust using equivalent widths. *Astron. & Astrophys.*, 529 (Apr. 2011), L4. doi:10.1051/0004-6361/201116723. http://dx.doi.org/10.1051/0004-6361/201116723. (cited on page 87)

Conley, A.; Guy, J.; Sullivan, M.; Regnault, N.; Astier, P.; Balland, C.; Basa, S.; Carlberg, R. G.; Fouchez, D.; Hardin, D.; et al., 2011. Supernova Constraints and Systematic Uncertainties from the First Three Years of the Supernova Legacy Survey. *Astrophys. Journals*, 192, 1 (Jan. 2011), 1. doi:10.1088/0067-0049/192/1/1. (cited on pages 25, 35, 38, 42, 47, and 125)

Conley, A.; Sullivan, M.; Hsiao, E. Y.; Guy, J.; Astier, P.; Balam, D.; Balland, C.; Basa, S.; Carlberg, R. G.; Fouchez, D.; et al., 2008. SiFTO: An Empirical Method for Fitting SN Ia Light Curves. *The Astrophys. J.*, 681, 1 (Jul. 2008), 482–498. doi:10.1086/588518. http://dx.doi.org/10.1086/588518. (cited on page 36)

Contreras, C.; Hamuy, M.; Phillips, M. M.; Folatelli, G.; Suntzeff, N. B.; Persson, S. E.; Stritzinger, M.; Boldt, L.; Gonzá lez, S.; Krzeminski, W.; et al., 2010. The Carnegie Supernova Project: First Photometry Data Release of Low-Redshift Type Ia Supernovae. *Astron. J.*, 139, 2 (Feb. 2010), 519–539. doi:10.1088/0004-6256/139/2/519. (cited on page 44)

Cousins, A. W. J., 1976. VRI standards in the E regions. *Memoirs Royal Astron. Soc.*, 81 (Jan. 1976), 25. (cited on page 44)

Croft, R. A. C. and Dailey, M., 2015. On the measurement of cosmological parameters. (cited on page 19)

Dai, M.; Jones, D. O.; Kenworthy, W. D.; Kessler, R.; Pierel, J. D. R.; Foley, R. J.; Jha, S. W.; and Scolnic, D. M., 2023. Propagating Uncertainties in the SALT3 Model-training Process to Cosmological Constraints. *The Astrophys. J. Suppl. Ser.*, 267, 1 (Jun. 2023), 1. doi:10.3847/1538-4365/acd051. http://dx.doi.org/10.3847/1538-4365/acd051. (cited on pages 122 and 148)

Dark Energy Survey Collaboration; Abbott, T.; Abdalla, F. B.; Aleksić, J.; Allam, S.; Amara, A.; Bacon, D.; Balbinot, E.; Banerji, M.; Bechtol, K.; et al., 2016. The Dark Energy Survey: more than dark energy - an overview. *Mon. Notices Royal Astron. Soc.*, 460, 2 (Aug. 2016), 1270–1299. doi:10.1093/mnras/stw641. (cited on page 125)

Davies, R. L.; Efstathiou, G.; Fall, S. M.; Illingworth, G.; and Schechter, P. L., 1983. The kinematic properties of faint elliptical galaxies. *Astrophys. J.*, 266 (Mar. 1983), 41–57. doi:10.1086/160757. (cited on page 6)

Davis, T. M.; Hinton, S. R.; Howlett, C.; and Calcino, J., 2019. Can redshift errors bias measurements of the Hubble Constant? *Mon. Notices Royal Astron. Soc.*, 490, 2 (Sep. 2019), 2948–2957. doi:10.1093/mnras/stz2652. https://doi.org/10.1093/mnras/stz2652. (cited on page 9)

Dawson, K. S.; Kneib, J.-P.; Percival, W. J.; Alam, S.; Albareti, F. D.; Anderson, S. F.; Armengaud, E.; Aubourg, □.; Bailey, S.; Bautista, J. E.; Berlind, A. A.;

Bershady, M. A.; Beutler, F.; Bizyaev, D.; Blanton, M. R.; Blomqvist, M.; Bolton, A. S.; Bovy, J.; Brandt, W. N.; Brinkmann, J.; Brownstein, J. R.; Burtin, E.; Busca, N. G.; Cai, Z.; Chuang, C.-H.; Clerc, N.; Comparat, J.; Cope, F.; Croft, R. A. C.; Cruz-Gonzalez, I.; Costa, L. N. d.; Cousinou, M.-C.; Darling, J.; Macorra, A. d. l.; Torre, S. d. l.; Delubac, T.; Bourboux, H. d. M. d.; Dwelly, T.; Ealet, A.; Eisenstein, D. J.; Eracleous, M.; Escoffier, S.; Fan, X.; Finoguenov, A.; Font-Ribera, A.; Frinchaboy, P.; Gaulme, P.; Georgakakis, A.; Green, P.; Guo, H.; Guy, J.; Ho, S.; Holder, D.; Huehnerhoff, J.; Hutchinson, T.; Jing, Y.; Jullo, E.; Kamble, V.; Kinemuchi, K.; Kirkby, D.; Kitaura, F.-S.; Klaene, M. A.; Laher, R. R.; Lang, D.; Laurent, P.; Goff, J.-M. L.; Li, C.; Liang, Y.; Lima, M.; Lin, Q.; Lin, W.; Lin, Y.-T.; Long, D. C.; Lundgren, B.; MacDonald, N.; Maia, M. A. G.; Malanushenko, E.; Malanushenko, V.; Mariappan, V.; McBride, C. K.; McGreer, I. D.; Ménard, B.; Merloni, A.; Meza, A.; Montero-Dorta, A. D.; Muna, D.; Myers, A. D.; Nandra, K.; Naugle, T.; Newman, J. A.; Noterdaeme, P.; Nugent, P.; Ogando, R.; Olmstead, M. D.; Oravetz, A.; Oravetz, D. J.; Padmanabhan, N.; Palanque-Delabrouille, N.; Pan, K.; Parejko, J. K.; Pâris, I.; Peacock, J. A.; Petitjean, P.; Pieri, M. M.; Pisani, A.; Prada, F.; Prakash, A.; Raichoor, A.; Reid, B.; Rich, J.; Ridl, J.; Rodriguez-Torres, S.; Rosell, A. C.; Ross, A. J.; Rossi, G.; Ruan, J.; Salvato, M.; Sayres, C.; Schneider, D. P.; Schlegel, D. J.; Seljak, U.; Seo, H.-J.; Sesar, B.; Shandera, S.; Shu, Y.; Slosar, A.; Sobreira, F.; Streblyanska, A.; Suzuki, N.; Taylor, D.; Tao, C.; Tinker, J. L.; Tojeiro, R.; Vargas-Magaña, M.; Wang, Y.; Weaver, B. A.; Weinberg, D. H.; White, M.; Wood-Vasey, W. M.; Yeche, C.; Zhai, Z.; Zhao, C.; Zhao, G.-b.; Zheng, Z.; Zhu, G. B.; and Zou, H., 2016. THE SDSS-IV EXTENDED BARYON OSCILLATION SPECTROSCOPIC SURVEY: OVERVIEW AND EARLY DATA. *The Astron. J.*, 151, 2 (Feb. 2016), 44. doi:10.3847/0004-6256/151/2/44. http://dx.doi.org/10.3847/0004-6256/151/2/44. (cited on page 56)

DES Collaboration; Abbott, T. M. C.; Acevedo, M.; Aguena, M.; Alarcon, A.; Allam, S.; Alves, O.; Amon, A.; Andrade-Oliveira, F.; Annis, J.; et al., 2024a. The Dark Energy Survey: Cosmology Results With ~1500 New High-redshift Type Ia Supernovae Using The Full 5-year Dataset. *arXiv e-prints*, (Jan. 2024), arXiv:2401.02929. doi:10.48550/arXiv.2401.02929. (cited on pages 2, 25, 49, 56, 59, and 123)

DES Collaboration; Abbott, T. M. C.; Adamow, M.; Aguena, M.; Allam, S.; Alves, O.; Amon, A.; Andrade-Oliveira, F.; Asorey, J.; Avila, S.; et al., 2024b. Dark Energy Survey: A 2.1% measurement of the angular Baryonic Acoustic Oscillation scale at redshift $z_{\rm eff} = 0.85$ from the final dataset. *arXiv e-prints*, (Feb. 2024), arXiv:2402.10696. doi:10.48550/arXiv.2402.10696. (cited on page

49)

DESI Collaboration; Adame, A. G.; Aguilar, J.; Ahlen, S.; Alam, S.; Alexander, D. M.; Alvarez, M.; Alves, O.; Anand, A.; Andrade, U.; et al., 2024a. DESI 2024 III: Baryon Acoustic Oscillations from Galaxies and Quasars. *arXiv e-prints*, (Apr. 2024), arXiv:2404.03000. doi:10.48550/arXiv.2404.03000. (cited on page 54)

DESI Collaboration; Adame, A. G.; Aguilar, J.; Ahlen, S.; Alam, S.; Alexander, D. M.; Alvarez, M.; Alves, O.; Anand, A.; Andrade, U.; et al., 2024b. DESI 2024 VI: Cosmological Constraints from the Measurements of Baryon Acoustic Oscillations. *arXiv e-prints*, (Apr. 2024), arXiv:2404.03002. doi:10.48550/arXiv.2404.03002. (cited on pages 54 and 146)

Dhawan, S.; Goobar, A.; Smith, M.; Johansson, J.; Rigault, M.; Nordin, J.; Biswas, R.; Goldstein, D.; Nugent, P.; Kim, Y.; et al., 2021. The Zwicky Transient Facility Type Ia supernova survey: first data release and results. *Mon. Notices Royal Astron. Soc.*, 510, 2 (Nov. 2021), 2228–2241. doi:10.1093/mnras/stab3093. http://dx.doi.org/10.1093/mnras/stab3093. (cited on page 50)

Dicke, R. H.; Peebles, P. J. E.; Roll, P. G.; and Wilkinson, D. T., 1965. Cosmic Black-Body Radiation. *The Astrophys. J.*, 142 (Jul. 1965), 414. doi:10.1086/148306. http://dx.doi.org/10.1086/148306. (cited on page 14)

Dilday, B.; Kessler, R.; Frieman, J. A.; Holtzman, J.; Marriner, J.; Miknaitis, G.; Nichol, R. C.; Romani, R.; Sako, M.; Bassett, B.; et al., 2008. A Measurement of the Rate of Type Ia Supernovae at Redshift $z \approx 0.1$ from the First Season of the SDSS-II Supernova Survey. *The Astrophys. J.*, 682, 1 (Jul. 2008), 262–282. doi:10.1086/587733. http://dx.doi.org/10.1086/587733. (cited on page 41)

Dixon, M.; Lidman, C.; Mould, J.; Kelsey, L.; Brout, D.; Möller, A.; Wiseman, P.; Sullivan, M.; Galbany, L.; Davis, T. M.; et al., 2022. Using host galaxy spectroscopy to explore systematics in the standardization of Type Ia supernovae. *Mon. Notices Royal Astron. Soc.*, 517, 3 (Oct. 2022), 4291–4304. doi:10.1093/mnras/stac2994. http://dx.doi.org/10.1093/mnras/stac2994. (cited on pages 38 and 98)

Dopita, M.; Hart, J.; McGregor, P.; Oates, P.; Bloxham, G.; and Jones, D., 2007. The Wide Field Spectrograph (WiFeS). *arXiv e-prints*, (2007). doi:10.48550/arxiv.0705.0287. https://arxiv.org/abs/0705.0287. (cited on page 147)

Efstathiou, G., 2024. Evolving Dark Energy or Supernovae Systematics? doi:10.48550/arxiv.2408.07175. https://arxiv.org/abs/2408.07175. (cited on pages xiv and 112)

Einstein, A. and Rosen, N., 1937. On gravitational waves. *J. Frankl. Inst.*, 223, 1 (Jan. 1937), 43–54. doi:10.1016/s0016-0032(37)90583-0. http://dx.doi.org/10.1016/S0016-0032(37)90583-0. (cited on page 15)

Einstein, A. B., 1917. Cosmological Considerations in the General Theory of Relativity. In *Cosmological Considerations in the General Theory of Relativity*. (cited on page 2)

Ellis, R. S.; Sullivan, M.; Nugent, P. E.; Howell, D. A.; Gal-Yam, A.; Astier, P.; Balam, D.; Balland, C.; Basa, S.; Carlberg, R. G.; et al., 2008. Verifying the Cosmological Utility of Type Ia Supernovae: Implications of a Dispersion in the Ultraviolet Spectra. *The Astrophys. J.*, 674, 1 (Feb. 2008), 51–69. doi:10.1086/524981. http://dx.doi.org/10.1086/524981. (cited on page 36)

Faber, S. M. and Jackson, R. E., 1976. Velocity dispersions and mass-to-light ratios for elliptical galaxies. *Astrophys. J.*, 204 (Mar. 1976), 668–683. doi:10.1086/154215. (cited on page 6)

Fakhouri, H. K.; Boone, K.; Aldering, G.; Antilogus, P.; Aragon, C.; Bailey, S.; Baltay, C.; Barbary, K.; Baugh, D.; Bongard, S.; et al., 2015. Improving Cosmological Distance Measurements Using Twin Type Ia Supernovae. *The Astrophys. J.*, 815, 1 (Dec. 2015), 58. doi:10.1088/0004-637x/815/1/58. http://dx.doi.org/10.1088/0004-637X/815/1/58. (cited on page 18)

Fitzpatrick, E., 1999. Correcting for the Effects of Interstellar Extinction. *Publ. Astron. Soc. Pac.*, 111, 755 (Jan. 1999), 63–75. doi:10.1086/316293. http://dx.doi.org/10.1086/316293. (cited on pages 94 and 117)

Flaugher, B., 2006. The Dark Energy Survey instrument design. In *Ground-based and Airborne Instrumentation for Astronomy*. Spie. doi:10.1117/12.672433. http://dx.doi.org/10.1117/12.672433. (cited on page 49)

Flaugher, B.; Diehl, H. T.; Honscheid, K.; Abbott, T. M. C.; Alvarez, O.; Angstadt, R.; Annis, J. T.; Antonik, M.; Ballester, O.; Beaufore, L.; et al., 2015. The Dark Energy Camera. *Astron. J.*, 150, 5 (Nov. 2015), 150. doi:10.1088/0004-6256/150/5/150. (cited on pages 58, 79, and 147)

Foley, R. J.; Scolnic, D.; Rest, A.; Jha, S. W.; Pan, Y.; Riess, A. G.; Challis, P.; Chambers, K. C.; Coulter, D. A.; Dettman, K. G.; et al., 2017. The Foundation Supernova Survey: motivation, design, implementation, and first data release. *Mon. Notices Royal Astron. Soc.*, 475, 1 (Dec. 2017), 193–219. doi:10.1093/mnras/stx3136. http://dx.doi.org/10.1093/mnras/stx3136. (cited on pages 44, 77, and 148)

Fortunato, M.; Blundell, C.; and Vinyals, O., 2017. Bayesian Recurrent Neural

Networks. doi:10.48550/arxiv.1704.02798. https://arxiv.org/abs/1704.02798. (cited on page 106)

Freedman, W. L. and Madore, B. F., 2023. The Cepheid Extra-galactic Distance Scale: Past, Present and Future. *arXiv e-prints*, (Aug. 2023), arXiv:2308.02474. doi:10.48550/arXiv.2308.02474. (cited on page 12)

Fremling, C.; Miller, A. A.; Sharma, Y.; Dugas, A.; Perley, D. A.; Taggart, K.; Sollerman, J.; Goobar, A.; Graham, M. L.; Neill, J. D.; et al., 2020. The Zwicky Transient Facility Bright Transient Survey. I. Spectroscopic Classification and the Redshift Completeness of Local Galaxy Catalogs. *The Astrophys. J.*, 895, 1 (May 2020), 32. doi:10.3847/1538-4357/ab8943. http://dx.doi.org/10.3847/1538-4357/ab8943. (cited on page 50)

Friedmann, A., 1922. Ü ber die Krü mmung des Raumes. *Zeitschrift fur Physik*, 10 (Jan. 1922), 377–386. doi:10.1007/bf01332580. (cited on page 3)

Frieman, J. A.; Bassett, B.; Becker, A.; Choi, C.; Cinabro, D.; DeJongh, F.; Depoy, D. L.; Dilday, B.; Doi, M.; Garnavich, P. M.; et al., 2007. The Sloan Digital Sky Survey-ii Supernova Survey: Technical Summary. *The Astron. J.*, 135, 1 (Dec. 2007), 338–347. doi:10.1088/0004-6256/135/1/338. http://dx.doi.org/10.1088/0004-6256/135/1/338. (cited on pages 35 and 70)

Fukugita, M.; Ichikawa, T.; Gunn, J. E.; Doi, M.; Shimasaku, K.; and Schneider, D. P., 1996. The Sloan Digital Sky Survey Photometric System. *The Astron. J.*, 111 (Apr. 1996), 1748. doi:10.1086/117915. http://dx.doi.org/10.1086/117915. (cited on page 17)

Galbany, L.; Smith, M.; Duarte, P. S.; González-Gaitán, S.; Pessa, I.; Sako, M.; Iglesias-Páramo, J.; López-Sánchez, A. R.; Mollá, M.; and Vílchez, J. M., 2022. Aperture-corrected spectroscopic Type Ia supernova host galaxy properties. *Astron. & Astrophys.*, 659 (Mar. 2022), A89. doi:10.1051/0004-6361/202141568. http://dx.doi.org/10.1051/0004-6361/202141568. (cited on pages 38 and 98)

Gamow, G., 1946. Expanding Universe and the Origin of Elements. *Phys. Rev.*, 70 (Oct. 1946), 572–573. doi:10.1103/PhysRev.70.572.2. https://link.aps.org/doi/10.1103/PhysRev.70.572.2. (cited on page 13)

Ganeshalingam, M.; Li, W.; Filippenko, A. V.; Anderson, C.; Foster, G.; Gates, E. L.; Griffith, C. V.; Grigsby, B. J.; Joubert, N.; Leja, J.; et al., 2010. Results of the Lick observatory supernova search follow-up photometry program: BVRI light curves of 165 Type Ia supernovae. *The Astrophys. J. Suppl. Ser.*, 190, 2 (Sep. 2010), 418–448. doi:10.1088/0067-0049/190/2/418. http://dx.doi.org/10.1088/0067-0049/190/2/418. (cited on page 44)

Goldhaber, G.; Groom, D. E.; Kim, A.; Aldering, G.; Astier, P.; Conley, A.; Deustua, S. E.; Ellis, R.; Fabbro, S.; Fruchter, A. S.; et al., 2001. Timescale Stretch Parameterization of Type Ia Supernova B-Band Light Curves. *The Astrophys. J.*, 558, 1 (Sep. 2001), 359–368. doi:10.1086/322460. http://dx.doi.org/10.1086/322460. (cited on page 80)

Goldstein, D. A.; D'Andrea, C. B.; Fischer, J. A.; Foley, R. J.; Gupta, R. R.; Kessler, R.; Kim, A. G.; Nichol, R. C.; Nugent, P. E.; Papadopoulos, A.; et al., 2015. Automated Transient Identification In The Dark Energy Survey. *The Astron. J.*, 150, 3 (Aug. 2015), 82. doi:10.1088/0004-6256/150/3/82. http://dx.doi.org/10.1088/0004-6256/150/3/82. (cited on page 79)

Goobar, A. and Perlmutter, S., 1995. Feasibility of Measuring the Cosmological Constant Lambda and Mass Density Omega Using Type IaSupernovae. *The Astrophys. J.*, 450 (Sep. 1995), 14. doi:10.1086/176113. https://doi.org/10.1086/176113. (cited on pages 20 and 28)

Guy, J.; Astier, P.; Baumont, S.; Hardin, D.; Pain, R.; Regnault, N.; Basa, S.; Carlberg, R. G.; Conley, A.; Fabbro, S.; et al., 2007. SALT2: using distant supernovae to improve the use of Type Ia supernovae as distance indicators. *Astron. & Astrophys.*, 466, 1 (Apr. 2007), 11–21. doi:10.1051/0004-6361:20066930. (cited on pages 18, 36, 40, 47, 80, and 127)

Guy, J.; Astier, P.; Nobili, S.; Regnault, N.; and Pain, R., 2005. SALT: a spectral adaptive light curve template for Type Ia supernovae. *Astron. & Astrophys.*, 443, 3 (Nov. 2005), 781–791. doi:10.1051/0004-6361:20053025. http://dx.doi.org/10.1051/0004-6361:20053025. (cited on pages 36, 39, and 46)

Guy, J.; Sullivan, M.; Conley, A.; Regnault, N.; Astier, P.; Balland, C.; Basa, S.; Carlberg, R. G.; Fouchez, D.; Hardin, D.; et al., 2010. The Supernova Legacy Survey 3-year sample: Type Ia supernovae photometric distances and cosmological constraints. *Astron. & Astrophys.*, 523 (Nov. 2010), A7. doi:10.1051/0004-6361/201014468. http://dx.doi.org/10.1051/0004-6361/201014468. (cited on pages 25, 35, 38, 47, and 87)

Hamuy, M.; Folatelli, G.; Morrell, N. I.; Phillips, M. M.; Suntzeff, N. B.; Persson, S. E.; Roth, M.; Gonzalez, S.; Krzeminski, W.; Contreras, C.; et al., 2006. The Carnegie Supernova Project: The Low-Redshift Survey. *Publ. Astron. Soc. Pac.*, 118, 839 (Jan. 2006), 2–20. doi:10.1086/500228. (cited on page 35)

Hamuy, M.; Phillips, M. M.; Suntzeff, N. B.; Schommer, R. A.; Maza, J.; and Aviles, R., 1996. The Absolute Luminosities of the Calan/Tololo Type Ia Supernovae. *The Astron. J.*, 112 (Dec. 1996), 2391. doi:10.1086/118190. http://dx.doi.org/10.1086/118190. (cited on pages 20, 43, 45, and 46)

Hayden, B. T.; Garnavich, P. M.; Kessler, R.; Frieman, J. A.; Jha, S. W.; Bassett, B.; Cinabro, D.; Dilday, B.; Kasen, D.; Marriner, J.; et al., 2010. The Rise and Fall of Type Ia Supernova Light Curves in the SDSS-II Supernova Survey. *The Astrophys. J.*, 712, 1 (Mar. 2010), 350–366. doi:10.1088/0004-637x/712/1/350. http://dx.doi.org/10.1088/0004-637X/712/1/350. (cited on page 80)

Heymans, C.; Grocutt, E.; Heavens, A.; Kilbinger, M.; Kitching, T. D.; Simpson, F.; Benjamin, J.; Erben, T.; Hildebrandt, H.; Hoekstra, H.; et al., 2013. CFHTLenS tomographic weak lensing cosmological parameter constraints: Mitigating the impact of intrinsic galaxy alignments. *Mon. Notices Royal Astron. Soc.*, 432, 3 (05 2013), 2433–2453. doi:10.1093/mnras/stt601. https://doi.org/10.1093/mnras/stt601. (cited on page 15)

Heymans, C.; Tröster, T.; Asgari, M.; Blake, C.; Hildebrandt, H.; Joachimi, B.; Kuijken, K.; Lin, C.; Sánchez, A. G.; van, D. B. J. L.; et al., 2021. KiDS-1000 Cosmology: Multi-probe weak gravitational lensing and spectroscopic galaxy clustering constraints. *Astron. & Astrophys.*, 646 (Feb. 2021), A140. doi:10.1051/0004-6361/202039063. http://dx.doi.org/10.1051/0004-6361/202039063. (cited on page 15)

Hicken, M.; Challis, P.; Jha, S.; Kirshner, R. P.; Matheson, T.; Modjaz, M.; Rest, A.; Michael, W. W.; Bakos, G.; Barton, E. J.; et al., 2009. CfA3: 185 Type Ia supernova light curves from the CfA. *The Astrophys. J.*, 700, 1 (Jul. 2009), 331–357. doi:10.1088/0004-637x/700/1/331. http://dx.doi.org/10.1088/0004-637X/700/1/331. (cited on pages 35, 44, 47, and 77)

Hicken, M.; Challis, P.; Kirshner, R. P.; Rest, A.; Cramer, C. E.; Wood-Vasey, W. M.; Bakos, G.; Berlind, P.; Brown, W. R.; Caldwell, N.; et al., 2012. CfA4: Light curves for 94 Type Ia supernovae. *The Astrophys. J. Suppl. Ser.*, 200, 2 (May 2012), 12. doi:10.1088/0067-0049/200/2/12. http://dx.doi.org/10.1088/0067-0049/200/2/12. (cited on pages 35, 44, and 77)

Hildebrandt, H.; Viola, M.; Heymans, C.; Joudaki, S.; Kuijken, K.; Blake, C.; Erben, T.; Joachimi, B.; Klaes, D.; Miller, L.; et al., 2016. KiDS-450: cosmological parameter constraints from tomographic weak gravitational lensing. *Mon. Notices Royal Astron. Soc.*, 465, 2 (Nov. 2016), 1454–1498. doi:10.1093/mnras/stw2805. http://dx.doi.org/10.1093/mnras/stw2805. (cited on page 15)

Hinshaw, G.; Spergel, D. N.; Verde, L.; Hill, R. S.; Meyer, S. S.; Barnes, C.; Bennett, C. L.; Halpern, M.; Jarosik, N.; Kogut, A.; et al., 2003. First-Year Wilkinson Microwave Anisotropy Probe (WMAP) Observations: The Angular Power Spectrum. *The Astrophys. J. Suppl. Ser.*, 148, 1 (Sep. 2003), 135–159. doi:10.1086/377225. https://doi.org/10.1086%2F377225. (cited on page 14)

Hinton, S. and Brout, D., 2020. Pippin: A pipeline for supernova cosmology. *J. Open Source Softw.*, 5, 47 (2020), 2122. doi:10.21105/joss.02122. https://doi.org/10.21105/joss.02122. (cited on pages 58, 121, and 126)

Hinton, S. R.; Davis, T. M.; Kim, A. G.; Brout, D.; D'Andrea, C. B.; Kessler, R.; Lasker, J.; Lidman, C.; Macaulay, E.; Möller, A.; et al., 2019. Steve: A Hierarchical Bayesian Model for Supernova Cosmology. *Astrophys. J.*, 876, 1 (May 2019), 15. doi:10.3847/1538-4357/ab13a3. (cited on pages 50 and 125)

Hlozek, R.; Kunz, M.; Bassett, B.; Smith, M.; Newling, J.; Varughese, M.; Kessler, R.; Bernstein, J. P.; Campbell, H.; Dilday, B.; et al., 2012. Photometric Supernova Cosmology With Beams And Sdss-ii. *The Astrophys. J.*, 752, 2 (May 2012), 79. doi:10.1088/0004-637x/752/2/79. http://dx.doi.org/10.1088/0004-637X/752/2/79. (cited on page 114)

Holman, R. and Naidu, S., 2004. Dark Energy from Wet Dark Fluid. doi:10.48550/arxiv.astro-ph/0408102. https://arxiv.org/abs/astro-ph/0408102. (cited on page 8)

Holtzman, J. A.; Marriner, J.; Kessler, R.; Sako, M.; Dilday, B.; Frieman, J. A.; Schneider, D. P.; Bassett, B.; Becker, A.; Cinabro, D.; et al., 2008. The Sloan Digital Sky Survey-ii: Photometry And Supernova Ia Light Curves From The 2005 Data. *The Astron. J.*, 136, 6 (Nov. 2008), 2306–2320. doi:10.1088/0004-6256/136/6/2306. http://dx.doi.org/10.1088/0004-6256/136/6/2306. (cited on pages 40 and 47)

Howell, D. A.; Sullivan, M.; Perrett, K.; Bronder, T. J.; Hook, I. M.; Astier, P.; Aubourg, E.; Balam, D.; Basa, S.; Carlberg, R. G.; et al., 2005. Gemini Spectroscopy of Supernovae from the Supernova Legacy Survey: Improving High-Redshift Supernova Selection and Classification. *Astrophys. J.*, 634, 2 (Dec. 2005), 1190–1201. doi:10.1086/497119. (cited on page 36)

Hubble, E. P., 1925. NGC 6822, a remote stellar system. *The Astrophys. J.*, 62 (Dec. 1925), 409. doi:10.1086/142943. http://dx.doi.org/10.1086/142943. (cited on page 1)

Huff, E. M.; Eifler, T.; Hirata, C. M.; Mandelbaum, R.; Schlegel, D.; and Seljak, U., 2014. Seeing in the dark - II. Cosmic shear in the Sloan Digital Sky Survey. *Mon. Notices Royal Astron. Soc.*, 440, 2 (03 2014), 1322–1344. doi:10.1093/mnras/stu145. https://doi.org/10.1093/mnras/stu145. (cited on page 15)

Ivezić, V.; Kahn, S. M.; Tyson, J. A.; Abel, B.; Acosta, E.; Allsman, R.; Alonso, D.; AlSayyad, Y.; Anderson, S. F.; Andrew, J.; et al., 2019. LSST: From Science Drivers to Reference Design and Anticipated Data Products. *Astrophys. J.*, 873 (Mar. 2019), 111. doi:10.3847/1538-4357/ab042c. (cited on page 105)

James, F., 1994. *MINUIT Function Minimization and Error Analysis: Reference Manual Version 94.1*. (cited on page 99)

Jarvis, M.; Jain, B.; Bernstein, G.; and Dolney, D., 2006. Dark Energy Constraints from the CTIO Lensing Survey. *The Astrophys. J.*, 644, 1 (Jun. 2006), 71. doi:10.1086/503418. https://dx.doi.org/10.1086/503418. (cited on page 15)

Jennings, E. and Madigan, M., 2017. astroABC: An Approximate Bayesian Computation Sequential Monte Carlo sampler for cosmological parameter estimation. *Astron. Comput.*, 19 (Apr. 2017), 16–22. doi:10.1016/j.ascom.2017.01.001. (cited on pages 125 and 153)

Jennings, E.; Wolf, R.; and Sako, M., 2016. A new approach for obtaining cosmological constraints from Type Ia Supernovae using Approximate Bayesian Computation. *arXiv e-prints*, (Nov. 2016), arXiv:1611.03087. doi:10.48550/arXiv.1611.03087. (cited on pages 125 and 153)

Jha, S.; Kirshner, R. P.; Challis, P.; Garnavich, P. M.; Matheson, T.; Soderberg, A. M.; Graves, G. J. M.; Hicken, M.; Alves, J. F.; Arce, H. G.; et al., 2006. UBVRILight Curves of 44 Type Ia Supernovae. *The Astron. J.*, 131, 1 (Jan. 2006), 527–554. doi:10.1086/497989. http://dx.doi.org/10.1086/497989. (cited on pages 35, 44, 45, and 46)

Jha, S.; Riess, A. G.; and Kirshner, R. P., 2007. Improved Distances to Type Ia Supernovae with Multicolor Light-Curve Shapes: MLCS2k2. *Astrophys. J.*, 659, 1 (Apr. 2007), 122–148. doi:10.1086/512054. (cited on pages 39, 40, and 80)

Johnson, H. L. and Morgan, W. W., 1953. Fundamental stellar photometry for standards of spectral type on the revised system of the Yerkes spectral atlas. *The Astrophys. J.*, 117 (May 1953), 313. doi:10.1086/145697. http://dx.doi.org/10.1086/145697. (cited on page 44)

Jones, D. O.; Scolnic, D. M.; Foley, R. J.; Rest, A.; Kessler, R.; Challis, P. M.; Chambers, K. C.; Coulter, D. A.; Dettman, K. G.; Foley, M. M.; et al., 2019. The Foundation Supernova Survey: Measuring Cosmological Parameters with Supernovae from a Single Telescope. *Astrophys. J.*, 881, 1 (Aug. 2019), 19. doi:10.3847/1538-4357/ab2bec. (cited on pages 25, 44, and 45)

Jones, D. O.; Scolnic, D. M.; Riess, A. G.; Kessler, R.; Rest, A.; Kirshner, R. P.; Berger, E.; Ortega, C. A.; Foley, R. J.; Chornock, R.; et al., 2017. Measuring the Properties of Dark Energy with Photometrically Classified Pan-STARRS Supernovae. I. Systematic Uncertainty from Core-collapse Supernova Contamination. *The Astrophys. J.*, 843, 1 (Jun. 2017), 6. doi:10.3847/1538-4357/aa767b. http://dx.doi.org/10.3847/1538-4357/aa767b. (cited on pages 107, 114, and 119)

Joudaki, S.; Blake, C.; Heymans, C.; Choi, A.; Harnois-Deraps, J.; Hildebrandt, H.; Joachimi, B.; Johnson, A.; Mead, A.; Parkinson, D.; et al., 2016. CFHTLenS revisited: assessing concordance with Planck including astrophysical systematics. *Mon. Notices Royal Astron. Soc.*, 465, 2 (Dec. 2016), 2033–2052. doi:10.1093/mnras/stw2665. https://doi.org/10.1093/mnras/stw2665. (cited on page 15)

Joyce, A.; Lombriser, L.; and Schmidt, F., 2016. Dark Energy Versus Modified Gravity. *Annu. Rev. Nucl. Part. Sci.*, 66, 1 (2016), 95–122. doi:10.1146/annurev-nucl-102115-044553. https://doi.org/10.1146/annurev-nucl-102115-044553. (cited on page 8)

KAGRA Collaboration, 2019. KAGRA: 2.5 generation interferometric gravitational wave detector. *Nat. Astron.*, 3, 1 (Jan. 2019), 35–40. doi:10.1038/s41550-018-0658-y. https://doi.org/10.1038%2Fs41550-018-0658-y. (cited on page 16)

KAGRA Collaboration, 2020. Overview of KAGRA: KAGRA science. (cited on page 16)

Kaiser, N., 1992. Weak Gravitational Lensing of Distant Galaxies. *Astrophys. J.*, 388 (Apr. 1992), 272. doi:10.1086/171151. (cited on page 15)

Kaiser, N.; Wilson, G.; and Luppino, G. A., 2000. Large-Scale Cosmic Shear Measurements. *arXiv e-prints*, (Mar. 2000), astro-ph/0003338. doi:10.48550/arXiv.astro-ph/0003338. (cited on page 15)

Kamenshchik, A.; Moschella, U.; and Pasquier, V., 2001. An alternative to quintessence. *Phys. Lett. B*, 511, 2–4 (Jul. 2001), 265–268. doi:10.1016/s0370-2693(01)00571-8. http://dx.doi.org/10.1016/S0370-2693(01)00571-8. (cited on page 8)

Kelsey, L.; Sullivan, M.; Wiseman, P.; Armstrong, P.; Chen, R.; Brout, D.; Davis, T. M.; Dixon, M.; Frohmaier, C.; Galbany, L.; et al., 2023. Concerning colour: The effect of environment on Type Ia supernova colour in the dark energy survey. *Mon. Notices Royal Astron. Soc.*, 519, 2 (Feb. 2023), 3046–3063. doi:10.1093/mnras/stac3711. (cited on pages 53, 98, and 126)

Kenworthy, W. D.; Jones, D. O.; Dai, M.; Kessler, R.; Scolnic, D.; Brout, D.; Siebert, M. R.; Pierel, J. D. R.; Dettman, K. G.; Dimitriadis, G.; et al.,

2021. SALT3: An Improved Type Ia Supernova Model for Measuring Cosmic Distances. *The Astrophys. J.*, 923, 2 (Dec. 2021), 265. doi:10.3847/1538-4357/ac30d8. http://dx.doi.org/10.3847/1538-4357/ac30d8. (cited on pages xiii, 53, 58, 59, 69, 80, 97, 122, and 148)

Kessler, R., 2024. *SNANA User's Manual: Simulation, Light curve Fits, BBC, Create-Covariance, Batch Utilities*. Available at https://cdn.githubraw.com/RickKessler/SNANA/f657449c/doc/snana_manual.pdf. (cited on pages 70, 72, and 76)

Kessler, R.; Bassett, B.; Belov, P.; Bhatnagar, V.; Campbell, H.; Conley, A.; Frieman, J. A.; Glazov, A.; González-Gaitán, S.; Hlozek, R.; et al., 2010. Results from the Supernova Photometric Classification Challenge. *Publ. Astron. Soc. Pac.*, 122, 898 (Dec. 2010), 1415–1431. doi:10.1086/657607. http://dx.doi.org/10.1086/657607. (cited on page 80)

Kessler, R.; Becker, A. C.; Cinabro, D.; Vanderplas, J.; Frieman, J. A.; Marriner, J.; Davis, T. M.; Dilday, B.; Holtzman, J.; Jha, S. W.; et al., 2009a. First-year Sloan Digital Sky Survey-ii Supernova Results: Hubble Diagram And Cosmological Parameters. *The Astrophys. J. Suppl. Ser.*, 185, 1 (Oct. 2009), 32–84. doi:10.1088/0067-0049/185/1/32. http://dx.doi.org/10.1088/0067-0049/185/1/32. (cited on pages 25, 40, and 70)

Kessler, R.; Bernstein, J. P.; Cinabro, D.; Dilday, B.; Frieman, J. A.; Jha, S.; Kuhlmann, S.; Miknaitis, G.; Sako, M.; Taylor, M.; et al., 2009b. SNANA: A Public Software Package for Supernova Analysis. *Publ. Astron. Soc. Pac.*, 121, 883 (Sep. 2009), 1028. doi:10.1086/605984. (cited on pages xiii, 40, 47, 58, 59, 69, 70, 80, and 126)

Kessler, R.; Brout, D.; D'Andrea, C. B.; Davis, T. M.; Hinton, S. R.; Kim, A. G.; Lasker, J.; Lidman, C.; Macaulay, E.; Möller, A.; et al., 2019a. First cosmology results using Type Ia supernova from the Dark Energy Survey: simulations to correct supernova distance biases. *Mon. Notices Royal Astron. Soc.*, 485, 1 (May 2019), 1171–1187. doi:10.1093/mnras/stz463. (cited on pages 49 and 128)

Kessler, R.; Marriner, J.; Childress, M.; Covarrubias, R.; D'Andrea, C. B.; Finley, D. A.; Fischer, J.; Foley, R. J.; Goldstein, D.; Gupta, R. R.; et al., 2015. The Difference Imaging Pipeline for the Transient Search in the Dark Energy Survey. *Astron. J.*, 150, 6 (Dec. 2015), 172. doi:10.1088/0004-6256/150/6/172. (cited on pages 49 and 79)

Kessler, R.; Narayan, G.; Avelino, A.; Bachelet, E.; Biswas, R.; Brown, P. J.; Chernoff, D. F.; Connolly, A. J.; Dai, M.; Daniel, S.; et al., 2019b. Models and Simulations for the Photometric LSST Astronomical Time Series

Classification Challenge (PLAsTiCC). *Publ. Astron. Soc. Pac.*, 131, 1003 (Sep. 2019), 094501. doi:10.1088/1538-3873/ab26f1. (cited on page 126)

Kessler, R. and Scolnic, D., 2017. Correcting Type Ia Supernova Distances for Selection Biases and Contamination in Photometrically Identified Samples. *Astrophys. J.*, 836, 1 (Feb. 2017), 56. doi:10.3847/1538-4357/836/1/56. (cited on pages xiii, 48, 58, 59, 110, 125, and 128)

Kessler, R.; Vincenzi, M.; and Armstrong, P., 2023. Binning is Sinning: Redemption for Hubble Diagram Using Photometrically Classified Type Ia Supernovae. *The Astrophys. J. Lett.*, 952, 1 (Jul. 2023), L8. doi:10.3847/2041-8213/ace34d. http://dx.doi.org/10.3847/2041-8213/ace34d. (cited on pages 113 and 119)

Kilbinger, M.; Fu, L.; Heymans, C.; Simpson, F.; Benjamin, J.; Erben, T.; Harnois-Déraps, J.; Hoekstra, H.; Hildebrandt, H.; Kitching, T. D.; et al., 2013. CFHTLenS: combined probe cosmological model comparison using 2D weak gravitational lensing. *Mon. Notices Royal Astron. Soc.*, 430, 3 (02 2013), 2200–2220. doi:10.1093/mnras/stt041. https://doi.org/10.1093/mnras/stt041. (cited on page 15)

Kim, A.; Goobar, A.; and Perlmutter, S., 1996. A Generalized K Correction for Type IA Supernovae: Comparing R-band Photometry beyond z=0.2 with B, V, and R-band Nearby Photometry. *Publ. Astron. Soc. Pac.*, 108 (Feb. 1996), 190. doi:10.1086/133709. http://dx.doi.org/10.1086/133709. (cited on page 28)

Knop, R. A.; Aldering, G.; Amanullah, R.; Astier, P.; Blanc, G.; Burns, M. S.; Conley, A.; Deustua, S. E.; Doi, M.; Ellis, R.; et al., 2003. New Constraints on Ω_M, Ω_Λ, and w from an Independent Set of 11 High-Redshift Supernovae Observed with the Hubble Space Telescope. *The Astrophys. J.*, 598, 1 (Nov. 2003), 102–137. doi:10.1086/378560. http://dx.doi.org/10.1086/378560. (cited on pages 45 and 46)

Komatsu, E.; Dunkley, J.; Nolta, M. R.; Bennett, C. L.; Gold, B.; Hinshaw, G.; Jarosik, N.; Larson, D.; Limon, M.; Page, L.; et al., 2009. Five- yearWilkinsonMicrowaveAnisotropyProbeObservations: CosmologicalInterpretation. *The Astrophys. J. Suppl. Ser.*, 180, 2 (Feb. 2009), 330–376. doi:10.1088/0067-0049/180/2/330. https://doi.org/10.1088%2F0067-0049%2F180%2F2%2F330. (cited on page 14)

Kovacs, E., 2024. GitHub - evevkovacs/ML-SN Classifier: Machine- Learning Algorithm for Supernova Classification — github.com. Accessed 05-12-2024. (cited on page 105)

Kowalski, M.; Rubin, D.; Aldering, G.; Agostinho, R. J.; Amadon, A.; Amanullah, R.; Balland, C.; Barbary, K.; Blanc, G.; Challis, P. J.; et al., 2008. Improved Cosmological Constraints from New, Old, and Combined Supernova Data Sets. *The Astrophys. J.*, 686, 2 (Oct. 2008), 749–778. doi:10.1086/589937. http://dx.doi.org/10.1086/589937. (cited on pages 25 and 46)

Kremer, G. M., 2003. Cosmological models described by a mixture of van der Waals fluid and dark energy. *Phys. Rev. D*, 68, 12 (Dec. 2003). doi:10.1103/physrevd.68.123507. http://dx.doi.org/10.1103/PhysRevD.68.123507. (cited on page 8)

Krisciunas, K.; Contreras, C.; Burns, C. R.; Phillips, M. M.; Stritzinger, M. D.; Morrell, N.; Hamuy, M.; Anais, J.; Boldt, L.; Busta, L.; et al., 2017. The Carnegie Supernova Project. I. Third Photometry Data Release of Low-redshift Type Ia Supernovae and Other White Dwarf Explosions. *Astron. J.*, 154, 5 (Nov. 2017), 211. doi:10.3847/1538-3881/aa8df0. (cited on page 77)

Krisciunas, K.; Phillips, M. M.; Stubbs, C.; Rest, A.; Miknaitis, G.; Riess, A. G.; Suntzeff, N. B.; Roth, M.; Persson, S. E.; and Freedman, W. L., 2001. Optical and Infrared Photometry of the Type Ia Supernovae 1999da, 1999dk, 1999gp, 2000bk, and 2000ce. *The Astron. J.*, 122, 3 (Sep. 2001), 1616–1631. doi:10.1086/322120. http://dx.doi.org/10.1086/322120. (cited on page 46)

Krisciunas, K.; Phillips, M. M.; Suntzeff, N. B.; Persson, S. E.; Hamuy, M.; Antezana, R.; Candia, P.; Clocchiatti, A.; DePoy, D. L.; Germany, L. M.; et al., 2004a. Optical and Infrared Photometry of the Nearby Type Ia Supernovae 1999ee, 2000bh, 2000ca, and 2001ba. *The Astron. J.*, 127, 3 (Mar. 2004), 1664–1681. doi:10.1086/381911. http://dx.doi.org/10.1086/381911. (cited on page 46)

Krisciunas, K.; Suntzeff, N. B.; Phillips, M. M.; Candia, P.; Prieto, J. L.; Antezana, R.; Chassagne, R.; Chen, H.; Dickinson, M.; Eisenhardt, P. R.; et al., 2004b. Optical and Infrared Photometry of the Type Ia Supernovae 1991T, 1991bg, 1999ek, 2001bt, 2001cn, 2001cz, and 2002bo. *The Astron. J.*, 128, 6 (Dec. 2004), 3034–3052. doi:10.1086/425629. http://dx.doi.org/10.1086/425629. (cited on page 46)

Kunz, M.; Hlozek, R.; Bassett, B. A.; Smith, M.; Newling, J.; and Varughese, M., 2012. BEAMS: Separating the Wheat from the Chaff in Supernova Analysis. *Astrostatistical Challenges for New Astron.*, (Oct. 2012), 63–86. doi:10.1007/978-1-4614-3508-2_4. http://dx.doi.org/10.1007/978-1-4614-3508-2%5F4. (cited on pages 110, 125, and 128)

Lampeitl, H.; Smith, M.; Nichol, R. C.; Bassett, B.; Cinabro, D.; Dilday, B.; Foley, R. J.; Frieman, J. A.; Garnavich, P. M.; Goobar, A.; et al., 2010. The

Effect of Host Galaxies on Type Ia Supernovae in the SDSS-II Supernova Survey. *Astrophys. J.*, 722, 1 (Oct. 2010), 566–576. doi:10.1088/0004-637x/722/1/566. (cited on pages 38 and 98)

Lasker, J.; Kessler, R.; Scolnic, D.; Brout, D.; Burke, D. L.; D'Andrea, C. B.; Davis, T. M.; Hinton, S. R.; Kim, A. G.; Li, T. S.; et al., 2019. First cosmology results using Type Ia supernovae from the dark energy survey: effects of chromatic corrections to supernova photometry on measurements of cosmological parameters. *Mon. Notices Royal Astron. Soc.*, 485, 4 (Jun. 2019), 5329–5344. doi:10.1093/mnras/stz619. (cited on pages 49, 53, 99, and 126)

Lee, J.; Acevedo, M.; Sako, M.; Vincenzi, M.; Brout, D.; Sanchez, B.; Chen, R.; Davis, T. M.; Jarvis, M.; Scolnic, D.; et al., 2023. The Dark Energy Survey Supernova Program: Corrections on Photometry Due to Wavelength-dependent Atmospheric Effects. *The Astron. J.*, 165, 6 (May 2023), 222. doi:10.3847/1538-3881/acca15. http://dx.doi.org/10.3847/1538-3881/acca15. (cited on pages 53 and 99)

Leibundgut, B.; Schommer, R.; Phillips, M.; Riess, A.; Schmidt, B.; Spyromilio, J.; Walsh, J.; Suntzeff, N.; Hamuy, M.; Maza, J.; et al., 1996. Time Dilation in the Light Curve of the Distant Type Ia Supernova SN1995K. *The Astrophys. J.*, 466, 1 (Jul. 1996), L21–l24. doi:10.1086/310164. https://doi.org/10.1086/310164. (cited on page 20)

Lemaître, G., 1927. Un Univers homogè ne de masse constante et de rayon croissant rendant compte de la vitesse radiale des né buleuses extra-galactiques. *Ann. de la Socitè Sci. de Bruxelles*, 47 (Jan. 1927), 49–59. (cited on page 3)

Lemaitre, G., 1934. Evolution of the Expanding Universe. *Proc. National Acad. Sci.*, 20, 1 (Jan. 1934), 12–17. doi:10.1073/pnas.20.1.12. https://doi.org/10.1073/pnas.20.1.12. (cited on page 5)

Lewis, A. and Bridle, S., 2002. Cosmological parameters from CMB and other data: A Monte Carlo approach. *Phys. Rev. D*, 66, 10 (Nov. 2002), 103511. doi:10.1103/PhysRevD.66.103511. (cited on pages xiii, 58, and 59)

Lidman, C.; Tucker, B. E.; Davis, T. M.; Uddin, S. A.; Asorey, J.; Bolejko, K.; Brout, D.; Calcino, J.; Carollo, D.; Carr, A.; et al., 2020. OzDES multi-object fibre spectroscopy for the Dark Energy Survey: results and second data release. *Mon. Notices Royal Astron. Soc.*, 496, 1 (May 2020), 19–35. doi:10.1093/mnras/staa1341. http://dx.doi.org/10.1093/mnras/staa1341. (cited on pages 79 and 105)

LIGO Collaboration, 2016a. Localization and Broadband Follow-up of the Gravitational-Wave Transient GW150914. *The Astrophys. J.*, 826, 1 (Jul. 2016), L13. doi:10.3847/2041-8205/826/1/l13. https://doi.org/10.3847%2F2041-8205%2F826%2F1%2Fl13. (cited on page 15)

LIGO Collaboration, 2016b. Observation of Gravitational Waves from a Binary Black Hole Merger. *Phys. Rev. Lett.*, 116, 6 (Feb. 2016). doi:10.1103/physrevlett.116.061102. https://doi.org/10.1103%2Fphysrevlett.116.061102. (cited on page 15)

LIGO Collaboration and Virgo Collaboration, 2017. GW170817: Observation of Gravitational Waves from a Binary Neutron Star Inspiral. *Phys. Rev. Lett.*, 119 (Oct. 2017), 161101. doi:10.1103/PhysRevLett.119.161101. https://link.aps.org/doi/10.1103/PhysRevLett.119.161101. (cited on page 16)

LIGO Collaboration and Virgo Collaboration, 2021. GWTC-2: Compact Binary Coalescences Observed by LIGO and Virgo during the First Half of the Third Observing Run. *Phys. Rev. X*, 11, 2 (Jun. 2021). doi:10.1103/physrevx.11.021053. https://doi.org/10.1103%2Fphysrevx.11.021053. (cited on page 16)

LIGO Collaboration; Virgo Collaboration; and DES Collaboration, 2019. First Measurement of the Hubble Constant from a Dark Standard Siren using the Dark Energy Survey Galaxies and the LIGO/Virgo Binary –Black-hole Merger GW170814. *The Astrophys. J.*, 876, 1 (Apr. 2019), L7. doi:10.3847/2041-8213/ab14f1. https://doi.org/10.3847/2041-8213/ab14f1. (cited on page 16)

LIGO Collaboration; Virgo Collaboration; and KAGRA Collaboration, 2021. GWTC-3: Compact Binary Coalescences Observed by LIGO and Virgo During the Second Part of the Third Observing Run. (cited on page 16)

Lin, H.; Dodelson, S.; Seo, H.; Soares-Santos, M.; Annis, J.; Hao, J.; Johnston, D.; Kubo, J. M.; Reis, R. R. R.; and Simet, M., 2012. The Sdss Co-add: Cosmic Shear Measurement. *The Astrophys. J.*, 761, 1 (Nov. 2012), 15. doi:10.1088/0004-637x/761/1/15. https://dx.doi.org/10.1088/0004-637X/761/1/15. (cited on page 15)

Linder, E. V., 2003. Exploring the Expansion History of the Universe. *Phys. Res. Lab.*, 90, 9 (Mar. 2003), 091301. doi:10.1103/PhysRevLett.90.091301. (cited on page 7)

LSST Science Collaboration; Abell, P. A.; Allison, J.; Anderson, S. F.; Andrew, J. R.; Angel, J. R. P.; Armus, L.; Arnett, D.; Asztalos, S. J.; Axelrod, T. S.;

et al., 2009. LSST Science Book, Version 2.0. *arXiv e-prints*, (Dec. 2009), arXiv:0912.0201. (cited on pages 2 and 125)

Macaulay, E.; Nichol, R. C.; Bacon, D.; Brout, D.; Davis, T. M.; Zhang, B.; Bassett, B. A.; Scolnic, D.; Möller, A.; D'Andrea, C. B.; et al., 2019. First cosmological results using Type Ia supernovae from the Dark Energy Survey: measurement of the Hubble constant. *Mon. Notices Royal Astron. Soc.*, 486, 2 (Jun. 2019), 2184–2196. doi:10.1093/mnras/stz978. (cited on pages 13 and 50)

MacCoun, R. and Perlmutter, S., 2015. Blind analysis: Hide results to seek the truth. *Nature*, 526, 7572 (Oct. 2015), 187–189. doi:10.1038/526187a. (cited on page 20)

Mandel, K. S.; Narayan, G.; and Kirshner, R. P., 2011. Type Ia supernova light curve inference: Hierarchical models in the optical and near-infrared. *The Astrophys. J.*, 731, 2 (Apr. 2011), 120. doi:10.1088/0004-637x/731/2/120. http://dx.doi.org/10.1088/0004-637X/731/2/120. (cited on page 18)

Mandel, K. S.; Thorp, S.; Narayan, G.; Friedman, A. S.; and Avelino, A., 2021. A hierarchical Bayesian SEDmodel for Type Ia supernovae in the optical to near-infrared. *Mon. Notices Royal Astron. Soc.*, 510, 3 (Dec. 2021), 3939–3966. doi:10.1093/mnras/stab3496. https://doi.org/10.1093%2Fmnras%2Fstab3496. (cited on page 125)

Marriner, J.; Bernstein, J. P.; Kessler, R.; Lampeitl, H.; Miquel, R.; Mosher, J.; Nichol, R. C.; Sako, M.; Schneider, D. P.; and Smith, M., 2011. A more general model for the intrinsic scatter in Type Ia supernova distance moduli. *The Astrophys. J.*, 740, 2 (Sep. 2011), 72. doi:10.1088/0004-637x/740/2/72. http://dx.doi.org/10.1088/0004-637X/740/2/72. (cited on pages 42, 48, 110, 111, and 128)

Martin, B.; Lidman, C.; Brout, D.; Tucker, B. E.; Dixon, M.; and Armstrong, P., 2024. O II as an effective indicator of the dependence between the standardized luminosities of Type Ia supernovae and the properties of their host galaxies. *Mon. Notices Royal Astron. Soc.*, 533, 3 (Aug. 2024), 2640–2655. doi:10.1093/mnras/stae1996. http://dx.doi.org/10.1093/mnras/stae1996. (cited on page 148)

Massey, R.; Rhodes, J.; Leauthaud, A.; Capak, P.; Ellis, R.; Koekemoer, A.; Réfrégier, A.; Scoville, N.; Taylor, J. E.; Albert, J.; et al., 2007. COSMOS: Three-dimensional Weak Lensing and the Growth of Structure. *The Astrophys. J. Suppl. Ser.*, 172, 1 (Sep. 2007), 239. doi:10.1086/516599. https://dx.doi.org/10.1086/516599. (cited on page 15)

Meldorf, C.; Palmese, A.; Brout, D.; Chen, R.; Scolnic, D.; Kelsey, L.; Galbany, L.; Hartley, W. G.; Davis, T. M.; Drlica-Wagner, A.; et al., 2022. The Dark Energy Survey Supernova Program results: Type Ia supernova brightness correlates with host galaxy dust. *Mon. Notices Royal Astron. Soc.*, 518, 2 (Oct. 2022), 1985–2004. doi:10.1093/mnras/stac3056. http://dx.doi.org/10.1093/mnras/stac3056. (cited on pages 38 and 122)

Mena-Fernández, J.; Rodríguez-Monroy, M.; Avila, S.; Porredon, A.; Chan, K. C.; Camacho, H.; Weaverdyck, N.; Sevilla-Noarbe, I.; Sanchez, E.; Toribio San Cipriano, L.; et al., 2024. Dark Energy Survey: Galaxy Sample for the Baryonic Acoustic Oscillation Measurement from the Final Dataset. *arXiv e-prints*, (Feb. 2024), arXiv:2402.10697. doi:10.48550/arXiv.2402.10697. (cited on page 49)

Miknaitis, G.; Pignata, G.; Rest, A.; Wood-Vasey, W. M.; Blondin, S.; Challis, P.; Smith, R. C.; Stubbs, C. W.; Suntzeff, N. B.; Foley, R. J.; et al., 2007. The ESSENCE Supernova Survey: Survey Optimization, Observations, and Supernova Photometry. *The Astrophys. J.*, 666, 2 (Sep. 2007), 674–693. doi:10.1086/519986. http://dx.doi.org/10.1086/519986. (cited on pages 35, 38, and 46)

Miralda-Escude, J., 1991. The Correlation Function of Galaxy Ellipticities Produced by Gravitational Lensing. *Astrophys. J.*, 380 (Oct. 1991), 1. doi:10.1086/170555. (cited on page 15)

Misner, C. W.; Thorne, K. S.; and Wheeler, J. A., 1970. *Gravitation*. W. H. Freeman Princeton University Press. https://books.google.com.au/books?id=fYA2nQEACAAJ. (cited on page 2)

Mitra, A.; Kessler, R.; More, S.; Hlozek, R.; and The LSST Dark Energy Science Collaboration, 2022. Using Host Galaxy Photometric Redshifts to Improve Cosmological Constraints with Type Ia Supernova in the LSST Era. *arXiv e-prints*, (Oct. 2022), arXiv:2210.07560. doi:10.48550/arXiv.2210.07560. (cited on pages 122 and 125)

Möller, A. and de Boissière, T., 2020. SuperNNova: an open-source framework for Bayesian, neural network-based supernova classification. *Mon. Notices Royal Astron. Soc.*, 491, 3 (Jan. 2020), 4277–4293. doi:10.1093/mnras/stz3312. (cited on pages xiii, 58, 59, 67, 105, and 128)

Moshafi, H. and Bahraminasr, M., 2018. A Guide for CosmoMC Installation and Running. doi:10.48550/arxiv.1808.05080. https://arxiv.org/abs/1808.05080. (cited on pages 69 and 119)

Mosher, J.; Guy, J.; Kessler, R.; Astier, P.; Marriner, J.; Betoule, M.; Sako, M.; El-Hage, P.; Biswas, R.; Pain, R.; et al., 2014. Cosmological Parameter Uncertainties From Salt-ii Type Ia Supernova Light Curve Models. *The Astrophys. J.*, 793, 1 (Aug. 2014), 16. doi:10.1088/0004-637x/793/1/16. http://dx.doi.org/10.1088/0004-637X/793/1/16. (cited on page 47)

Narayan, G.; Rest, A.; Tucker, B. E.; Foley, R. J.; Wood-Vasey, W. M.; Challis, P.; Stubbs, C.; Kirshner, R. P.; Aguilera, C.; Becker, A. C.; et al., 2016. Light Curves of 213 Type Ia Supernovae from the ESSENCE Survey. *Astrophys. Journals*, 224, 1 (May 2016), 3. doi:10.3847/0067-0049/224/1/3. (cited on pages 35, 38, and 39)

Neyman, J., 1937. Outline of a Theory of Statistical Estimation Based on the Classical Theory of Probability. *Philos. Trans. Royal Soc. London. Ser. A, Math. Phys. Sci.*, 236, 767 (Aug. 1937), 333–380. doi:10.1098/rsta.1937.0005. https://doi.org/10.1098/rsta.1937.0005. (cited on pages 124 and 126)

Nørgaard-Nielsen, H. U.; Hansen, L.; Jørgensen, H. E.; Salamanca, A. A.; Ellis, R. S.; and Couch, W. J., 1989. The discovery of a Type Ia supernova at a redshift of 0.31. *Nature*, 339, 6225 (Jun. 1989), 523–525. doi:10.1038/339523a0. http://dx.doi.org/10.1038/339523a0. (cited on page 20)

Nugent, P.; Kim, A.; and Perlmutter, S., 2002. *K*-Corrections and Extinction Corrections for Type Ia Supernovae. *Publ. Astron. Soc. Pac.*, 114, 798 (Aug. 2002), 803–819. doi:10.1086/341707. https://doi.org/10.1086/341707. (cited on pages 28 and 29)

Oke, J. B. and Gunn, J. E., 1983. Secondary standard stars for absolute spectrophotometry. *The Astrophys. J.*, 266 (Mar. 1983), 713. doi:10.1086/160817. http://dx.doi.org/10.1086/160817. (cited on page 17)

Palmese, A.; Bom, C. R.; Mucesh, S.; and Hartley, W. G., 2023. A Standard Siren Measurement of the Hubble Constant Using Gravitational-wave Events from the First Three LIGO/Virgo Observing Runs and the DESILegacy Survey. *The Astrophys. J.*, 943, 1 (Jan. 2023), 56. doi:10.3847/1538-4357/aca6e3. https://doi.org/10.3847/1538-4357/aca6e3. (cited on page 16)

Palmese, A.; deVicente, J.; Pereira, M. E. S.; Annis, J.; Hartley, W.; Herner, K.; Soares-Santos, M.; Crocce, M.; Huterer, D.; Hernandez, I. M.; et al., 2020. A Statistical Standard Siren Measurement of the Hubble Constant from the LIGO/Virgo Gravitational Wave Compact Object Merger GW190814 and Dark Energy Survey Galaxies. *The Astrophys. J.*, 900, 2 (Sep. 2020), L33. doi:10.3847/2041-8213/abaeff. https://doi.org/10.3847/2041-8213/abaeff. (cited on page 16)

Pan, Y. C.; Sullivan, M.; Maguire, K.; Hook, I. M.; Nugent, P. E.; Howell, D. A.;

Arcavi, I.; Botyanszki, J.; Cenko, S. B.; DeRose, J.; et al., 2013. The host galaxies of Type Ia supernovae discovered by the Palomar Transient Factory. *Mon. Notices Royal Astron. Soc.*, 438, 2 (Dec. 2013), 1391–1416. doi:10.1093/mnras/stt2287. http://dx.doi.org/10.1093/mnras/stt2287. (cited on pages 38 and 98)

Penzias, A. A. and Wilson, R. W., 1965. A Measurement of Excess Antenna Temperature at 4080 Mc/s. *Astrophys. J.*, 142 (Jul. 1965), 419–421. doi:10.1086/148307. (cited on page 13)

Perley, D. A.; Fremling, C.; Sollerman, J.; Miller, A. A.; Dahiwale, A. S.; Sharma, Y.; Bellm, E. C.; Biswas, R.; Brink, T. G.; Bruch, R. J.; et al., 2020. The Zwicky Transient Facility Bright Transient Survey. II. A Public Statistical Sample for Exploring Supernova Demographics∗. *The Astrophys. J.*, 904, 1 (Nov. 2020), 35. doi:10.3847/1538-4357/abbd98. http://dx.doi.org/10.3847/1538-4357/abbd98. (cited on page 50)

Perlmutter, S., 1995. Four Papers by the Supernova Cosmology Project. Ernest Orlando Lawrence Berkeley National Laboratory, Berkeley, CA (US). https://www.osti.gov/biblio/938413. (cited on page 28)

Perlmutter, S.; Aldering, G.; Goldhaber, G.; Knop, R. A.; Nugent, P.; Castro, P. G.; Deustua, S.; Fabbro, S.; Goobar, A.; Groom, D. E.; et al., 1999. Measurements of Ω and Λ from 42 High-Redshift Supernovae. *Astrophys. J.*, 517, 2 (Jun. 1999), 565–586. doi:10.1086/307221. (cited on pages 2, 7, 20, 25, 27, 33, 34, 46, 125, and 146)

Perlmutter, S.; Deustua, S.; Gabi, S.; Goldhaber, G.; Groom, D.; Hook, I.; Kim, A.; Kim, M.; Lee, J.; Pain, R.; Pennypacker, C.; Small, I.; Goobar, A.; Ellis, R.; Glazebrook, K.; McMahon, R.; Boyle, B.; Bunclark, P.; Carter, D.; Irwin, M.; Newberg, H.; Filippenko, A. V.; Matheson, T.; Dopita, M.; Mould, J.; and Couch, W., 1996. Scheduled Discoveries of 7+ High-Redshift Supernovae: First Cosmology Results and Bounds on q_0. doi:10.48550/ARXIV.ASTRO-PH/9602122. https://arxiv.org/abs/astro-ph/9602122. (cited on page 28)

Perlmutter, S.; Gabi, S.; Goldhaber, G.; Goobar, A.; Groom, D. E.; Hook, I. M.; Kim, A. G.; Kim, M. Y.; Lee, J. C.; Pain, R.; et al., 1997. Measurements of the Cosmological Parameters Ω and Λ from the First Seven Supernovae at $z \geq 0.35$. *The Astrophys. J.*, 483, 2 (Jul. 1997), 565–581. doi:10.1086/304265. http://dx.doi.org/10.1086/304265. (cited on page 31)

Peterson, E. R.; Jones, D. O.; Scolnic, D.; Sánchez, B. O.; Do, A.; Riess, A. G.; Ward, S. M.; Dwomoh, A.; de, J. T.; Jha, S. W.; et al., 2023. The DEHVILS survey overview and initial data release: high-quality near-infrared Type Ia supernova light curves at low redshift. *Mon. Notices Royal Astron. Soc.*, 522, 2 (Apr. 2023), 2478–2494. doi:10.1093/mnras/stad1077. http://dx.doi.org/10.1093/mnras/stad1077. (cited on page 121)

Peterson, E. R.; Kenworthy, W. D.; Scolnic, D.; Riess, A. G.; Brout, D.; Carr, A.; Courtois, H.; Davis, T.; Dwomoh, A.; Jones, D. O.; et al., 2022. The Pantheon+ Analysis: Evaluating Peculiar Velocity Corrections in Cosmological Analyses with Nearby Type Ia Supernovae. *The Astrophys. J.*, 938, 2 (Oct. 2022), 112. doi:10.3847/1538-4357/ac4698. http://dx.doi.org/10.3847/1538-4357/ac4698. (cited on page 122)

Phillips, M. M., 1993. The Absolute Magnitudes of Type Ia Supernovae. *Astrophys. J.*, 413 (Aug. 1993), L105. doi:10.1086/186970. (cited on pages 20 and 29)

Pierel, J. D. R.; Jones, D. O.; Kenworthy, W. D.; Dai, M.; Kessler, R.; Ashall, C.; Do, A.; Peterson, E. R.; Shappee, B. J.; Siebert, M. R.; et al., 2022. SALT3-NIR: Taking the Open-source Type Ia Supernova Model to Longer Wavelengths for Next-generation Cosmological Measurements. *The Astrophys. J.*, 939, 1 (Oct. 2022), 11. doi:10.3847/1538-4357/ac93f9. http://dx.doi.org/10.3847/1538-4357/ac93f9. (cited on pages 121 and 148)

Planck Collaboration; Ade, P. A. R.; Aghanim, N.; Armitage-Caplan, C.; Arnaud, M.; Ashdown, M.; Atrio-Barandela, F.; Aumont, J.; Baccigalupi, C.; Banday, A. J.; et al., 2014. Planck 2013 results. XVI. Cosmological parameters. *Astron. & Astrophys.*, 571 (Oct. 2014), A16. doi:10.1051/0004-6361/201321591. https://doi.org/10.1051%2F0004-6361%2F201321591. (cited on page 14)

Planck Collaboration; Ade, P. A. R.; Aghanim, N.; Arnaud, M.; Ashdown, M.; Aumont, J.; Baccigalupi, C.; Banday, A. J.; Barreiro, R. B.; Bartlett, J. G.; et al., 2016. Planck 2015 results. XIII. Cosmological parameters. *Astron. & Astrophys.*, 594 (Sep. 2016), A13. doi:10.1051/0004-6361/201525830. (cited on pages 14 and 50)

Planck Collaboration; Aghanim, N.; Akrami, Y.; Ashdown, M.; Aumont, J.; Baccigalupi, C.; Ballardini, M.; Banday, A. J.; Barreiro, R. B.; Bartolo, N.; et al., 2020. Planck 2018 results. *Astron. & Astrophys.*, 641 (Sep. 2020), A6. doi:10.1051/0004-6361/201833910. https://doi.org/10.1051%2F0004-6361%2F201833910. (cited on pages 14 and 56)

Popovic, B.; Brout, D.; Kessler, R.; and Scolnic, D., 2023. The Pantheon+ Analysis: Forward Modelling the Dust and Intrinsic Color Distributions of Type Ia Supernovae, and Quantifying Their Impact on Cosmological Inferences. *The Astrophys. J.*, 945, 1 (Mar. 2023), 84. doi:10.3847/1538-4357/aca273. http://dx.doi.org/10.3847/1538-4357/aca273. (cited on page 122)

Popovic, B.; Brout, D.; Kessler, R.; Scolnic, D.; and Lu, L., 2021. Improved Treatment of Host-galaxy Correlations in Cosmological Analyses with Type Ia Supernovae. *The Astrophys. J.*, 913, 1 (May 2021), 49. doi:10.3847/1538-4357/abf14f. http://dx.doi.org/10.3847/1538-4357/abf14f. (cited on pages 38, 51, 53, 94, 120, 121, and 126)

Popovic, B.; Scolnic, D.; Vincenzi, M.; Sullivan, M.; Brout, D.; Chen, R.; Patel, U.; Peterson, E. R.; Kessler, R.; Kelsey, L.; et al., 2024. Amalgame: cosmological constraints from the first combined photometric supernova sample. *Mon. Notices Royal Astron. Soc.*, 529, 3 (Feb. 2024), 2100–2115. doi:10.1093/mnras/stae420. http://dx.doi.org/10.1093/mnras/stae420. (cited on pages 69 and 121)

Pritchard, J. K.; Seielstad, M. T.; Perez-Lezaun, A.; and Feldman, M. W., 1999. Population growth of human Y chromosomes: a study of Y chromosome microsatellites. *Mol. Biol. Evol.*, 16, 12 (Dec. 1999), 1791–1798. doi:10.1093/oxfordjournals.molbev.a026091. http://dx.doi.org/10.1093/oxfordjournals.molbev.a026091. (cited on page 152)

Pskovskii, I. P., 1977. Light curves, color curves, and expansion velocity of type I supernovae as functions of the rate of brightness decline. *Sov. Astron.*, 21 (Dec. 1977), 675. (cited on page 20)

Qu, H.; Sako, M.; Mö ller, A.; and Doux, C., 2021. SCONE: Supernova Classification with a Convolutional Neural Network. *Astron. J.*, 162, 2 (Aug. 2021), 67. doi:10.3847/1538-3881/ac0824. (cited on pages xiii, 58, 59, 67, 69, 105, and 128)

Qu, H.; Sako, M.; Vincenzi, M.; Sánchez, C.; Brout, D.; Kessler, R.; Chen, R.; Davis, T.; Galbany, L.; Kelsey, L.; et al., 2024. The Dark Energy Survey Supernova Program: Cosmological Biases from Host Galaxy Mismatch of Type Ia Supernovae. *The Astrophys. J.*, 964, 2 (Mar. 2024), 134. doi:10.3847/1538-4357/ad251d. http://dx.doi.org/10.3847/1538-4357/ad251d. (cited on page 122)

Rest, A.; Scolnic, D.; Foley, R. J.; Huber, M. E.; Chornock, R.; Narayan, G.; Tonry, J. L.; Berger, E.; Soderberg, A. M.; Stubbs, C. W.; et al., 2014. Cosmological constraints from measurments of Type Ia supernovae discovered during the first 1.5yr of the Pan-STARRS1 survey. *The Astrophys. J.*, 795, 1 (Oct. 2014), 44. doi:10.1088/0004-637x/795/1/44. http://dx.doi.org/10.1088/0004-637X/795/1/44. (cited on pages 25, 42, and 48)

Riess, A. G.; Filippenko, A. V.; Challis, P.; Clocchiatti, A.; Diercks, A.; Garnavich, P. M.; Gilliland, R. L.; Hogan, C. J.; Jha, S.; Kirshner, R. P.; et al., 1998. Observational Evidence from Supernovae for an Accelerating

Universe and a Cosmological Constant. *Astron. J.*, 116, 3 (Sep. 1998), 1009–1038. doi:10.1086/300499. (cited on pages 2, 7, 20, 25, 27, 33, 34, 45, 46, 125, and 146)

Riess, A. G.; Kirshner, R. P.; Schmidt, B. P.; Jha, S.; Challis, P.; Garnavich, P. M.; Esin, A. A.; Carpenter, C.; Grashius, R.; Schild, R. E.; et al., 1999. *BVRI* Light Curves for 22 Type Ia Supernovae. *The Astron. J.*, 117, 2 (Feb. 1999), 707–724. doi:10.1086/300738. http://dx.doi.org/10.1086/300738. (cited on pages 20, 35, 44, 45, and 46)

Riess, A. G.; Nugent, P. E.; Gilliland, R. L.; Schmidt, B. P.; Tonry, J.; Dickinson, M.; Thompson, R. I.; Budavari, T.; Casertano, S.; Evans, A. S.; et al., 2001. The Farthest Known Supernova: Support for an Accelerating Universe and a Glimpse of the Epoch of Deceleration. *The Astrophys. J.*, 560, 1 (Oct. 2001), 49–71. doi:10.1086/322348. http://dx.doi.org/10.1086/322348. (cited on page 45)

Riess, A. G.; Press, W. H.; and Kirshner, R. P., 1996. A Precise Distance Indicator: Type Ia Supernova Multicolor Light-Curve Shapes. *Astrophys. J.*, 473 (Dec. 1996), 88. doi:10.1086/178129. (cited on page 30)

Riess, A. G.; Strolger, L.; Casertano, S.; Ferguson, H. C.; Mobasher, B.; Gold, B.; Challis, P. J.; Filippenko, A. V.; Jha, S.; Li, W.; et al., 2007. New Hubble Space Telescope Discoveries of Type Ia Supernovae at $z \geq 1$: Narrowing Constraints on the Early Behavior of Dark Energy. *The Astrophys. J.*, 659, 1 (Apr. 2007), 98–121. doi:10.1086/510378. http://dx.doi.org/10.1086/510378. (cited on pages 40, 45, and 46)

Riess, A. G.; Strolger, L.; Tonry, J.; Casertano, S.; Ferguson, H. C.; Mobasher, B.; Challis, P.; Filippenko, A. V.; Jha, S.; Li, W.; et al., 2004. Type Ia Supernova Discoveries at $z > 1$ from the Hubble Space Telescope: Evidence for Past Deceleration and Constraints on Dark Energy Evolution. *The Astrophys. J.*, 607, 2 (Jun. 2004), 665–687. doi:10.1086/383612. http://dx.doi.org/10.1086/383612. (cited on pages 45 and 46)

Rigault, M.; Brinnel, V.; Aldering, G.; Antilogus, P.; Aragon, C.; Bailey, S.; Baltay, C.; Barbary, K.; Bongard, S.; Boone, K.; et al., 2020. Strong dependence of Type Ia supernova standardization on the local specific star formation rate. *Astron. & Astrophys.*, 644 (Dec. 2020), A176. doi:10.1051/0004-6361/201730404. http://dx.doi.org/10.1051/0004-6361/201730404. (cited on pages 38 and 98)

Rigault, M.; Smith, M.; Goobar, A.; Maguire, K.; Dimitriadis, G.; Johansson, J.; Nordin, J.; Burgaz, U.; Dhawan, S.; Sollerman, J.; Regnault, N.; Kowalski, M.; Nugent, P.; Andreoni, I.; Amenouche, M.; Aubert, M.; Barjou-Delayre, C.; Bautista, J.; Bellm, E.; Betoule, M.; Bloom, J. S.; Carreres, B.; Chen, T. X.; Copin, Y.; Deckers, M.; de Jaeger, T.; Feinstein, F.; Fouchez, D.; Fremling, C.; Galbany, L.; Ginolin, M.; Graham, M.; Groom, S. L.; Harvey, L.; Kasliwal, M. M.; Kenworthy, W. D.; Kim, Y.-L.; Kuhn, D.; Kulkarni, S. R.; Lacroix, L.; Laher, R. R.; Masci, F. J.; Müller-Bravo, T. E.; Miller, A.; Osman, M.; Perley, D.; Popovic, B.; Purdum, J.; Qin, Y.-J.; Racine, B.; Reusch, S.; Riddle, R.; Rosnet, P.; Rosselli, D.; Ruppin, F.; Senzel, R.; Rusholme, B.; Schweyer, T.; Terwel, J. H.; Townsend, A.; Tzanidakis, A.; Wold, A.; and Yan, L., 2025. ZTF SN Ia DR2: Overview. *Astron. & Astrophys.*, 694 (Feb. 2025), A1. doi:10.1051/0004-6361/202450388. http://dx.doi.org/10.1051/0004-6361/202450388. (cited on pages 44 and 50)

Robertson, H. P., 1929. OnTheFoundationsOfRelativisticCosmology. *Proc. National Acad. Sci.*, 15, 11 (Nov. 1929), 822–829. doi:10.1073/pnas.15.11.822. https://doi.org/10.1073/pnas.15.11.822. (cited on page 3)

Rose, B. M.; Popovic, B.; Scolnic, D.; and Brout, D., 2022. Constraining RV variation using highly reddened Type Ia supernovae from the Pantheon+ sample. *Mon. Notices Royal Astron. Soc.*, 516, 4 (Sep. 2022), 4822–4832. doi:10.1093/mnras/stac2500. http://dx.doi.org/10.1093/mnras/stac2500. (cited on page 122)

Ross, A. J.; Samushia, L.; Howlett, C.; Percival, W. J.; Burden, A.; and Manera, M., 2015. The clustering of the SDSS DR7 main Galaxy sample – I. A 4 per cent distance measure at z = 0.15. *Mon. Notices Royal Astron. Soc.*, 449, 1 (Mar. 2015), 835–847. doi:10.1093/mnras/stv154. http://dx.doi.org/10.1093/mnras/stv154. (cited on page 50)

Roszkowski, L.; Sessolo, E. M.; and Trojanowski, S., 2018. WIMPdark matter candidates and searches - current status and future prospects. *Reports on Prog. Phys.*, 81, 6 (May 2018), 066201. doi:10.1088/1361-6633/aab913. https://doi.org/10.1088%2F1361-6633%2Faab913. (cited on page 6)

Rubin, D.; Aldering, G.; Barbary, K.; Boone, K.; Chappell, G.; Currie, M.; Deustua, S.; Fagrelius, P.; Fruchter, A.; Hayden, B.; et al., 2015. UNITY: Confronting Supernova Cosmology's Statistical and Systematic Uncertainties in a Unified Bayesian Framework. *Astrophys. J.*, 813, 2 (Nov. 2015), 137. doi:10.1088/0004-637x/813/2/137. (cited on page 125)

Rubin, D.; Aldering, G.; Betoule, M.; Fruchter, A.; Huang, X.; Kim, A. G.; Lidman, C.; Linder, E.; Perlmutter, S.; Ruiz-Lapuente, P.; et al., 2023. Union Through UNITY: Cosmology with 2,000 SNe Using a Unified Bayesian Framework. *arXiv e-prints*, (Nov. 2023), arXiv:2311.12098. doi:10.48550/arXiv.2311.12098. (cited on pages 25, 48, and 52)

Rubin, V. C. and Ford, W. K. J., 1970. Rotation of the Andromeda Nebula from a Spectroscopic Survey of Emission Regions. *Astrophys. J.*, 159 (Feb. 1970), 379. doi:10.1086/150317. (cited on page 6)

Sako, M.; Bassett, B.; Becker, A.; Cinabro, D.; DeJongh, F.; Depoy, D. L.; Dilday, B.; Doi, M.; Frieman, J. A.; Garnavich, P. M.; et al., 2007. The Sloan Digital Sky Survey-ii Supernova Survey: Search Algorithm And Follow-up Observations. *The Astron. J.*, 135, 1 (Dec. 2007), 348–373. doi:10.1088/0004-6256/135/1/348. http://dx.doi.org/10.1088/0004-6256/135/1/348. (cited on page 35)

Sánchez, B. O.; Brout, D.; Vincenzi, M.; Sako, M.; Herner, K.; Kessler, R.; Davis, T. M.; Scolnic, D.; Acevedo, M.; Lee, J.; et al., 2024. The Dark Energy Survey Supernova Program: Light curves and 5-Year data release. *arXiv e-prints*, (Jun. 2024), arXiv:2406.05046. doi:10.48550/arXiv.2406.05046. (cited on pages 73 and 77)

Sánchez, B. O.; Kessler, R.; Scolnic, D.; Armstrong, R.; Biswas, R.; Bogart, J.; Chiang, J.; Cohen-Tanugi, J.; Fouchez, D.; Gris, P.; et al., 2022. SNIa Cosmology Analysis Results from Simulated LSST Images: From Difference Imaging to Constraints on Dark Energy. *Astrophys. J.*, 934, 2 (Aug. 2022), 96. doi:10.3847/1538-4357/ac7a37. (cited on page 125)

Sandage, A. and Tammann, G. A., 1985. *Supernovae as Distance Indicators: Proceedings of a Workshop Held at the Harvard-Smithsonian Center for Astrophysics September 27-28, 1984*. Springer Berlin Heidelberg. ISBN 9783540393269. doi:10.1007/3-540-15206-7. http://dx.doi.org/10.1007/3-540-15206-7. (cited on page 20)

Schlafly, E. F.; Finkbeiner, D. P.; Schlegel, D. J.; Jurić, M.; Ivezić, V.; Gibson, R. R.; Knapp, G. R.; and Weaver, B. A., 2010. The Blue Tip Of The Stellar Locus: Measuring Reddening With The Sloan Digital Sky Survey. *The Astrophys. J.*, 725, 1 (Nov. 2010), 1175–1191. doi:10.1088/0004-637x/725/1/1175. http://dx.doi.org/10.1088/0004-637X/725/1/1175. (cited on pages 19 and 117)

Schmidt, B. P.; Suntzeff, N. B.; Phillips, M. M.; Schommer, R. A.; Clocchiatti, A.; Kirshner, R. P.; Garnavich, P.; Challis, P.; Leibundgut, B.; Spyromilio, J.; et al., 1998. The High-Z Supernova Search: Measuring Cosmic Deceleration and Global Curvature of the Universe Using Type Ia Supernovae. *Astrophys. J.*, 507, 1 (Nov. 1998), 46–63. doi:10.1086/306308. (cited on pages 2, 7, 20, 25, 27, 46, and 146)

Schrabback, T.; Hartlap, J.; Joachimi, B.; Kilbinger, M.; Simon, P.; Benabed, K.; Bradač, M.; Eifler, T.; Erben, T.; Fassnacht, C. D.; et al., 2010. Evidence of the accelerated expansion of the Universe from weak lensing tomography with

COSMOS. *Astron. Astrophys.*, 516 (Jun. 2010), A63. doi:10.1051/0004-6361/200913577. https://doi.org/10.1051%2F0004-6361%2F200913577. (cited on page 15)

Schutz, B. F., 1986. Determining the Hubble constant from gravitational wave observations. *Nature*, 323, 6086 (Sep. 1986), 310–311. doi:10.1038/323310a0. https://doi.org/10.1038/323310a0. (cited on page 16)

Scolnic, D.; Brout, D.; Carr, A.; Riess, A. G.; Davis, T. M.; Dwomoh, A.; Jones, D. O.; Ali, N.; Charvu, P.; Chen, R.; et al., 2022. The Pantheon+ Analysis: The Full Data Set and Light-curve Release. *The Astrophys. J.*, 938, 2 (Oct. 2022), 113. doi:10.3847/1538-4357/ac8b7a. http://dx.doi.org/10.3847/1538-4357/ac8b7a. (cited on pages 51 and 120)

Scolnic, D.; Casertano, S.; Riess, A.; Rest, A.; Schlafly, E.; Foley, R. J.; Finkbeiner, D.; Tang, C.; Burgett, W. S.; Chambers, K. C.; et al., 2015. Supercal: Cross-calibration of Multiple Photometric Systems to Improve Cosmological Measurements with Type Ia Supernovae. *Astrophys. J.*, 815, 2 (Dec. 2015), 117. doi:10.1088/0004-637x/815/2/117. (cited on pages 48 and 77)

Scolnic, D.; Rest, A.; Riess, A.; Huber, M. E.; Foley, R. J.; Brout, D.; Chornock, R.; Narayan, G.; Tonry, J. L.; Berger, E.; et al., 2014. Systematic uncertainties associated with the cosmological analysis of the first Pan-STARRS1 Type Ia supernova sample. *The Astrophys. J.*, 795, 1 (Oct. 2014), 45. doi:10.1088/0004-637x/795/1/45. http://dx.doi.org/10.1088/0004-637X/795/1/45. (cited on pages 25, 42, and 48)

Scolnic, D. M.; Jones, D. O.; Rest, A.; Pan, Y. C.; Chornock, R.; Foley, R. J.; Huber, M. E.; Kessler, R.; Narayan, G.; Riess, A. G.; et al., 2018. The Complete Light-curve Sample of Spectroscopically Confirmed SNe Ia from Pan-STARRS1 and Cosmological Constraints from the Combined Pantheon Sample. *Astrophys. J.*, 859, 2 (Jun. 2018), 101. doi:10.3847/1538-4357/aab9bb. (cited on pages 25 and 48)

Sevilla-Noarbe, I.; Bechtol, K.; Carrasco, K. M.; Carnero, R. A.; Becker, M. R.; Drlica-Wagner, A.; Gruendl, R. A.; Rykoff, E. S.; Sheldon, E.; Yanny, B.; et al., 2021. Dark Energy Survey Year 3 Results: Photometric Data Set for Cosmology. *The Astrophys. J. Suppl. Ser.*, 254, 2 (May 2021), 24. doi:10.3847/1538-4365/abeb66. http://dx.doi.org/10.3847/1538-4365/abeb66. (cited on page 53)

Shapley, H. and Curtis, H. D., 1921. The Scale of the Universe. *Bull. National Res. Counc.*, 2, 11 (May 1921), 171–217. (cited on page 1)

Smith, M.; D'Andrea, C. B.; Sullivan, M.; Möller, A.; Nichol, R. C.; Thomas, R. C.; Kim, A. G.; Sako, M.; Castander, F. J.; Filippenko, A. V.; et al., 2020a. First Cosmology Results using Supernovae Ia from the Dark Energy Survey: Survey Overview, Performance, and Supernova Spectroscopy. *The Astron. J.*, 160, 6 (Nov. 2020), 267. doi:10.3847/1538-3881/abc01b. http://dx.doi.org/10.3847/1538-3881/abc01b. (cited on pages 49, 78, and 129)

Smith, M.; Sullivan, M.; Wiseman, P.; Kessler, R.; Scolnic, D.; Brout, D.; D'Andrea, C. B.; Davis, T. M.; Foley, R. J.; Frohmaier, C.; et al., 2020b. First cosmology results using Type Ia supernovae from the Dark Energy Survey: the effect of host galaxy properties on supernova luminosity. *Mon. Notices Royal Astron. Soc.*, 494, 3 (Apr. 2020), 4426–4447. doi:10.1093/mnras/staa946. http://dx.doi.org/10.1093/mnras/staa946. (cited on pages 49 and 98)

Smith, S., 1936. The Mass of the Virgo Cluster. *Astrophys. J.*, 83 (Jan. 1936), 23. doi:10.1086/143697. (cited on page 6)

Smoot, G. F.; Bennett, C. L.; Kogut, A.; Wright, E. L.; Aymon, J.; Boggess, N. W.; Cheng, E. S.; de Amici, G.; Gulkis, S.; Hauser, M. G.; et al., 1992. Structure in the COBE Differential Microwave Radiometer First-Year Maps. *Astrophys. J.*, 396 (Sep. 1992), L1. doi:10.1086/186504. (cited on page 14)

Springel, V.; White, S. D. M.; Jenkins, A.; Frenk, C. S.; Yoshida, N.; Gao, L.; Navarro, J.; Thacker, R.; Croton, D.; Helly, J.; et al., 2005. Simulations of the formation, evolution and clustering of galaxies and quasars. *Nature*, 435, 7042 (Jun. 2005), 629–636. doi:10.1038/nature03597. https://doi.org/10.1038/nature03597. (cited on page 6)

Stritzinger, M. D.; Phillips, M. M.; Boldt, L. N.; Burns, C.; Campillay, A.; Contreras, C.; Gonzalez, S.; Folatelli, G.; Morrell, N.; Krzeminski, W.; et al., 2011. The Carnegie supernova project: Second photometry data release of low-redshift Type Ia supernovae. *The Astron. J.*, 142, 5 (Oct. 2011), 156. doi:10.1088/0004-6256/142/5/156. http://dx.doi.org/10.1088/0004-6256/142/5/156. (cited on page 44)

Sullivan, M.; Conley, A.; Howell, D. A.; Neill, J. D.; Astier, P.; Balland, C.; Basa, S.; Carlberg, R. G.; Fouchez, D.; Guy, J.; et al., 2010. The dependence of Type Ia Supernovae luminosities on their host galaxies: SN Ia host galaxies. *Mon. Notices Royal Astron. Soc.*, (May 2010), no–no. doi:10.1111/j.1365-2966.2010.16731.x. http://dx.doi.org/10.1111/j.1365-2966.2010.16731.x. (cited on pages 19, 38, and 98)

Sullivan, M.; Guy, J.; Conley, A.; Regnault, N.; Astier, P.; Balland, C.; Basa, S.; Carlberg, R. G.; Fouchez, D.; Hardin, D.; et al., 2011. SNLS3: Constraints On Dark Energy Combining The Supernova Legacy Survey Three-year Data

With Other Probes. *The Astrophys. J.*, 737, 2 (Aug. 2011), 102. doi:10.1088/0004-637x/737/2/102. https://doi.org/10.1088/0004-637x/737/2/102. (cited on pages 25, 35, and 47)

Sullivan, M.; Howell, D. A.; Perrett, K.; Nugent, P. E.; Astier, P.; Aubourg, E.; Balam, D.; Basa, S.; Carlberg, R. G.; Conley, A.; et al., 2006. Photometric Selection of High-Redshift Type Ia Supernova Candidates. *The Astron. J.*, 131, 2 (Feb. 2006), 960–972. doi:10.1086/499302. http://dx.doi.org/10.1086/499302. (cited on page 36)

Suzuki, N.; Rubin, D.; Lidman, C.; Aldering, G.; Amanullah, R.; Barbary, K.; Barrientos, L. F.; Botyanszki, J.; Brodwin, M.; Connolly, N.; et al., 2012. The hubble space telescopecluster supernova survey. V. Improving the dark-energy constraints above $z > 1$ and building an early-type-hosted supernova sample. *The Astrophys. J.*, 746, 1 (Jan. 2012), 85. doi:10.1088/0004-637x/746/1/85. http://dx.doi.org/10.1088/0004-637X/746/1/85. (cited on pages 25 and 47)

Taylor, G.; Jones, D. O.; Popovic, B.; Vincenzi, M.; Kessler, R.; Scolnic, D.; Dai, M.; Kenworthy, W. D.; and Pierel, J. D. R., 2023. SALT2 versus SALT3: Updated model surfaces and their impacts on Type Ia supernova cosmology. *Mon. Notices Royal Astron. Soc.*, (Jan. 2023). doi:10.1093/mnras/stad320. (cited on pages xiii, 53, 58, 59, 69, 80, 97, 122, 126, and 148)

Taylor, G.; Lidman, C.; Popovic, B.; and Abbot, H. J., 2024. Training custom light curve models of SN Ia sub-populations selected according to host galaxy properties. *Mon. Notices Royal Astron. Soc.*, 528, 3 (Jan. 2024), 4643–4656. doi:10.1093/mnras/stae293. http://dx.doi.org/10.1093/mnras/stae293. (cited on page 122)

Taylor, G.; Lidman, C.; Tucker, B. E.; Brout, D.; Hinton, S. R.; and Kessler, R., 2021. A revised SALT2 surface for fitting Type Ia supernova light curves. *Mon. Notices Royal Astron. Soc.*, 504, 3 (Jul. 2021), 4111–4122. doi:10.1093/mnras/stab962. (cited on pages 121, 122, and 127)

The Dark Energy Survey Collaboration, 2005. The Dark Energy Survey. *arXiv e-prints*, (Oct. 2005), astro-ph/0510346. doi:10.48550/arXiv.astro-ph/0510346. (cited on page 49)

Tonry, J. L.; Schmidt, B. P.; Barris, B.; Candia, P.; Challis, P.; Clocchiatti, A.; Coil, A. L.; Filippenko, A. V.; Garnavich, P.; Hogan, C.; et al., 2003. Cosmological Results from High-z Supernovae. *The Astrophys. J.*, 594, 1 (Sep. 2003), 1–24. doi:10.1086/376865. http://dx.doi.org/10.1086/376865. (cited on pages 45 and 46)

Toy, M.; Wiseman, P.; Sullivan, M.; Frohmaier, C.; Palmese, A.; Graur, O.; Popovic, B.; Davis, T. M.; Galbany, L.; Kelsey, L.; et al., 2023. Rates and properties of Type Ia supernovae in galaxy clusters within the Dark Energy Survey. *arXiv e-prints*, (Feb. 2023), arXiv:2302.05184. doi:10.48550/arXiv.2302.05184. (cited on page 126)

Tripp, R., 1998. A two-parameter luminosity correction for Type Ia supernovae. *Astron. & Astrophys.*, 331 (Mar. 1998), 815–820. (cited on page 127)

Uddin, S. A.; Mould, J.; Lidman, C.; Ruhlmann-Kleider, V.; and Hardin, D., 2017. Cosmological Inference from Host-Selected Type Ia Supernova Samples. *Publ. Astron. Soc. Aust.*, 34 (2017). doi:10.1017/pasa.2017.2. http://dx.doi.org/10.1017/pasa.2017.2. (cited on page 18)

Unnikrishnan, C. S., 2023. LIGO-India: A Decadal Assessment on Its Scope, Relevance, Progress, and Future. (cited on page 16)

Van Waerbeke, L.; Mellier, Y.; Erben, T.; Cuillandre, J. C.; Bernardeau, F.; Maoli, R.; Bertin, E.; McCracken, H. J.; Le Fèvre, O.; Fort, B.; et al., 2000. Detection of correlated galaxy ellipticities from CFHT data: first evidence for gravitational lensing by large-scale structures. *Astron. & Astrophys.*, 358 (Jun. 2000), 30–44. doi:10.48550/arXiv.astro-ph/0002500. (cited on page 15)

Vincenzi, M.; Brout, D.; Armstrong, P.; Popovic, B.; Taylor, G.; Acevedo, M.; Camilleri, R.; Chen, R.; Davis, T. M.; Hinton, S. R.; et al., 2024. The Dark Energy Survey Supernova Program: Cosmological Analysis and Systematic Uncertainties. *arXiv e-prints*, (Jan. 2024), arXiv:2401.02945. doi:10.48550/arXiv.2401.02945. (cited on pages 25, 49, 56, 59, 67, 113, 123, 146, and 147)

Vincenzi, M.; Sullivan, M.; Firth, R. E.; Gutiérrez, C. P.; Frohmaier, C.; Smith, M.; Angus, C.; and Nichol, R. C., 2019. Spectrophotometric templates for core-collapse supernovae and their application in simulations of time-domain surveys. *Mon. Notices Royal Astron. Soc.*, 489, 4 (Sep. 2019), 5802–5821. doi:10.1093/mnras/stz2448. http://dx.doi.org/10.1093/mnras/stz2448. (cited on pages 107, 111, and 114)

Vincenzi, M.; Sullivan, M.; Graur, O.; Brout, D.; Davis, T. M.; Frohmaier, C.; Galbany, L.; Gutiérrez, C. P.; Hinton, S. R.; Hounsell, R.; et al., 2021. The Dark Energy Survey supernova programme: modelling selection efficiency and observed core-collapse supernova contamination. *Mon. Notices Royal Astron. Soc.*, 505, 2 (May 2021), 2819–2839. doi:10.1093/mnras/stab1353. http://dx.doi.org/10.1093/mnras/stab1353. (cited on page 122)

Vincenzi, M.; Sullivan, M.; Möller, A.; Armstrong, P.; Bassett, B. A.; Brout, D.; Carollo, D.; Carr, A.; Davis, T. M.; Frohmaier, C.; et al., 2023. The Dark

Energy Survey supernova program: cosmological biases from supernova photometric classification. *Mon. Notices Royal Astron. Soc.*, 518, 1 (Jan. 2023), 1106–1127. doi:10.1093/mnras/stac1404. (cited on pages 122 and 126)

Virgo Collaboration, 2014. Advanced Virgo: a second-generation interferometric gravitational wave detector. *Class. Quantum Gravity*, 32, 2 (Dec. 2014), 024001. doi:10.1088/0264-9381/32/2/024001. https://doi.org/10.1088%2F0264-9381%2F32%2F2%2F024001. (cited on page 16)

Walker, A. G., 1935. On Riemanntan Spaces With Spherical Symmetry About A Line, And The Conditions For Isotropy In Genj Relativity. *The Q. J. Math.*, 6, 1 (01 1935), 81–93. doi:10.1093/qmath/os-6.1.81. (cited on page 3)

Wiseman, P.; Sullivan, M.; Smith, M.; Frohmaier, C.; Vincenzi, M.; Graur, O.; Popovic, B.; Armstrong, P.; Brout, D.; Davis, T. M.; et al., 2021. Rates and delay times of Type Ia supernovae in the Dark Energy Survey. *Mon. Notices Royal Astron. Soc.*, (Jul. 2021). doi:10.1093/mnras/stab1943. http://dx.doi.org/10.1093/mnras/stab1943. (cited on page 122)

Wittman, D. M.; Tyson, J. A.; Kirkman, D.; Dell'Antonio, I.; and Bernstein, G., 2000. Detection of weak gravitational lensing distortions of distant galaxies by cosmic dark matter at large scales. *Nature*, 405, 6783 (May 2000), 143–148. doi:10.1038/35012001. (cited on page 15)

Wood-Vasey, W. M.; Miknaitis, G.; Stubbs, C. W.; Jha, S.; Riess, A. G.; Garnavich, P. M.; Kirshner, R. P.; Aguilera, C.; Becker, A. C.; Blackman, J. W.; et al., 2007. Observational Constraints on the Nature of Dark Energy: First Cosmological Results from the ESSENCE Supernova Survey. *Astrophys. J.*, 666, 2 (Sep. 2007), 694–715. doi:10.1086/518642. (cited on pages 25, 35, 39, 40, and 46)

Yoo, A. B.; Jette, M. A.; and Grondona, M., 2003. *SLURM: Simple Linux Utility for Resource Management*, 44–60. Springer Berlin Heidelberg. ISBN 9783540397274. doi:{10.1007/10968987_3}. http://dx.doi.org/10.1007/10968987%5F3. (cited on page 67)

York, D. G.; Adelman, J.; Anderson, J. J. E.; Anderson, S. F.; Annis, J.; Bahcall, N. A.; Bakken, J. A.; Barkhouser, R.; Bastian, S.; Berman, E.; et al., 2000. The Sloan Digital Sky Survey: Technical Summary. *The Astron. J.*, 120, 3 (Sep. 2000), 1579–1587. doi:10.1086/301513. http://dx.doi.org/10.1086/301513. (cited on page 40)

Yuan, F.; Lidman, C.; Davis, T. M.; Childress, M.; Abdalla, F. B.; Banerji, M.; Buckley-Geer, E.; Carnero, R. A.; Carollo, D.; Castander, F. J.; et al., 2015. OzDES multifibre spectroscopy for the Dark Energy Survey: first-year operation and results. *Mon. Notices Royal Astron. Soc.*, 452, 3 (Jul. 2015), 3047–3063. doi:10.1093/mnras/stv1507. http://dx.doi.org/10.1093/mnras/stv1507. (cited on pages 79 and 105)

ZTF Bright Transient Survey, 2024. ZTF Bright Transient Survey — sites.astro.caltech.edu. Accessed 17-04-2024. (cited on page 50)

Zuntz, J.; Paterno, M.; Jennings, E.; Rudd, D.; Manzotti, A.; Dodelson, S.; Bridle, S.; Sehrish, S.; and Kowalkowski, J., 2015. CosmoSIS: Modular cosmological parameter estimation. *Astron. Comput.*, 12 (Sep. 2015), 45–59. doi:10.1016/j.ascom.2015.05.005. (cited on pages xiii, 58, 59, and 119)

Zwicky, F., 1933. Die Rotverschiebung von extragalaktischen Nebeln. *Helvetica Phys. Acta*, 6 (Jan. 1933), 110–127. (cited on page 6)